UC San Diego
UC San Diego Electronic Theses and Dissertations

Title
Carbon nanotubes : synthesis, characterization, and applications

Permalink
https://escholarship.org/uc/item/4r9754mx

Author
Deck, Christian Peter

Publication Date
2009

Peer reviewed|Thesis/dissertation

eScholarship.org Powered by the California Digital Library
University of California

UNIVERSITY OF CALIFORNIA, SAN DIEGO

Carbon Nanotubes: Synthesis, Characterization, and Applications

A dissertation submitted in partial satisfaction of the requirements for the degree

Doctor of Philosophy

in

Materials Science and Engineering

by

Christian Peter Deck

Committee in Charge:

Professor Kenneth S. Vecchio, Chair
Professor Prabhakar Bandaru
Professor Michael Heller
Professor Michael Sailor
Professor Frank Talke

2009

Copyright

Christian Peter Deck, 2009

All rights reserved

The dissertation of Christian Peter Deck is approved, and it is acceptable in quality and form for publication on microfilm and electronically:

_____

_____

_____

_____

_____

Chair

University of California, San Diego

2009

Dedication

To my Grandfathers

for introducing me to science,

And to my family and friends

for their support

Table of Contents

Signature Page……. iii

Dedication.....iv

Table of Contents v

List of Figures.....x

List of Tables.....xxxi

Acknowledgements xxxiii

Vita xxxv

Abstract.....xxxvii

1. Introduction 1

2. Background.....6

2.1 Discovery.....6

2.2 Description 8

2.2.1 Dimensions.....9

2.2.2 Chirality.....11

2.3 Material Properties 13

2.3.1 Mechanical Properties 13

2.3.2 Electrical Properties.....20

2.3.3 Optical Properties 24

2.3.4 Thermal Properties 27

2.4 Nanotube Formation Theory 29

2.4.1 Role of Carbon Source 41

2.4.2 Role of Catalysts 47
2.4.3 Effects of Substrate 53
2.4.4 Catalyst Poisoning and Growth Termination 66
2.4.5 Aligned Nanotube Growth 73
2.4.6 Alternate Nanotube morphologies 76
2.5 Nanotube Growth Methods 80
2.5.1 Chemical Vapor Deposition 81
2.5.2 Thermal Chemical Vapor Deposition 84
2.5.3 Floating Catalyst CVD 86
2.5.4 CVD Modifications 88
2.5.5 Other Growth Methods 89
2.5.5.1 Arc Discharge 90
2.5.5.2 Laser Ablation 91
2.6 Characterization of Carbon Nanotubes 93
2.7 Carbon Nanotube Applications 98
2.7.1 Nanotube-Based sensors 99
2.7.2 Macro-scale nanotube-based materials 102
2.7.2.1 Nanotube/Polymer Composites 103
2.7.2.2 Pure nanotube fibers and sheets 108
2.7.3 Nanotubes for Electronic Applications 119
2.7.4 Other Nanotubes applications 122
3. Procedure 125

3.1 Chemical Vapor Deposition Process 126
3.1.1 Floating Catalyst Growth 129
3.1.2 Thermal CVD Substrate Preparation 132
3.1.3 Thermal CVD with a liquid carbon source 135
3.1.4 Thermal CVD with a gaseous carbon source 137
3.2 Product Collection and Analysis 138
4. Results and Discussion 141
5. Nanotube Growth and Characterization 142
5.1 Floating Catalyst CVD Growth 143
5.1.1 Growth Rates 146
5.1.2 Growth Mechanism 149
5.2 Thermal CVD Growth 155
5.2.1 Growth Rates 160
5.2.2 Growth Mechanism 171
5.2.3 Growth Termination 180
5.3 Nanotube Characterization 185
5.3.1 Control of Carbon Nanotube Diameter 186
5.3.2 Ammonia Effects during Growth 201
5.3.2.1 Effects of Ammonia Concentration 204
5.3.2.2 Discussion of Growth Enhancement 205
5.4 Control of Bamboo Morphology 208
5.4.1 Nitrogen introduction via Pyridine 209

5.4.1.1 Pyridine and Ammonia Comparison 214
5.4.2 Effects of Nitrogen on Bamboo Morphology 218
5.4.3 Morphological control during growth 229
6. Nanotube Material Properties and Applications 239
6.1 Floating-Catalyst Characterization 240
6.1.1 TMA testing results 244
6.1.2 In-Situ testing results 247
6.1.3 Implications on Mat structure 248
6.1.4 Time-dependent responses 256
6.1.5 Electrical Resistance of CNT paper 259
6.2 Thermal CVD Characterization 265
6.2.1 In-Situ Mechanical Testing 266
6.2.2 Comparison of Thermal and Floating-Catalyst Growth 276
6.2.3 Optical Properties 281
6.2.4 Flexural Rigidity determination 285
6.2.4.1 Experimental Set-up and Results 286
6.2.4.2 Fluid Flow and Nanotube Deflection modeling 293
6.2.4.3 Determination of the Flexural Rigidity 299
6.2.4.4 Flow Sensors and Time-Dependent Response 306
6.3 Production of Bulk nanotube-based materials 310
6.3.1 CVD Optimization for Spinnable CNTs 313
6.3.2 Development and Results of Spinning Process 316

7. Conclusions 323

8. References 329

List of Figures

Figure 2-1: (a)-(c) Transmission electron microscope images of carbon nanotubes published by Iijima in 1991 [3], (d) progression of approximate number of carbon nanotube-related journal article publications annually (data from inspect article database). 7

Figure 2-2: Representations of short lengths of single-walled carbon nanotubes and atomic resolution STM image of a carbon nanotube [20, 21] 9

Figure 2-3: (left) Carbon nanotubes with 12mm length, uniformly grown over a 4" diameter substrate, (right) Current record 18mm long carbon nanotube array, grown at the University of Cincinnati [32] 10

Figure 2-4: (left) Illustration of Chiral vectors and Chiral angles on a two dimensional graphite sheet, (right) semi-conducting and metallic nanotubes [27] 11

Figure 2-5: Schematic diagram of two of the main chiralities of nanotubes showing a nanotube with (a) zigzag chirality and (b) armchair chirality [40]..... 13

Figure 2-6: Determination of the elastic modulus of a carbon nanotube by tensile testing using an AFM [57]..... 15

Figure 2-7: (left) Experimental and (right) simulation results showing modulus reduction with increasing carbon nanotube diameter [64, 66] 16

Figure 2-8: (a-d) Superplastic behavior of SWNT under tensile loading at 2000°C [69] (e) motion of Stone-Wales defects (shaded region) as mechanism for plasticity [68]..... 18

Figure 2-9: (a) Simulated SWNT deformations under bending [66, 73] and twisting [61], (b-d)TEM images of localized deformation in MWNTs [68] 19

Figure 2-10: (left) Stepwise current carrying breakdown in multi-walled carbon nanotubes exceeding the current carrying capacity, (right) Drop in current with successive removal of concentric shells [100, 101]. 22

Figure 2-11: (a) Absorbance vs. Energy for s-polarized light, (b) Absorbance vs. Energy for p-polarized light, (c), schematic showing direction of s- and p-polarization [111] 26

Figure 2-12: (a) Variation with absorbance with energy and alignment, (b) reduction in absorbance per unit length of nanotube mats decreasing with increasing growth showing improving alignment [111]. 27

Figure 2-13: Growth Mechanisms for carbon filaments from metal catalyst particles (a) Diffusion of carbon into and through catalyst particle during carbon fiber formation [7], (b)-(e) Carbon structures formed with decreasing catalyst size, from film to small particle. 33

Figure 2-14: (a) Carbon content in Fe catalyst particles during nanotube growth, super saturation is required prior to nanotube precipitation [154] (b) catalyst encapsulation, SWNT growth, or amorphous carbon deposition can occur depending on temperature [156]..... 34

Figure 2-15: Schematic of the various processes occurring during Carbon nanotube growth (a) carbon diffusion through surface layer, (b) formation of an

amorphous carbon surface coating, (c) completely coated, poisoned catalyst particle (adapted from [158]) 36

Figure 2-16: Potential energy per carbon atom as a function of number of atoms, plotted for a graphene structure and four nanotube structures [148]..... 37

Figure 2-17: TEM images of capped multi-walled carbon nanotubes [91]. 39

Figure 2-18: (a)-(d) Defect elimination sequences in the graphitic lattice [168], (e),(f) Potential lattice positions and energy levels for carbon atoms at the exposed edge of an uncapped carbon nanotube, relative to a free carbon atom [171]. 40

Figure 2-19: Average reported growth temperatures in CVD nanotube synthesis for common carbon sources [6, 35, 36, 63, 64, 78, 84, 87, 94, 95, 111, 128, 152, 162, 174, 181, 185-189, 192-261], Heat of Reaction values from [262] 44

Figure 2-20: Relationship between (left) nanotube growth and reaction temperature [198] and (right) growth rate and ethylene partial pressure [197]..... 45

Figure 2-21: (left) Gas composition during thermal cracking of propane as function of temperature, (right) Gas composition during Fe/Pd catalyst assisted decomposition of propane [183]..... 48

Figure 2-22: (left) Single-walled Nanotube diameter distributions produced using Co-Mo bi-metallic catalysts and thermal CVD [287], (right) Increases in average tube diameter with sulfur as a co-catalyst [286]. 51

Figure 2-23: (a-d) Evolution of Au thin film morphology with increasing deposition thickness, (e) Variation in particle size and spacing with average film thickness for two different deposition rates [303]. 56

Figure 2-24: Thin film morphology changes with increasing deposition: (a) Frank-van der Merwe 2-D film growth, (b) Stranski-Krastanov 2-D and 3-D growth, (c) Volmer-Weber 3-D growth, (d) schematic of processes occurring during thin film growth [304]. 57

Figure 2-25: (left) Ti substrate LEIS signal as a function of thickness of deposited metal, (right) schematic of deposited morphology as function of metal-oxide heat of formation [311]. 59

Figure 2-26: (a-d) Schematic of liquid-like particle coalescence process, (e) Effects of temperature on particle size, (f) Influence of heating time on particle size (Substrate interaction strength decreases from Al_2O_3 to SiO_2 to C) [313].. 61

Figure 2-27: (a) weak catalyst-substrate interaction, catalyst is too large for growth, (b) metal island is appropriate size and shape for growth, (c) metal-substrate interaction is too strong, growth does not occur, (d), excessive amorphous carbon deposition prevents growth. 63

Figure 2-28: Catalyst-substrate interaction models (a) Tip growth model with weak catalyst-substrate interaction forces, and (b) Root growth model with strong catalyst-substrate interaction forces [151]. 64

Figure 2-29: Root tip model of carbon nanotube growth demonstrating diffusion of carbon through substrate to reach catalytic particles [321]. 66
Figure 2-30: Typical plots of nanotube length as a function of reaction time, as reported by various groups [158, 179, 181, 189, 323, 324]. 67
Figure 2-31: (left) Continuous carbon fiber growth rate with intermittent hydrogen treatment during synthesis [6], (right) Constant growth rate obtained with water-assisted CVD [197]. 69
Figure 2-32: (a) Increased growth with water-assisted CVD [189], (b) Optimal water/C2H4 ratio determined by Futaba et al. [340] 71
Figure 2-33: Crowding mechanism for carbon nanotube alignment (a) initiation of growth with poor alignment (b) impingement and aligned growth. 74
Figure 2-34: Carbon nanotube alignment mechanism in an electric field [227, 350].. 76
Figure 2-35: (a-d) Formation mechanism of bamboo carbon nanotubes via tip growth, (e-f) formation of a partial bamboo compartment, (h-l) bamboo synthesis via base growth [360, 365]. 79
Figure 2-36: Progression of "world-record" carbon nanotube lengths with growth by various methods [31, 33-36, 87, 158, 188, 189, 214, 217, 221, 229-231, 246, 321, 323, 346, 389-391]. 84
Figure 2-37: Typical equipment set-up for thermal chemical vapor deposition growth of carbon nanotubes [403]. 85
Figure 2-38: Spray pyrolysis equipment set-up for vapor phase carbon nanotubes formation [242]. 88

Figure 2-39: Arc Discharge nanotube growth equipment with a horizontal orientation, showing deposit locations [281] 91
Figure 2-40: Typical laser ablation apparatus for production of carbon nanotubes, nanotubes are collected downstream from the argon flow [436]. 92
Figure 2-41: Typical Raman scan for multi-walled carbon nanotubes and a schematic of the in-plane vibration responsible for the G-peak [445] 95
Figure 2-42: (left) Wet spinning process for CNT-PVA fiber production, (right) examples of CNT composite fibers produced using this method [486]. 104
Figure 2-43: Carbon nanotube reinforcements in a polystyrene composite showing (a) nanotubes spanning the crack width, and (b) separation of nanotubes from matrix material after fracture [502]. 106
Figure 2-44: (left) Decrease in electrical resistance with increasing stretch-induced nanotube alignment, (right) improved thermal conductivity with increased alignment [508] 107
Figure 2-45: (left) Increase in electrical conductivity with increasing nanotube weight percent in CNT-PVA composites [512], (right) Thermal conductivity increase with nanotube content in CNT-epoxy composites [129]..... 108
Figure 2-46: Relationship between twist angle and yarn/fiber modulus ratio 110
Figure 2-47: (left) Direct spinning of carbon nanotube fibers and sheets from the CVD furnace, (right) SEM images of nanotube based ropes [239]. 111

Figure 2-48: Mechanical properties of direct spun SWNT ropes (left) Specific-stress-strain curves compared to Kevlar, (right) specific strength and stiffness comparison [240]. 112

Figure 2-49: Spinning yarns of carbon nanotubes from aligned nanotube mats, magnified views show twist angle and draw direction [201, 204] 113

Figure 2-50: Effects of CNT mat length (left) and CNT rope twist (right) on strength of CNT ropes [202] 114

Figure 2-51: (a) Variation in sheet resistance with original nanotube array length and nanotube diameter (influenced by the Fe catalyst film thickness) [519] (b) nanotube sheets as a source of polarized incandescent light [203] 118

Figure 2-52: Schematic (left) and Input-output curve (right) for a nanotube-based NOT gate [106]..... 120

Figure 2-53: (a)Carbon nanotube film sheet conductance increases with increasing nanotube concentration, inset shows percolation threshold at 6ml solution, (b) Optical transmittance drop with sheet resistance [109]. ... 122

Figure 3-1: Typical floating catalyst CVD setup for carbon nanotube growth..... 131

Figure 3-2: Schematic for thermal CVD nanotube growth with a liquid hydrocarbon source. Typical reaction parameters are given, and either bubbling or the needle/syringe method was used for hydrocarbon introduction. 136

Figure 3-3: Complete thermal CVD set-up for growth using gaseous carbon sources and real-time monitoring of water content 138

Figure 3-4: Sample carbon nanotube Raman spectra, with individual peak fits and peak fit sum, showing good agreement with Raman data 140

Figure 4-1: Examples of aligned carbon nanotube mats grown via floating catalyst CVD (left) and via thermal CVD (right) 141

Figure 5-1: Examples of floating catalyst CVD growth of aligned carbon nanotube mats using ferrocene and benzene, SEM and TEM imaging 145

Figure 5-2: Typical Raman spectra for nanotubes grown using floating catalyst CVD 145

Figure 5-3: Examples of nanotubes grown under alternate conditions (a,b) growth with Nickelocene and Cobaltocene, (c,d) growth with $FeCl_2$ and $CoCl_2$ and alcohol, (e) growth on Hydroxyapatite, (f) growth on Ti 6-4 foils. 146

Figure 5-4: Carbon nanotube mat length and growth rate as a function of reaction time for floating catalyst CVD synthesis..... 148

Figure 5-5: Long carbon nanotube mats grown using floating catalyst CVD, ~1mm length (left) and ~6mm length (right)..... 148

Figure 5-6: Results of sequential vapor phase CVD growth runs, the taller region was grown in the 1st run, shorter mat at base was produced by the 2nd run.. 151

Figure 5-7: (a,b) Multi-layered CNT mat, produced by pulsing reactants, (c) Bi-layered CNT mat produced by varying catalyst material, upper layer (grown first) was catalyzed using nickelocene, lower layer with ferrocene, (d) Bi-layer nanotube structure using cobalt and iron catalysts 152

Figure 5-8: Examples of (a) catalyst particles encapsulated within CNT walls and (b) diameter or growth direction changes occurring at catalyst particles ... 154

Figure 5-9: Examples of thermal CVD nanotube growth, TEM images show straight-walled and bamboo morphologies ... 157

Figure 5-10: Typical Raman spectra for straight-walled and bamboo nanotubes grown via thermal CVD ... 157

Figure 5-11: Thermal CVD growth with 5nm Fe film catalysts and various carbon sources: (a) acetone, (b) ethanol, (c) acetylene, and (d) xylene ... 158

Figure 5-12: (a) Growth using catalysts from cobalt-molybdenum acetate solutions, (b) catalysts from $Fe(NO_3)_3$ solutions, (c) TiC powder catalysts ... 159

Figure 5-13: Thermal CVD growth on various substrates (a) patterned using e-beam lithography, (b) TEM grid mask patterning, (c) 10nm Ni catalyst on 40nm Ti, (d) 10nm Ni catalyst on 20nm Ti on 90nm W ... 160

Figure 5-14: Nanotube length as a function of reaction duration, thermal CVD with ethylene carbon source and Fe catalyst ... 161

Figure 5-15: Nanotube growth length as a function of reaction time, thermal CVD with Fe and Ni catalysts and a benzene carbon source ... 163

Figure 5-16: Comparison of growth with two carbon introduction rates (Fe thin film catalyst and thermal CVD synthesis) ... 164

Figure 5-17: Growth rate as a function of thermal CVD reaction time for (a) Fe and Ni catalyst films using benzene, and (b) Fe catalyst films with ethylene ... 165

Figure 5-18: Nanotube length as a function of benzene introduction rate (Fe and Ni catalysts, constant reaction duration) 168

Figure 5-19: Nanotube length and Raman G:D peak ratios as a function of benzene introduction rates for Ni-catalyzed thermal CVD nanotube growth, error bars represent standard deviation in length measurements 169

Figure 5-20: Long thermal CVD nanotubes: (a) ~190μm long nanotubes grown using benzene with ammonia (b) ~200μm nanotube grown using ethylene... 171

Figure 5-21: Thermal CVD re-growth (Ni on SiO_2) (left) sample after 1st growth process and partially removed, (right) sample after 2nd growth process 173

Figure 5-22: Layered nanotube mats grown using 3nm (left) and 10nm (right) iron films on alumina on silicon substrates..... 174

Figure 5-23: Location of catalyst particles at tube ends for growth via tip growth with nickel catalysts on silicon wafer substrates 175

Figure 5-24: Relation between catalyst particle size and observed growth mechanism (Ni catalyst on quartz, single thermal CVD run)..... 176

Figure 5-25: Improvement in nanotube alignment from the top of the mat to the base... 180

Figure 5-26: Influence of ammonia on CNT growth via thermal CVD, (a) growth without ammonia and (b) growth with ~35% ammonia..... 181

Figure 5-27: Mats of nanotubes grown via thermal CVD showing reduced nanotube height within close proximity to the substrate edge 183

Figure 5-28: TEM images of nanotubes grown without NH_3 showing thick amorphous carbon sheaths coating a thin-walled inner nanotube 185

Figure 5-29: TEM images of carbon nanotubes grown via (a) floating catalyst CVD and (b,c) thermal CVD 186

Figure 5-30: Relation between catalyst film thickness and carbon nanotube diameter 188

Figure 5-31: (a) Catalyst distribution within a nanotube mat with thick metal films, (b) EDS composition map of a larger metal particle within a nanotube mat 190

Figure 5-32: Influence of growth substrate on carbon nanotube diameters, 3nm Fe catalyst films with C_2H_4 thermal CVD synthesis, SEM micrographs are at the same magnification 192

Figure 5-33: AFM scans and roughness measurements of 5nm Fe films as-deposited and after heating to 750C in argon (AFM scan scales are equal) 193

Figure 5-34: AFM surface roughness and particle size trends for 5nm Fe films on different substrate materials (a) and for varying Fe film thicknesses (b) 194

Figure 5-35: (a) AFM surface roughness and particle heights, (b) nanotube diameters using ethylene (750°C) and benzene (900°C), and AFM scans of Fe films after heating to 750°C (c, 50nm scale) and 900°C (d, 100nm scale) 195

Figure 5-36: Nanotube diameters as a function of reaction temperature (5nm Fe on alumina with ethylene) 197

Figure 5-37: Influence of benzene introduction rate on CNT inner and outer diameters 200

Figure 5-38: SEM and TEM thermal CVD results with ammonia added during different stages of growth 202

Figure 5-39: Raman spectra for CNTs growth via thermal CVD with no ammonia and ammonia added during different stages of the CVD process 203

Figure 5-40: (a) Raman Spectra for varying ammonia concentrations, (b) example SEM image of CNT growth at 50% ammonia, (c) Raman G:D: peak area ratios as a function of ammonia concentration 204

Figure 5-41: Thermal CVD results without ammonia, and with (a) nitrogen carrier gas, and (b) argon carrier gas 206

Figure 5-42: Thermal CVD results using a benzene carbon source and an argon reaction gas with low concentrations of (a) hydrogen, and (b) ammonia 206

Figure 5-43: TEM images of thermal CVD results, (a) pure Ar carrier gas, (b) Ar with low H_2 concentration, and (c) Ar with low NH_3 concentrations 207

Figure 5-44: (a) Vapor phase CVD growth using benzene with 1wt.% ferrocene, (b) growth with 10vo.% pyridine, and (c) growth with 1vo.% pyridine..... 210

Figure 5-45: TEM images of CNTs grown with ~1wt.% ferrocene and (a) 5% pyridine, (b) 10% pyridine, and (c) nanotubes grown with only benzene 210

Figure 5-46: Bamboo compartment orientation relative to catalyst particle location: transmission (left) and atomic number-contrast (right) imaging modes. 211

Figure 5-47: (a) Raman spectra for varying pyridine concentrations, (b) Mat length and Raman G:D peak hieght ratio as a function of pyridine concentration 212

Figure 5-48: Temperature controlled oxidation burn-off rate as a function of temperature and pyridine concentration in reactant solution..... 213

Figure 5-49: Growth of nanotube mats using thermal CVD with C_2H_4 and (a) only argon, (b) argon with ammonia, and (c) argon with pyridine 214

Figure 5-50: Nanotube structures using thermal CVD growth and (a) argon only, (b), argon with ammonia, and (c) argon with pyridine 214

Figure 5-51: Bamboo Nanotubes: (a) floating catalyst CVD with C_6H_6 and pyridine, (b) thermal CVD with C_2H_4 and pyridine, (c) thermal CVD with C_6H_6 and NH_3, and (d) thermal CVD with C_2H_4 and NH_3 215

Figure 5-52: Bamboo CNTs grown using floating catalyst CVD with ammonia (left) and pyridine (right) 217

Figure 5-53: (a) Outer diameter-Inner diameter ratios for tubes grown with pyridine and ammonia, (b) Raman spectra for nanotubes grown under various conditions, and (c) Raman G-D and 2D-D peak height ratios 218

Figure 5-54: Schematics of bamboo compartment formation mechanisms (lattice strain due to nitrogen incorporation and increased bulk carbon diffusion)..... 219

Figure 5-55: Average spacing between adjacent bamboo compartments as a function of ammonia concentration (left) and pyridine concentration (right) 221
Figure 5-56: Average compartment spacing normalized to tube diameter as a function of ammonia concentration (left) and pyridine concentration (right) 223
Figure 5-57: Effects of temperature on bamboo spacing (left), spacing normalized to tube diameter (right) 225
Figure 5-58: SEM and TEM images of a nanotube grown from a nitrogen-containing catalyst particle, magnified views show bamboo morphology 226
Figure 5-59: Variation of bamboo compartment spacing along nanotube length (measured from nanotubes pictured in Figure 5-58) 227
Figure 5-60: Nanotubes grown using floating catalyst CVD with controlled pyridine addition containing tubes with both straight and bamboo morphologies 231
Figure 5-61: (a) straight-walled nanotubes, and (b) a mixture of straight-walled and bamboo nanotubes produced during a single synthesis run 233
Figure 5-62: Transition from thin walled bamboo morphology (growth with ammonia) to thicker walled bamboo morphology (growth with pyridine) observed along the lengths of individual nanotubes 234
Figure 5-63: Raman spectra comparison between straight-walled, bamboo, and mixed nanotubes grown using thermal CVD 235
Figure 5-64: Raman spectra comparison between straight-walled, bamboo, and mixed nanotubes grown using floating catalyst CVD 237

Figure 6-1: Schematic showing compression and tension test configurations, with both parallel & perpendicular orientations 241

Figure 6-2: SEM Stage Attachment: either the blade attachment (a) or a load cell attachment (b) can be used, sample is held at (c) with rotation and 2-axis motion control independent of blade/load cell attachment..... 242

Figure 6-3: Cutting sequence, arrows show sample movement (a) sample is positioned and moved into blade, (b) sample is pulled away from blade, Sectioning off a portion of the CNT mat, (c) example of final cut sample. 243

Figure 6-4: (a) Carbon nanotube compressive stress-strain response, loaded parallel to tube axis (b) Average carbon nanotube compressive stress-strain response in both parallel and perpendicular orientations 244

Figure 6-5: Average Nanotube Tensile Stress-Strain response, TMA tests..... 245

Figure 6-6: (a) SEM image of CNT mat showing low tube density and tube spacing, and (b) TEM micrograph showing tube inner and outer diameter variation 246

Figure 6-7: Comparison of strain calculated from micrometer position and strain measured directly from nanotube mat sample, tension tests 247

Figure 6-8: In-Situ Carbon Nanotube Tension and Compression Stress-Strain Results (Stresses corrected for actual area)..... 248

Figure 6-9: Strain recovery in Carbon Nanotube mats between Compression tests, Values next to data points indicate % strain recovered from previous test. 249

Figure 6-10: Large scale buckling of carbon nanotube mats observed in compression... 251

Figure 6-11: (a) SEM micrograph of glue failure, (b) micrograph of nanotube mat after failure under tensile loading, (500 µm scale), (c),(d) failure surface of CNT mat, showing loose nanotube ends caused by nanotube slip and pull-out (20µm scale bars)..... 252

Figure 6-12: Time dependent response of nanotube mats; in the tension test, each strain step is ~0.1% strain, in compression, each strain step is ~2%..... 256

Figure 6-13: (a), (b), and (c) Maxwell Stress relaxation plots for tension, compression, and unloading, (d) Relaxation Modulus plotted against strain for two compression tests..... 259

Figure 6-14: (a) Schematic showing fabrication of (b) carbon nanotube paper..... 262

Figure 6-15: (a) Two-point resistance measurement schematic, (b) CNT paper resistance as a function of probe spacing 263

Figure 6-16: (a) CNT paper resistance as a function of nanotube mass and catalyst concentration used during growth (b) contact resistance vs. iron content 263

Figure 6-17: (a) Nanotube paper resistance as a function of tube morphology, (b) TEM image of a bamboo nanotube, showing wall angle measurement 265

Figure 6-18: (a) Schematic of load cell and straining apparatus used for in-situ compression testing of thermal CVD grown carbon nanotube mats, (b) magnified view of probe tip with ~1mm^2 cross-sectional area 269

Figure 6-19: Compressive stress-strain response of Thermal CVD grown nanotubes 270

Figure 6-20: Buckle formation during compression of thermal CVD grown nanotubes 271

Figure 6-21: Recovery of Thermal CVD nanotubes after compression to 79% strain 271

Figure 6-22: Displacement of nanotube mat adjacent to probe indentation..... 272

Figure 6-23: (a) Measured deflections of CNT mats as a function of distance from the probe edge for a loading and unloading test sequence, positive positions represent regions of the mat which are not directly compressed and distances are measured away from the probe edge] 274

Figure 6-24: (a),(b) SEM images taken during compression testing, showing probe and sample deflections, (c),(d),(e) SEM stage, sample holder dimensions, and M/EI values along sample holder height 275

Figure 6-25: (a) Time-dependency observed for the relaxation modulus in thermal CVD nanotubes, (b) variation of relaxation modulus with strain for loading and unloading 276

Figure 6-26: Compressive stress-strain reponse of carbon nanotubes grown using floating-catalyst CVD (FC-CVD) and thermal CVD (T-CVD) 277

Figure 6-27: (a),(b) SEM image and schematic showing compression and buckling in mats of floating catalyst CVD nanotubes, (c),(d) Compression and buckling in thermal CVD nanotube mats 279
Figure 6-28: Comparison of FC-CVD and thermal CVD nanotubes in compression (a) Average percent stress relaxation during each strain step, (b) Time-dependent variation in relaxation modulus for loading and unloading . 280
Figure 6-29: Equipment schematic for nanotube light polarization experiments 282
Figure 6-30: Normalized transmitted laser intensity as a function of polarizer angle, green curve shows control sample (no nanotubes), red and blue curves show results for nanotube samples at two different positions. 283
Figure 6-31: Relationship between angle of minimum transmitted intensity and nanotube orientation (relative to the plane of polarization of the incident laser) 284
Figure 6-32: (a-c) Patterned nanotube mats, comprising vertically aligned multiwalled nanotubes, with 38μm, 19μm, and 5μm pattern sizes were grown on quartz substrates through chemical vapor deposition. 287
Figure 6-33: A schematic of the experimental set-up for observing the nanotube deflections, during fluid flow, through the transmitted laser intensity variations and CCD image processing. 288
Figure 6-34: (a) Schematic of sample arrangement: The substrate with nanotubes was installed at the center of the quartz tube (b) and (c) show CCD images taken of the sample through the tube (b) and through the flat plate (c) 289

Figure 6-35: (a) Schematic of coverage-related transmitted laser intensity drop, (b) the transmitted laser intensity is reduced by 51.8% and 32.3% when CNTs were arrayed in mesh pattern with 50.2% and 35.2% coverage, respectively..... 290

Figure 6-36: Schematic of the CNT arrays shows of the effect of fluid flow on aligned CNT mat patterns. The displacement d is correlated with a measured variation in the transmitted laser intensity. The representative laser spot is colored in red and the dark squares are CNT ensembles..... 290

Figure 6-37: (a) The variation in the transmitted laser intensity is a very sensitive function of the fluid velocity, and can be used for (b) digital calibration of the flow. (c) The data points show a decrease in the transmission with increased nanotube deflection caused by fluid motion..... 292

Figure 6-38: The images captured by CCD (from the top of CNT samples, with focal plane at CNT tips) when the flow velocity is (a) 0 m/s and (b) 30 m/s The images show a CNT deflection of ~ 2 μm under the flow. 292

Figure 6-39: The shearing of carbon nanotube arrays, can be modeled as cantilevers through solid mechanics (the outlines depict the close correspondence between the theory and experimentally observed shear)..... 296

Figure 6-40: (a-c) Simulations of fluid velocity, drag force, and CNT deflection along CNT height for CNTs placed 2 and 100 μm from the leading edge of the substrate. (d-f) Simulations of flow velocities of 10 m/s and 30 m/s, for CNTs 100 μm away from the leading edge..... 299

Figure 6-41: (a) Deflections of CNT mats obtained through laser intensity variations, plotted as a function of air velocity, for five different CNT samples. (b) The deflections were also measured through CCD image processing, and were compared using the same EI value fitted from (a)..... 301

Figure 6-42: Our experimental results are modeled well by considering a Knudsen number (Kn) modified Stokes-Oseen expression and appropriate molecular dynamics and fluid mechanics simulations 306

Figure 6-43: Deflections calculated via light transmission as a function of flow velocity of air and Ar were plotted and compared. A fit relating deflection to air velocities was scaled by the ratio of the density of argon to the density of air.. 307

Figure 6-44: Time-dependent recovery observed in aligned carbon nanotube mats subjected to fluid drag forces 309

Figure 6-45: (a) SEM image of "spinnable" CNTs, (b) TEM image of bamboo CNTs grown in this work, (c) TEM images of "spinnable" CNTs [263] 311

Figure 6-46: (a) "spinnable" carbon nanotubes, (b) thicker, bamboo nanotubes grown using the 2006 CVD recipe, (c) improved growth using the 2008 recipe... 316

Figure 6-48: Apparatus designed for in-situ nanotube spinning attempts..... 318

Figure 6-49: (a) low magnification view of metal probe tip, (b) spinning probe, (c) magnified view of probe tip showing roughened surface 318

Figure 6-50: In-situ spinning results for floating catalyst CVD nanotubes 319

Figure 6-51: Dual linear translation stages used to adjust sample and probe positions during spinning and drawing attempts 320
Figure 6-52: Results of spinning and drawing attempts using (a) a wooden toothpick probe, and (b) adhesive tape 321

List of Tables

Table 2-1: Summary of types of carbon nanotubes and their electrical behavior as determined by their chirality and chiral vectors [27, 38]. 12

Table 2-2: Comparison of modulus, tensile strength, and density of carbon nanotubes and other selected materials 16

Table 2-3: Activation energies for the growth of carbon filaments and the diffusion of carbon through selected metal catalysts [8, 9] 30

Table 5-1: Parameters used for Floating Catalyst CVD carbon nanotube growth.. 144

Table 5-2: Summary of Floating Catalyst CVD Growth parameters used 147

Table 5-3: Reaction parameters used for thermal CVD nanotube growth..... 156

Table 5-4: Summary of Thermal CVD Growth parameters, gaseous carbon source 161

Table 5-5: Summary of synthesis conditions for Thermal CVD, liquid carbon source 162

Table 5-6: Floating catalyst CVD growth recipe with Pyridine addition 209

Table 5-7: Thermal CVD growth parameters with Pyridine addition 213

Table 5-8: Floating catalyst CVD growth recipe with Ammonia..... 216

Table 6-1: Summary of modulus results for nanotube mats. Corrected in-situ results have been adjusted to remove stress relaxation effect. Relaxation data has been corrected for the small (~5%) relaxation due to equipment used. 258

Table 6-2: Summary of compressive testing results for floating catalyst and thermal CVD nanotube samples 281

Table 6-3: Growth conditions for CNT mats used in flexural rigidity experiments 287

Table 6-4: Characteristic length scales used to simulate fluid flow through nanotube arrays 293

Table 6-5: Boundary Conditions used to calculate nanotube deflections 297

Table 6-6: Nanotube sample dimensions, positions on substrate, and velocity ranges used for deflection measurement tests 300

Table 6-7: Comparison of important CVD synthesis parameters for reported "spinnable" CNTs and our method 311

Table 6-8: Comparison of nanotube properties for spinnable CNTs [189, 201, 203, 204, 263], and nanotubes grown using two different methods in this work 316

Acknowledgements

This work would not have been possible without the help and support of numerous people, both at UC San Diego and in my personal life. I would like to acknowledge the assistance and guidance of my advisor, Dr. Kenneth Vecchio during the course of my graduate work. He has provided valuable discussion and direction throughout my research. Professor Prabhakar Bandaru has also been a great source of help during this work, and my collaboration with him on the measurement of the flexural rigidity of nanotube mats has been very rewarding. Professor Frank Talke was very generous in providing access to his lab for Raman spectrometry. In addition, I would like to thank the two other members of my committee, Professors Michael Heller and Michael Sailor, for their time and assistance.

I would also like to acknowledge the contributions provided by my fellow graduate students at UCSD, and the other members of Dr. Vecchio's lab. During the course of this research I have worked closely with Erik McKee (Vecchio lab), Chinung Ni (Bandaru lab), and Ralf Brunner (Talke lab). Erik and I worked closely together on nanotube synthesis and characterization during almost the entire course of my research, and I appreciate his help in the lab and our collaboration on various projects and papers. My investigation of the flexural rigidity of carbon nanotube mats was performed in cooperation with Chinung, and his excellent work on the optical measurements was invaluable to this project. My collaboration with Ralf began very early during my research, and his help with nanotube synthesis and Raman measurements is greatly appreciated. I would also like to thank the other members of

Dr. Vecchio's lab. Fengchun Jiang, Raghav Adharapurapu, Justin Cheney, Zhang Xing, Hesham Khalifa, and Robb Kulin have been an important source of support, camaraderie, and inspiration during the course of my research.

In addition to my advisors and co-workers, none of this research would have been possible without the help and support of my friends and family. I would like to thank my parents, Peter and Kathy, my brother Jon, my sisters Anna and Katherine, my grandparents and extended family, and Kersten Wehde for being so understanding, patient, and supportive during my studies.

Chapter 5, in part, is a reprint of the material as it appears in "Synthesis Optimization and Characterization of Multiwalled Carbon Nanotubes", in Journal of Electronic Materials, v.35, n.2, pp.211-223, 2006, Deck, Christian P.; McKee, Gregg S.B.; and Vecchio, Kenneth S. The dissertation author was the primary investigator and author of this paper.

Chapter 6, in part, is a reprint of the material as it appears in "Mechanical behavior of ultralong multiwalled carbon nanotube mats", in Journal of Applied Physics, v.101, 023512, 2007, Deck, Christian P.; Flowers, Jason; McKee, Gregg S.B.; Vecchio, Kenneth S.; and "Optical Determination of the Flexural Rigidity of Carbon Nanotube Ensembles", *Applied Physics Letters,* v.92, 173106, 2008, Deck, Christian; Ni, Chinung; Vecchio, Kenneth; Bandaru, Prabhakar R. The dissertation author was the primary investigator and author of these papers.

Vita

2002	Bachelor of Science, University of California, San Diego
2003-2009	Teaching Assistant, Department of Mechanical Engineering University of California, San Diego
2004	Master of Science, University of California, San Diego
2009	Doctor of Philosophy, University of California, San Diego

Publications

Deck, C. P. and Vecchio, K. S., "Growth of Well-Aligned Carbon Nanotube Layers in Successive Layers", **J. Phys. Chem. B**, v.109, pp.12353-12357, 2005

Deck, C. and Vecchio, K. S., "Growth Mechanism of vapor phase CVD-grown Multi-walled carbon nanotubes", **Carbon**, v.43, pp.2608-2617, 2005

Deck, C. and Vecchio, K. S., "Prediction of Carbon Nanotube growth success by the analysis of carbon-catalyst binary phase diagrams", **Carbon**, v.44, pp.267-275, 2006

Deck, C. P., McKee, G. S. B., and Vecchio, K. S., "Synthesis Optimization and Characterization of Multiwalled Carbon Nanotubes", **Journal of Electronic Materials**, v.35, n.2, pp.211-223, 2006

Deck, C. P., Flowers, J., McKee, G. S. B., and Vecchio, K. S., "Mechanical Behavior of Ultra-long Multi-walled Carbon Nanotube Mats", **Journal of Applied Physics**, v.101, n.2, 023512, 2007, *selected for the Virtual Journal of Nanoscale Science & Technology, 02-05-2007*

Ni, C., Deck, C. P., Vecchio, K. S., and Bandaru, P., "Carbon Nanotube-Based Fluid Flow/Shear Sensors", in *Nanowires and Carbon Nanotubes - Science and Applications*, edited by P. Bandaru, M. Endo, I.A. Kinloch, A.M. Rao (Mater. Res. Soc. Symp. Proc. **963E**, Warrendale, PA, 2007), 0963-Q23-03

Nichols, J. A., Saito, H., Deck, C. P., and Bandaru, P., "Artificial introduction of defects into vertically aligned multiwalled carbon nanotube ensembles: Application to electrochemical sensors", **Journal of Applied Physics**, v.102, n.6, 064306, 2007, *selected for the Virtual Journal of Nanoscale Science & Technology, 10-15-2007*

Deck, C., Ni, C., Vecchio, K. S., and Bandaru, P. R., "Optical Determination of the Flexural Rigidity of Carbon Nanotube Ensembles", **Applied Physics Letters**, v.92, n.17, 173106, 2008, *selected for the Virtual Journal of Nanoscale Science & Technology, 05-12-2008*

Professional Societies

The Materials Research Society (2004)
President, UC San Diego Chapter, 6/07-current
Treasurer, UC San Diego Chapter, 9/04-current

The Minerals, Metals, and Materials Society (TMS) (2004)

Tau Beta Pi, National Engineering Honor Society (2002)

Fields of Study

Major Field: Materials Science and Engineering

Studies in Mechanical Engineering and Nanotechnology

Professors Kenneth S. Vecchio and Prabhakar Bandaru

ABSTRACT OF THE DISSERTATION

Carbon Nanotubes: Synthesis, Characterization, and Applications

by

Christian Peter Deck

Doctor of Philosophy in Materials Science and Engineering

University of California, San Diego, 2009

Professor Kenneth S. Vecchio, Chair

Carbon nanotubes (CNTs) possess exceptional material properties, making them desirable for use in a variety of applications. In this work, CNTs were grown using two distinct catalytic chemical vapor deposition (CVD) procedures, floating catalyst CVD and thermal CVD, which differed in the method of catalyst introduction. Reaction conditions were optimized to synthesize nanotubes with desired characteristics, and the effects of varying growth parameters were studied. These parameters included gas composition, temperature, reaction duration, and catalyst and

substrate material. The CNT products were then examined using several approaches. For each CVD method, nanotube growth rates were determined and the formation and termination mechanisms were investigated. The effects of reaction parameters on nanotube diameters and morphology were also explored to identify means of controlling these important properties.

In addition to investigating the effects of different growth parameters, the material properties of nanotubes were also studied. The floating catalyst CVD method produced thick mats of nanotubes, and the mechanical response of these samples was examined using in-situ compression and tension testing. These results indicated that mat structure is composed of discontinuous nanotubes, and a time-dependent response was also observed. In addition, the electrical resistance of bulk CNT samples was found to increase for tubes grown with higher catalyst concentrations and with bamboo morphologies. The properties of nanotubes synthesized using thermal CVD were also examined. Mechanical testing was performed using the same in-situ compression approach developed for floating catalyst CVD samples. A second characterization method was devised, where an optical approach was used to measure the deflection of patterned nanotubes exposed to an applied fluid flow. This response was also simulated, and comparisons with the experimental data were used to determine the flexural rigidity of these CNT arrays.

In this work, two potential applications for carbon nanotubes were also considered. Using the experimental method employed for flexural rigidity measurements, a carbon nanotube-based fluid flow sensor that offered fast response

and repeatability was demonstrated. There is also great interest in CNTs for high strength applications, and the growth of nanotubes for the spin-processing of CNTs into micron-scale fibers was also investigated.

1. Introduction

Carbon nanotubes are an exciting form of carbon, which, despite their relatively recent discovery, have generated tremendous interest within the materials science community. Much effort has focused on the understanding of the synthesis and formation of these structures, and on the measurement of their impressive properties. This work has directly led to the discovery and demonstration of numerous applications that utilize the unique aspects of this material. The structure of carbon nanotubes resembles a graphene sheet rolled upon itself, forming tubes with diameters in the nanometer range. The synthesis of this material is relatively straightforward, and well-aligned forests of nanotubes can be grown using simple chemical vapor deposition techniques. Continuing refinements to the nanotube synthesis process have resulted in a steady progression of the lengths of these structures, which can currently reach centimeter-scales, and commercial production of bulk nanotubes has brought the cost of these tubes down significantly.

Ultimately, the import of this material beyond the field of nanotechnology will be determined in part by the use of nanotubes in applications. Whether these applications take advantage of the mechanical, electrical, or other properties of carbon nanotubes, the ability to understand and carefully control their growth will be critical. In this work, carbon nanotubes were grown using several variations of a catalytic chemical vapor deposition process, and the effects of different reaction parameters were examined. The nanotube products were characterized using a combination of approaches, including scanning and transmission electron microscopy, atomic force

microscopy, Raman spectroscopy, and several novel methods of mechanical and optical testing.

This paper begins by providing an extensive review of carbon nanotubes. Their discovery and material properties are explained, and their physical structure is described. The growth mechanism of carbon nanotubes is presented, including descriptions of the roles of the carbon source, the catalyst, and the substrate. The processes by which aligned growth and growth termination occurs, as well as the formation of different structure is also explained. Chemical vapor deposition, the most commonly used method for carbon nanotube synthesis, is described in detail, along with several modifications to this growth process and some alternate synthesis methods. The background section concludes by detailing some common characterization techniques in addition to a number of potential applications and industries in which carbon nanotubes may be used.

While all the nanotubes studied in this work were grown using chemical vapor deposition (CVD) techniques, three distinct variations to this process were used, which differing primarily in the methods of reactant introduction. Catalyst material was either introduced in solution with the carbon source (floating catalyst CVD) or deposited prior to growth (thermal CVD, usually as a thin film), and either liquid or gaseous carbon sources were used. After these methods for nanotube synthesis have been described, the results are presented, and have been separated into several sections.

The first experiments done in this work were focused on the optimization of various growth parameters for each other CVD variations. These parameters included reactant gas composition and flow rate, reaction temperature, and reaction duration. Significant differences were observed between nanotubes produced using these methods, and for each approach, growth rates were determined and nanotube growth mechanisms identified using electron microscopy. The effects of catalyst metal, thickness, and substrate material were then investigated, specifically to discover the influence of these parameters on nanotube diameters. These reaction variables, in addition to carbon introduction rate and temperature were all found to significantly impact catalyst particle sizes and corresponding nanotube diameters, and method to manipulate these parameters to control diameter were explored.

One additional parameter, the reaction gas composition, was found to play a very significant role in nanotube synthesis. In particular, thermal CVD growth using liquid carbon sources was found to significantly improve (through a reduction in amorphous carbon deposition) upon the addition of ammonia to the reaction. The mechanism for this improvement was investigated, and an additional effect of the ammonia addition, the formation of nanotubes with bamboo morphology, was also identified. Two mechanisms have been proposed to explain the growth of nanotubes with bamboo morphology, and a series of experiments were performed to determine which mechanism was acting in this work. Several variations to the standard nanotube growth conditions were identified as methods to provide control over nanotube morphology (for the formation of either straight-walled or bamboo tubes).

In addition to exploring the effects of different reaction parameters on the growth of carbon nanotubes, several approaches were used to characterize the material properties of these tubes. The nanotubes studied in this work were divided according to the synthesis method used for their growth, and specific aspects (such as longer mats with floating-catalyst growth or patterning with thermal CVD) made some of the characterization techniques better suited for certain tubes. For longer mats of floating-catalyst nanotubes, an apparatus was designed to perform compression and tension testing in-situ inside a scanning electron microscope. The results form this work provided modulus values for these samples, and also led to the discovery of a time-dependent response. In particular, the tensile response indicated that the structure of the long nanotube mats produced using this synthesis method was similar to that of nanotube yarns or strands (rather than continuous nanotubes spanning the mat height). Due to the large quantity of nanotube product obtained using the floating catalyst synthesis method, bulk nanotube samples were also produced and simple electrical resistance measurements were performed. This work was focused on the effects of impurities and different tube morphologies on their electrical properties.

Nanotubes grown using thermal CVD were also characterized, using some techniques similar to those used for floating catalyst nanotubes, as well as some new approaches. These nanotubes could not be grown to the same heights as those produced using floating catalyst methods, and as a result, only limited tests could be performed with the in-situ straining apparatus in the SEM. Difficulties in sample attachment excluded tensile tests; however, compression testing was performed and

the responses of tubes grown using various CVD methods were found to differ significantly. In addition to direct compression testing, the optical properties of these samples were studied, and from this work a novel mechanical characterization process was developed which used variations in transmitted laser intensities to measure deformation. In this approach, nanotube deflections under applied fluid flows were measured, and these results were correlated with simulations of the fluid flow and tube deformations. An extension of this experiment led to the demonstration of a nanotube-based device for fluid flow and shear force sensing applications.

The final set of experiments performed in this work involved the adjustment of synthesis parameters to produce nanotubes that were more well-suited for processing into macroscopic nanotube-based materials. This post-growth processing can be used to produce nanotube ropes and sheets, and has been reported by several groups in the literature. An optimization of our growth procedure was performed in order to more closely match the characteristics of our tubes (length, diameter, and morphology), to those reported in these other studies, and several devices were constructed to attempt the processing of these tubes into ropes and sheets.

This dissertation concludes with a summary of the main discoveries in this work, and some thoughts on potential avenues of future research.

2. Background

Even though carbon nanotubes were only discovered fairly recently, they have generated great interest within the materials science community, and there has been an extensive amount of research performed in this area. The focus of this work has ranged from studying the properties and formation mechanisms of nanotubes to optimizing growth methods and investigating numerous potential applications. Accordingly, this background Section will explain the catalyst-assisted formation mechanism of carbon nanotubes and describe common nanotube synthesis techniques and some nanotube-based applications. For the latter portion, the most emphasis will be placed on the chemical vapor deposition (CVD) synthesis method used in this work and the specific applications researched; other growth methods and applications will be briefly mentioned. Additionally, for some of the results and discussion Sections in this dissertation, a brief background summary will be included when necessary, providing a review of information particularly relevant to each specific topic.

2.1 Discovery

Until the early 1980's, elemental carbon was known to exist in only three forms, as amorphous carbon and in crystalline forms of diamond and graphite. In 1985, Kroto *et al.* observed a large number of clusters of sixty carbon atoms in the soot generated by the laser vaporization of a graphite target [1]. This new, stable form of carbon, called C_{60}, or buckminsterfullerene, existed in the form of a hollow carbon cage. In addition to C_{60}, a number of other stable fullerenes were discovered, and a

large amount of research was performed in this new field. An improved method for the production of these molecules was proposed in 1990, which created fullerenes from carbon vaporized by an electric arc between two graphite electrodes [2].

In 1991, while performing research on fullerenes grown using this new arc discharge technique, fibrous soot deposited on the cathode of the apparatus was analyzed by a group led by Sumio Iijima [3]. Figure 2-1a-c shows these filamentary structures, and this report is widely referred to as the first published images of carbon nanotubes. Following this article, the level of interest and the amount of research conducted on carbon nanotubes has increased steadily (Figure 2-1d).

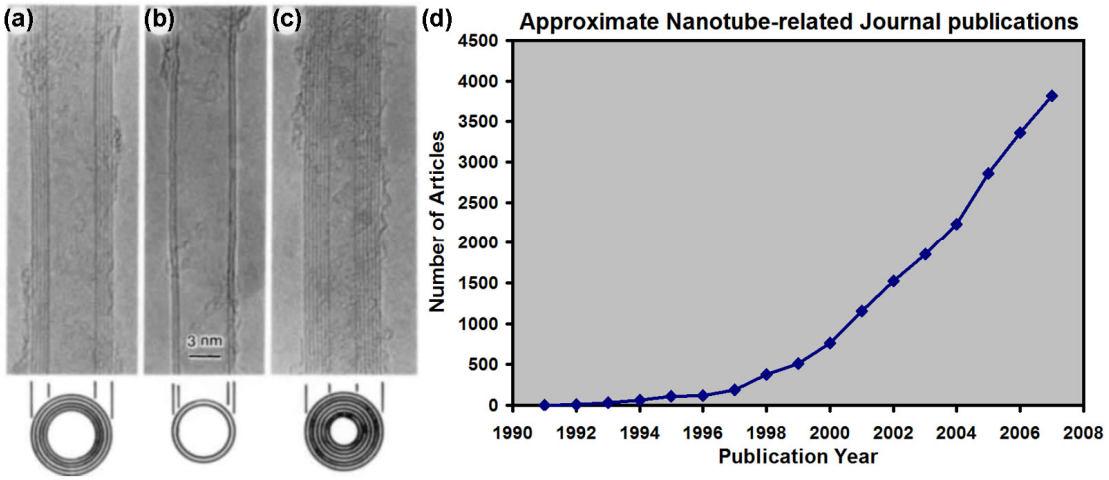

Figure 2-1: (a)-(c) Transmission electron microscope images of carbon nanotubes published by Iijima in 1991 [3], (d) progression of approximate number of carbon nanotube-related journal article publications annually (data from inspect article database).

While this 1991 report sparked the explosion of interest and research in these nano-structures, nano-scale carbon filaments and tubes had been reported previously. Carbon nanotubes had been produced as early as 1952 during research into carbon filament formation [4]. Bacon reported on the growth of carbon filaments with

diameters less than 100nm and proposed a growth mechanism in 1960 [5], and Baker *et al.* produced metal-catalyzed carbon filaments as small as 15 nm diameter starting in 1972 [6-10]. Oberlin *et al.* reported hollow carbon filaments with diameters ranging from 2nm to 50nm in 1976, including what could possibly be the first published image of single-walled nanotubes [11]. The first confirmed reports of single-walled nanotubes did not occur until 1993, when they were synthesized using the arc discharge technique and independently reported by Bethune *et al.* [12] and Iijima *et al.* [13].

These structures are also naturally occurring and carbon nanotubes and other fullerenes have not only been found on earth, but have actually existed for millions and millions of years. Fullerenes have been observed in pre-Cambrian rock [14], glassy rocks formed by lightning strikes [15], and in a 1.85 billion year old meteorite impact crater [16]. Carbon nanotubes have been found in the soot deposited by burning pine wood [17], in 400 year old Damascus steel sword blades [18], and in 10000 year old ice [19].

2.2 Description

Carbon nanotubes can be classified using several different methods, but the most common distinction made between nanotubes is in regards to the number of walls in the tube. By this criteria nanotubes can fall into two main categories; they are either single-walled nanotubes (SWNTs) consisting of a tube with a wall thickness of only one carbon atom, or multi-walled nanotubes (MWNTs) composed of many concentric tubes or shells. In either case, the walls of the tubes are made of sheets of

carbon atoms arranged in a hexagonal lattice, with a carbon atom sitting at each corner of each hexagon, the same as in a graphite sheet. Figure 2-2 illustrates a model of two short lengths of carbon nanotubes and an atomic resolution scanning tunneling microscopy (STM) nanotube image, showing the hexagonal graphitic structure of the tubes. Nanotubes typically have extremely high aspect ratios, and in some situations can be considered as essentially one-dimensional molecules.

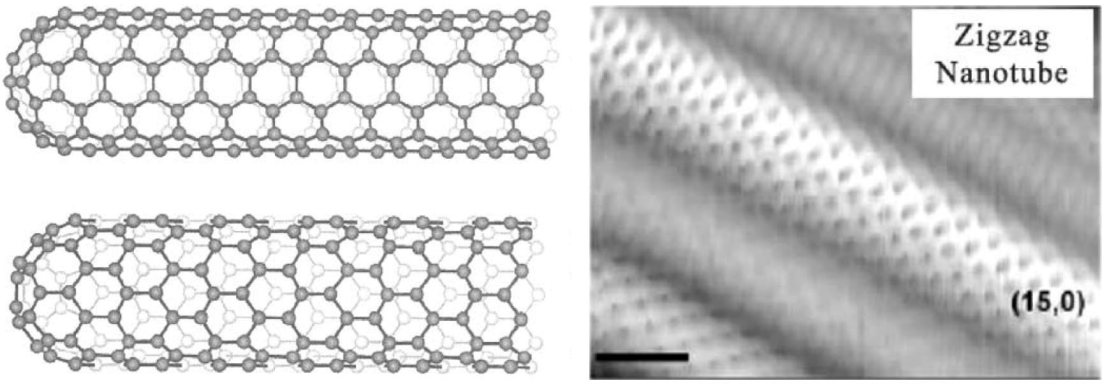

Figure 2-2: Representations of short lengths of single-walled carbon nanotubes and atomic resolution STM image of a carbon nanotube [20, 21]

2.2.1 Dimensions

Many of the interesting properties of carbon nanotubes stem from the fact that they are essentially one-dimensional molecules. Single-walled carbon nanotubes range in diameter from 0.4nm to as high as 6.0nm [22, 23], and diameters of multi-walled nanotubes, which can be composed of numerous of concentric tubes, can grow as large as roughly 100nm [24, 25]. The distance between these layers is equal to 0.34nm, the same as the spacing distance between graphite sheets [26]. The carbon-carbon inter-atomic spacing in nanotubes is also equal to that in graphite, or 0.142nm [27]. While very high aspect ratio carbon structures can form with diameters larger

than 100nm (diameters approaching millimeter scale [28]), these tend to exhibit different structures than multi-walled carbon nanotubes (such as a scroll-like structure [5] or a hollow core with an amorphous or graphitic sheath [29]), and are typically called carbon filaments or carbon fibers [6, 9, 10]. Depending on growth conditions, carbon nanotubes have been grown to significant lengths, and the record for the longest nanotubes reported has been broken and re-broken many times [30, 31]. The current "record" length is 18mm [32-34] for mats of aligned tubes (as shown in Figure 2-3), and 4cm and 10cm for individual single- and multi-walled tubes, respectively [35, 36].

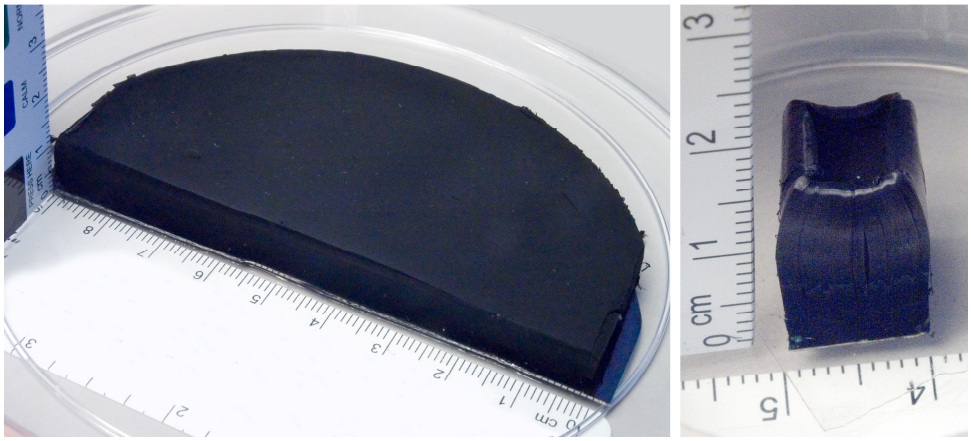

Figure 2-3: (left) Carbon nanotubes with 12mm length, uniformly grown over a 4" diameter substrate, (right) Current record 18mm long carbon nanotube array, grown at the University of Cincinnati [32]

With additional refinements in growth techniques, the maximum length of nanotubes is likely to continue to increase. Nanotubes can also be grown in alternate morphologies, including a bamboo structure and in branched structures; these are discussed in Section 2.4.5.

2.2.2 Chirality

The dimensions of a carbon nanotube, as well as the absence of defects in its structure are the most critical factors for potential mechanical applications. However, with regards to the electrical properties of a nanotube, the chirality of the tube is perhaps the most important property. Chirality describes the orientation of the hexagonal lattice of the graphite sheets relative to the axis of the tube, and this has many implications to the electrical properties of the nanotube. These differences in the orientation of the lattice can be noted in terms of two vectors, which describe how a graphene sheet could be rolled to form a nanotube, as shown in Figure 2-4.

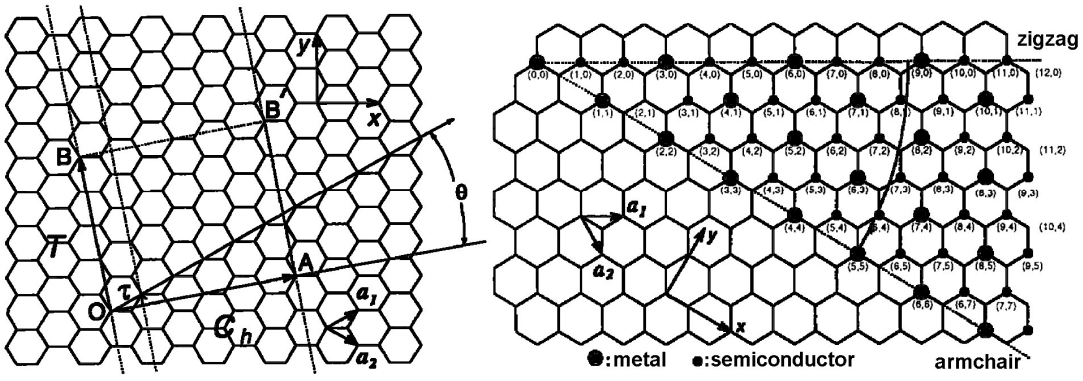

Figure 2-4: (left) Illustration of Chiral vectors and Chiral angles on a two dimensional graphite sheet, (right) semi-conducting and metallic nanotubes [27]

In the example depicted in Figure 2-4, a carbon nanotube would be formed by rolling the graphite sheet to connect point A to the origin ("O") and point B' to point B. The chirality of a tube is determined by the direction of the vector connecting the origin to point A and is defined as a sum of integer multiples of the lattice vectors a_1 and a_2. This can be written in short as the integers, (n,m), as shown in Equation (2-1)

[27, 37], and these constants can also be used to calculate the diameter of the resulting nanotubes as well as the chiral angle (Equation (2-2) [37] and Equation (2-3) [27], respectively). In these Equations, $\alpha_{C\text{-}C}$ is equal to the inter-atomic carbon-carbon spacing (1.421 Å in graphite), or the length of the unit vectors a_1 or a_2 divided by the square root of three.

$$C = n\vec{a}_1 + m\vec{a}_2 \equiv (n, m) \qquad (2\text{-}1)$$

$$d = \frac{\sqrt{3}a_{C-C}\sqrt{n^2 + nm + m^2}}{\pi} \qquad (2\text{-}2)$$

$$\theta = \tan^{-1}\left(\frac{\sqrt{3}m}{2n + m}\right) \qquad (2\text{-}3)$$

Carbon nanotubes can be split into three classes based their chirality as determined by the values of the integers n and m; this is summarized in Table 2-1. The chirality of a carbon nanotube also determines whether it behaves as a metallic material or a semi-conducting material, and the conditions required to determine this behavior are also listed in Table 2-1 and depicted graphically in Figure 2-4.

Table 2-1: Summary of types of carbon nanotubes and their electrical behavior as determined by their chirality and chiral vectors [27, 38].

CNT Type	Condition	Notation	Chiral angle	Metallic	Semi-conducting
"Zigzag"	$m = 0$	(n,0)	θ=0°	(n/3) is an integer	(n/3) is not an integer
"Chiral"	$n \neq m$	(n,m)	0°<θ<30°	(2n+m)/3 is an integer	(2n+m)/3 is not an integer
"Armchair"	$n = m$	(n,n)	θ=30°	All armchair CNTs are metallic	

The magnitude of the semi-conductor band gap, especially for cases of small diameter single-walled nanotubes, is inversely proportional to the tube radius, as illustrated in Equation (2-4) [38, 39]. The terms zigzag and armchair describe the

appearance of an open end of the respective nanotube, and examples of both a zigzag and an armchair carbon nanotube are shown in Figure 2-5.

$$Gap \propto \frac{1}{R} \qquad (2\text{-}4)$$

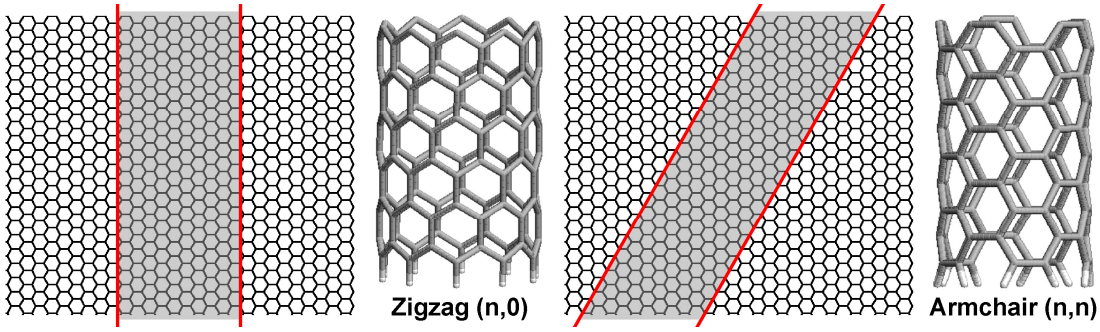

Figure 2-5: Schematic diagram of two of the main chiralities of nanotubes showing a nanotube with (a) zigzag chirality and (b) armchair chirality [40]

2.3 Material Properties

Due to their strong carbon bonds, unusual geometry, and nanometer-scale size, carbon nanotubes exhibit interesting material properties that make them desirable for many potential applications. While other materials may share some comparable properties with carbon nanotubes, such as size and shape (inorganic nanowires) or mechanical strength (carbon fiber), no other material possesses the combination of properties found in carbon nanotubes.

2.3.1 Mechanical Properties

The bonding in carbon nanotubes is very similar to that found in graphite, where carbon atoms are arranged in a hexagonal lattice. Graphene has recently been shown to have excellent mechanical properties (E≈1 TPa, σ=130 GPa [41, 42]). While the in-plane bonding in the lattice of bulk graphite is very strong ($E = 1/S_{11} =$

1.02 ± 0.03 TPa [43]), the out-of-plane bonding in the c-direction is much weaker; as a result graphite is a very soft material (G≈0.18-0.35 GPa [43], τ_{max}≈4.8 MPa [44]). In single-walled carbon nanotubes, the only bonding present is the strong in-plane bonding, found along the length of the nanotubes, making them extremely stiff and strong, and thought to be the strongest material known [45] (although defects can be found at the ends of tubes). Out-of-plane bonding can be found in-between concentric tubes in multi-walled nanotubes, and this can affect their mechanical response, as described below.

As a result of this extremely strong carbon-carbon covalent bonding, nanotubes are able to withstand large elastic deformations under very high stresses and yet still return to their original shape. For individual, single-walled nanotubes, the accepted value of the elastic modulus is roughly one TPa [46-55]. This has been determined by both theoretical and experimental means; an example of the latter is shown in Figure 2-6, where tensile tests were performed on nanotubes by bonding the tubes directly to AFM probe tips [56, 57]. While this modulus value is generally accepted (and in good agreement with the in-plane modulus of graphite [43]), there has been some discussion about how to accurately obtain the wall thickness of a single-walled nanotube [58, 59]. Published wall thickness values used in various computer simulations have differed by up to one order of magnitude (centered around 3.4Å, the sheet spacing in graphite) leading to a wide range in reported modulus values in some cases [59-61].

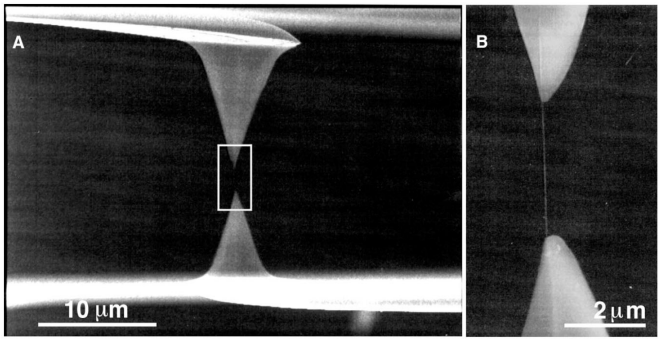

Figure 2-6: Determination of the elastic modulus of a carbon nanotube by tensile testing using an AFM [57].

A number of studies have found that the mechanical properties of carbon nanotubes vary significantly with their diameter. Some early reports compared very small diameter nanotubes grown via arc discharge to larger diameter tubes grown using catalytic CVD techniques and attributed the roughly 10-fold drop in modulus to higher defect concentrations in the CVD-grown tubes [62, 63]. However, more recent reports have measured high (~1 TPa) modulus values for small (5nm) multi-walled carbon nanotubes grown using CVD methods. Both experimental [64] and simulation [65, 66] results have shown reduced modulus with increasing tube diameter (Figure 2-7), suggesting that nanotube dimensions, rather than growth process, can contribute significantly to variations in reported mechanical properties.

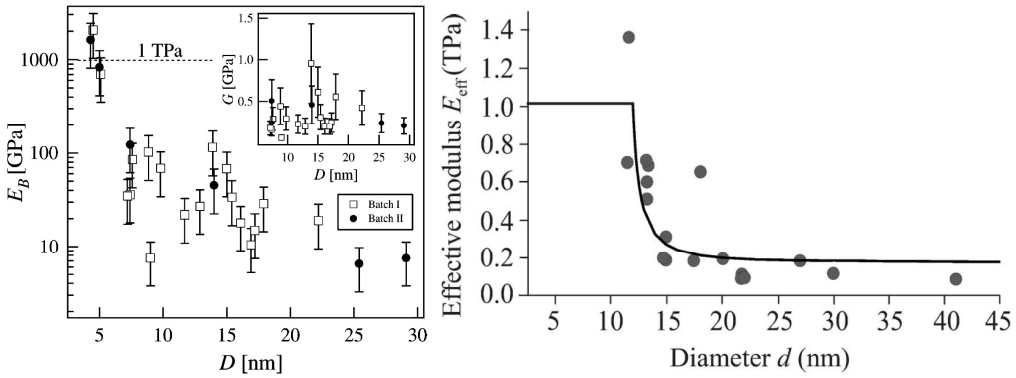

Figure 2-7: (left) Experimental and (right) simulation results showing modulus reduction with increasing carbon nanotube diameter [64, 66]

Small diameter nanotubes have stiffness, strength, and density advantages over today's common steels and aluminums. Even some of the hardest materials available, such as ceramics and carbides, have elastic modulus values only about half that of nanotubes. The only material known, which has comparable properties to carbon nanotubes, is diamond at roughly three times the relative density. The average accepted mechanical properties of single-walled carbon nanotubes are presented in Table 2-2, along with the modulus values, tensile strengths, and densities of some other materials for comparison.

Table 2-2: Comparison of modulus, tensile strength, and density of carbon nanotubes and other selected materials

Material	Modulus of Elasticity	Maximum Tensile Strength	Density
CNTs	1000 GPa [46-51]	11-150 GPa [53-57]	1.34 g/cc [26]
Carbon Steel	200 GPa [67]	0.4-0.8 GPa [67]	7.87 g/cc [67]
6061 Al Alloy	69 GPa [67]	0.24-0.46 GPa [67]	2.7 g/cc [67]
Titanium Carbide	448-451 GPa [67]	0.2-0.3 GPa [67]	4.94 g/cc [67]
Carbon Fiber	170-830 GPa [67]	2.1-5.45 GPa [67]	1.7-2.1 g/cc [67]
Diamond	700-900 GPa [67]	10 GPa [67]	3.52 g/cc [67]
Graphite	4.8 GPa [67]	0.08 GPa [67]	2.25 g/cc [67]

Under tensile stresses exceeding the yield stress, carbon nanotubes will begin to plastically deform, and have been reported to survive high strain levels before failure. This process occurs through the formation and movement of pentagonal and heptagonal defects in the graphitic lattice (called Stone-Wales defects, see Section 2.4). Pairs of these defects can move in a helical path away from the original defect location, resulting in a region of reduced tube diameter and an overall lengthening of the nanotube in the tensile direction [68]. Maximum tensile strain at failure for single walled nanotubes has been reported as roughly 15% at room temperature, although some simulations have suggested the elastic limit could be as high as 40% strain [61]. At elevated temperatures, however, the movement of these defects is fully activated, and nanotubes have been shown to survive strains as high as 280% at 2000°C before failure, as shown in Figure 2-8 [69]. In multi-walled nanotubes, relatively weak bonding forces hold concentric tubes together, and tensile failure can sometimes occur by the sliding of concentric tubes past each other. This failure method is referred to as "sword-in-sheath", and in these situations the mechanical properties for a multi-walled nanotube are altered and reduced; this, along with variations in properties with diameter, has resulted in a range of reported modulus values varying from 270 GPa to 1100 GPa for multi-walled tubes [57, 62].

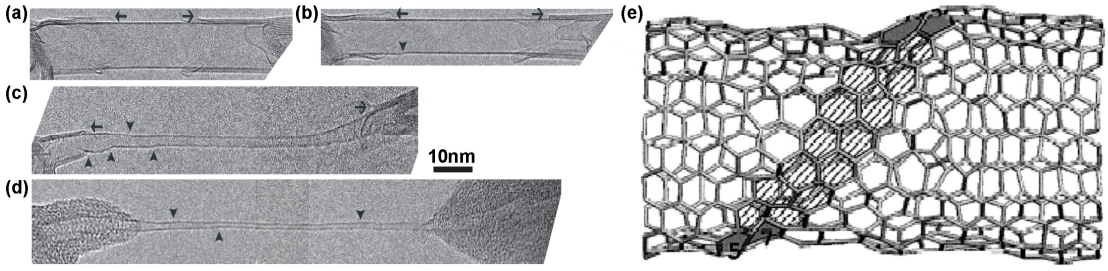

Figure 2-8: (a-d) Superplastic behavior of SWNT under tensile loading at 2000℃ [69] (e) motion of Stone-Wales defects (shaded region) as mechanism for plasticity [68]

In both compression and bending, the very high aspect ratio of carbon nanotubes makes them susceptible to high localized strains due to buckling. For nanotubes, the local critical buckling strain, critical curvature, and bending modulus decreases as tube diameter increases [68, 70-74], as tube wall thickness decreases [73], and as tube length increases [75]. Both bending and torsion stiffness increase with increasing tube diameters [68], and a series of kinks can form in the tube walls as bucking occurs [61]. These types of deformations are shown in Figure 2-9. Simulations have also suggested that critical bending curvatures are independent of tube aspect ratio, provided the tube is not very short ($L/d<10$) [73]. Due to the strong carbon-carbon bonding, nanotubes can withstand significant bending and buckling elastically, without any bond breaking or switching [53, 61, 76]. At increasing strains (and decreasing radius of curvature), the response can vary depending on the structure and quality of the nanotubes. Multi-walled tubes with good graphitization can undergo substantial plastic deformation via wall folding and other mechanisms, while nanotubes with high defect concentrations can fracture with little to no plastic deformation [76].

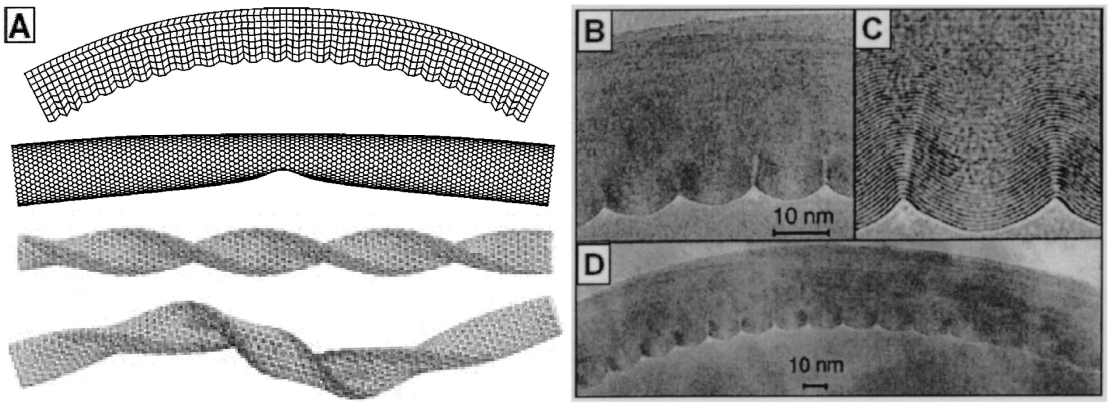

Figure 2-9: (a) Simulated SWNT deformations under bending [66, 73] and twisting [61], (b-d)TEM images of localized deformation in MWNTs [68]

The mechanical response of structures containing many nanotubes, such as in aligned mats or ropes is also of interest. Arrays of aligned multi-walled nanotubes have shown high fatigue life under cyclical compressive loading ($>10^6$ cycles) [77] and sequential buckling under increasing compressive strains [78]. This buckling continues until a critical compressive strain of roughly 60%, at which the mat has densified significantly. At this point the tubes begin to collapse and the effective modulus increases significantly, similar to the response observed in the collapse of an open-cell foam [77, 78]. In these bundles, the mechanical properties are a function of not only the strength of the individual nanotubes but also of van der Waals forces which exist between neighboring tubes. Van der Waals forces arise due to dipole-dipole and other intermolecular interactions, and the energy associated with these forces drops rapidly with the sixth power of the distance separating atoms or molecules. The van der Waals energy between two bodies can be calculated using the Lennard-Jones potential, and is given by Equation (2-5). This energy is a function of V_1 and V_2 (the volumes of each body), ρ_1 and ρ_2 (the number of atoms per unit volume

in each), r (the distance between atoms), and C (the atom-atom pair potential coefficient) [79, 80]. This atom-atom pair potential is related to the Hamaker constant ($A=\pi^2 C\rho_1\rho_2$), which is estimated as 2.38×10^{-19} joules for the interaction between two carbon nanotubes [79]. With very small separation distances these forces can be quite significant, van der Waals forces of ~1.35nN per nm are estimated for a carbon nanotube on a graphite surface (with the graphite interlayer spacing of 0.34nm taken as the separation distance) [81]. These forces drop considerably (to ~6.8pn/nm) if the tube is separated from the graphite surface by "peeling" rather than all at once [82]. While these values were found for nanotubes on flat surfaces, the forces between two adjacent tubes (such as nanotubes within a bundles or mat) can also be calculated [83]. The properties of ropes and bundles of carbon nanotubes are also of interest for many applications [84], and the response of these materials is discussed in more detail in Section 2.7.2.2.

$$E_{vdW}(r) = \int_{V_1}\int_{V_2} \frac{C\rho_1\rho_2}{r^6} dV_1 dV_2 \qquad (2\text{-}5)$$

2.3.2 Electrical Properties

As introduced in Section 2.2.2, nanotubes can exhibit either conducting or semi-conducting behavior, depending on their diameter and chirality (the orientation of the graphitic lattice relative to the tube axis). Metallic nanotubes have shown very high current carrying capacity and electrical conductivity, and the properties of semi-conducting tubes can vary with dimensions and doping.

Theoretical predictions have surmised that defect-free metallic nanotubes could show ballistic conductance due to lack of scattering, where the resistance would not vary with the length of the nanotube [85, 86]. This has been verified experimentally with relatively short tubes [87-89], with momentum mean free paths as high as 30μm [90]. The ballistic resistance in metallic single-walled tubes has been estimated to be 6.45 kΩ [91-93], while the resistance of multi-walled tubes is slightly higher at 12.9 kΩ [94, 95]. Electrical resistivity has been estimated as low as 10^{-6} Ωcm for single-walled tubes [92, 96] and $3x10^{-5}$ Ωcm for multi-walled nanotubes [97]. Electrical resistance has also been shown to increase linearly with increasing temperature [98, 99].

In metallic nanotubes, the current is carried on the surface of the tube, in the same manner as current flow over metallic wires. For multi-walled tubes, this current is carried by the outermost tube layers, and little current flows between layers, giving multi-walled tubes similar resistances to single-walled nanotubes. The strong covalent carbon-carbon bonding in nanotubes also gives them high resistance to electro-migration, a current-assisted diffusion process that is temperature independent. For very small diameter metal wires, this effect can cause failure at relatively low currents, resulting in a current carrying capacity of roughly 10 nA/nm^2. In defect-free carbon nanotubes, as a result of the strong covalent bonding and the lack of scattering due to ballistic electron transport (minimizing joule heating), the current carrying capacity can exceed 10 $\mu A/nm^2$, a factor of one thousand greater than standard metallic wires [100]. While both metals and nanotubes carry currents on their surfaces, the failure

method of nanotubes under excessive current is very different from that of regular metals. When the current carrying capacity of a regular metallic wire is reached, complete failure occurs, and the wire breaks; in nanotubes, only partial failure occurs. Because only the outer surface carries the charge, when the current capacity is reached, the outer shell of the tube fails, causing the current to drop. In a multi-walled nanotube, this exposes a new tube layer, which allows the current to continue to flow [98, 100, 101]. This breakdown results in a unique "step" failure process, as shown in Figure 2-10.

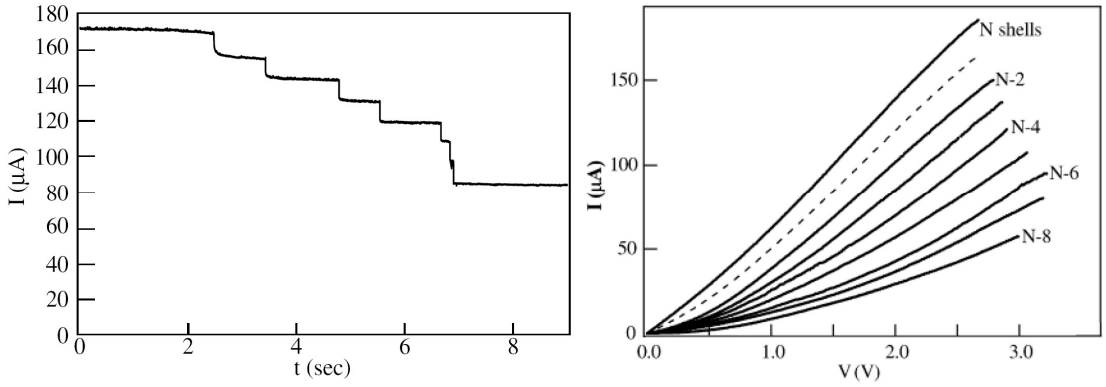

Figure 2-10: (left) Stepwise current carrying breakdown in multi-walled carbon nanotubes exceeding the current carrying capacity, (right) Drop in current with successive removal of concentric shells [100, 101].

The conducting behavior of carbon nanotubes can vary depending on the chirality of the nanotube, and can be determined through the chiral indices (n,m), as described in Section 2.2.2. These conditions determine the conducting properties of single-walled carbon nanotubes in an undistorted state and of semi-infinite length. However, these simple rules can no longer be applied to tubes whose length is very short (less than ten nanometers), or which have been mechanically deformed [102]. A

normally metallic “armchair” type nanotube will develop a band gap and exhibit semi-conducting properties if it is subjected to axial twisting, and this band gap is linearly proportional to the angle of the twist [102]. However, above a certain angle, kinks will begin to form, which lead to the collapse of the tube. The bending of carbon nanotubes can also affect the electrical properties, and computational simulations of electrical resistance in bent carbon nanotubes show a slight decrease in conductivity with increasing bending angle. As with twisting, at angles greater than roughly forty-five degrees the strain can cause kinks can form in the tube wall and the resistance of the tube increases significantly [102]. In non-vacuum conditions, simulations have shown deformations in nanotube walls caused by collisions with inert gases can also affect the electrical properties of single-walled tubes [103]. Deformations of arrays of aligned nanotubes can show an effect opposite to that observed in individual tubes, and under compression the resistance of mats of aligned nanotubes dropped due to densification of the structure [77].

While the conducting properties of single-walled nanotubes are determined as a function of the chirality, electrical properties become extremely complex when multi-walled nanotubes are considered, as each of the many concentric tubes can have varying properties. Predictions have suggested that in defect-free multi-walled tubes current would only be carried by the outer tube; however, experiments have shown that a number of the outermost shells can influence the conducting behavior [101]. Current-induced breakdown has been used to selectively remove outer layers in a multi-walled tube, allowing successive shells to be characterized, indicating multi-

walled tubes contain both conducting and semi-conducting tubes [104]. This breakdown technique has also been used to selectively destroy metallic single-walled tubes within a nanotube bundle, leaving only semi-conducting tubes [104].

The electronic properties of carbon nanotubes can be further manipulated by the addition of dopants along the length of the tube, similar to the way doping is used on silicon in the semiconductor industry. As-grown semi-conducting nanotubes tend to exhibit p-type semi-conducting behavior [105-107]. However, through doping or annealing processes, nanotubes may be changed to behave as n-type transistors. The annealing process occurs in a vacuum at roughly 200°C for roughly 10 hours, after which the semi-conducting properties have changed to n-type. This conversion can also occur by evaporating potassium dopants onto the nanotubes [106, 108]. This conversion can also be reversed, by exposing the n-type nanotubes to oxygen, causing a reversion to the original p-type characteristics [106, 107].

While one of the main challenges to utilizing the mechanical strength of carbon nanotubes is to successfully translate these properties to the macro-scale, there have already been numerous reports of interesting electrical properties in bulk nanotube-based materials. For example, very low density mats of tangled nanotubes can act as conducting, near-transparent films [109]. These and other potential applications are discussed in more detail in Sections 2.7.2.2 and 2.7.3.

2.3.3 Optical Properties

Due to their structure and geometry, carbon nanotubes have interesting optical properties, particularly in their absorbance, which varies with light energy and

polarization. Low density aligned carbon nanotubes arrays have also recently been announced as the “darkest” material known, with a reported reflectance of 0.045% that can vary with nanotube diameter and spacing [110]. This low reflectance is a result of strong absorbance and random scattering due to the nanoscale surface roughness of the nanotube array. In carbon nanotubes, absorbance increases with increasing light energy until a peak found between roughly 4.5eV and 5.25eV, with the former peak attributed to surface π-plasmon excitations and the latter peak attributed to bulk excitations [111-113]. A maximum in the dielectric function for in-plane graphite occurs at 4.5eV, while in the c-direction a maximum is found at roughly 5.2eV [114].

The response to light polarization can be divided into two components, s-polarization, which is polarized perpendicular to the tube axis, and p-polarization which is aligned parallel to the tube axis [115]. For s-polarization, no dependence on the angle θ between the nanotube axis and light incidence is observed, as the dominant absorption is due to dipoles perpendicular to the nanotube axis. With p-polarization, a strong dependence on θ is found (with absorption increasing as θ increases), as absorption occurs by collinear dipoles parallel to the tube axis. Small absorption peaks at roughly 0.64eV, 0.93eV, and 1.45eV are also observed, which correspond to energies between different band and subband gaps in single-walled tubes [111, 116]. These results are shown in Figure 2-11.

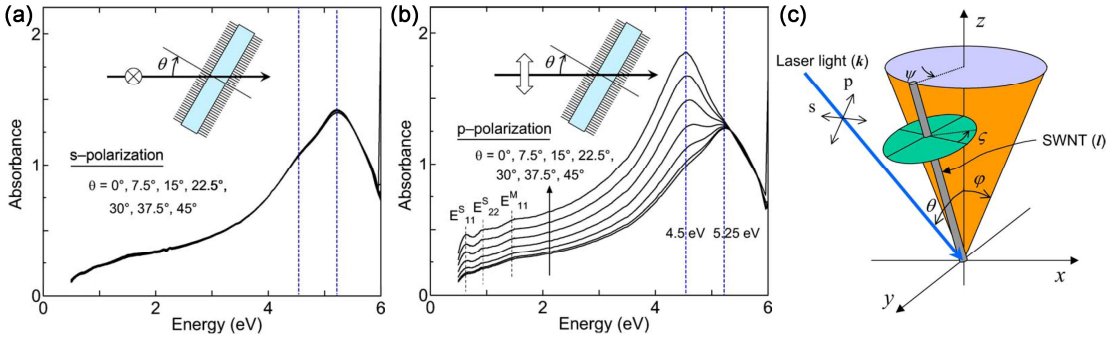

Figure 2-11: (a) Absorbance vs. Energy for s-polarized light, (b) Absorbance vs. Energy for p-polarized light, (c), schematic showing direction of s- and p-polarization [111]

With lower energy incident light (<3.0eV), the absorbance is reported to increase with $\sin^2(\theta)$, and this relation can be used to estimate absorbance for $\theta=90°$. The optical absorption anisotropy (α) and polarization (ρ) can then be calculated as a function of light energy based on the absorbance at $\theta=0°$ ($\Lambda_\perp$) and at $\theta=90°$ ($\Lambda_\parallel$) using Equations (2-6) and (2-7) [115]. Absorption anisotropy and polarization values range from ~0.7 to~0.4 and decrease with increasing light energy. In addition, the polarizability of a single-walled nanotube increases slightly with increasing tube radius and can vary with tube deformation [117, 118].

$$\alpha \equiv \frac{\Lambda_\parallel - \Lambda_\perp}{\Lambda_\parallel + 2\Lambda_\perp} = \frac{1}{2}\left(3\left\langle \cos^2 \varphi \right\rangle - 1\right) \qquad (2\text{-}6)$$

$$\rho \equiv \frac{\Lambda_\parallel - \Lambda_\perp}{\Lambda_\parallel + \Lambda_\perp} \qquad (2\text{-}7)$$

Due to the dependence of absorption on the orientation of the nanotube axis to the polarization of the incident light (with reduced absorbance as θ approaches 0° up to ~4.5eV energy), the optical absorbance can be used to characterize the alignment of nanotube mats, as shown in Figure 2-12. If this incident light is directed normal to the

substrate, then θ=0° for perfectly aligned tubes and θ increases with misalignment. A decrease in absorbance is observed with increasing growth time, indicating alignment improves as the tubes lengthen (as predicted by the crowding alignment mechanism, see Section 2.4.5) [111]. Carbon nanotubes dispersed in solution have also shown optical anisotropy when aligned by an applied electric field [119]. In addition, due to this polarization dependent optical absorbance, Raman spectra can also be influenced by the polarization of the incident laser light; different radial breathing mode peaks can dominate and G- and D-band intensities can vary depending on the angle between the polarization direction and the nanotube axis (see Section 2.6 for more information on Raman spectroscopy) [120-124].

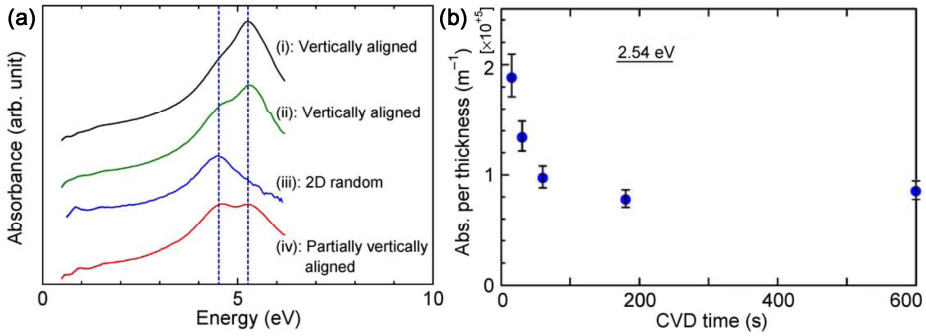

Figure 2-12: (a) Variation with absorbance with energy and alignment, (b) reduction in absorbance per unit length of nanotube mats decreasing with increasing growth showing improving alignment [111].

2.3.4 Thermal Properties

In addition to their interesting mechanical, electrical, and optical properties, carbon nanotubes also have thermal properties that make them advantageous for many applications. Several simulations have suggested that the thermal conductance of carbon nanotubes is in the range of 1000-6600 W/m-K, comparable to the thermal

conductivity of diamond and roughly one order of magnitude higher than some of the most thermally conductive metals [125-127]. These high simulated values have not yet been verified experimentally (thermal conductivity has been reported in the 200-300 W/m-K range), likely due to defects in the nanotube structure [128, 129]. Although the electron conduction in nanotubes has been found to be ballistic in nature, ballistic phonon transfer has not been observed [130]. The exceptional predicted thermal conductivity of nanotubes makes them appealing for applications where heat needs to be dissipated quickly, such as in cooling integrated circuits [131], and nanotube-based thermal interface materials with thermal resistances as low as 12 mm^2 K/W have been fabricated [132].

While this high thermal conductivity is of interest for many applications, other thermal characterization has also been performed. The specific heat of bundles of single-walled nanotubes has been reported as 600mJ/g-K at room temperature, very similar to values for bulk graphite [129]. Carbon nanotubes also have an interesting thermal expansion response. Graphite has a very high coefficient of thermal expansion in the c-direction (α=26-30x10^{-6}/°K), but actually has a negative coefficient of thermal expansion along the in-plane direction at temperatures up to ~400°C (due to in-plane contraction according to Poisson's ratio) [133, 134]. Simulations of expansion in single-walled nanotubes have predicted volumetric contraction to occur with heating up until roughly 800°K and linear contraction along the tube axis until temperatures of roughly 1300°K. This unexpected result is due to pinching, bending, and twisting of nanotubes with heating, although these effects could be suppressed in

multi-walled tubes or in tightly packed bundles [135]. Another study used x-ray diffraction to characterize expansion in single-walled nanotube bundles and showed a small, slightly negative contraction in the nanotube radius, but a large expansion in the inter-tube gap distance within the bundle (α=42x10^{-6}/°K) [136].

2.4 Nanotube Formation Theory

There has been much research published explaining the growth mechanism responsible for the formation of carbon nanotubes during the synthesis reaction. These theories have been based on theoretical modeling as well as experimental observations, and have explained nanotube formation both with and without the presence of a catalyst. With any growth procedure, prior to nanotube growth, the decomposition of a carbon source must occur (whether in the form of hydrocarbons in a CVD process, or as solid graphite in a laser ablation or arc discharge process). Many different carbon sources have been used to synthesize carbon nanotubes, with similar carbon structures produced even when using a variety of carbon sources [137]; the effects of using different hydrocarbon in CVD growth is discussed in Section 2.4.1. For catalytically assisted nanotube growth, experimental research has shown that the activation energy of metal-catalyzed carbon filament growth is similar to the activation energy for carbon diffusion through the corresponding metal film, as shown in Table 2-3 [8]. This suggests that the diffusion of carbon through the metal catalyst is the rate limiting step in the reaction.

Table 2-3: Activation energies for the growth of carbon filaments and the diffusion of carbon through selected metal catalysts [8, 9]

Catalyst	Activation energy for carbon filament growth (kcal/mole)	Activation energy for carbon diffusion (kcal/mole)
Vanadium	27.6 ± 3	27.8 [138]
Molybdenum	38.8 ± 4	41.0
α-Iron	16.1 ± 2 [9]	10.5-16.5
Cobalt	33.2 ± 4 [9]	34.7
Nickel	34.7 ± 4 [6]	33.0-34.8
Chromium	26.5	27.1 ± 3.6 [9]

For nanotubes grown using metal catalysts, the carbon decomposition needs to occur in the presence of nanometer scale metal particles. In chemical vapor deposition reactions, the catalyst is often in the form of a thin metal layer deposited on the substrate prior to growth, and catalyst particle formation occurs due to a combination of the elevated temperatures occurring during the reaction and surface tension and metal substrate interaction energies. These energies will result in the separation of the continuous metal film into small, discrete metal catalyst particles, or islands, whose size and spacing can be influenced by varying the thickness of the catalyst layer and temperature [139-144]. In some growth methods, however, the catalyst is added during the actual reaction and not deposited as a separate step prior to the growth procedure. In these cases, the catalyst is initially found either in its pure form (combined with a graphite target or anode in laser ablation or arc discharge), or in a compound, such as ferrocene, which is added to the chemical vapor deposition reaction. In either process, whether as a result of vaporization due to laser or electrical energy or through thermal decomposition of a compound, small metal clusters are generated. For procedures where a catalyst is added during the reaction, the reaction

temperature can also influence the size of the resulting particles [145, 146], and it has been suggested that the larger particles observed at higher temperatures are formed by collisions resulting in the combination of smaller clusters [147]. Parameters which are important for controlling the formation of these small catalyst particles are discussed in more detain in Sections 2.4.2 and 2.4.3. These catalytic metal particles and decomposing hydrocarbons are precursors to the actual formation of carbon nanotubes.

The accepted growth theory for substrate-supported, catalyst-assisted synthesis of carbon nanotubes via chemical vapor deposition [148] has been adapted from mechanisms for the growth of carbon filaments [6, 8], and is also very similar to the vapor-liquid-solid (VLS) mechanism describing the growth of inorganic nanowires and other structures [149]. Essentially, the decomposition of the carbon source on the catalyst particle causes carbon to diffuse into the catalyst, eventually saturating the metal particle with carbon. Once saturation is reached, additional carbon will precipitate out of the catalyst with a graphitic structure. The morphology of this structure is determined by the size and shape of the catalyst particle and can also be influenced by the composition of the catalyst and the reaction gases.

For a flat substrate, experiments have shown that graphitic carbon can be produced from an amorphous carbon source using a metal film as a catalyst [150]. At elevated temperatures, the solubility of carbon in the metal is increased, and amorphous carbon (whether deposited before heating or added while at temperature) diffuses into the film. Upon cooling (with the carbon solubility limit decreasing),

carbon precipitates out of the metal film in the form of well-ordered graphite sheets, whose basal plane is oriented parallel to the metal surface. If the metal film surface is curved, rather than flat, or if the metal exists as discrete islands, the basal plane of the graphitic lattice will attempt to mimic the surface; however, the graphitic sheets will be strained as a result of this curvature. At sufficiently high levels of curvature, found in particles with diameters in the range of tenths of microns, filaments of carbon will be formed, rather than sheets [7, 151]. At this level of curvature, the strain energy is too great to form a continuous graphite coat encasing the particle, and excess carbon would precipitate with the basal plane oriented tangential to the particle surface, producing a fiber. At the scale required to produce carbon filaments, minimization of strain energy is thought to cause graphite crystallites to grow approximating the curved surface, as illustrated in Figure 2-13 [152]. If the catalyst particles are spherical or ellipsoid in shape, carbon atoms will diffuse out of the particle at regions of lower curvature, and the high strain energy found at regions of high curvature can prevent a continuous filament from forming, producing a hollow fiber [7, 10].

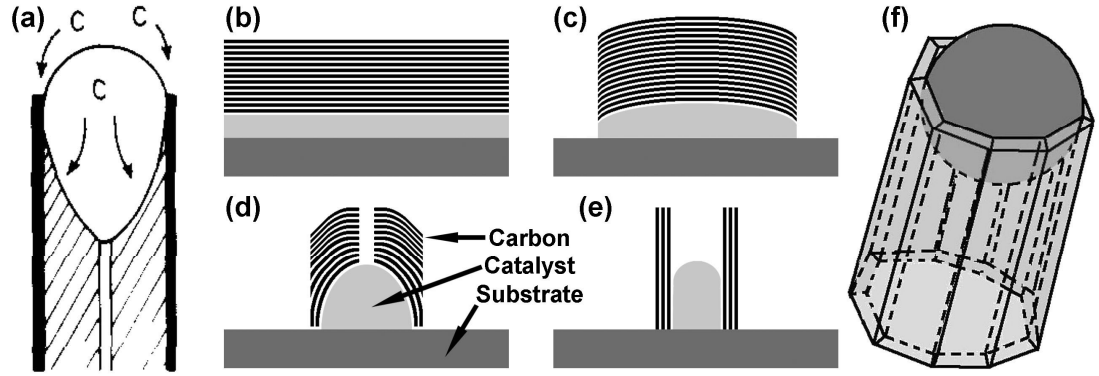

Figure 2-13: Growth Mechanisms for carbon filaments from metal catalyst particles (a) Diffusion of carbon into and through catalyst particle during carbon fiber formation [7], (b)-(e) Carbon structures formed with decreasing catalyst size, from film to small particle, (f) Approximation by graphitic crystallites of a curved particle surface (based on [152]).

As carbon precipitation occurs at the surface of the catalyst, the metal particle dimensions determine the size of the carbon nanotube or filament, and this correlation has often been observed for both filament growth [152] and carbon nanotube growth [153-155]. If the metal particles are decreased in size below that required to form carbon filaments, multi-walled carbon nanotubes will form, and with subsequent size reduction, single-walled tubes (although the very small particles required for single-walled growth may not be stable for certain catalyst-substrate combinations). The transition from filament formation to multi-walled carbon nanotube formation will occur when it is energetically more favorable to form a continuous surface of graphite rather than a piece-wise approximation of the surface due to the strain caused by high curvature in the metal particle [148, 152]. Similar to carbon filament formation, this theory predicts carbon nanotube growth by a precipitation of carbon from the catalyst particles, forming either multi- or single-walled tubes depending on the size of the

metal clusters used. For the growth of single-walled carbon nanotubes, simulations have shown that the catalyst must reach a super saturated level before nanotube formation starts, as the concentration of surface carbon atoms precipitating out must be high enough that they can start forming a graphitic lattice with each other (Figure 2-14) [154, 156, 157].

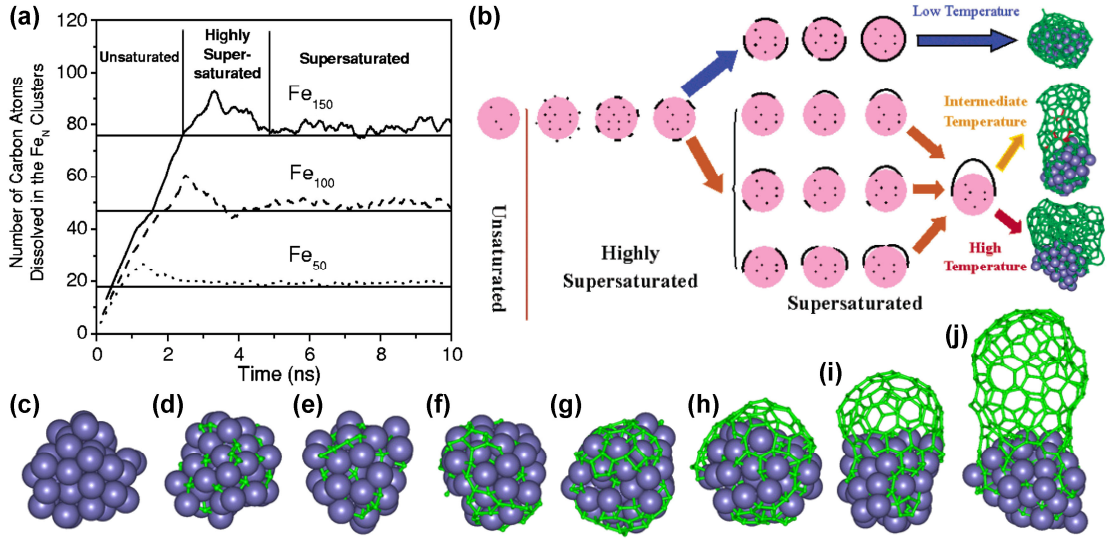

Figure 2-14: (a) Carbon content in Fe catalyst particles during nanotube growth, super saturation is required prior to nanotube precipitation [154] (b) catalyst encapsulation, SWNT growth, or amorphous carbon deposition can occur depending on temperature [156] , (c-f) catalyst particle during highly supersaturated region, (g-j) particle during supersaturated region (from molecular dynamics simulations) [157].

Once the growth of the carbon nanotube has been initiated, additional growth and lengthening occur as more carbon diffuses into the metal catalyst particle [11, 158]. This carbon then travels along a concentration gradient and diffuses out of the catalyst particle, lengthening the tube from its base [159]. The newest region of the tube displaces and pushes the older region outward, away from the catalyst, which increases the length of the tube. This process will continue, and the tube will lengthen

until growth is terminated. Some early theories of nanotube growth suggested that this concentration gradient arises as a result of the decomposition process of the hydrocarbon source on the catalyst particle. If the decomposition is exothermic then localized heating of the catalyst particle can occur, leading to increased carbon solubility (due to the elevated temperature) creating a temperature and concentration gradient. However, carbon nanotube growth has been reported with carbon species that do not decompose exothermically, and the extremely small size of metal particles required for nanotube growth makes it very unlikely that a temperature gradient could be maintained [155, 159]. The driving force for carbon diffusion through the catalyst particle and into the nanotube is likely due to super-saturation of the particle at the exposed surface (Figure 2-14).

For very small catalyst particles, such as those found in single-walled nanotube growth, molecular dynamics results published by Ding *et al.* have suggested that the catalyst particle remains liquid during growth [154, 156, 160, 161]. For these small particles, carbon diffusion occurs through the bulk of the particle according to the vapor-liquid-solid model. However, for larger catalysts, such as those found in multi-walled nanotube growth, a distinct core and surface region can form, and carbon diffusing to the nanotube travels primarily through the surface region. There can be several processes occurring simultaneously during growth; these are illustrated in Figure 2-15. Initially hydrocarbon molecules impinge on the catalyst surface, decompose, and diffuse into the bulk of the catalyst particle. Once saturation in the core has been reached, a disordered surface layer forms, and carbon atoms diffuse

along this region and precipitate out of the particle into the nanotube (Figure 2-15a). Simultaneously, a carbonaceous layer forms on the surface of the particle. This occurs due to gas-phase decomposition of the hydrocarbon and deposition of this carbon as a coating on the catalyst particle (Figure 2-15b). As this coating grows the catalyst surface area available for carbon deposition and diffusion into the nanotube decreases; eventually the particle is completely covered and nanotube growth stops (Figure 2-15c).

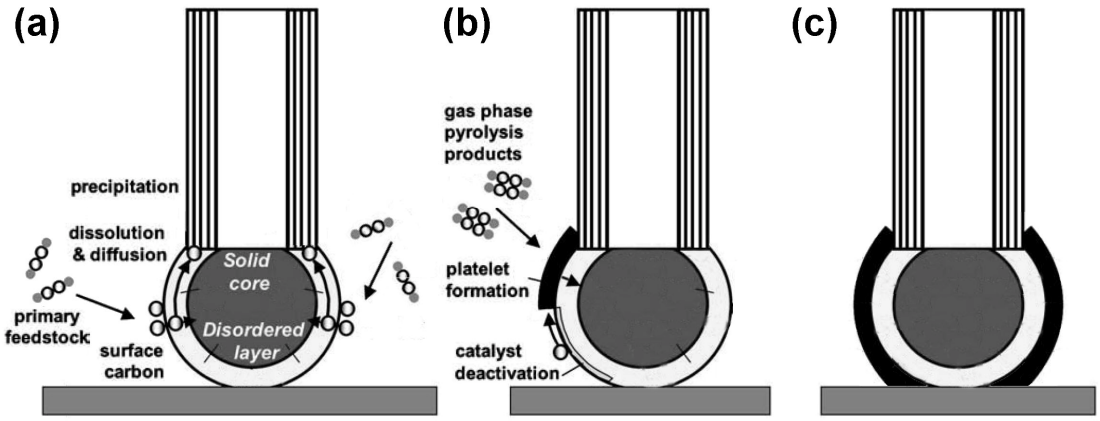

Figure 2-15: Schematic of the various processes occurring during Carbon nanotube growth (a) carbon diffusion through surface layer, (b) formation of an amorphous carbon surface coating, (c) completely coated, poisoned catalyst particle (adapted from [158])

At the initiation and early stages of growth, the nanotube is the most favorable form of carbon energetically, and is therefore the most stable, with smaller diameter tubes showing higher stability than larger tubes [148, 162]. For a single-walled nanotube with a very small diameter, the graphitic lattice is under a large amount of strain due to its small radius; however, because of its tube structure, dangling bonding sites exist only at the open tube ends, and the number of these sites is minimized. The

dependence of the strain energy (σ) per carbon atom on the tube radius (R) is given in Equation (2-8) [163], where E is the elastic modulus, *a* is the representative tube wall thickness, and Ω is the area per carbon atom.

$$\frac{\sigma}{N} = \frac{Ea^3}{24}\frac{\Omega}{R^2} \qquad (2\text{-}8)$$

For a very small number of atoms (for a sufficiently short nanotube), the energy reduction from minimizing the number of open bonding sites offsets the high strain in the lattice. As the length of a given tube increases, the strain energy per atom is unchanged, but the total strain energy increases due to the increase in the total number of atoms in the system. The most energetically stable state will change as a result of this, leading to increasing tube diameters with increasing system size (where strain energy is decreased at the expense of additional dangling bond sites). This trend is indicated in Figure 2-16, where potential energy per atom is calculated as a function of the total number of atoms in the system.

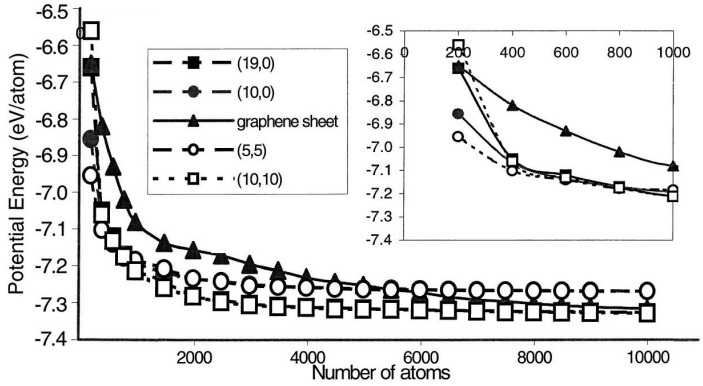

Figure 2-16: Potential energy per carbon atom as a function of number of atoms, plotted for a graphene structure and four nanotube structures [148].

For larger and longer nanotubes, multi-walled nanotubes can exhibit greater stability than single-walled tubes, as the reduced strain energy found in the outer shells

balances the added bond sites at the tube ends [148]. Ultimately, carbon fibers and then graphitic sheets become the most favorable, as the presence of dangling bond sites around the perimeter of the sheets is balanced by the reduction of strain energy due to the elimination of curvature [148, 164]. A catalyst reduces the energy needed to form a carbon nanotube, and a tube grown in the presence of a catalyst will be more stable than one grown independently [164]. While nanotubes are energetically favorable at nucleation, they quickly become a meta-stable phase as they grow. The strain energy, and corresponding stability of a carbon nanotube is primarily a function of its radius, and essentially independent of its chirality; tubes with comparable diameters but different chiral angles demonstrate similar stabilities [148, 163].

As the nanotube grows, one end of the carbon nanotubes will be closed by the catalyst particle; however, the tube's open end will contain dangling bond sites and growth can also occur by deposition of carbon atoms on this open end. Carbon atoms bonding to these sites will be incorporated into the hexagonal graphitic lattice, lengthening the tube and providing new dangling bond sites to allow the growth process to continue. In multi-walled tubes, this growth can be preceded by the formation of temporary bonds between carbon atoms and the concentric shells of the tube [165]. However, these same temporary bonds can lead to the termination of growth if enough form to cause tube closure [165-167]. This closure can happen very rapidly; as a result catalyst assisted growth occurs predominantly at the catalyst end, with very little growth at the open end prior to closure. A similar closure method can also take place in single-walled tubes as a result of bonding between nearby bond sites

on the end of a single-walled tube. This can lead to the elimination of available bond sites and tube closure, terminating growth at the tip. Simulations have demonstrated that single-walled tubes of less than roughly 3nm in diameter can close spontaneously by this method, unless supported by a catalyst particle, although in some growth methods (such as with arc discharge growth), highly concentrated electrical fields at the open ends of nanotubes can keep them from closing [168]. The closure of carbon nanotubes is accomplished by "capping" the open end with a fullerene-based hemisphere, shown in Figure 2-17. These hemispheres cannot be composed entirely of the hexagonal structures found in the main walls of the carbon nanotube, and must contain pentagonal defects [169], which can result in curved or conical shapes [170].

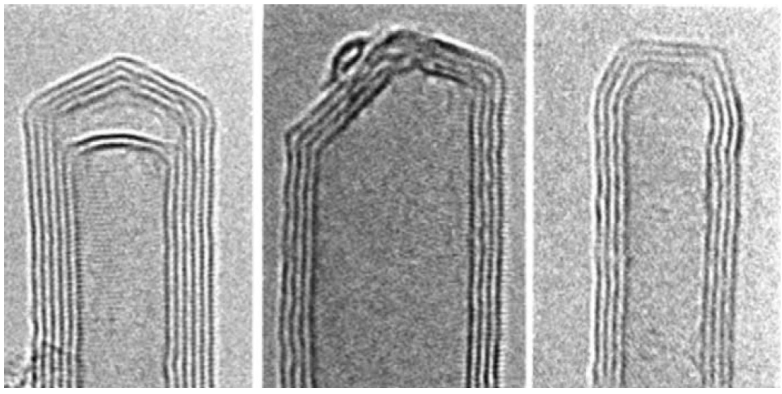

Figure 2-17: TEM images of capped multi-walled carbon nanotubes [91].

Energy considerations also govern the formation of these pentagonal defects, as well as heptagonal seven-sided defects, and the replacement of these defects by a perfect hexagonal lattice. In the graphitic lattice, a hexagon is the most stable and energetically favorable structure. The formation of a new hexagon in this lattice requires two new carbon atoms to bond to the structure, and this process occurs in two separate steps. Initially, either a pentagonal or heptagonal defect is formed, which

only requires the addition of a single carbon atom. Upon the addition of a second carbon atom and a small amount of energy to overcome the activation energy, the lattice defect is eliminated and converted to a perfect hexagonal unit. Figure 2-18 illustrates four possible routes for this conversion, as well as a plot of the energy levels for these lattice positions relative to the energy state of a free carbon atom. It has also been proposed that metal catalysts can aid in the annealing of these lattice defects [171]. During growth defects can become incorporated into the lattice, and pairs of pentagonal-heptagonal rings in the lattice (called Stones-Wales defects), often occur due to their low formation energy [172].

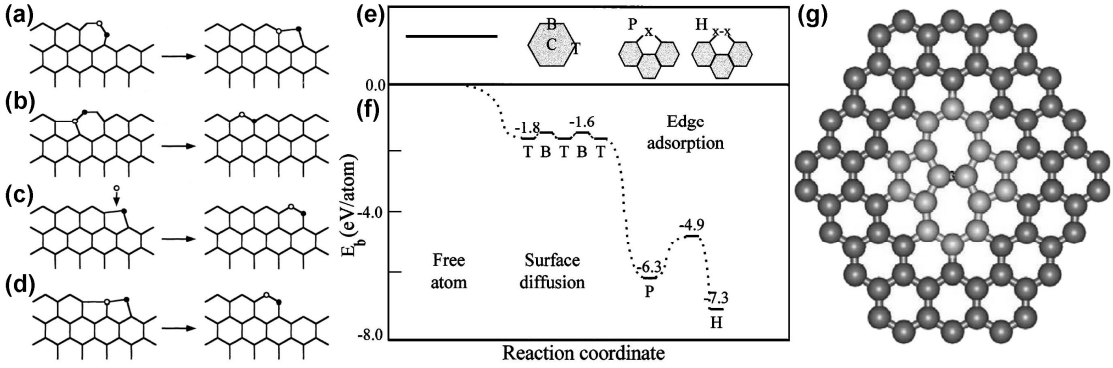

Figure 2-18: (a)-(d) Defect elimination sequences in the graphitic lattice [168], (e),(f) Potential lattice positions and energy levels for carbon atoms at the exposed edge of an uncapped carbon nanotube, relative to a free carbon atom [171], (g) example of a 5-7-7-5 Stone-Wales defect in the center of a graphitic lattice [172].

Just as with bulk metals, semiconductors, and other crystals, it is extremely difficult to produce a defect-free structure and during growth a number of these pentagonal or heptagonal defects may remain in the carbon nanotube lattice. The inclusion of pentagonal defects will encourage constriction and eventual closure of the tube diameter, while the presence of heptagonal defects will tend to expand the tube

diameter. This phenomenon has been used to explain the presence of tubes with a bamboo-type structure [173] (explained in more detail in Section 2.4.5). These defects can be removed with a high temperature heat treatment in a vacuum or inert environment. Increased diffusion at elevated temperatures can allow pentagonal and heptagonal defects to recombine into an undistorted hexagonal lattice (similar to dislocation annihilation during heat treatment of metals). Reported annealing temperatures have ranged from 1700°C to 3000°C, leading to improved graphitization and partial (though not complete) removal of defects [63, 174].

2.4.1 Role of Carbon Source

In any carbon nanotube synthesis reaction, a source of carbon is required for growth. In the literature, carbon nanotubes have been successfully synthesized from a wide range of carbon sources, including amorphous carbon [175-177], graphitic rods [178], hydrocarbons (both in liquid and gaseous forms), alcohols (including methanol, ethanol, and propanol [179]), and some other carbon sources (CO, diethyl ether, acetone, [179] etc.). Some of these sources (such as graphitic rods) are used only in particular synthesis methods, and hydrocarbons are by far the most widely used.

The stability of various hydrocarbons will affect the temperature at which self-pyrolysis occurs. During self-pyrolysis, the breakdown of hydrocarbons leads to the formation of a range of carbon structures, including amorphous carbon and potentially graphitic or nanotube deposits. In order to reduce the build-up of unwanted amorphous carbon (which can lead to catalyst poisoning, see Section 2.4.4), it is desirable to select a growth temperature range below that at which the desired

hydrocarbon undergoes self-pyrolysis. This will result in localized catalytic decomposition, which can occur on transition metal surfaces [180-183]. Above these temperatures, and with gas environments that do not suppress this breakdown, hydrocarbons can decompose and deposit amorphous carbon on the walls of existing tubes (increasing diameters), on the surfaces of catalyst particles, and on other surfaces in the reaction tube [8, 184-187].

For optimal nanotube growth, the selection of a carbon source will influence other reaction parameters. Growth typically occurs in an inert environment (such as argon or helium [179]) to avoid oxidation and burning of the nanotube product at the high temperature used (nanotubes can begin to burn in the presence of oxygen at temperature as low as ~500°C, depending on the defect concentration [188]). Hydrogen is often added to the reaction gas (in concentration ranging from ~5vol.% up to 100% [189]), and the presence of hydrogen can inhibit excess hydrocarbon decomposition by blocking active sites on the nanotube surface and limiting carbon deposition [190] or by pushing a typical decomposition reaction shown in Equation (2-9) to the left. The carbon to hydrogen ratio in the hydrocarbon will affect the amount of hydrogen released during decomposition, and the optimal reaction gas composition can be adjusted to compensate for this. An ideal reaction temperature will vary depending on the stability of the hydrocarbon used, with unwanted amorphous carbon deposition occurring at excessive temperatures. Alternatively, a carbon source may be selected that undergoes endothermic decomposition (as determined by the heat of reaction), which can result in significantly reduced

amorphous carbon formation at higher temperatures [191]. Sample reactions are listed in Equations (2-9) and (2-10).

$$CH_4 \leftrightarrow C + 2H_2,\ \Delta H° = +74.4kJ/mol \quad (2\text{-}9)$$

$$2CO \leftrightarrow C + CO_2,\ \Delta H° = -172kJ/mol \quad (2\text{-}10)$$

A very wide range of hydrocarbon and other carbon species have been used for nanotube growth, including C_6H_6 (used for the first reported nanotube growth via chemical vapor deposition [174]), CH_4 [192], C_2H_2 [193], C_2H_4 [194], C_3H_6 [179], C_8H_{10} [195], C_6H_{14} [196], and more. The decomposition of these varied hydrocarbons will occur at different temperatures; however, even when using the same hydrocarbon, the synthesis temperatures reported for published nanotube CVD growth recipes have spanned a wide range. By taking a survey of reported synthesis temperatures, average growth condition can be identified that indicate typical CVD conditions for a range of hydrocarbons; these are shown in Figure 2-19. Note that the use of certain, more uncommon carbon sources (such as hexane, C_6H_{14}) has only been reported by a few groups, and the particular growth methods used in those few examples may not provide the best representation of the suitable growth temperature range for that hydrocarbon. The average reaction temperatures used tend to follow the same trend of the heat of reaction for decomposition of the various carbon sources (the inverse of their heats of formation), with less stable compounds (such as C_2H_2) decomposing at lower temperatures.

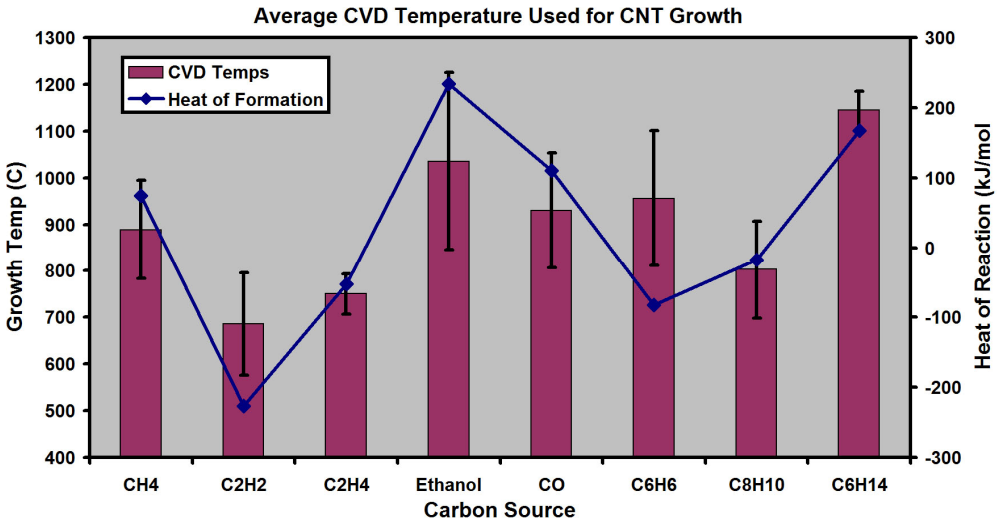

Figure 2-19: Average reported growth temperatures in CVD nanotube synthesis for common carbon sources [6, 35, 36, 63, 64, 78, 84, 87, 94, 95, 111, 128, 152, 162, 174, 181, 185-189, 192-261], Heat of Reaction values from [262]

The concentration of the carbon source in the reaction gas mixture can vary, although low concentration are typically used for growth occurring at atmospheric pressure and higher concentrations only commonly used in low pressure CVD systems [263]. The first carbon nanotubes produced by chemical vapor deposition were grown by using a much lower carbon source partial pressure than that used for the production of vapor grown carbon fibers on which the synthesis process was based [174, 251]. Limiting the carbon available for growth is important, as the deposition of amorphous carbon on tube walls, while an important process in carbon fiber growth, is to be avoided in carbon nanotube production. An optimal carbon introduction rate would occur when carbon diffusion through the catalyst is the rate-limiting step; at lower hydrocarbon concentrations carbon availability can be rate limiting. Growth rates and production can increase by increasing the concentration [247, 264], as shown in Figure

2-20, and this result is similar to that seen in carbon fiber synthesis [265]. However, once the carbon concentration has increased until its availability is no longer rate limiting, additional carbon will decrease nanotube quality, thickening the tubes due to amorphous carbon deposition and reducing alignment [197]. In addition, as diffusion rates increase with higher temperatures, nanotube growth is accelerated with increased reaction temperature, and high purity products can be obtained, provided the reaction temperature does not exceed the self-pyrolysis temperature of the carbon source used [197, 198, 264], as shown in Figure 2-20.

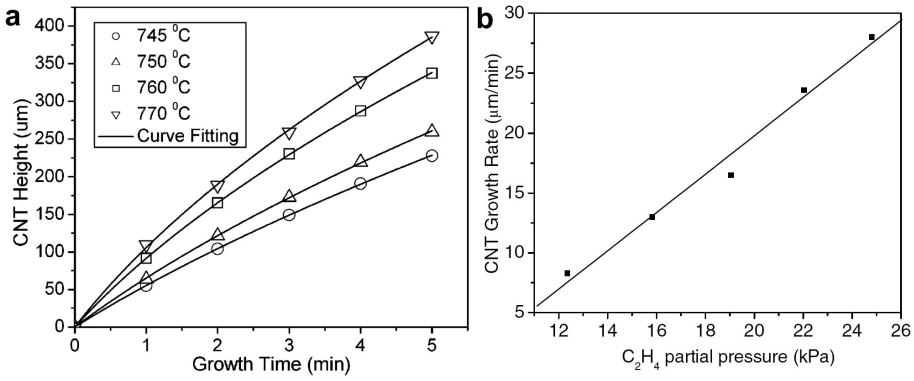

Figure 2-20: Relationship between (left) nanotube growth and reaction temperature [198] and (right) growth rate and ethylene partial pressure [197]

For example, the use of methane allows for higher temperatures to be used (greater than 1000°C in some reports) without significant amorphous carbon deposition, producing single-walled tubes with better structure [220]. Another important parameter is the dwell time of the reactant gases in the furnace and in the vicinity of the substrate for nanotube growth. If the dwell time (a function of the volumetric gas flow rate and reaction chamber cross-Section) is too short, production

will be decreased, and strategies to increase yield (such as increasing the carbon source concentration) may not be effective [190, 252].

During hydrocarbon decomposition, and prior to carbon deposition (either through the catalyst and into the nanotube or as amorphous soot), a number of intermediate reactions can occur [266, 267]. Recent studies on soot formation from various hydrocarbon sources have shown that ethylene can decompose and forms not only soot and H_2, but also significant concentrations of C_2H_2 (as well as trace CH_4, C_6H_6, and other hydrocarbons), while both benzene and acetylene primarily form soot and H_2 (with other trace products) [190, 267, 268]. This suggests that for many hydrocarbons (such as ethylene), acetylene is an important intermediate species in carbon nanotube growth, and is present in some concentrations during the reaction, even if acetylene was not the original hydrocarbon source used. Preheating, or passing the carbon source through a zone of moderate temperature can promote these intermediate reactions and is often used to improve synthesis [152], with up to 1500% increase in growth rates reported [269]. At low hydrogen concentrations, benzene was found to be the most important species for the formation of soot while acetylene was the most important species at higher hydrogen concentrations (ethylene also contributes to soot formation) [190, 268, 270]. Very little soot was formed directly by methane, which would instead react to sequentially form C_2H_6, C_2H_4, and finally C_2H_2 [266, 268]. Hydrogen can act to block active sites which assist in carbon deposition, and increases in hydrogen partial pressure (or increases in H:C ratio in the hydrocarbon source) reduce soot formation [271]. Due to this effect, saturated

hydrocarbons (CH_4) are often used for single-walled nanotube synthesis, while unsaturated hydrocarbons (C_6H_6, C_2H_4, C_2H_2, etc.) are used for the production of multi-walled nanotubes (although other process parameters can strongly affect the nanotube products) [155].

With the use of other (non-hydrocarbon) sources, some other considerations need to be taken into account. The presence of oxygen in alcohols and other potential carbon sources (acetone, etc.) can lead to the formation of oxygen-containing radicals during decomposition, and this by-product has been shown to enhance single-walled nanotube growth [179]. Carbon monoxide has also been used for nanotube growth; however, CO is very stable, and requires high temperature or pressure conditions during the reaction to successfully produce nanotubes [253, 254]. These higher temperatures required during carbon monoxide growth can lead to nanotube products with fewer defects when compared with some other carbon sources. CO has also been mixed with more commonly used hydrocarbon gases (such as C_2H_4) to promote hydrocarbon decomposition on the metal catalysts and enhance growth [269].

2.4.2 Role of Catalysts

While nanotubes can be synthesized directly from a carbon source using certain growth methods (such as with arc discharge or laser ablation), growth without catalysts often necessitates very high temperatures, and the majority of growth methods (including the commonly used CVD methods) typically require the use of a suitable catalyst during growth. A catalyst for nanotube growth is typically a nano-scale metal particle with sizes ranging from as small as one nanometer up to several

tens of nanometers, but larger metal films (such as Ni films with nano-scale surface roughness [272]) have also been used.

In carbon nanotube growth, the catalyst particle not only influences the size and structure of the resulting carbon nanotube or fiber, but can also act as a catalyst for the decomposition of the hydrocarbon used as a carbon source. This decomposition can occur at temperatures lower than those typically used for carbon nanotube synthesis, with nickel nanoparticles catalyzing the decomposition of methane [182] and propane, benzene, and cyclohexane decomposing with iron catalysts [183] at temperatures as low as 500°C. This decomposition can be observed by monitoring the evolution of reactant and product species as a function of temperature, as shown in Figure 2-21.

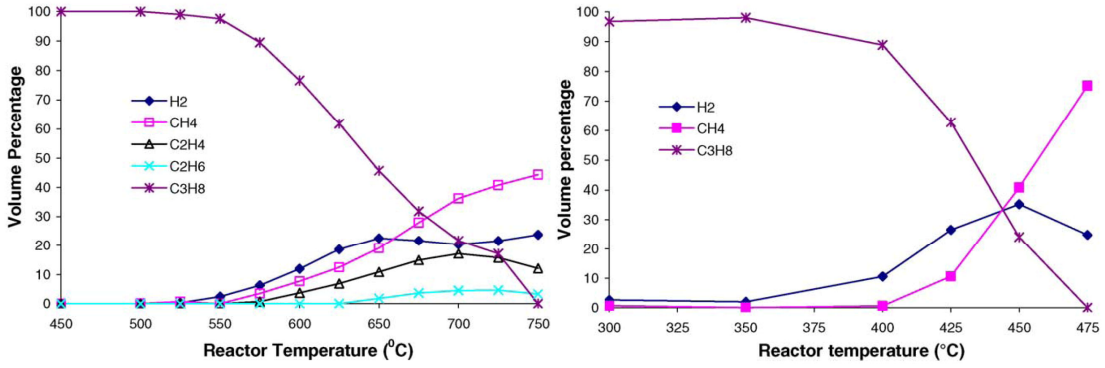

Figure 2-21: (left) Gas composition during thermal cracking of propane as function of temperature, (right) Gas composition during Fe/Pd catalyst assisted decomposition of propane [183].

More important than their use in aiding the decomposition of hydrocarbons is the role of catalysts in transforming carbon obtained by this decomposition into an ordered nanotube structure. The size of the catalyst particle is critical to this process, and graphite sheets, carbon fibers, carbon nanotubes, and carbon capsule structures

can all be potential products, with their synthesis controlled by catalyst size [139, 273]. For carbon nanotubes, there is a strong correlation between the catalyst particle size and the nanotube diameter, and this relation holds for both single- and multi-walled nanotubes [188, 274, 275]. With otherwise identical growth conditions, careful control of catalyst particle size (through catalyst thin film deposition thickness) can allow selective production of single-, double-, and multi-walled tubes (from iron catalyst diameters of 1-2 nm, 3-5 nm, and 6+ nm, respectively) [188].

The successful growth of carbon nanotubes has been reported from catalyst particles that are in either the solid or liquid states, depending on parameters such as catalyst composition, size, and reaction temperature. For very small particles (of the size required for very small single-walled nanotube growth), the binding energy per atom can be significantly reduced compared to a bulk form of the catalyst. As a result these small metal particles may be unstable and could evaporate under the reaction conditions, preventing them from catalyzing the synthesis of nanotubes [254, 276]. In addition, small catalyst particles can exist in the liquid state at temperatures significantly below the bulk melting point [161, 277]. In some metals, specific eutectic compositions in the metal-carbon phase diagram have melting temperatures close to the range of temperatures used in the growth procedures. Surface interfacial energies between the metal catalyst and the nanotube wall have also been thought to potentially contribute to a reduction in the melting point of the catalyst particle [278]. While catalyst size can play a large role in nanotube formation, the catalyst state (liquid or solid), does not appear to be as critical of a factor.

A very wide range of metals have been reported as successful catalysts in the synthesis of carbon nanotubes and include iron [243, 274, 279], nickel [139, 182], cobalt [63, 280], chromium [9], vanadium [8], boron [273], platinum [281], gold [282, 283], palladium [281-283], molybdenum [162], copper [284], and rhodium [281]. However, the range of conditions required for growth or the quality of the nanotube products may be limited with some of these metals, and iron is the most widely used catalyst, followed closely by nickel and cobalt. Although single-element catalysts are often used, bi-metallic catalysts have also been investigated with success, and are commonly used as a means to increase production of single-walled carbon nanotubes. A number of elements have been used, including molybdenum [158, 221], yttrium [285], ruthenium [181], sulfur [286], rhodium [116], and bismuth [286].

One of the most common co-catalysts for the production of single-walled nanotubes is molybdenum, which has been used most often with cobalt [111, 232, 287-290] as well as some other metals [162, 217, 291, 292]. Cobalt by itself will normally produce multi-walled tubes, and some reports have suggested that pure molybdenum is a poor catalyst, however, the interaction of these two metals results in the growth of predominantly single-walled tubes, with very high single-walled nanotube yields [290]. Concentrations of the secondary catalyst element may be relatively small; one recent study found optimal growth with a 16:1 primary catalyst (Fe) to co-catalyst (Mo) ratio [221]. As catalyst particle size influences tube diameter, single-walled nanotube growth can only occur in the presence of very small (1-2 nm) catalysts, and molybdenum is thought to stabilize these particles. It has been proposed

that the formation of molybdenum carbide during the growth reaction leads to the release of metallic cobalt in the form of extremely small particles. The average diameter of these single-walled tubes can also be controlled, with increasing temperatures [287] or variations in the catalyst composition [286] leading to larger diameters, as shown in Figure 2-22.

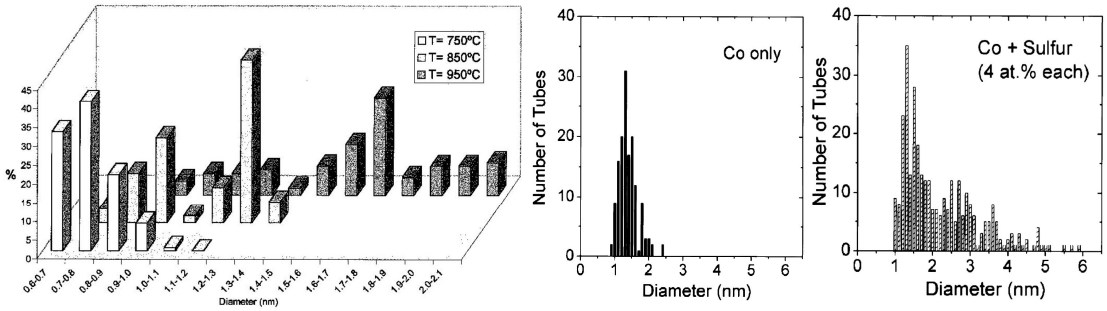

Figure 2-22: (left) Single-walled Nanotube diameter distributions produced using Co-Mo bi-metallic catalysts and thermal CVD [287], (right) Increases in average tube diameter with sulfur as a co-catalyst [286].

The introduction of the catalyst material to the nanotube synthesis reaction will vary depending on the growth procedure used. In arc discharge or laser vaporization growth processes, metal catalysts can be embedded in the solid graphite targets used as carbon sources (see Section 2.5.5). For the much more common chemical vapor deposition method of growth, the catalyst is often introduced in a solution during the reaction or deposited on a substrate in the form of a thin film or nano-scale particles prior to growth. These catalyst solutions are often composed of metal salts (such as chlorides [293], sulfates [279], or nitrates [182]) or other metal compounds [145], including ferrocene ($Fe(C_5H_5)_2$ [234]) and iron pentacarbonyl ($Fe(CO)_5$ [254, 294]) dissolved in alcohols [247] or liquid hydrocarbons (such as benzene [242] or xylene [215]). These solutions are introduced by evaporating them into the gas stream or by

bubbling the gas through the liquid, and the concentration can be varied to control the amount of catalyst material introduced to the reaction. Alternately, a substrate (such as quartz or alumina) can be dipped into the solution then allowed to dry. As the solvent evaporates, small metal catalyst particles are deposited on the surface, with solution concentration affecting catalyst size and spacing. Other nano-sized particle sources can also be used, such as Fe_2O_3 particles suspended in ferrofluid [206]. Thin metal films are also often used as catalyst sources, and are deposited through e-beam evaporation, sputtering, or some similar method. Regardless of the original source, the size of these particles during nanotube growth will depend not only on the initial amount of catalyst present (determined by solution concentration or film thickness), but also on growth conditions and substrate-metal interactions (see Section 2.4.3).

It has been argued by some groups that the carbide form of the catalyst is the active species in nanotube growth, while other groups have argued that growth occurs when the catalyst is in a pure metal or metal oxide state. According to the most commonly accepted nanotube and nanofiber formation theory, growth follows the super-saturation of the catalyst particle with carbon [137, 295, 296], implying that the metal carbide form of the particle (forming in situ from metal particles at the start of the reaction) is the active catalyst (although there is some debate over the exact metal-carbon ratio in the carbide [11]). Other reports have indicated that both pure metal and metal oxide catalysts can also work to synthesize carbon nanotubes. Growth has been observed using both iron oxide and pure iron catalyst particles (with faster growth obtained with iron oxide, although other reaction conditions could also

influence this effect) [297]. Reaction temperature and catalyst composition can also determine a catalyst's effectiveness, with bi-metallic Fe/Mo oxides catalyzing single-walled nanotube growth at lower temperatures (680°C) with no growth reported with iron oxide catalyst until much higher temperatures were used (900°C) [292]. In cases where growth has been reported with pure metal catalysts, carbon diffusion into the growing nanotube would occur along the surface of the particle, and with metal oxide catalysts carbon could still saturate the particle, although with different solubility limits than found in pure metal catalysts. Some difficulty has also been encountered in identifying the precise catalyst composition during growth, as carbon solubility can vary widely between the growth temperature and when the sample has been cooled to room temperature for analysis, and significant carbon precipitation out of the catalyst particle could occur during this cooling.

2.4.3 Effects of Substrate

In the vapor phase synthesis of carbon nanotubes, where nucleation and growth can occur while suspended in the reaction gas, a model is only needed to describe the formation of nanotubes from the metal catalyst particles. However, in substrate supported growth, the interaction of these metal particles and the substrate must also be addressed, and the choice of substrate can influence the resulting nanotube diameters and can even determine if growth will occur at all. A variety of materials have been used as substrates for carbon nanotube growth, including metals [132, 249, 258], carbonates [63], and several oxides (MgO, CaO, TiO_2, ZrO_2, etc. [206, 230, 298]). However, the most commonly used substrates are silica (SiO_2) and alumina

(Al_2O_3), and this discussion of the effects of catalyst-substrate interactions will focus on metal catalysts deposited on oxide substrates.

Due to substrate-catalyst interactions, the substrate choice can also influence the catalyst particle size during growth [299], which is very important, particularly during single-walled nanotube synthesis. The amount of catalyst material deposited can be varied using several processing techniques (such as adjusting the concentration of a catalyst solution or the thickness of a thin metal film), however catalyst particle coalescence due to heating can also influence the effective catalyst size. For example, silicon oxide is commonly used as a growth substrate (either in the form of quartz slides or as a native oxide on a silicon wafer); however, single-walled nanotube growth on these surfaces has been difficult. To achieve SWNT growth, catalysts supported on alumina substrates are typically used [187, 300, 301], including alumina-aerogel substrates, which provide very high surface areas and increased yields [191, 302]. During heating, small metal catalyst particles can move on the substrate surface and aggregate into large particles that may no longer support single-walled or even multi-walled nanotube growth. This process may occur for several minutes before equilibrium is reached [217]. It is important to understand this movement, and a number of different reaction parameters (such as reaction gas composition [274]) are thought to play a role. One of the largest effects is due to catalyst-support interactions, and there have been a number of theories proposed to explain the different results observed with different catalyst-substrate combinations.

One of the most common methods of depositing catalyst material on a substrate is through the evaporation of a metal film on the surface. During this process, the metal film will transition between several morphologies, depending on deposition thickness [303]. For very thin film thicknesses, metal atoms evaporated from the source will deposit on the substrate surface and then translate across the surface. These atoms will either cluster to form small particles, meet and join existing particles, or evaporate off the substrate [304]. As deposition continues, more and more of these adatoms will join existing clusters, increasing their size rather than creating new particles. These clusters will then start to impinge on neighboring clusters and form a series of interconnected networks; this coalescence can result in an overall decrease in energy [305], and as this occurs the average spacing between particles will decrease. Eventually these networks will completely cover the substrate surface to create a continuous thin metal film. This surface evolution and the relationship between average particle size and spacing and the average film thickness are illustrated in Figure 2-23. The presence of different gases and variations in substrate temperature during evaporation can influence this evolution, with larger particles observed as the substrate is heated [303].

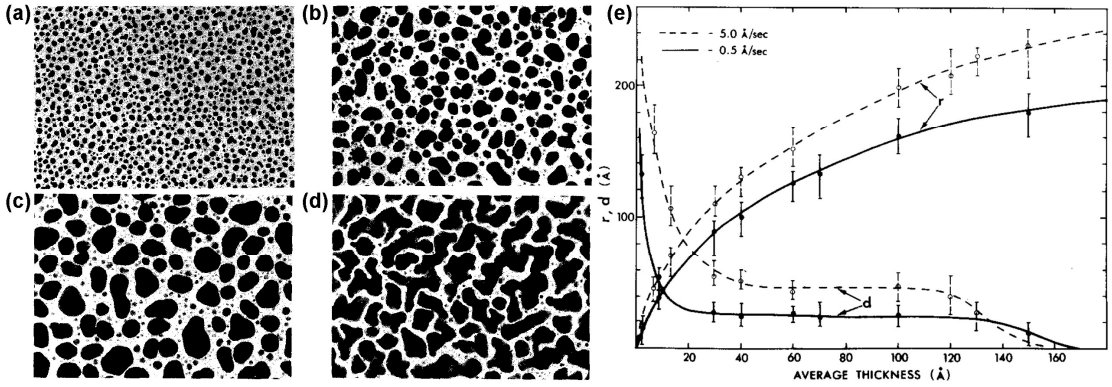

Figure 2-23: (a-d) Evolution of Au thin film morphology with increasing deposition thickness, (e) Variation in particle size and spacing with average film thickness for two different deposition rates [303].

The thicknesses at which these transitions will occur (isolated particles, connected network, continuous film) will be largely influenced by the metal-substrate interactions, as well as evaporation process parameters [304-307]. For metal-substrate combinations where the metal adatoms exhibit stronger interactions with each other than with the surface, isolated structures will form as islands on the substrate; this is termed Volmer-Weber growth. Frank-van der Merwe growth occurs when the adatoms are strongly attracted to the substrate and continuous two-dimensional films form when this occurs. An intermediate process, called Stranski-Krastanov growth can also occur, where the first few monolayers deposited form a continuous film and additional deposition beyond this critical thickness results in the growth of three-dimensional islands on the surface. These processes are illustrated in Figure 2-24. Iron particles that have successfully catalyzed the growth of carbon nanotubes have been observed to form by both the Stranski-Krastanov and Volmer-Weber methods, depending on the substrate used [308]. The energy associated with the desorption of adatoms from the substrate surface and from metal islands wetting on the surface, as

well as strain energy mismatch between the substrate and deposited film will influence which growth mode occurs. In addition, the deposition temperature can affect the morphology of the islands as they grow, and the island density on the surface [309].

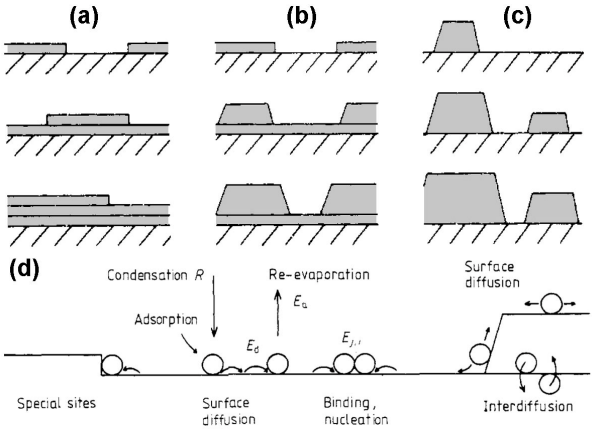

Figure 2-24: Thin film morphology changes with increasing deposition: (a) Frank-van der Merwe 2-D film growth, (b) Stranski-Krastanov 2-D and 3-D growth, (c) Volmer-Weber 3-D growth, (d) schematic of processes occurring during thin film growth [304].

Once the metal film evaporation process has been completed, additional changes in morphology can occur as the substrate is heated to the reaction temperature and growth is initiated. These same heating effects can also lead to changes in particle size and distribution when small metal particles are used (dispersed or evaporated out of solution onto the surface) rather than thin films. Regardless of the initial metal form (film or particles), this island coalescence can occur at elevated temperatures due to structural relaxation of the metal particles [297, 307], and substrate-catalyst interactions can greatly influence this agglomeration. These interactions can include chemical or electronic interactions as well as physical interactions. As mentioned in Section 2.4.2, the metal particles used during synthesis have to be within an

appropriate size range to catalyze the growth of carbon nanotubes. If excessive diffusion can occur between the catalyst material and the selected substrate material, the active catalyst layer could be lost due to the formation of an intermetallic. This is seen when bare silicon wafers are used as substrates, where metal films can form silicide regions (which do not catalyze nanotube growth) rather than remain as stable, individual catalyst particles [310]. Thin SiO_2 barrier layers are required between the silicon wafer substrate and the metal to ensure particle stability, and either the native oxide layer or thermally grown SiO_2 films can serve this purpose. Both length control and patterning of carbon nanotube growth have been achieved using this effect by controlling SiO_2 film thickness and coverage on bare silicon wafers [235, 255-257].

For suitable oxide surfaces, strong metal support interaction (SMSI) can occur when strong interactions between the catalyst particle and the cationic sites on the support are present. In this interaction, the metal catalyst can partially reduce the oxide substrate and a slight negative charge can be transferred to the catalyst, enhancing the interaction [206]. This occurs most often with substrates that are easy to reduce (such as TiO_2) and with metal catalysts that can dissociate H_2 (such as Ni). Alternately, for substrates that are not easily reduced but act as strong Lewis bases (such as CaO), exposed oxygen anion sites on the surface can transfer a negative charge to the catalyst, and as this electron donation increases, the substrate-metal interaction strength increases [206]. In either case, the negative charge transfer to the catalyst particle can result in electron sharing between the catalyst and any adsorbates on the catalyst (such as hydrocarbons), weakening the adsorbate bonding and leading

to dissociation. However, while this charge sharing can enhance the catalytic ability of the metal in the dissociation of hydrocarbons during nanotube growth, the metal particle still must have an appropriate size and shape for nanotube formation. Very strong substrate-catalyst interactions lead to increased support reduction and oxygen diffusion between the metal and substrate surface, and for metal-support combination that show these effects, the metal may form an oxide and coat the substrate in a continuous film, rather than as discrete particles [311]. With metal-substrate combinations where only very weak reduction of the support occurs, the interactions are weaker and the deposited metal may take the form of small metal islands. An example of this is shown in Figure 2-25, where different metals were deposited on TiO_2 substrates. With increasing heats of formation of metal-oxygen bonds (Hf: -5.8 eV, Cr: -3.6eV, Fe: -2.8 eV, Cu: -1.7 eV), the thickness of the reduced Ti region at the surface of the TiO_2 substrate decreases and the surface-metal interaction weakens; as this occurs the deposited metal assumes a more island-like structure [311].

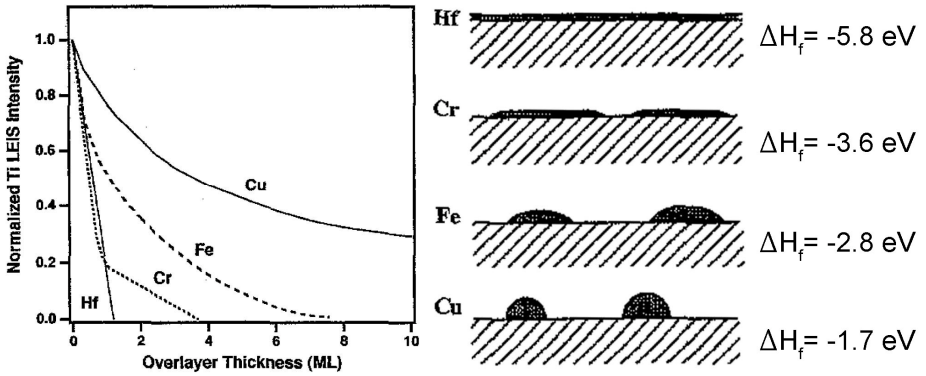

Figure 2-25: (left) Ti substrate LEIS signal as a function of thickness of deposited metal, (right) schematic of deposited morphology as function of metal-oxide heat of formation [311].

For a given metal-substrate combination, it may be energetically favorable to assume a morphology of fewer larger particles compared with the many, smaller particles that may form during deposition. In equilibrium, a metal particle size will balance strain energy due to differences in lattice constants and thermal expansion mismatch (increasing with larger particles) and increased surface energy (larger with many small particles) [312]. During heating and at the elevated temperatures required for carbon nanotube growth, these nanoscale particles can show liquid-like behavior at temperatures below their bulk melting points [161]. Bridges can form to span small distances between adjacent particles, facilitating the coalescence of two smaller islands into one larger particle [313]. This motion leads to an increase in average particle size, and this effect is more pronounced at elevated temperatures and with metal-substrate combinations with weaker interactions [220, 243]. Coalescence can occur abruptly (if the metal is in a liquid-like state) or gradually, as in Ostwald ripening processes), and in either case, after a sufficient heating time, the metal islands will tend to reach an equilibrium size [313]. This process is illustrated in Figure 2-26, and the final size of the sintered particles is a function of the materials used, the metal film thickness, and the heating time and temperature [155, 314-316].

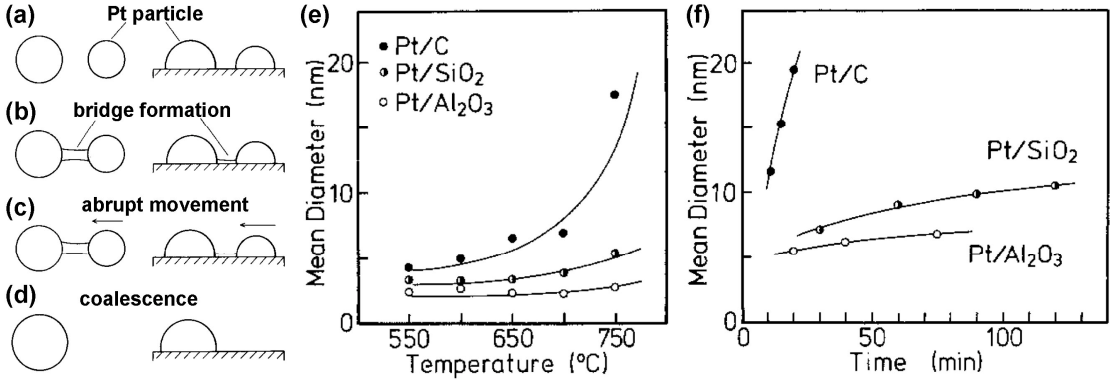

Figure 2-26: (a-d) Schematic of liquid-like particle coalescence process, (e) Effects of temperature on particle size, (f) Influence of heating time on particle size (Substrate interaction strength decreases from Al_2O_3 to SiO_2 to C) [313].

In addition to the influence of electronic metal-substrate interactions on particle coalescence, surface roughness has also been thought to affect the shape and size of metal particles on a substrate. Increased roughness or surface porosity can inhibit the coalescence of smaller particles at elevated temperatures by providing topological barriers to particle motion [205, 317]. In particular, it has been suggested that Al_2O_3 surfaces tend to have higher roughness than SiO_2 surfaces, and this helps prevent particle agglomeration on the alumina [207, 300]. Substrate orientation can also affect results, as the atomic arrangements (and therefore metal-substrate interactions) vary on different crystal faces [236]; differences have also been observed between growth on crystalline and amorphous surfaces [205]. Reaction gases can also affect the particle shape and size distribution after heating, with large gas-substrate interaction promoting small island formation and strong gas-metal interactions promoting thin film structures (such as the use of hydrogen to promote wetting [300]). This relation is given by the Young-Dupre Equation, where γ gives the surface

energies of each interface (with S, G, and M denoting substrate, gas, and metal, respectively), and θ gives the contact angle of the metal particle on the surface [318].

$$\gamma_{SG} = \gamma_{SM} + \gamma_{MG} \cos\theta \qquad (2\text{-}11)$$

During this process (metal film evaporation or particle preparation, and subsequent heating to nanotube synthesis temperature), the substrate and catalyst material can strongly influence the final particle size (in addition to other parameters, such as metal film thickness, temperature, etc.). If weak interactions exist between the metal catalyst and support surface, the particles can grow too large during the heating process (through coalescence), and no longer be an appropriate size to catalyze carbon nanotube growth. Alternately, if the catalyst-substrate interactions are strong, the particles may wet too well to the surface (or diffuse into the surface to form silicides, etc.) and will also be unsuccessful catalysts. These conditions are illustrated schematically in Figure 2-27. Metal particles need to have both an appropriate size and shape on the substrate surface in order to catalyze the growth of carbon nanotubes, although multi-walled tube growth has been reported across a broad range of process parameters and with a range of catalyst and substrate combinations. However, variations in substrate-catalyst interactions between different metals can lead to the growth of multi-walled nanotubes with different diameters (under otherwise identical synthesis conditions) [319]. These substrate effects are much more important when single-walled nanotube growth is desired, as the suitable catalyst size range is much more restricted than for multi-walled growth. Substrate-catalyst interactions can also affect catalyst spacing, influencing the resulting nanotube mat density.

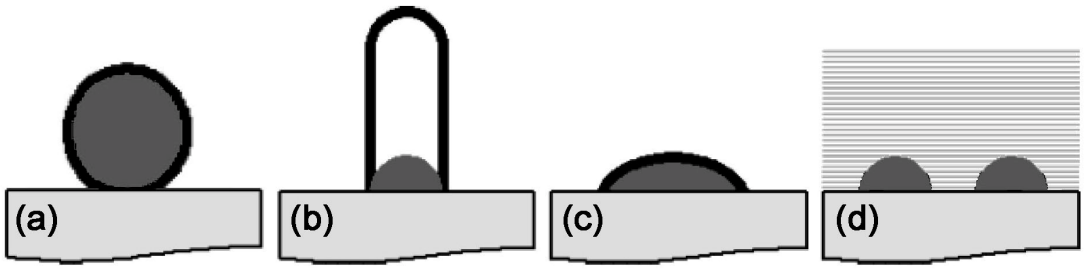

Figure 2-27: (a) weak catalyst-substrate interaction, catalyst is too large for growth, (b) metal island is appropriate size and shape for growth, (c) metal-substrate interaction is too strong, growth does not occur, (d), excessive amorphous carbon deposition prevents growth due to high temperature or hydrocarbon concentration [300].

For suitable combinations of catalyst material, quantity, particle shape, substrate composition, and substrate surface morphology, the resulting growth can be classified into two different mechanisms, differing in the interaction between the catalyst particle and substrate surface. These mechanisms are based on theories originally used for carbon filament growth and experimental results have been observed supporting both of these models, suggesting that either can be valid, depending on growth processes and parameters. The two theories differ in the motion of the catalyst particle relative to the substrate surface during nanotube growth; in the extrusion, or root growth model, the catalyst particle remains fixed to the substrate surface, and in the tip growth model, the particle detaches from the surface and moves with the tip of the nanotube as it grows [7, 148, 151]. The type of growth which occurs (base vs. tip), will be determined by the interaction forces between the particular metal catalyst and particular substrate used, as illustrated in Figure 2-28 [151].

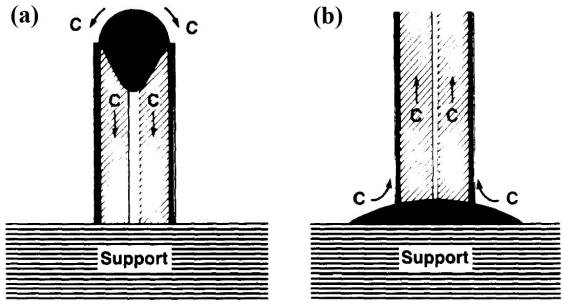

Figure 2-28: Catalyst-substrate interaction models (a) Tip growth model with weak catalyst-substrate interaction forces, and (b) Root growth model with strong catalyst-substrate interaction forces [151].

For specific substrate-catalyst combinations, where stronger interaction forces are found between the catalyst and the inner tube walls than with the substrate surface, tube growth will occur by the tip growth model. As additional carbon diffuses out of the catalyzed particle, the tube will extend away from the substrate, carrying the metal catalyst particle with it [11, 148, 151, 320]. In this method, the tube is in contact with the substrate at one end and is filled by the catalyst particle at the other end; this growth method is often verified experimentally using electron microscopy by observing tubes grown with metal caps at one end. In some results, metal catalyst particles have been found encapsulated away from the ends of the tubes [278], and a variation to this tip growth theory explains this using a liquid phase catalyst VLS growth model. According to this theory, under certain synthesis conditions catalyst particles may exist in liquid form (see Section 2.4.2), which could not only catalyze the growth at the tube end, but could also become encapsulated inside the tube as a result of capillary action.

In situations where the interfacial energies are greater between the catalyst and the substrate than between the metal and the nanotube walls, the catalyst will remain

on the substrate surface [151, 153, 321]. During this root growth process, the tube grows upwards, away from the substrate surface [148], and this is the preferred growth method for single-walled carbon nanotubes synthesis [155, 231]. Growth will continue as additional carbon reaches the catalyst and diffuses into the elongating nanotube, pushing the tube upwards. The gaseous carbon source can pass through gaps between adjacent nanotubes or can diffuse through the substrate surface to reach the catalyst particle, as illustrated in Figure 2-29. If the mat of carbon nanotubes grows sufficiently large and dense, the flow of carbon to the catalyst location at the bases of the tubes could eventually be interrupted, preventing further growth by this mechanism [162, 198]. It has been suggested that growth may also proceed by carbon deposition directly on the upper end of the tubes, provided the tube ends remain open during synthesis [165, 322]. An exposed, uncapped nanotube end will contain a number of available dangling bonds that can serve as sites for hydrocarbon decomposition. Carbon can then become incorporated into the graphitic lattice, causing the nanotube to grow from its upper end. However, exposed bonds at the open end of a nanotube would be unstable, and tube closure by “capping” (described in Section 2.4) is likely to preclude any significant growth at these open ends.

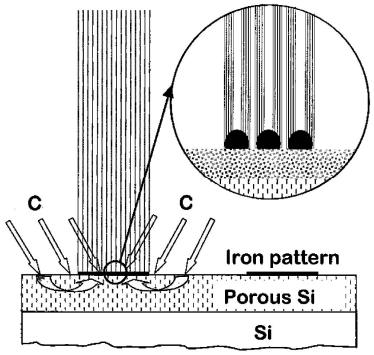

Figure 2-29: Root tip model of carbon nanotube growth demonstrating diffusion of carbon through substrate to reach catalytic particles [321].

2.4.4 Catalyst Poisoning and Growth Termination

To improve carbon nanotube yields during growth, it is important to both prolong the synthesis reaction duration and to maximize nanotube growth rates during the entire course of that reaction. Towards this goal, many published reports of nanotube synthesis optimization have included plots relating the length of nanotube produced with the reaction time. As nanotube growth rate is often limited by the diffusion of carbon through the metal catalyst particles, this diffusion rate (and the corresponding growth rate) should remain constant provided the reaction conditions (temperature, gas supply, etc.) do not change and additional carbon is supplied and the catalyst remains active. Under constant reaction conditions, growth of nanotubes to a desired length could be accomplished by simply prolonging the synthesis reaction until a pre-determined time has elapsed. However, while most growth methods do not change synthesis parameters during growth, a decrease in nanotube growth rate with time is almost always reported with a complete termination of growth beyond some reaction duration. Many published results plotting growth rate, mass gain, or

maximum length against reaction time show this trend (see Figure 2-30). This observation holds true for the growth of single- and multi-walled nanotubes and carbon fiber, and occurs with a range of reaction temperatures, catalyst metals, and carbon sources.

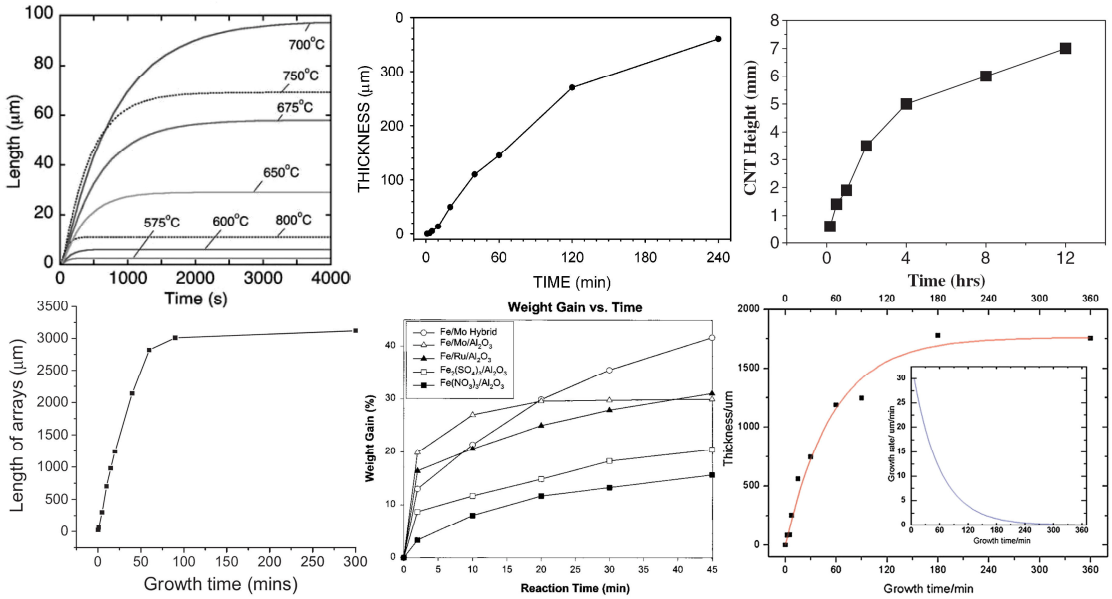

Figure 2-30: Typical plots of nanotube length as a function of reaction time, as reported by various groups [158, 179, 181, 189, 323, 324].

In some reports and under certain base-growth reaction conditions, this decrease in growth rate can be due to reduced diffusion of reactant gases to the substrate surface with increasing nanotube mat heights [199, 325]. In these situations, both a linear and parabolic dependency is observed between nanotube height and reaction time (following a Deal-Grove type diffusion law [326]), with a reduction in growth rate occurring as the diffusion length of reactants through the thickening nanotube mat increases. Methods to maintain short diffusion lengths throughout synthesis (such as by limiting substrate dimensions or using patterned catalysts) can be

used to prevent this slowing and sustain near-constant growth rates. In addition, limited availability of carbon reactants during synthesis can result in reduced growth rates (such as by using extremely low hydrocarbon partial pressures rather than due to reduced diffusion through growing nanotube mats). However, reduced growth rates (and eventual cessation in growth) are most commonly attributed to a different mechanism: the poisoning of the catalyst particle.

During synthesis, amorphous carbon can build up on the exposed surface of the metal particle, preventing further carbon from diffusing into the catalyst as more of its surface becomes encapsulated (see Figure 2-15) [158]. This process is referred to as catalyst "poisoning" and can terminate carbon nanotube growth prematurely [153, 327, 328]. A similar effect has also been observed through sulfur contamination, which serves to block the catalyst surface and inhibit additional carbon diffusion [147, 329]. Once carbon can no longer diffuse into the catalyst particle, growth will stop and the continuation of the reaction (and the continued introduction of the carbon source) will result in amorphous carbon deposition on other surfaces. These can include the reaction chamber walls or the outer tube surface [184], causing the tube diameter to increase as an amorphous carbon sheath builds up. This contamination is similar to that obtained if high reaction temperatures or hydrocarbon concentrations are used and self-pyrolysis occurs.

Several techniques can be used to prevent this unwanted carbon deposition and to prolong the period of maximum growth to achieve longer and longer nanotube mats prior to the termination of the reaction. These can be divided into two categories:

techniques that are used during growth and techniques where growth must be interrupted to remove carbon contamination. This problem has been recognized as early as 1972 in studies of carbon fiber, where growth would terminate prematurely due to amorphous carbon build-up. Baker *et al.* demonstrated the re-activation of catalysts by interrupting the growth reaction and replacing the acetylene flow in the reaction by either hydrogen or oxygen [6]. When oxygen was introduced amorphous carbon was selectively burned off first, followed by the graphitic carbon fiber, eventually leaving just the original nickel catalysts (which could then be re-used). With hydrogen amorphous carbon could be removed without damage to the carbon fiber, and growth could be restarted and a constant growth rate maintained, as shown in Figure 2-31. A similar result can be obtained by using sputter etching to remove the carbon cap poisoning the catalyst. If this etching is carefully controlled the catalyst and nanotubes can remain intact and growth on the existing tubes can be restarted and continued [330].

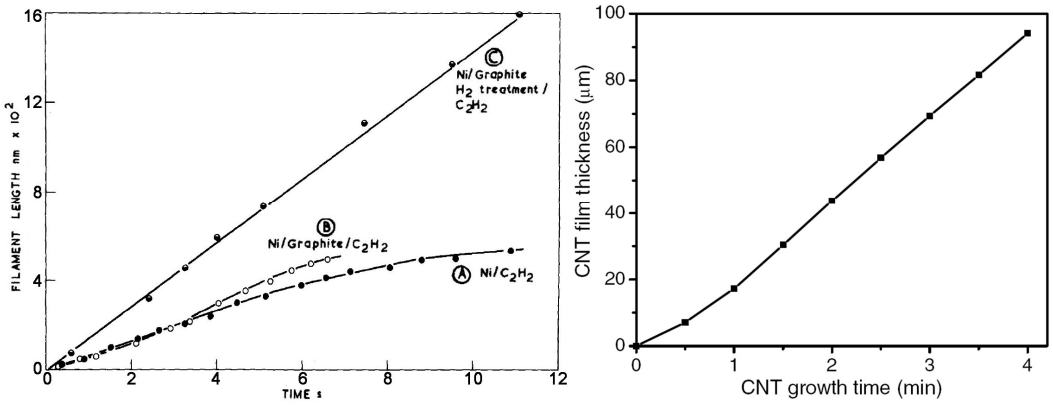

Figure 2-31: (left) Continuous carbon fiber growth rate with intermittent hydrogen treatment during synthesis [6], (right) Constant growth rate obtained with water-assisted CVD [197].

While growth rates can be maintained with these treatments, growth interruptions are required, reducing the overall nanotube production rate. More recently, synthesis optimizations have been achieved where controlled amounts of etching gases are added (either weak oxidizers or hydrogen derived from H_2 or from the decomposition of ammonia [331]). Figure 2-31 shows the constant growth rates possible using this approach. If the concentration of these gases is too low catalyst poisoning will not be adequately prevented while excessive concentrations can etch the nanotubes themselves and reduce growth [264]. However, different groups have reported growth in conditions ranging from very dilute hydrogen concentrations in the reaction gas to almost pure hydrogen [189, 332], so many other process variables can influence the optimal gas mixture. In addition to inhibiting catalyst poisoning, hydrogen has also been used to aid in nanotube nucleation and nitrogen (from ammonia gas) is thought to decrease the activation energy for growth by reducing strain energy in the tube walls [333]; these effects can both promote rapid growth. Ammonia has also been reported to etch the catalyst layer [334] and to prevent the formation of an oxide layer on the metal catalyst surface [335] as well as to reduce the formation of amorphous carbon [194, 310, 336]. Nitrogen from the ammonia gas can also become incorporated into the catalyst layer, which is thought to increase its productivity [337]. Alcohols have been used as a carbon source with good results, where OH radicals released during alcohol decomposition can help remove amorphous carbon [338, 339]. Oxygen can also be used directly, although in low concentrations (~1%) to limit oxidation of the nanotubes themselves [225]. One of the more

successful strategies for preventing catalyst poisoning has been the recent use of small amount of water vapor in the CVD reaction (typically less than several hundred parts per million) [188, 218, 301, 340]. This vapor functions as a weak oxidizer to remove unwanted carbon deposition during the course of growth and can act continually [207, 231, 341] or be used intermittently in a series of etching steps [94, 197, 199]. The improvement in growth with water vapor is shown in Figure 2-32. While water vapor, hydrogen, ammonia, and oxygen can all act to reduce amorphous carbon deposition and poisoning, growth termination will still eventually occur, although this can be delayed considerably.

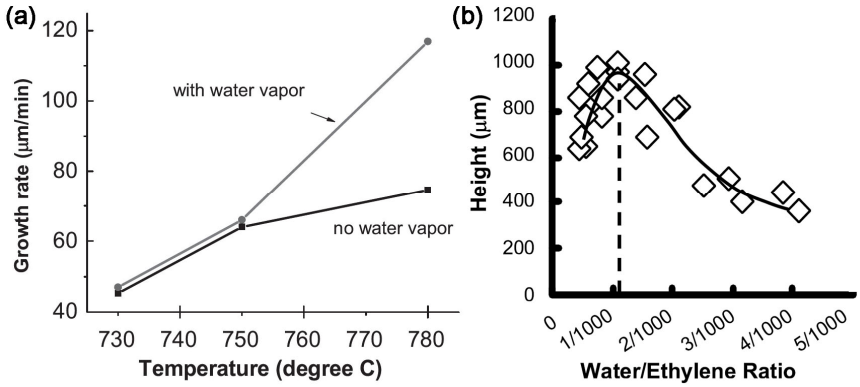

Figure 2-32: (a) Increased growth with water-assisted CVD [189], (b) Optimal water/C2H4 ratio determined by Futaba et al. [340]

Two final methods for achieving prolonged growth and constant growth rates during synthesis have been described in the literature. With careful control over reaction conditions, gas flow, and turbulence inside the reaction chamber, catalyst-substrate interactions can be minimized and the catalyst can "float" in the gas flow [87, 192]. Growth can continue while the catalyst is suspended above the substrate, producing very long tubes. Alternately, as existing catalysts are deactivated through

poisoning, new catalyst material can be added to the reaction, and this can be accomplished using floating catalyst growth methods (see Section 2.5.3). However, drawbacks to both these procedures (such as difficulty in forming densely packed nanotube arrays or patterns and discontinuous growth of tubes along the mat length), make them unsuitable as a synthesis methods for many applications.

For optimal growth, not only does catalyst poisoning need to be reduced or eliminated, but the growth rate of the nanotubes needs to be maximized. The activation energy for catalyst assisted carbon nanotube growth is related to the activation energy for diffusion of carbon through the metal catalyst, suggesting that methods to increase diffusion could be applied to speed synthesis. Faster growth can typically be achieved with smaller, more numerous catalyst particles, as the total catalyst surface area is larger (for hydrocarbon decomposition) and the diffusion length through each particle is shorter [297, 314]. As a result of this effect, single-walled carbon nanotubes (most commonly supported on alumina substrates, see Section 2.4.3) typically grow faster than multi-walled carbon nanotubes. Under optimal conditions nanotube growth rates can be quite fast; initial growth rates as high as 220 µm/s have been reported [342] and sustained growth rates reaching 2.5 µm/s for aligned multi-walled nanotube arrays [95, 343], 4.2 µm/s for single-walled arrays [231] and 11 µm/s for isolated single-walled tubes [36] have been achieved. Both elevated temperatures (which can increase the diffusion rate of carbon through the catalyst [194, 344]), and increased hydrocarbon concentrations can lead to faster initial growth rates; however, these can both accelerate poisoning, reducing the ultimate

length [158]. In order to maximize nanotube length, an intermediate carbon source concentration is often used [225, 342] and the reaction temperature should minimize the self-pyrolysis of the hydrocarbon source.

2.4.5 Aligned Nanotube Growth

Most nanotubes produced using arc discharge and laser ablation techniques, as well as the first demonstrated production of nanotubes via chemical vapor deposition (CVD) methods (see Section 2.5) resulted in un-aligned tubes [174]. This is undesirable, as the growth of un-aligned tubes can terminate as tubes impinge upon each other. However, under specific conditions, well-aligned nanotube structures can often be produced using chemical vapor deposition methods [145, 264, 321, 345] (even with process improvements nanotube products from arc discharge, laser ablation, and other techniques still tend to be in the form of disordered deposits). Alignment can occur from both the base-growth and tip-growth mechanisms described in Section 2.4.3, although it has been suggested that alignment is easier to achieve when base growth is occurring [308]. Initially tubes can nucleate and grow in random orientations on the substrate surface. Tubes aligned near to parallel to the surface, quickly stop growing as they come into contact with the bases of other tubes on the substrate. Tubes aligned closer to perpendicular will grow away from the surface, with small changes in growth direction occurring as a result of van der Waals forces and contact between adjacent tubes. This impingement (referred to as the crowding mechanism) begins to influence growth very early in the reaction (30-100 seconds) [111], and will result in a mat of very well-aligned tubes [145, 152, 321, 346]. Figure

2-33 shows the initial nanotube nucleation and the impingement, which occurs due to crowding, leading to well aligned bundles of tubes. Alternately, during the initial stages of growth, a randomly aligned, two dimensional network of nanotubes can form [325]. Under the base growth mechanism, this network will lift off from the substrate surface as growth continues; this tangled region will prevent nanotubes from growing in different directions and result in a nanotube forest with a smooth upper surface (although slight bending of tubes along their length could occur due to non-uniform growth rates).

Under adverse growth conditions, such as with high hydrocarbon concentrations (which can lead to rapid catalyst poisoning), growth can be limited and sufficient crowding cannot occur to produce alignment [324]. In addition, alignment may be poor if the catalyst particle sizes are outside an optimal range or if they are distributed too sparsely over the substrate surface [297, 325, 347].

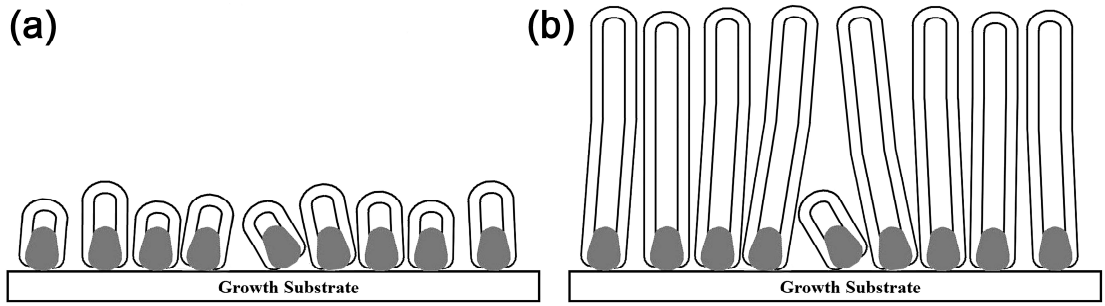

Figure 2-33: Crowding mechanism for carbon nanotube alignment (a) initiation of growth with poor alignment (b) impingement and aligned growth.

This orientation is maintained throughout growth, and will remain even when separated from the substrate due to Van der Waals forces between neighboring tube walls [152]. This alignment has also been observed in single-walled carbon nanotubes

produced by vapor phase growth, where bundles with thicknesses in the tens of nanometers can form independently of any substrate [348]. These structures are also held together by Van der Waals forces between adjacent tubes.

In addition to this crowding effect, which can lead to alignment with any CVD growth process provided the catalyst spacing on the substrate is suitably dense, other external influences can be applied during synthesis to promote alignment. Nanotubes have been reported to preferentially grow in the direction of electric field lines, and this has been achieved by biasing the substrate [349] and with plasma-assisted CVD methods [227, 328, 350-352] (see Section 2.5.4), and these fields can be manipulated through the use of metal blocks to produce aligned, angled growth [353]. These field lines can exert an electrostatic force on the catalyst, and if the nanotube deviates from parallel growth, these forces can lead to the development of compressive or tensile stresses between the particle and the nanotube walls. It has been proposed that these stresses can slightly change carbon diffusion rates through the particle, slowing the elongation speed in the compressive region and directing the growth direction back towards parallel [227]. This mechanism is illustrated in Figure 2-34.

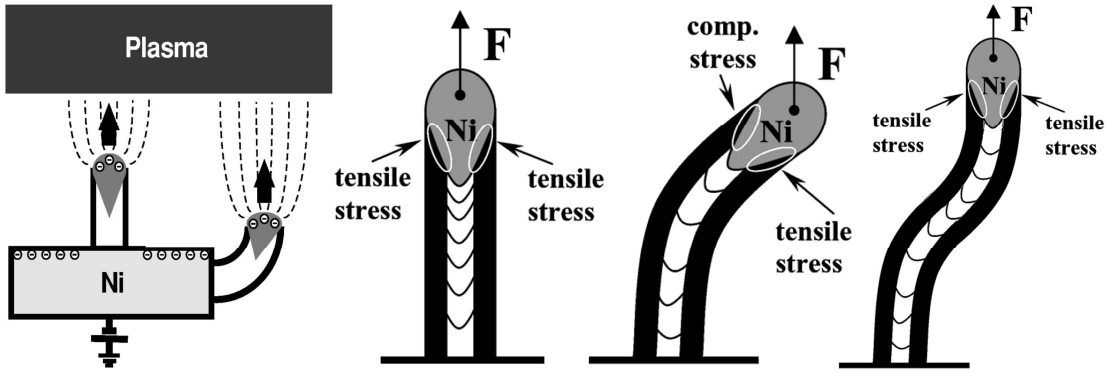

Figure 2-34: Carbon nanotube alignment mechanism in an electric field [227, 350].

2.4.6 Alternate Nanotube morphologies

Most carbon nanotubes referred to in the literature share similar structures, and are long straight tubes with the graphite lattice in the walls aligned parallel to the tube axis. Other structures are possible (see Figure 2-13c-d), although these are typically only found in larger diameter carbon fibers [354, 355] and are not observed in carbon nanotubes (with diameters less than roughly 100nm). However, under certain synthesis conditions, carbon nanotubes can be grown with different wall structures (where the graphite lattice is no longer parallel to the tube axis) and with different geometries (rather than long, straight tubes).

The most common alternate nanotube structure is the bamboo morphology, where the graphite lattice can be angled relative to the tube axis, leading to bridging of the nanotube core by the innermost walls, creating a compartmentalized structure. This effect is most often achieved when nitrogen is present in the reaction [333, 356-358], typically in the form of ammonia gas [359] (which is often added to inhibit catalyst poisoning). However, nitrogen, while promoting the growth of bamboo

nanotubes, is not required for bamboo growth, and this morphology may occur in nitrogen-free synthesis reactions [360]. In many cases, however, ammonia gas or other nitrogen species are used during growth and a resulting bamboo structure is reported, yet when growth mechanisms are discussed no correlation or connection is drawn between this bamboo morphology and the presence of nitrogen in the reaction [361-363]. The spacing between subsequent compartments in bamboo nanotubes has been shown to decrease with increasing ammonia concentrations [260] and hydrocarbon partial pressures [363], while the relationship between this spacing and temperature is unclear, with one group reporting decreased spacing with temperature [194], and increased spacing reported in another study [260]. The intermittent introduction of ammonia during synthesis can also be used to grow nanotubes with alternating straight-walled and bamboo regions [359].

Several theories have been proposed to explain the formation of this bamboo structure. One of the first, by Iijima *et al.* in 1992, describes how the incorporation of pentagonal defects into the hexagonal lattice can lead to tube closure. If these defects form in the inner shells of a multi-walled tube, closure of the central tube can occur while growth continues in the surrounding tubes. Closure of these central tubes at different locations along the length of the tube will lead to the segmented, “bamboo” morphology, which has been experimentally observed [173, 364]. The incorporation of nitrogen into the nanotube lattice has been proposed to reduce strain, and this could assist in the formation of the increased curvature found in the bamboo compartment walls [333, 356].

Bamboo nanotube formation has also been described in terms of increased bulk carbon diffusion through the catalyst particle [194, 344, 365]. Typical straight-walled nanotube growth models describe carbon diffusion through a disordered surface region on the metal particle with carbon traveling directly to the growing nanotube walls without passing through the center of the catalyst (see Section 2.4). With increased diffusion through the particle, rather than around its surface, graphitic layers can form on the catalyst inside the tube. As these layers grow they will eventually span the opening between the inner tube walls; at this point they fuse with the walls, and this new compartment is separated from the catalyst as the tube continues to grow [365, 366]. This process can occur either continuously or in an incremental fashion. Once this bamboo segment has attached to the inner tube walls, interactions between the catalyst surface and this segment may "trap" the metal particle in place. If this occurs tensile stresses will develop at this interface as the tube continues to grow and attempts to move away from the catalyst particle. Compressive lateral forces can also act on the particle as additional carbon is precipitated through the sides of the catalyst. These forces will eventually overcome the interaction energy between the catalyst and the bamboo compartment, ejecting the catalyst and allowing the nanotube growth to continue through the repetition of this process [211, 360]. Transition metals have been shown to catalyze the decomposition of ammonia, leading to the formation of nitrides and both hydrogen and nitrogen gas [367]. The presence of nitrogen can also reduce the solubility limit of carbon in iron, resulting in carbide formation at lower carbon concentrations [368]. In addition, a study by Lin *et al.* showed that carbon diffusion

rates through iron, nickel, and cobalt (the most common nanotube catalysts) were increased when nitrogen was also present in the metal [369, 370]. This increased diffusion rate will enhance bulk carbon diffusion through the catalyst particle, facilitating the formation of nanotubes with bamboo morphology, and this process can occur through either tip- or base-growth mechanisms, as shown in Figure 2-35.

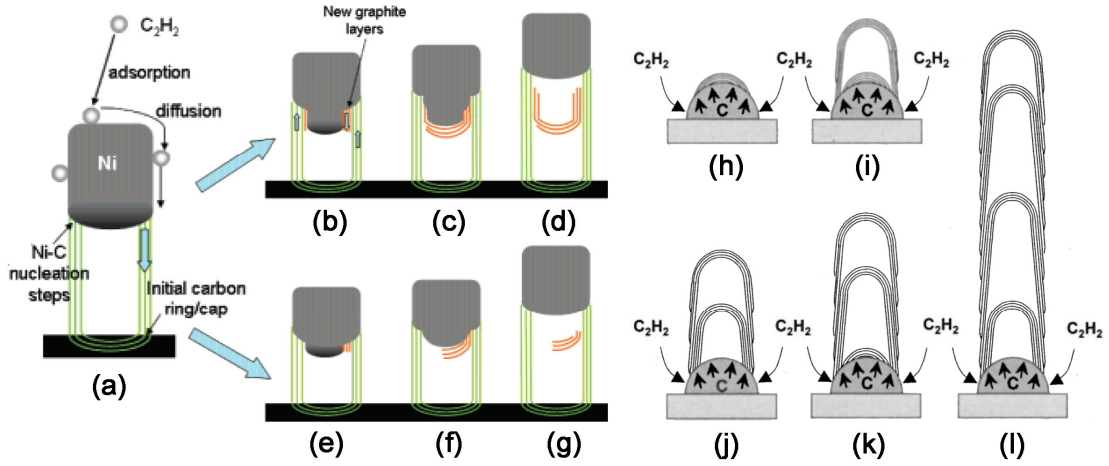

Figure 2-35: (a-d) Formation mechanism of bamboo carbon nanotubes via tip growth, (e-f) formation of a partial bamboo compartment, (h-l) bamboo synthesis via base growth [360, 365].

While bamboo carbon nanotubes have a compartmentalized internal structure, they still often grow as long, straight tubes. Two other reported nanotube morphologies differ in their external shape: coiled carbon nanotubes and branched carbon nanotubes. Coiled nanotubes have been reported under a range of synthesis conditions. Chemical vapor deposition with melamine ($C_3H_6N_6$) added as a reactant or with cupric acetate or zinc catalyst solutions have produced coiled structures [357, 371-373]. It has been proposed that non-symmetrical diffusion routes through the catalyst particles can lead to coiled structures [372, 374-376], and under certain

conditions changes in catalyst particle structure with aging can lead to this effect [371].

Branched nanotubes structures have been fabricated by a number of means. Titanium can be introduced to the growth reaction as a co-catalyst, depositing on, and initiating branch growth on nanotube walls [377, 378]. Under some conditions (such as if additional catalyst material is added during growth), adjacent metal particles can fuse together to create a junction and continue growth as a single tube [359, 379]. Branched structures can also be obtained without the introduction of additional catalyst material. Under certain growth condition with plasma-enhanced CVD, the size of the primary catalyst particle can be reduced by sputtering, and this catalyst material can be re-deposited on the side of the nanotubes and serve as new catalyst particles for continued growth [380]. With larger catalysts (used for thick multi-walled nanotube or carbon fiber growth), particle geometry can contribute to branching, where multiple tubes can grow from regions of high curvature on the same metal particle [11, 381]. Additionally, the reduced melting temperatures observed for very small metal particles can lead to liquid phase catalysts that can separate into multiple branches during growth [382].

2.5 Nanotube Growth Methods

The formation of carbon nanotubes has been widely studied, and many varied synthesis methods have been reported [175, 177, 383-387]. However, the majority of the studies on nanotube growth have used one of three primary growth techniques. Arc discharge was the first method demonstrated to create nanotubes and uses a high

voltage arc to vaporize a graphite target [3]. Laser ablation is used to synthesize nanotubes through a mechanism similar to that in arc discharge, however, high energy laser pulses are used to vaporize a carbon target rather than the high voltages used in the arc discharge method [178]. Chemical vapor deposition (CVD) techniques can also be used to grow carbon nanotubes; this is most commonly accomplished by the decomposition of a carbon source in the presence of a metal catalyst [174]. Chemical vapor deposition techniques are quite versatile, and many variations to the basic CVD technique have been reported. There are advantages and disadvantages to each of these methods, in terms of purity of the product, expense, and potential for large scale carbon nanotube synthesis. CVD growth methods tend to be the most widespread due to their lower relative cost, the ease of production of aligned and patterned nanotube forests, and recent advances overcoming some initial drawbacks.

2.5.1 Chemical Vapor Deposition

Chemical vapor deposition (CVD) is a simple method of nanotube production that can produce a wide range of carbon nanotube structures [224] at relatively low temperature (typically in the 600°C to 1100°C range). The use of CVD to produce carbon nanotubes was first demonstrated by Endo *et al.*, in 1993 [174], although Baker *et al.* had demonstrated the formation of carbon filaments by the decomposition of acetylene as early as 1972 [6]. In an inert gas environment (such as nitrogen [229], helium [204], or argon), a carbon containing source gas or liquid is fed into a reaction tube (often quartz) inside a furnace. Typical carbon containing sources used in this method include acetylene (C_2H_2), ethylene (C_2H_4), benzene (C_6H_6), and methane

(CH_4) (see Section 2.4.1). The decomposition, or cracking, of the hydrocarbons is achieved through the catalytic action of metal particles at elevated temperatures or by heating the carbon source to above its self-pyrolysis temperature. In the former case carbon diffuses into the catalyst particles; in the latter case carbon can deposit in the form of soot on exposed surfaces within the reaction zone. In some chemical vapor deposition processes, additional energy sources, such as plasma or laser, are also used to assist in the hydrocarbon decomposition. In almost all nanotube-producing CVD reactions, a catalyst is used, and a wide range of metals have been successfully used (see Section 2.4.2). The catalyst is typically deposited on the substrate surface prior to the growth reaction, although it can also be fed into the reaction chamber simultaneously with the carbon source. During the reaction, and in the presence of a proper metal catalyst, carbon will diffuse into these metal clusters and carbon nanotubes will form. There are several variations to this basic process described in the literature.

The use of chemical vapor deposition methods for nanotube growth has several benefits, including ease of scaling up to commercial production, and the production of long, aligned mats of tubes. Single-walled tubes can be produced, and control over nanotube diameter can be obtained by careful selection of the type and amount of catalyst used (see Section 2.4.2). With some early CVD growth, the tubes often contained high levels of defects, which reduced the effective strength and stiffness compared to tubes made with the other methods [62]. However, improvements to this process have helped to eliminate this drawback, and post-synthesis heat treatment can

also be used to remove defects [388]. The simplicity of the CVD method, combined with its commercial and cost benefits, makes it the most widely used nanotube production method. In addition, there has been an effort by many groups (beginning shortly after the discovery of carbon nanotubes) to increase the maximum length to which they could be grown. One of the biggest challenges for many nanotube-based applications is to scale nanotubes to a size that takes advantage of their desirable properties beyond the nanometer and micron levels. The synthesis of longer nanotubes can not only help alleviate many drawbacks currently faced by macro-scale nanotube applications (such as poor performance of CNT-based composites due to low CNT-matrix interfacial strength, see Section 2.7.2.1), but also increase yield and production rates, reducing currently high nanotube synthesis costs. Chemical vapor deposition growth has proven the most effective of the numerous nanotube growth methods towards achieving this goal. Steady refinements to the CVD process (such as efforts to avoid catalyst poisoning described in Section 2.4.4) have resulted in the breaking and re-breaking of “world-record” claims to the longest published nanotubes, as shown in Figure 2-36.

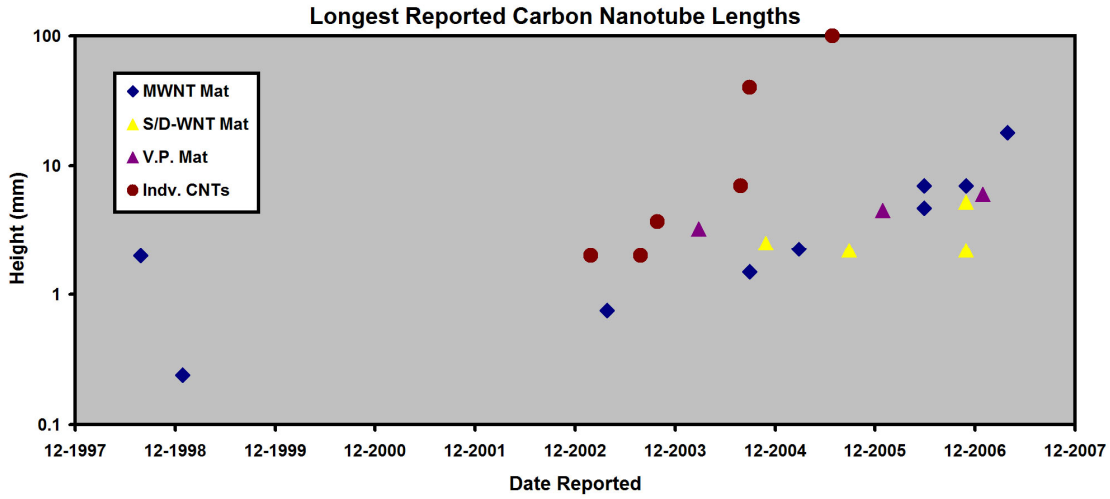

Figure 2-36: Progression of "world-record" carbon nanotube lengths with growth by various methods [31, 33-36, 87, 158, 188, 189, 214, 217, 221, 229-231, 246, 321, 323, 346, 389-391].

2.5.2 Thermal Chemical Vapor Deposition

Thermal chemical vapor deposition is one of the most basic methods of nanotube production. A carbon source is fed into the reaction chamber, which is held at a temperature high enough for the decomposition of the hydrocarbon source gas on the metal catalyst particles to occur. A wide variety of carbon sources have been used to successfully grow carbon nanotubes, including benzene [392], xylene [393, 394], acetylene [395-397], and methane [398-400] (Section 2.4.1). A transition metal, such as iron, cobalt, or nickel, is typically used as a catalyst (Section 2.4.2), and is often deposited in a thin layer [319, 401, 402] or precipitated out of solution as nanoscale particles and supported on a substrate (Section 2.4.3). In thermal CVD this catalyst deposition is performed prior to the growth reaction. Temperatures used during

thermal CVD are typically in the 550-1200°C range [196, 259], and a diagram of a simple equipment set-up is shown in Figure 2-37.

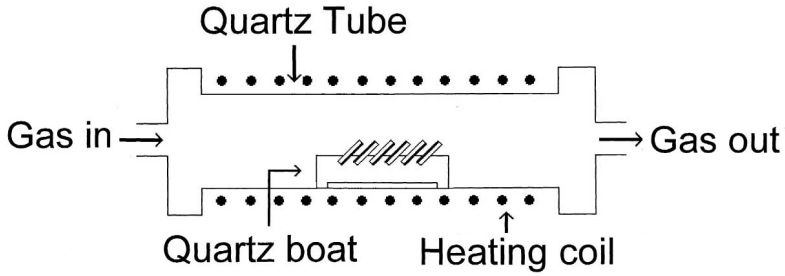

Figure 2-37: Typical equipment set-up for thermal chemical vapor deposition growth of carbon nanotubes [403].

During growth, an inert carrier gas (such as argon) is used to carry the carbon source into the reaction chamber; gaseous hydrocarbons are simply mixed with the carrier gas, while liquid hydrocarbons can be allowed to evaporate into the inert gas stream. With appropriate reaction conditions, carbon nanotubes will grow on the catalyst-treated substrates, and the diameters and lengths of the resulting nanotubes can be controlled by varying reaction parameters, such as catalyst film thickness, carbon feed rate, and total reaction time [142, 259, 272, 404]. With sufficient catalyst distribution over the substrate surface, the nanotubes are grown in a very well-aligned orientation, and either multi-walled or single-walled tubes can be produced. While thermal CVD is commonly performed with good success at atmospheric pressures, low pressure growth can also be performed by simply pumping down the reaction chamber during synthesis. A low partial pressure of the hydrocarbon source is desirable to prevent excessive formation of unwanted carbon byproducts, and growth at low total reaction pressure ensures this low partial pressure. This allows the use of

higher hydrocarbon introduction rates; as an example, Zhang *et al.* were able to increase acetylene flow 40-fold in their thermal CVD process by reducing the pressure from atmospheric to 2 torr [263].

Thermal chemical vapor deposition is the most commonly used growth method, due to its simple set-up and ease of nanotube production under a wide range of conditions. In addition, when compared to other common growth methods, thermal CVD offers relatively inexpensive equipment and reactants, and due to its lower operating temperatures, much cheaper operating costs for production of nanotubes. For these reasons it is the growth method most often scaled up for commercial nanotube production. Thermal CVD also serves as a starting point for a range of modifications and improvements that have been reported to this simple chemical vapor deposition process. These variations include different methods of catalyst and reactant introduction (such as floating catalyst CVD) and the use of several different energy sources in addition to the furnace during the reaction.

2.5.3 Floating Catalyst CVD

A common variation to the thermal CVD procedure uses a bare substrate material (rather than a metal coated surface) and introduces the catalyst material as the growth reaction proceeds. The carbon source, usually in the form of a liquid hydrocarbon (such as benzene or xylene), is combined with a catalyst source (often ferrocene) to form a solution which is then fed into a heated furnace [30, 145, 146, 348, 405-408]. This reactant introduction can also occur by evaporating the catalyst into the gas [145] or by bubbling the gas through a catalyst solution [30, 406]. This

synthesis method has been referred to using a range of names, including floating catalyst CVD, vapor phase CVD, injection CVD, and spray pyrolysis CVD. During growth, decomposition of the metal compound results in the formation of nano-scale catalyst particles; this process can be assisted by hydrogen in the reaction and the particle size can vary depending on the reaction temperature [409]. This nucleation can occur in the vapor, unsupported by any surfaces (with floating catalysts) or the evaporated catalyst material can deposit on surfaces within the furnace and simultaneously start the growth of nanotubes (where growth can continue via the base growth mechanism [237]). Nanotube products can typically be collected in the exhaust gas from the furnace, from the furnace walls, or on substrate surfaces within the reaction chamber. Both multi- and single-walled nanotubes have been grown with a variety of catalysts and single-walled nanotube growth has also been reported with this process without the use of a catalyst [348, 405]. Nanotubes collected from the furnace walls or substrate surface can be very well aligned due to the same mechanisms described in Section 2.4.5. The concentration of the catalyst-carbon source solution, as well as growth temperature and other process parameters can influence the length, diameters, and morphology of the produced tubes [410].

Typically reactant solutions are allowed to evaporate slowly into the inert carrier gas; however, in some cases a high velocity gas stream is used to jet the reactant solution into the furnace [242]. This process is called spray pyrolysis CVD, where the solution is forced through a small nozzle by gas flows that can be 1000 times higher than commonly used; this atomizes the liquid and brings it into the

reaction chamber. Once inside the furnace the decomposition of the hydrocarbon and metal catalyst containing species can occur and nanotubes will form by the same process as described previously. An example of the equipment set-up used for the spray pyrolysis growth of carbon nanotubes is shown in Figure 2-38, where argon is being used to atomize a benzene and ferrocene mixture.

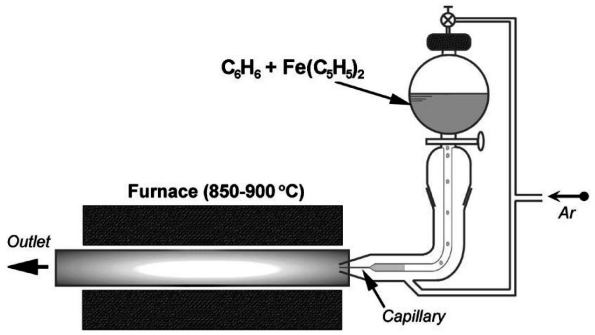

Figure 2-38: Spray pyrolysis equipment set-up for vapor phase carbon nanotubes formation [242].

2.5.4 CVD Modifications

While the most common CVD methods rely on only thermal energy during the reaction to facilitate hydrocarbon decomposition and carbon diffusion, a number of variations have been reported where additional energy sources are implemented.

A plasma-enhanced CVD process is often used, and in this technique the reaction chamber is modified to contain two electrodes, which create plasma surrounding the substrate. Due to the energy provided by this plasma, the thermal energy requirements for hydrocarbon decomposition are not as great, and nanotubes can be produced at much lower temperatures than with normal thermal CVD. This

method has been shown to produce nanotubes at temperatures as low as 330°C, using nickel, iron, or cobalt as a catalyst [314, 319, 328, 350, 411-415].

Other CVD methods have been developed that provide a localized heat source, allowing the hydrocarbon decomposition temperatures to be controlled separately and optimized independently from the substrate temperature. The entire reaction still occurs within a furnace; however lasers [294], molecular beams [179], and resistively heated tungsten filaments (at ~2000°C) [264, 274] have be used to provide local heating to aid in hydrocarbon decomposition. In particular, the use of lasers in this way has been known for many years, and laser have assisted in carbon fiber synthesis via the localized decomposition of hydrocarbons as early as 1972 [28].

A final variation on the standard chemical vapor deposition technique utilizes carbon monoxide as a carbon source and can efficiently produce single-walled nanotubes (with up to 97% purity) [253, 254]. In this variation, high pressures (between 1 and 50 atmospheres) are used to promote CO decomposition. This procedure is referred to as a HiPCO process, and carbon monoxide is combined with a metal catalyst compound at room temperature; this solution is then mixed with heated carbon monoxide and fed into a high pressure reaction chamber which is kept between 800°C and 1200°C.

2.5.5 Other Growth Methods

Although chemical vapor deposition is the most widely used carbon nanotube growth method (in both research and commercial growth), it is not the only process used to produce carbon nanotubes, and was not even the first reported method for

nanotube growth. Two other nanotube synthesis procedures (arc discharge and laser ablation) are used regularly, and these processes are briefly described below. A wide range of other methods have also successfully produced nanotubes (such as flame synthesis [384, 385, 416-418], electrochemical synthesis [386], and formation under ion or electron beam irradiation [176, 177]), although these techniques may not offer the highest quality, yields, or efficiency.

2.5.5.1 Arc Discharge

The nanotubes grown by Iijima and reported in the paper that sparked the recent interest in this field were created using the arc discharge method [3]. In arc discharge nanotube production, a carbon source is vaporized by an electric arc. As this carbon condenses it forms deposits of nanotube-containing soot on the inside of the arc discharge chamber, which can then be collected [419-422]. The very high temperature (as high as 4000°K [5, 420]) obtained using the arc discharge technique leads to nanotubes, which are highly graphitic in nature with few defects [421]. Figure 2-39 shows a typical arc discharge equipment set-up. A linear motion motor moves the anode forward as it is vaporized to maintain a constant distance to the cathode [423] and the carbon soot produced is deposited on the cathode and on the chamber above the arc.

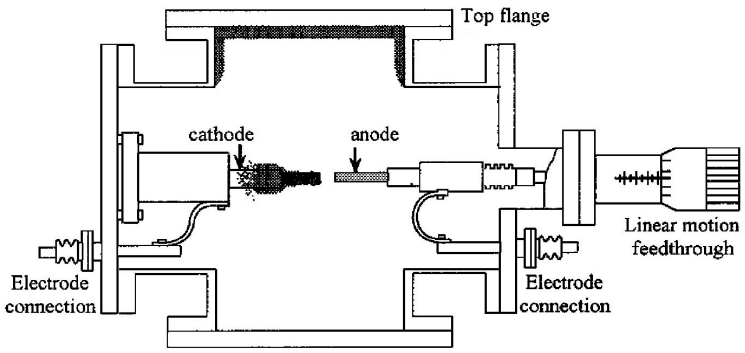

Figure 2-39: Arc Discharge nanotube growth equipment with a horizontal orientation, showing deposit locations [281]

The arc discharge technique can be used to grow either single or multi-walled carbon nanotubes, depending on the composition of the anode used in growth. Multi-walled nanotubes are produced with a pure carbon anode [424, 425] and the addition of a metal catalyst is used to produce single-walled nanotubes. A wide variety of metals have been shown to catalyze the formation of single-walled tubes in arc discharge, including some lanthanides (gadolinium, neodymium, and lanthanum), transition metals (cobalt, iron, nickel, and copper) [426, 427], and some platinum group metals (rhodium, palladium, and platinum) [281]. Differences in reaction atmosphere can also be used to control the diameters found in single-walled tubes, as variations in the reaction gas compositions are thought to affect the carbon condensation rate and the speed of nanotube growth [419].

2.5.5.2 Laser Ablation

Laser ablation is a technique originated by Richard Smalley at Rice University that uses a laser beam to vaporize a carbon target [178]. As with arc discharge growth, a solid graphitic carbon source is used, and very high temperatures are

required to vaporize this target. In this technique a laser beam is used and the reaction takes place inside a furnace in an inert gas environment. Typical furnace temperatures are 800°-1200°C [178, 428], but can be as low as 500°C [273], and argon [429-431] and hydrogen [22] can be used as inert carrier gases. Both CO_2 [432-434] and Nd:YAG [428, 431, 435] lasers have been used in continuous [432] or pulsed [436] operation to form nanotubes with this method. For single-walled nanotube growth, the graphite target is doped with a nickel or cobalt metal catalyst [437], and iron, platinum, copper, and yttrium have been used as co-catalysts [178, 438], producing yields of single-walled carbon nanotubes as high as 70 to 90% [439, 440]. Multi-walled nanotubes can be grown with a pure or boron-doped graphite target [273, 441]. Catalyst, temperature, and reaction gas variations can alter the diameter distribution of the single-walled tubes produced [22, 442]. A typical set-up of the equipment used in laser ablation is show in Figure 2-40, where an argon stream is used to carry the carbon and catalyst particles vaporized by the laser towards a collector (not shown).

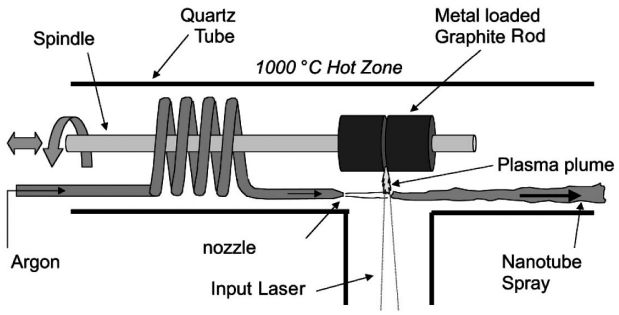

Figure 2-40: Typical laser ablation apparatus for production of carbon nanotubes, nanotubes are collected downstream from the argon flow [436].

2.6 Characterization of Carbon Nanotubes

In addition to specialized characterization techniques used to investigate particular properties of carbon nanotubes (such as mechanical, electrical, optical, etc.), there are several general approaches that are commonly used in the analysis of carbon nanotubes. These methods allow for the measurement of nanotube size as well as quality and presence of defects or contamination of the nanotubes. Electron microscopy is often used to image carbon nanotubes due to their very small size. Scanning electron microscopy (SEM) can be used to measure lengths of carbon nanotubes and assess the degree of alignment in carbon nanotube mats. Transmission electron microscopy (TEM) allows for higher magnifications (compared to SEM) that can be used to measure nanotube diameters, count the number of concentric walls (single-walled vs. multi-walled tubes), and view the tube morphology (straight or bamboo walls). Selected area and convergent beam electron diffraction can also be performed in the TEM to determine the crystalline lattice and orientation of catalyst particles and nanotubes. Energy dispersive x-ray spectroscopy is a technique that can be used with both SEM and TEM to measure the elemental composition of regions in the sample. High energy beam electrons may eject inner shell electrons from atoms in the sample, causing outer shell electrons to drop in to fill these holes. As these electrons drop from higher energy to lower energy states, an x-ray can be emitted with energy equal to the difference in energy between the two orbits, and this energy is characteristic for specific elements. These x-rays are collected, with x-rays of characteristic energies indicating the presence of particular elements. This technique

can be used to identify catalysts and contaminants within the sample [443]. Both SEM and TEM can also be used to identify the presence of contaminants (such as amorphous carbon particles) within the sample through visual inspection.

Another common method of imaging carbon nanotubes is through atomic force microscopy. Nanotubes are dispersed on a flat surface and a sharp probe tip on the end of a cantilever is brought into very close contact with the sample. As the probe is scanned across the surface, interactions between the tip and nanotubes on the substrate are detected through deflections in the cantilever supporting the probe, generating a topographical map of the surface. Nanotube lengths and diameters can be measured, and nano-indentation can be used to perform simple mechanical characterization.

In addition to imaging contaminants using electron microscopy, the presence of non-nanotube product can be characterized using thermal methods. Temperature controlled oxidation can be performed using a thermo-gravimetric analyzer, where the mass of the sample is measured as the temperature is ramped up in an atmosphere containing a small, controlled amount of oxygen [391, 444]. Nanotubes, having a higher thermal stability than amorphous carbon, will burn off at higher temperatures, and with increasing amorphous carbon contamination in the sample, the temperature corresponding to the peak burn-off rate will shift lower. In addition, after the mass loss has stabilized (after all nanotube and amorphous carbon product have burned off), the remaining mass gives an indication of the original non-carbon content of the sample (typically the mass of the residual catalyst).

Perhaps the most common method of characterizing the quality and purity of carbon nanotubes is the use of Raman spectroscopy. A nanotube sample is illuminated by a laser, and Raman scattering can be measured by shift in the wavelength of the laser light scattered from the sample relative to the incident laser. Incident photons can excite atoms in the sample to a higher energy state, and these atoms can then decay into a vibrational state. The increased energy of this phonon mode will result in a corresponding loss of energy in the scattered light, indicated by a shift to a longer wavelength. This shift is called a Raman shift, and the scattered light is referred to as Stokes radiation. Different atomic bonding arrangements have characteristic phonon modes, and as these modes are excited certain wavelength shifts will be measured, each relating to a particular vibrational mode. As a corollary to this effect, atoms which are already in an excited vibration state can relax due to interactions with the incident light, emitting "anti-Stokes" radiation whose wavelength has been shortened. This effect is not typically used to characterize carbon nanotubes, however. A typical Raman spectrum is shown in Figure 2-41.

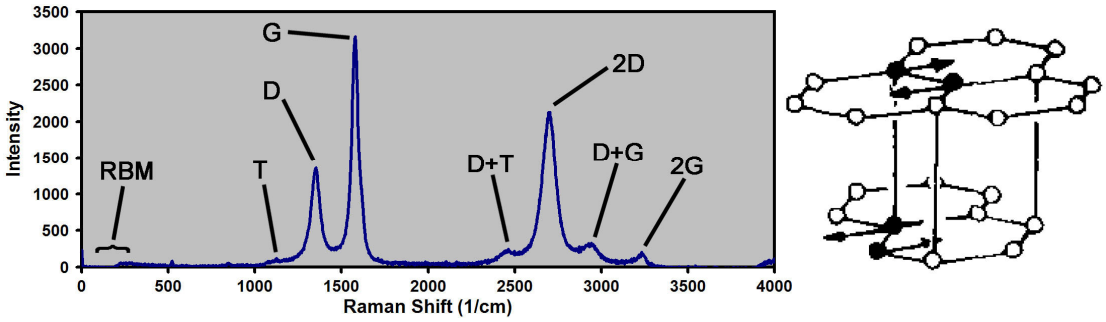

Figure 2-41: Typical Raman scan for multi-walled carbon nanotubes and a schematic of the in-plane vibration responsible for the G-peak [445]

There are a number of characteristic peaks observed in the Raman spectra of carbon nanotubes. The two most prominent peaks are the D-peak, occurring at ~1355 cm^{-1}, which is disorder induced, and the high energy mode G-peak, found at ~1590 cm^{-1}. The G-band is a Raman allowed peak for graphite (and is found in all sp^2 carbon materials) and arises due to in-plane vibrations (see Figure 2-41). The D-peak arises due to defect-induced scattering, where the presence of vacancies or impurities breaks the symmetry of the graphitic lattice. This band is dispersive, and is therefore influenced by the laser excitation energy [446], while the G-band is not. The G-peak intensity is often assumed to be independent of defect concentrations in the sample, and the ratio between the G- and D-peak heights or areas is often reported, with high ratios indicating a low defect concentration in the sample. This ratio is typically less than ten for multi-walled tubes and carbon fibers (but can reach twenty and drop as low as one for relatively good and poor quality tubes, respectively [344, 392]). In single-walled nanotubes the ratio is much larger than in multi-walled tubes, and can be as high as 100 for single-walled tubes with few defects [447]. This relation between the D- and G- peak areas can also be used to estimate the average in-plane crystallite size (L_a) in the sample, according to Equation (2-12) [388]. There can be a shoulder on the G-peak, located at ~1620 cm^{-1}, that is typical of defective graphite-like materials and is induced by mid-zone phonons [448]; due to this peak there can be a slight defect-induced influence on the G-peak [447]. In some cases another defect-induced peak is found at ~1085 cm^{-1} that has been referred to as the T-band in one report [449]. Additionally, defects in the lattice (such as dislocations or interstitial or

substitution atoms) can cause the energy associated with a particular vibration to spread over a wider range, resulting in broader or additional peaks [450].

$$L_a(nm) = \frac{4.4}{(A_D/A_G)} \qquad (2\text{-}12)$$

A number of second-order peaks are also observed. The larger peak at ~2700 cm^{-1} is variously referred to as either the 2D, D*, or the G' peak, and is an overtone of the D-peak and is located at twice the D-peak shift [446, 451]. Scattering related to the G'-band is not defect-induced, and it has been suggested that the G'-D and G'-G peak ratios are a better measure of the quality and crystallinity of nanotubes (rather than the G-D peak ratio commonly used [451]. Additionally, a 2G peak is found between 3180 cm^{-1} and 3250 cm^{-1} (approximately twice the G-peak shift) and a disorder-induced peak is located at roughly 2970 cm^{-1} (roughly equal to the sum of the D- and G- peak shifts). A smaller peak is sometimes reported at 2450 cm^{-1}, and has been identified as either a second order mode of a 1220 cm^{-1} vibration [445, 452], or as a combination mode of the T- and D-peaks [449, 453]. All these second-order peaks have been attributed to in-plane vibrational modes [445].

In addition to these first and second order peaks, radial breathing mode peaks can be observed in single-walled nanotube samples within the range of 150-300 cm^{-1}, which relate to radial vibration modes in very small tubes. The peaks will resonate with specific excitation energies [447], and their location is associated with the diameter of the nanotubes in the sample; these values are related by Equation (2-13). Size dependence is also observed with small diameter nanotubes for the G-peak, with

peaks for tubes less than roughly 5nm in diameter found as low as ~1500 cm^{-1} (compared to 1590 cm^{-1} for multi-walled tubes). For these small tubes, the G-peak for metallic single-walled tubes will occur at a slightly lower frequency than those of semi-conducting tubes with the same diameter [446, 447].

$$\omega_{RBM}\left(cm^{-1}\right) = 248 \Big/ d_{CNT}(nm) \qquad (2\text{-}13)$$

Typically a single wavelength source is used in Raman spectroscopy; however, the use of different energy laser sources can influence some results. For example, the shift associated with the G' (2D) peak is dispersive (having a strong dependence on the incident laser energy), shifting up with increasing light energy, while the frequencies of certain other second-order peaks have little dependence on the laser energy [452, 454]. The peak found at ~2450 cm^{-1} has also been reported to be dispersive, with a negative relation, where the frequency increases with decreasing laser energy [455]. In addition, the angle between the incident laser polarization and the nanotube axis can influence the peak intensities (particularly radial breathing mode peaks) due to the polarization ability of nanotubes [120-124]. As a result of this effect, sample alignment (random, well-aligned, etc.) can influence Raman results [111]. Sample heating can also cause slight shifts in peak locations.

2.7 Carbon Nanotube Applications

Carbon nanotubes possess a unique combination of exceptional mechanical strength and stiffness and interesting electrical, optical, and thermal properties. Coupled with their extremely small size, nanotubes have been shown to offer

improved performance in a wide range of existing applications and can also be used for many new applications, which would be otherwise impossible without a material with the properties of carbon nanotubes. The small scale of individual single- and multi-walled carbon nanotubes gives mats of these materials very high surface areas, and one application of interest is their use as sensors. Due to their remarkable mechanical properties, there has also been much work reported on the use of carbon nanotubes as strengthening agents in composites and on the fabrication of bulk materials made of pure carbon nanotubes. Nanotubes have also been investigated for electronic, energy, and other applications, such as in the fabrication of transparent conductive films, nano-scale transistors, field emission sources, solar cells, super capacitors, hydrogen storage cells, and more.

2.7.1 Nanotube-Based sensors

The very small size (corresponding to very high surfaces areas [456]) and material properties of carbon nanotubes have led to much work investigating their use in a wide range of sensor applications [457]. These sensors have been designed to use both individual nanotubes and mats of aligned nanotubes, and their operation has been based on both the electrical and mechanical properties of nanotubes.

Carbon nanotube-based gas sensors have been designed, where detection is accomplished through changes in the electrical properties of the nanotubes upon contact with different gases. In 2000, up to 100-fold changes in conductance were observed when single-walled carbon nanotubes (both semi-conducting and metallic, and both isolated and in mats) were exposed to NO_2 and NH_3 gases [458]. Charge

transfer between the adsorbed gases and the nanotubes led to changes in carrier concentrations, and sensitivities as high as 1000 and detection limits as low as 2ppm at room temperature were achieved. Nanotube-based sensors of inert gases have also been demonstrated, where deformations caused by collisions between gas species and the nanotube walls lead to changes in resistance (varying as a function of the mass of the colliding particle) [459]. Since then similar approaches have been used to create sensors for a wide range of gases, including I_2, CO, AsF_3, He, Ar, Ne, Kr, Xe, CH_4, N_2, O_2, CO_2, and more [457]. A different approach for gas-sensing uses nanotube mats, which have been infiltrated with polymers to create composite materials. Chemical absorption can cause the polymer matrix to swell or shrink, altering the spacing between nanotubes and causing a measurable, reproducible change in the resistance of the composite [460, 461]. Nanotubes have also been as a component in biosensors, where they can enhance the electrochemical activity of certain biomolecules. Nanotube arrays can act as supports and electrodes in these designs, with active species deposited directly on the nanotubes (such as with myoglobin [462]) or onto a polymer film coated over the nanotubes (as with glucose oxidase [463]).

Carbon nanotube sensors have also been designed with their operation based on the mechanical properties of nanotubes. One of the earliest of these applications (reported in 1996) was the use of carbon nanotubes as probes for scanning probe microscopy [464]. The very sharp tip of carbon nanotubes allows for improved resolution over conventional silicon-based probe tips (up to a tenfold decrease in tip

radius with single-walled tubes) [465], and chemically modified nanotube tips can also be used for chemical force mapping of surfaces [466]. Changes in the band gap and resistance of carbon nanotubes can vary with axial strain, and pressure sensors have been made, which use this piezoresistive property to measure strains in a nanotube suspended on a membrane separating regions of differing pressure [467-469]. This response can also be used to fabricate carbon nanotube-polymer composite strain gauges [470]. Pressure applied directly to carbon nanotubes or nanotube-based polymer composites (rather than applied to pressure-sensitive membranes) can result in shift in the location and intensities of certain Raman peaks. By monitoring the locations of the G peak (varying from 1580 cm^{-1} to 1615 cm^{-1}) and D* peak (from 2610 cm^{-1} to 2645 cm^{-1}), both pressures and the surface tensions of liquids can be measured [471-474]. Mass sensors with femtogram detection levels (10^{-15}g) can also be made by monitoring changes in the resonant frequency of carbon nanotubes as a function of the mass of attached molecules [475].

Of particular interest in this work is the use of nanotubes as a component in fluid flow sensors. To date there has been very limited research into this possible sensing application, and the published reports have used the same principle in their sensor design. Fluctuating coulombic fields in a passing liquid can cause the movement of free charge carriers in the nanotubes, causing a small current and voltage change as a result of fluid flow. This has been predicted theoretically [476] and shown experimentally in both single-walled nanotubes [477] and multi-walled nanotubes [478]. Not only can flow velocity be measured, but the ionic strength of the

passing fluid can also be detected, as the induced voltage increases with increasing ionic strength (for example with concentrated acid or salt solutions) [477, 478]. Different responses are also observed with aligned and un-aligned tubes, and as the flow direction varies relative to the tube alignment.

2.7.2 Macro-scale nanotube-based materials

Due to the exceptional mechanical properties observed in carbon nanotubes at the nano-scale, there has been much interest in their use as high strength materials. Currently, carbon fiber provides the benchmark for applications requiring high strength (~3 GPa [479]) and stiffness (~680 GPa or higher [480]) and low weight. Carbon nanotubes possess properties matching and in many cases exceeding those of carbon fiber, with modulus values of ~1TPa [47, 48, 50] and some ultimate tensile strength values reported as high as 150GPa [53, 54, 56, 57]. In addition, the high thermal conductivity [126] and attractive electrical properties of carbon nanotubes make them interesting in potential multi-functional material applications. Unfortunately, the small dimensions of as-synthesized carbon nanotubes make their handling difficult and their use in many applications impractical without further processing or improvements. Considerable effort has been expended to develop materials that take advantage of these properties on the macro-scale. There have been two main approaches towards achieving this goal: incorporating nanotubes into composite materials as fiber reinforcements and by producing macroscopic materials composed solely of carbon nanotubes.

2.7.2.1 Nanotube/Polymer Composites

Composite materials are often used to achieve a desirable combination of properties that may not be easily attainable with a single component material, and are commonly made by incorporating a high strength fiber within a polymeric, metallic, or ceramic matrix material. These fiber reinforced composites are often used in applications requiring lightweight materials with high strength and stiffness. As the fiber reinforcement contributes much to the overall strength of the composite (particularly when loaded parallel to the fiber direction), a material, which possess exceptional strength and stiffness (such as carbon nanotubes), would be of great interest for use in composite fabrication.

In experiments, carbon nanotube based composites have been created using a variety of different processing techniques. As polymers are commonly used in composites, the polymeric matrix can be dissolved in a solution, which can then be mixed with a second solution containing nanotubes in suspension. The dissolving agent is evaporated from the solution, leaving a nanotube reinforcing phase dispersed in a polymeric matrix [481-483]. A powdered form of the matrix material can also be combined with carbon nanotubes; this mixture can then be heated under pressure to create a composite material [484, 485]. Using these methods nanotube concentrations tend to be fairly low (typically less than ~5 wt.%). Carbon nanotube-polymer composites can also be produced by the wet spinning of fibers, as shown in Figure 2-42 [486-489]. In these methods, nanotubes are dispersed in a solution, which is then either allowed to coagulate, or from which the nanotubes are drawn. This process

results in fibers with higher nanotube concentrations (~20 wt.% and higher [487]) and with impressive mechanical properties (tensile strengths up to 1.8 GPa, modulus of roughly 15 GPa [486, 488]), but that still fall short of those of individual CNTs. Post-processing methods can be used to further increase the nanotube concentration by removing the dispersing liquids from the nanotube fibers. A wide range of polymers have been used as the matrix material in carbon nanotube reinforced composites, including epoxies [490, 491], polystyrene [492], polycarbonate [493], PMMA [482, 484, 494], and polyvinyl-alcohol [495], as well as some metals [496] and ceramics [485, 497].

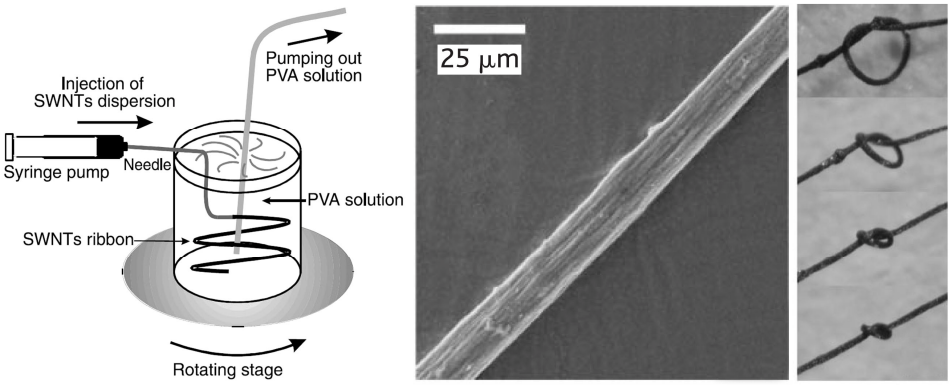

Figure 2-42: (left) Wet spinning process for CNT-PVA fiber production, (right) examples of CNT composite fibers produced using this method [486].

Carbon nanotubes serve the same role as a dispersed phase in composites as other common fiber materials in more conventional fiber-reinforced composites. These fibers strengthen the material by carrying loads that are transferred from the matrix phase to the fibers due to fiber-matrix interfacial shear stresses. As a crack grows through the material, nanotubes can span the crack opening, increasing the stress required to propagate it. As reported in epoxy composites with randomly

aligned CNTs, several nanotube orientations relative to the crack are observed, depending on the width of the crack and the length of the reinforcing nanotubes used [498]. When the crack opening is very small (less than one micron wide), nanotubes will span the crack, but were found to be angled and curved. As the crack opens, the nanotubes stretch to span the gap and are pulled to an alignment perpendicular to the crack growth direction. As the width of the crack continues to increase, the nanotubes will either pull out of the matrix or break. Nanotube pull-out is more commonly observed [499], as the tensile strength of carbon nanotubes (up to 150 GPA [53, 54, 56, 57]) is greater then the interfacial strength between CNTs and the matrix or between CNTs within a bundle (estimated to be less than 30 GPa [498]). For longer tubes, where the shear stress is carried over a larger interfacial area, additional crack growth will cause the tubes themselves to break, providing additional strengthening [500]. In the case of multi-walled carbon nanotubes, the sword-in-sheath failure mechanism has been observed [481]. Various treatments have been attempted to improve the bonding between the nanotubes and the matrix phase to help prevent tube-matrix separation [501]. Figure 2-43 illustrates the alignment of carbon nanotubes bridging a crack and strengthening the matrix material.

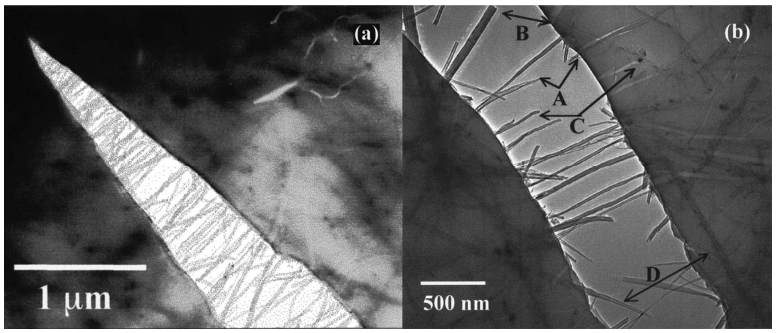

Figure 2-43: Carbon nanotube reinforcements in a polystyrene composite showing (a) nanotubes spanning the crack width, and (b) separation of nanotubes from matrix material after fracture [502].

Composites made using carbon nanotubes as the dispersed fiber reinforcement phase have shown improvements in a wide range of properties. Nanotube-based composites have been reported that are stiffer [501-504], stronger [501, 502, 504], harder [494, 496], tougher [505], and more wear resistant [496, 506], than the parent matrix material. The mechanical properties of carbon nanotube based composites have also been demonstrated to be superior to those of carbon fiber based composites, one of the best strengthening agents currently used [496, 504, 506]. In addition to improved mechanical properties, the high electrical and thermal conductivity of carbon nanotubes has led to composites with improved temperature resistance [507], thermal conductivity [129, 508, 509], electrical conductivity [510], and increased diffusion and glass transition temperature [511].

The benefits provided by using nanotubes in composite materials are dependent on several factors, including the nanotube alignment within the matrix (or lack of alignment) the weight percentage of nanotubes in the composite, and the type of nanotubes used. Alignment has been induced in nanotube-PVA composite fibers

through tensile loading, with decreased electrical resistance and increased thermal conductivity observed with increased alignment, as shown in Figure 2-44 [508]. Composites with aligned nanotubes have also been reported to have a higher storage modulus than composites containing randomly oriented nanotubes [503].

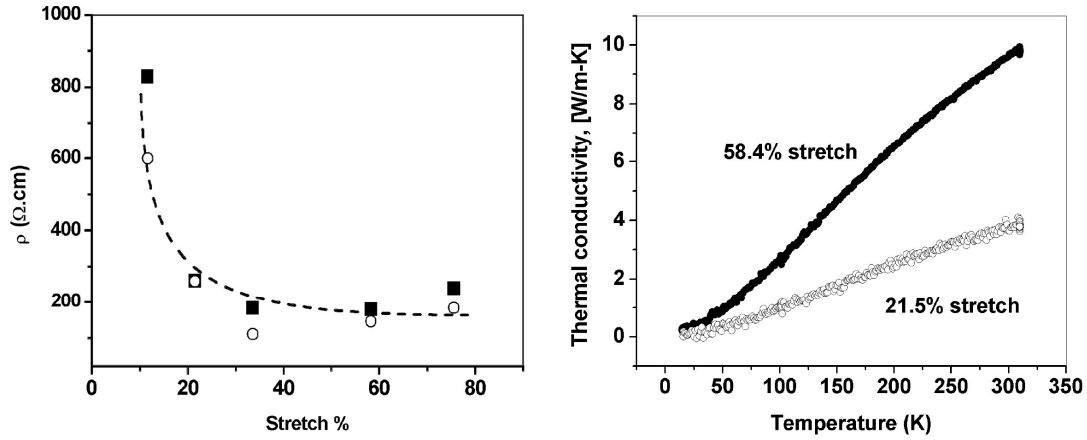

Figure 2-44: (left) Decrease in electrical resistance with increasing stretch-induced nanotube alignment, (right) improved thermal conductivity with increased alignment [508]

The properties of nanotube-based composites can also be controlled by varying the weight percentage of nanotubes used. Increases in the nanotube weight percentage have been shown to increase electrical [487, 508, 512] and thermal conductivity (Figure 2-45), as well as change optical absorption characteristics [510]. Mechanical properties can also vary with nanotube weight percent, with improved strength and stiffness observed for low to moderate nanotube concentrations [501, 504]. However, reductions in mechanical properties have been reported for high nanotube concentrations, due to poor dispersion of nanotubes within the matrix [513]. In addition, the use of single walled tubes (where a fraction of the tubes can be semi-

conducting) can lead to composites with higher electrical resistance than similar composites made with multi-walled tubes [487].

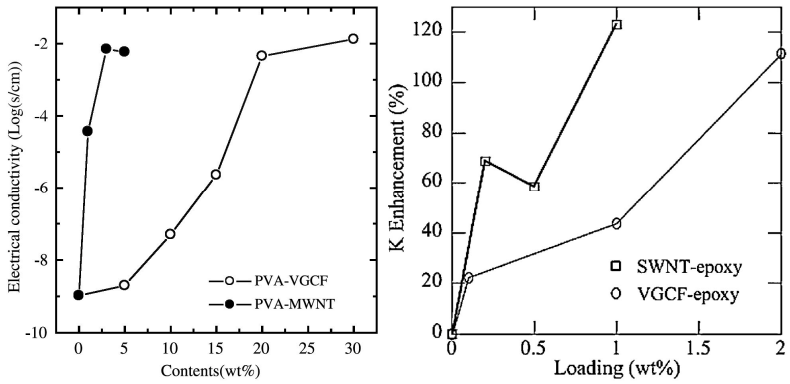

Figure 2-45: (left) Increase in electrical conductivity with increasing nanotube weight percent in CNT-PVA composites [512], (right) Thermal conductivity increase with nanotube content in CNT-epoxy composites [129]

2.7.2.2 Pure nanotube fibers and sheets

While nanotube-based composites (most commonly nanotube-polymer composites) have demonstrated improved mechanical properties compared to the bulk matrix material, they still fall well short of the exceptional properties of individual carbon nanotubes, often due to limitations in interfacial strength. To improve on these composites, several groups have worked to create bulk fibers and sheets composed entirely of carbon nanotubes. There have been two main approaches towards this goal; one method synthesizes and processes the nanotubes into fiber using a single, continuous technique, the other separates the growth of the nanotubes and the processing into distinct steps. Of the reports with separate nanotube synthesis and fiber fabrication stages, the majority use a dry method, which allows control over

many process parameters, although other methods, such as wet, solution-based approaches have been used [122, 514].

In contrast to CNT-based composites, which can often be molded into any desired shape, materials composed of pure carbon nanotubes have only been produced in sheet and fiber form to date. Carbon nanotube sheets can be layered and woven to make fabric, and nanotube fibers, the more commonly reported structure, can be twisted and braided into carbon nanotube ropes.

Fibers and yarns have long been studied in the textile industry, and the properties of yarns are a function of the constituent fiber properties and the spinning parameters used to create the yarn. One of the most important parameters is the twist angle, which influences the ratio between yarn and fiber modulus (from which a similar expression for yarn and fiber strength can be derived). This expression is given in Equation (2-14); the parameter k is defined in Equation (2-15) [515].

$$\frac{E_{yarn}}{E_{fiber}} = \cos^2\alpha\left[1 - \frac{k}{\sin\alpha}\right] \qquad (2\text{-}14)$$

$$k = \frac{\sqrt{2}}{3L_f}\left(\frac{aQ}{\mu}\right)^{1/2} \qquad (2\text{-}15)$$

A plot of the modulus ratio between the yarn and individual fibers is shown in Figure 2-46 for several k values. Yarn properties improve with decreasing k values, and k decreases as fiber length (L_f) and fiber friction (μ) increase, and as fiber diameter (a) decreases, and as the length of fiber as it travels from the surface to center of the yarn (Q) decreases.

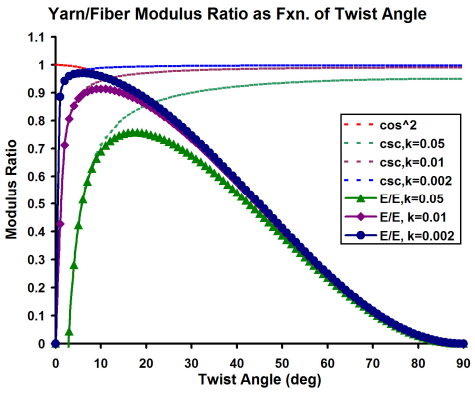

Figure 2-46: Relationship between twist angle and yarn/fiber modulus ratio

Increasing yarn twist increases friction between adjacent fibers. Under tensile strain, twist will result in a radial contraction, decreasing nanotube spacing, increasing van der Waals forces between tubes and resisting tube slippage. However, as twist angle increases, misalignment between fiber axis and the loading direction increases, reducing the effective yarn stiffness and leading to fiber breakage. An optimal twist angle can be determined using Equation (2-14), where fiber breakage and slippage are balanced. In addition, a critical fiber length can be identified, where fiber-fiber friction along a fiber's length exceeds the yield strength of an individual fiber. With fiber lengths exceeding this length, the strength of the yarn will approach the strength of the constituent fibers. Based on these considerations, yarns could be made stronger and stiffer by fabricating them from small diameter fibers that are as long as possible.

Currently there have been several procedures developed to process carbon nanotubes into longer, larger diameter fibers; these methods vary primarily in the sequence of nanotube growth and fiber processing. The spontaneous formation of bundles of single and double-walled nanotubes during growth has been reported [196, 261]. In these methods, catalytic CVD processes are used with floating catalyst

particles. Without the influence of a substrate, nanotubes growing from these particles form into long strands, held together by van der Waals forces. These spontaneous formation methods lack control over parameters such as nanotube length and fiber length and diameter. A similar method, which provides better control over the nanotube fiber properties, involves pulling nanotubes from the growth region in the CVD reaction [233, 238-240]. Carbon nanotube reactants are introduced at the top of a vertical furnace; nanotubes then form in the furnace hot zone and are allowed to deposit on the end of a long rod inserted into the furnace. This rod is then twisted and slowly removed from the furnace or simply wound up, pulling out with it either a twisted strand of carbon nanotubes or a sheet of carbon nanotubes (Figure 2-47).

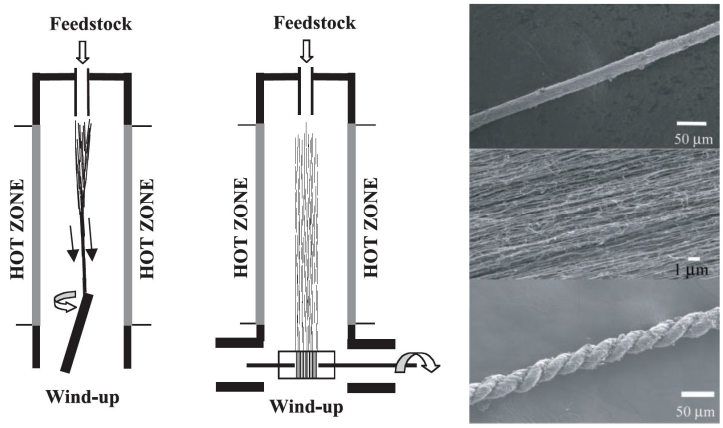

Figure 2-47: (left) Direct spinning of carbon nanotube fibers and sheets from the CVD furnace, (right) SEM images of nanotube based ropes [239].

With this method, the fibers can be pulled to any length desired as long as additional feedstock is added to continue the synthesis reaction. Additionally, there is control over parameters, which are important factors in fiber performance, such as fiber twist and diameter (which can be influenced by twist and draw speed), and individual nanotube diameter and length (which are affected by CVD parameters)

[233]. Nanotube orientation relative to the fiber axis has been shown to improve with increasing winding rate. Increased winding rates also produce nanotube ropes with lower linear density and higher specific strength and stiffness [240]. Density-specific mechanical properties of these ropes exceed those of many other high strength materials, including Kevlar and carbon fiber (Figure 2-48), with strengths up to 9 GPa and stiffness of roughly 350 GPa [240]. Recently, a New Hampshire based company, Nanocomp Technologies Inc., has used a similar technique to produce nanotube fibers up to 1000m in length and sheets covering several square feet [516, 517].

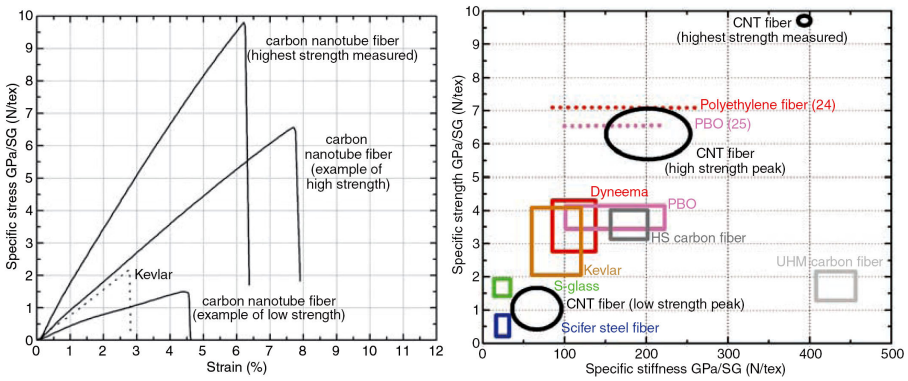

Figure 2-48: Mechanical properties of direct spun SWNT ropes (left) Specific-stress-strain curves compared to Kevlar, (right) specific strength and stiffness comparison [240].

While this single step method can continuously produce fibers of aligned nanotubes (as long as the CVD reaction is sustained), it was initially restricted by certain drawbacks, such as limited control of some individual nanotube or fiber properties. While further advances has provided improved control over this continuous spinning method, another method has also been recently reported which provides additional process control to addresses many of these shortcomings [189, 200-204, 210, 213, 263, 518]. If nanotubes are grown in tightly-packed, well-aligned

arrays and are weakly bonded to the substrate, nanotubes can be pulled and spun away from the substrate. Due to van der Waals interactions between tubes, these tubes carry adjacent tubes away with them, and as more nanotubes are pulled away, they continue to pull their other neighbors away with them. As they are drawn away the tubes become aligned in the pull direction and can form long nanotube yarns, as shown in Figure 2-49. This process can be initiated by simply bringing a sharp, roughened probe into contact with the side of the nanotube mat, causing nanotubes to stick to the point. This spindle can be spun (at speeds ranging from 1500 to 2500 rpm [201, 204]) as it is drawn from the mat (at roughly 5 cm/min [201]), twisting the nanotube yarn into rope. Further processing can be used to combine multiple ropes to form two-ply, four-ply, and knitted yarns [204]. While most groups reporting this spinning have been successful only when using highly aligned CNT arrays, spinning has also been achieved using tangled, "cotton-like" CNTs [200].

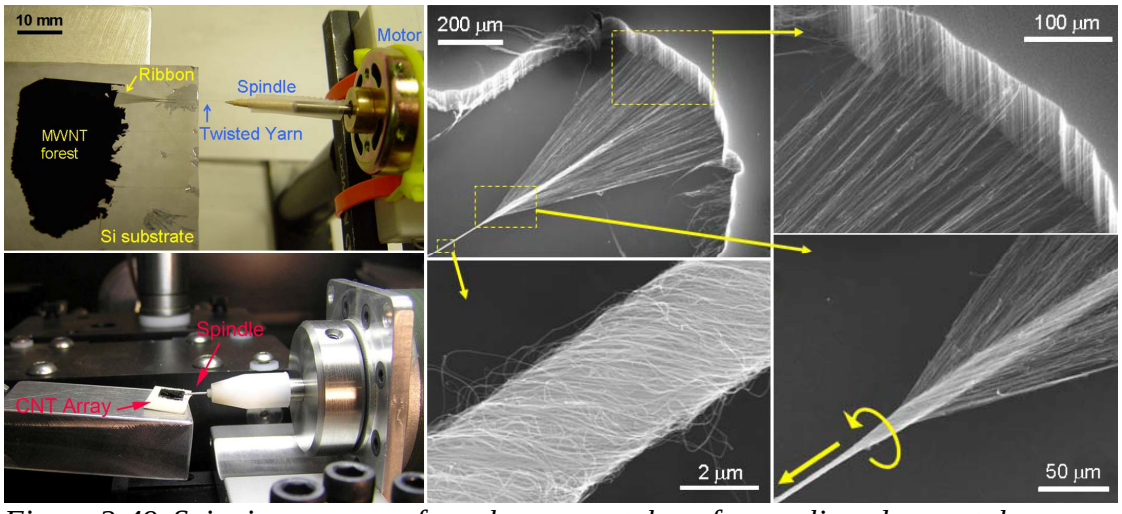

Figure 2-49: Spinning yarns of carbon nanotubes from aligned nanotube mats, magnified views show twist angle and draw direction [201, 204]

Yarns produced in this manner have several benefits. As the procedure for nanotube growth on a substrate is independent from the spinning process, their properties can be carefully controlled. This control can include diameter control (multi- or single-walled tubes) and length control (with longer tubes producing stronger fibers from Equations (2-14) and (2-15), as shown in Figure 2-50 [202, 518]. These nanotube yarns have been found to have toughness nearly 100 times higher than that of carbon fibers and roughly 30 times higher than Kevlar and specific strength and stiffness roughly five times higher than the strongest and toughest commercially available fibers [201]. In addition, the fiber parameters can be controlled during the spinning process. The width of the nanotube mat from which nanotubes were initially drawn controls the diameter of the resulting fiber (with thicker fibers coming from larger pull-out areas). As the nanotube yarn is pulled away from the mat it can be spun to create a twist angle in the yarn, and this angle can be controlled as a function of spinning speed and the yarn draw rate.

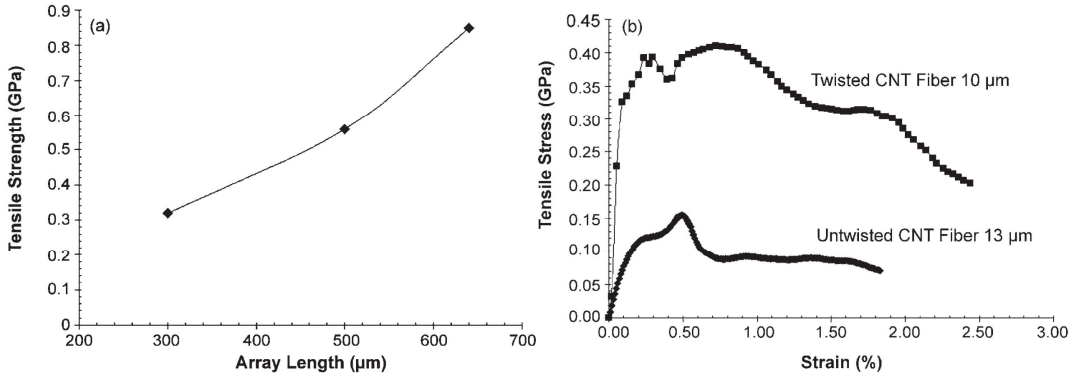

Figure 2-50: Effects of CNT mat length (left) and CNT rope twist (right) on strength of CNT ropes [202]

While this process seems straightforward, very few groups have reported spinning nanotubes into yarns in this fashion. In addition to perfecting the actual spinning process, the nanotubes from which these yarn are formed must have specific properties. It has been reported that in order for a nanotube mat to be "spinnable" the tubes must be very highly aligned and clean from impurities [263]. The bonding between the nanotubes and the substrate must be very weak, allowing the nanotubes to pull free from their support with minimal resistance, and both SiO_2 [204, 263] and Al_2O_3 [201, 202, 210] substrates have been used successfully. The most critical factor in this process is to maximize the van der Waals interactions between adjacent tubes in the mat. These forces must be high to allow tubes being pulled away from the mat to drag adjacent tubes away with them. As the magnitude of van der Waals forces decreases with the distance to the sixth power, minimizing the spacing between tubes is critical in order to maximize attractive interactions. Impurities within the nanotube mat can also create gaps, increasing separation between tubes; a very "clean" mat is required to avoid this problem. The area density of the nanotubes as they grow on the substrate must also be maximized. If the catalyst particles initiating nanotube growth can be packed more closely together, the resulting nanotubes will benefit from that increased packing. In addition, high packing density can help alignment via the "crowding" mechanism (see Section 2.4.5). Good alignment ensures that similar forces exist between tubes in all directions and throughout the mat; if these forces are non-uniform CNTs will separate in clumps and the continuous draw process will not work.

The nanotubes found in “spinnable” mats have also been reported to have smaller diameters than the “average” multi-walled nanotubes described in the literature (spinnable nanotubes have been DWNTs [201] or small, ~10-15 nm diameter MWNTs [202, 204, 263]). Catalyst particle size has been shown to closely relate to nanotube diameter, with smaller particles producing smaller nanotubes [143, 154, 188]. For a given quantity of starting catalyst material (a film of fixed thickness), the number of discrete catalyst particles formed from this film is inversely proportional to the volume of the particles. As a result, more numerous smaller particles will be packed closer together on the substrate surface; this can lead to a more tightly packed nanotube mat with increased van der Waals forces between adjacent tubes.

There are numerous benefits of using smaller diameter nanotubes for spinning. In addition to increased density on the substrate surface (increasing van der Waals forces making spinning easier, as described above), smaller nanotubes will also result in a stronger spun rope than possible with larger nanotubes. The packing of smaller nanotubes in the cross-Section of the rope can be tighter (similar to the increased packing on the substrate). This tight packing increases van der Waals forces between adjacent tubes in the rope, increasing friction among tubes. Increased friction will resist slippage between tubes and will result in a rope with properties more closely matching the desirable properties of the component nanotubes. These increased numbers of nanotubes in a given cross-sectional area of the spun yarn also allowing the load to spread over a larger number of nanotubes. In addition, mechanical testing

of multi-walled nanotubes has revealed that most of the load is carried only by the outer shell [57]. This is due to the weak inter-layer bonding in graphite. Multi-walled nanotubes have been found to fracture in a “sword-in-sheath” manner, where the outer tube will break and the inner tubes will pull out of the outer shell. Nanotubes with smaller cross-Section will have fewer inner shells, and a greater proportion of their cross-Section will carry load compared to larger diameter multi-walled tubes. Finally, yarns composed of smaller diameter nanotubes can be bent at sharper angles without damage, as the actual bending experienced by individual tubes within the rope will decrease as the ratio of their diameter to the rope diameter decreases.

In addition to the promising mechanical properties of carbon nanotube ropes, these materials have also been characterized electronically, optically, and thermally. The resistance of nanotube ropes increases as the length of the component nanotubes decreases, with conductivity of ropes made from 0.3mm CNTs reported as 22% lower than that is ropes made from 1.0mm CNTs [210]. This effect is due to the high contact resistance between adjacent tubes (relative to resistance along the length of a single tube); this influence is reduced with increasing CNT length. Additional post-processing treatments can provide further control over the conductivity of nanotube ropes [210]. Nanotube ropes can also be resistively heated to anneal the ropes into different shapes (such as coils and springs). This heat treatment also results in an increase in the rope stiffness (roughly twice the untreated value), although there is a reduction in tensile strain at failure [263].

During the rope spinning process, if a wider probe is used to contact the nanotube mat edge (rather than a sharp spindle), and the probe is not twisted during the draw process, a nanotube sheet can be produced rather than a rope [203, 519]. Nanotubes within the sheet are aligned along the draw direction, and resulting in interesting electrical and optical properties. Sheet resistance in the draw direction is roughly ten to twenty times lower than the resistance perpendicular to the draw, and resistance decreases as the length of the nanotube arrays used to make the sheet increases [519]. Optical transmission also varies with the light polarization angle relative to the draw direction. Both nanotube ropes [213] and sheets [203] can serve as incandescent light sources (Figure 2-51) and sheets can also be used as components in OLED light sources and can act as transparent, conducting films [203]. Similar nanotube films can also be fabricated using a solution-based approach, and this method and the electrical properties of these sheets are described in Section 2.7.3.

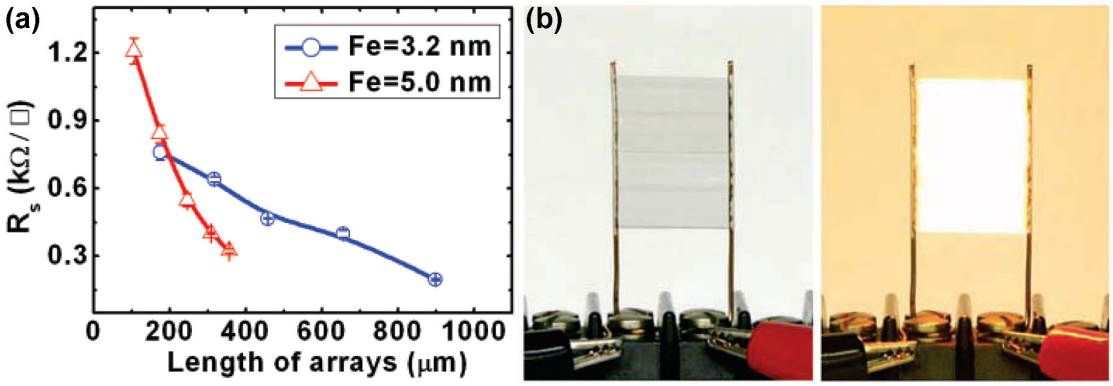

Figure 2-51: (a) Variation in sheet resistance with original nanotube array length and nanotube diameter (influenced by the Fe catalyst film thickness) [519] (b) nanotube sheets as a source of polarized incandescent light [203]

2.7.3 Nanotubes for Electronic Applications

As described in Section 2.3.2, nanotubes have very low resistance, very high current carrying capacities, and are not limited by electro-migration in the same way similar-sized metallic wires would be. Additionally, the high thermal conductance allows rapid dissipation of any heat generated during current flow. This combination of material properties has made them of interest to a wide range of electronic applications. One of the first electrical applications considered for carbon nanotubes was their use as nano-scale wires, and through the use of lithographic techniques to define catalyst regions, nanotube growth has been patterned to form electrical connections [520-522]. As-grown semiconducting nanotubes can also be used to form p-type transistors, and n-type transistors can be fabricated by doping or vacuum annealing the tubes [105-107, 523-525]. This annealing can be carried out at moderate temperatures (~200°C), and potassium doping can convert nanotubes to n-type, with oxygen doing converting them back to p-type. The conductivity of carbon nanotubes can also be altered by mechanical deformation, such as twisting and bending [102, 526]. In addition to producing simple on-off switches with carbon nanotube transistors, combinations of different transistor types can be used to form some of the basic components of logical circuits. Carbon nanotubes have been used to form functioning “NOT” logic gate in two ways, by connecting a p- and n- type tubes in series with electrodes, or by manipulating a single tube to contain both n-type and p-type semiconducting regions [106, 107, 527]. This fabrication process includes a combination of doping, vacuum annealing and selective masking of parts of the tubes

using lithographic methods. This is shown in Figure 2-52, where PMMA is used to mask a region on a nanotube, which can then be doped with potassium to convert that Section of the tube to an n-type semiconductor.

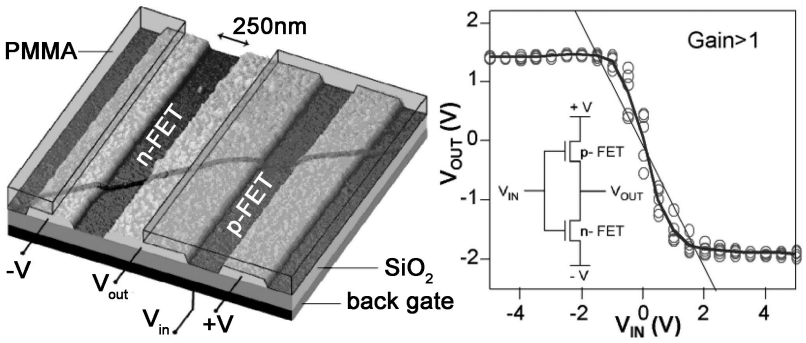

Figure 2-52: Schematic (left) and Input-output curve (right) for a nanotube-based NOT gate [106]

A network composed of metallic, p-type, and doped n-type semiconducting tubes could exploit these different electronic behaviors to potentially replace and significantly reduce the size of entire circuits currently made using metallic wires and silicon components. However, precise arrangement of many tubes of different types would be required for complete circuits, and methods to achieve the accuracy for this complex placement are still being developed. Even without this control, sparse networks of randomly arranged carbon nanotubes have been used to fabricate transparent, conducting films for applications such as optical coatings and as components in solar cells.

These nanotube sheets can also be made using a solution method [528], in addition to being drawn from a mat of aligned nanotubes (as described in Section 2.7.2.2). A dilute, surfactant based solution of carbon nanotubes can be vacuum filtered through a membrane, leaving a thin film of tangled carbon nanotubes lying

parallel to the filter surface. Following filtration the surfactant can be washed away and the membrane removed, leaving a free-standing film of carbon nanotubes. Films produced using this method have less alignment than those produced using the draw process described above (alignment only in the film plane, rather than in the draw direction), but still have interesting electrical and optical properties. Optical transmission in the visible light range is similar to that of the drawn nanotube films, but sheet resistance can be significantly lower (~30 Ω/□ vs. ~700 Ω/□) [203, 528]. Solution processed nanotube films can also be made in much larger sizes than the drawn sheets, as size is limited by filter area rather than nanotube mat and substrate size. For very sparse nanotube films, the percolation threshold may not be reached, and the film will lack a continuous, conductive path. Above this threshold (found in sheets made from roughly 6ml of a solution containing 0.2mg/L nanotubes in one study [109]) the sheet conductance increases with the nanotube concentration through a power law relation. Although higher nanotube concentrations can increase conductivity, this can also reduce the transparency of the film, illustrated in Figure 2-53 [109].

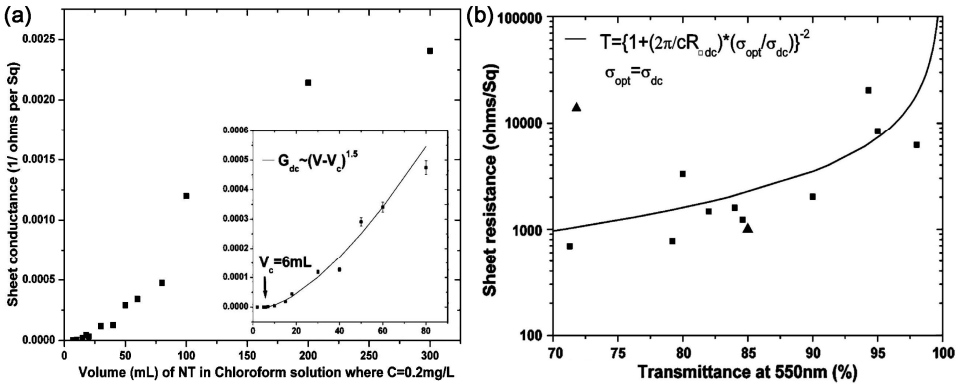

Figure 2-53: (a)Carbon nanotube film sheet conductance increases with increasing nanotube concentration, inset shows percolation threshold at 6ml solution, (b) Optical transmittance drop with sheet resistance [109].

2.7.4 Other Nanotubes applications

Carbon nanotubes have been investigated for use in a very wide range of applications, which seek to take advantage of their size, structure, and material properties. Their very high surface area and the ability to functionalize carbon nanotubes has made them useful for sensing applications, but these same properties have been applied to catalysis, where nanotube have been used as supports for various catalysts [529]. This high surface area has also been used to enhance the capacitance (by over a factor of five) of quick-charging capacitors fabricated from metal-nanotube-insulator-metal layers [530, 531]. Patterned arrays of carbon nanotubes have been coated with thin semiconductor layers and a transparent, conducting indium tin oxide film for use as solar cells. The three-dimensional structure allows for reflected light to be recaptured, providing up to a threefold improvement in power production [532].

This high surface area is also one of the features that has led to research in carbon nanotube-based hydrogen storage for applications such as hydrogen fuel cells

[533]. Both gas phase absorption and electrochemical mechanisms can promote this storage, which can increase with surface area [534, 535]. In gas phase intercalation, physical forces (such as Van der Walls forces) attract H_2 gas to the nanotubes; the high nanotube surface area leads to efficient storage via physisorption. Chemical forces can also act, and hydrogen can be incorporated into the nanotubes by chemisorption through covalent bonding [536]. Although there has been a range of values reported [533], hydrogen storage of several weight percent has been demonstrated experimentally via both chemisorption [537-539] and physisorption [540] in carbon nanotubes. Storage capacities can be increased on open tube ends (via chemisorption [541]), within open tubes and bundles of tubes through physisorption [542, 543], and by utilizing a combination of these absorption mechanisms.

While the small size of carbon nanotubes results in the high surface areas that are desirable for hydrogen storage and sensing applications, this small size also gives individual carbon nanotubes a near one-dimensional geometry. These dimensions make them ideal candidates as field emission sources, which has been demonstrated as early as 1995 [544-546]. Field emission occurs when a voltage is applied to a sharply pointed metal (or other solid), creating a concentrated electric field at the tip that extracts electrons. The very small radius of curvature found at the ends of carbon nanotubes gives them very sharp tips, which provide field enhancement factors up to 50,000 [547, 548]. This allows high current densities to be emitted efficiently for low applied voltages for both single-walled and multi-walled tubes [549, 550]. Single point field emission sources can be used for applications such as filaments for electron

microscopes; however, with nanotube-based field emitters, patterns of multiple field emission sources [321, 550, 551] can be fabricated using standard photolithography techniques on silicon substrates [420, 552-555]. By adding a phosphor screen in front of each separate field emission site, visible light can be produced, and these arrays can be used as bright, efficient flat panel displays [556].

3. Procedure

In this work, carbon nanotubes were synthesized using catalytic chemical vapor deposition (catalytic CVD) reactions, and a wide range of process parameters were studied. In order to isolate the effect of individual parameters, a versatile reaction set-up was designed to allow growth attempts under a wide range of conditions, including variations of reaction gas, carbon source, temperature, gas flow rate, and more. Three distinct synthesis set-ups were used, depending on if the carbon source was in a liquid or gas phase and the method of catalyst introduction; however, these designs shared several common features, which are described in Section 3.1. The catalyst material was either deposited on substrates prior to growth (for thermal CVD, Section 2.5.2) or mixed with the carbon source prior to introduction to the reaction chamber (floating catalyst CVD, Section 2.5.3). In floating catalyst CVD, the catalyst introduction occurs simultaneously with the nanotube synthesis, and this process is described in Section 3.1.1. For thermal CVD, the catalyst deposition was performed prior to nanotube synthesis, and the preparation for this step is outlined in Section 3.1.2. The general thermal CVD growth process is described in Sections 3.1.3 (for growth with liquid carbon sources) and 3.1.4 (for growth with gaseous carbon sources), and values for typically used synthesis parameters are given in more detail in Sections 5.1 and 5.2. Additional procedures were also used specifically for the different investigations that were performed during this work, and these are described in the appropriate parts in the results and discussion sections of this dissertation.

3.1 Chemical Vapor Deposition Process

Due to the various methods used for the introduction of carbon and catalyst reactants in this work, the synthesis chamber design had to be versatile in order to accommodate a number of alterations to the process. Several carbon sources were used in these experiments, and the CVD set-up was modified depending the phase of the carbon source (liquid or gas) and the method of catalyst introduction. Three configurations of the reaction equipment were required to provide the proper conditions for growth with these variations.

Despite the differences between these CVD configurations, the growth process was similar for all synthesis methods. Substrates were loaded into the reaction tube and positioned at the desired location within the furnace. The inlet and exhaust connections were then attached to the tube ends, and the argon flow was started and the furnace turned on. In some cases other gases were also added during heating (such as H_2 or NH_3). Once the desired reaction temperature had been reached and stabilized, the flow of other required reaction gases was initiated (if any) and the desired gas composition was obtained by adjusting the flowmeter for each gas. The introduction of the carbon source then began, either in gaseous form (Section 3.1.4), liquid form (Section 3.1.3), or as a catalyst solution (Section 3.1.1). After a pre-determined reaction duration (from minutes to hours), or after the consumption of a desired amount of reactant material, the furnace was turned off, and the flow of all gases save argon was stopped. Argon flow continued during cooling, which could take as little as

ten minutes (with the furnace lid opened) or as long as several hours (with the lid closed).

There were some features common to all the CVD variations used in this work. With the exception of compressed gas cylinders, all of the equipment used was stored inside a fume hood to allow for quick removal of any potentially hazardous gases involved in the growth of carbon nanotubes. In all experiments, the growth temperature was set and maintained by the use of a Lindberg/Blue M #TF55035A tube furnace, with a maximum temperature output of 1100°C, and the reaction chamber consisted of quartz tubing, approximately one inch in diameter and two feet in length (obtained from Quartz Scientific). An inert environment was achieved by a steady argon flow through the reaction chamber, and this flow was maintained during heating, growth, and cooling. Depending on the synthesis conditions required, up to two other gases could be added to the reaction (including hydrogen, ammonia, nitrogen, ethylene, and acetylene). The flow rate and mixing ratios of the gases were controlled using gas flow-meters, capable of regulating each flow between 40 and 700 sccm (standard cubic centimeters per minute). Smaller flows (down to ~10 sccm) were possible, although slight variations in flow rates at these low levels made precise, stable flow control difficult. Alternately, the flow meters could be bypassed, and flow regulated as a function of cylinder output pressure. This was only used for spray pyrolysis CVD growth (done very early in the course of this work) and in this case the only gas used was argon, with flow rates of up to ~10^5 sccm. Stainless steel or brass tubing was used to make all the required gas connections, with the exception of some

regions where flexible connections were required (such as where frequent connections and disconnections were made). In these regions, Tygon tubing was used, and the length of these sections was minimized to reduce any gas absorption or desorption from the tube walls.

During growth, it is important to ensure that the reaction chamber environment remains uncontaminated, not only so the gas mixture composition is unchanged, but to prevent excess oxygen from burning away the nanotube product in the high temperature synthesis conditions. A connection at the tube inlet is required to introduce the reaction gas to the furnace, and two methods were used to allow reaction gases to enter while preventing contamination. In addition, due to the large tube diameter, there exists a possibility of backflow at the tube exhaust (resulting in air entering the reaction chamber), and three methods were used to prevent this.

Initially rubber stoppers were pressed in place at the tube ends, and the junction between the tube and stopper was wrapped with electrical tape as an extra precaution against unwanted gas contamination. A 0.25” outer diameter quartz tube was inserted through each stopper, allowing the inlet gas line to be connected and providing a sufficiently small diameter to avoid backflow at the exhaust. Due to the slight positive pressure inside the reaction chamber, this rubber seal was thought to be sufficient to avoid outside contamination. Also, as growth temperatures were higher than the temperatures where carbon nanotube burn-off was observed (during thermal characterization, see Section 2.6), the successful growth of nanotubes at these high

temperatures demonstrated that the sealing methods used were sufficient to avoid excessive outside contamination.

However, as some runs were performed under vacuum or with high hydrogen concentrations, a more robust seal was required. In these cases, Quick-Disconnect to Kwik-Flange (KF) hybrid adaptors from MDC vacuum were used at both the exhaust and inlet ends. Coupled with a Kwik-Flange to Swagelok adaptor (also from MDC vacuum), these provided a convenient junction between the gas line tubing and the reaction chamber. These seals were rated up to $1x10^{-8}$ torr vacuum, and prevented any potential contamination from external sources. The final method of sealing the exhaust end of the reaction tube against possible backflow was the use of a separate quartz piece that formed a slip fit around the outside diameter of the reaction tube and then tapered to a 6.35mm hose connection.

In most cases, exhaust gases were released directly into the fume hood, although gases could pass through a coil of submerged copper tubing or be bubbled into a beaker of water for cooling if needed. Additionally, fiberglass insulation was wrapped around the reaction tube both where it entered and exited the furnace; this helped prevent heating at the tube ends which could have damaged the rubber stopper or adaptor o-rings and compromised the seal.

3.1.1 Floating Catalyst Growth

The first chemical vapor deposition technique used in this work was floating catalyst CVD, where a liquid hydrocarbon-catalyst mixture is evaporated into the furnace. Initial nanotube growth was by the spray pyrolysis variation of floating

catalyst CVD (modeled after that described by Kamalakaran *et al.* [242]), which uses a high speed gas flow (10^4-10^5 sccm) to aerosolize a reactant solution and jet it into the furnace. However, this method was soon converted to conventional floating catalyst CVD growth, where the reactant solution is evaporated into a slower inert gas flow (10^2-10^3 sccm). This method provided both improved growth and more efficient use of reactant material than the earlier spray pyrolysis method [252].

With this growth process, the liquid reactant solution was contained in a syringe and dispensed through a needle into the argon flow, where it was allowed to evaporate into the gas stream. The tip of this needle was inserted through the rubber stopper sealing the inlet end of the reaction tube, and to keep the liquid from pooling and running directly into the furnace, a ceramic boat was used to contain the solution while it evaporated. Disposable needles were used (McMaster-Carr), of either 25, 26, or 27 gauge (with 0.305mm, 0.254mm, and 0.203mm, respective inner diameters). The dispensing rate was controlled as a function of needle gauge and reactant height inside the syringe, and the reactant solution was introduced at rates typically ranging from 0.1-0.3 ml/min. Figure 3-1 shows a schematic of the complete setup used for floating catalyst CVD growth, with the syringe used to dispense liquid reactants into the argon flow shown in the photo on the right. Growth temperatures ranged from 800°C to 900°C, and synthesis reaction durations could last for several hours.

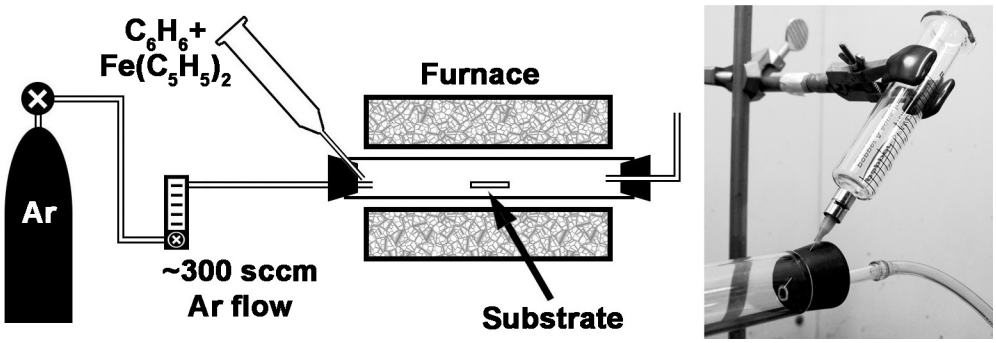

Figure 3-1: Typical floating catalyst CVD setup for carbon nanotube growth

In floating catalyst growth, the catalyst is continuously added to the reaction along with the carbon source, and this was accomplished by using a liquid solution containing these reactants, which is allowed to evaporate into the argon flow. Several different catalyst-hydrocarbon solutions and concentrations were tested. The most commonly used carbon source was benzene (C_6H_6, Omnisolv BX0212-6), although xylenes (C_8H_{10}) and some other solutions were also investigated (see Section 5.1). Ferrocene ($Fe(C_5H_5)_2$) was the most used source of catalyst material and was dissolved directly into benzene with concentrations ranging up to 8% by weight. Nickel and cobalt versions of this catalyst source were also used ($Ni(C_5H_5)_2$ and $Co(C_5H_5)_2$, respectively), as well as several metal chlorides and nitrates. While the metallocene catalysts dissolved directly into the benzene, the chlorides and nitrates were first dissolved into an alcohol solution, which was then fed into the reaction simultaneously along with the benzene carbon source.

With the floating catalyst CVD method, nanotube growth occurred on the reaction tube walls as well as on any substrates placed in the synthesis chamber. Several materials were used as substrates, including quartz slides and tubes (Quartz

Scientific), oxidized silicon wafers, titanium foils, hydroxyapatite (obtained from cuttlebone converted using a chemical and thermal process [557, 558]), and crystals of various minerals (quartz, aragonite, and calcite). Quartz slides were the most commonly used substrates, and were placed inside the main reaction tube at a distance between 7cm and 23cm into the furnace. Prior to growth, quartz substrates were cleaned with acetone and methanol. In many cases, particularly for the larger and more expensive quartz tubes, the substrate materials were reused for multiple tests. These substrates (as well as the reaction chamber itself), were mechanically brushed to remove as much of the carbon product as possible, then heated in air to high temperatures (700-900°C) to burn off any residual carbon material. If needed, an acid bath treatment (~12% HCl, Fisher Scientific), was then used to remove any residual catalyst particles present.

3.1.2 Thermal CVD Substrate Preparation

Substrates used for floating catalyst CVD were most often bare quartz slides, with catalyst material introduced during synthesis. However, in thermal CVD, a catalyst source had to be deposited on the substrates prior to growth, requiring additional preparation; several methods were used to achieve this.

Electron beam evaporation (Temescal BJD 1800) was used to deposit thin (1nm-50nm) films of various catalyst metals on different substrates, with an Inficon I/C5 controller used to monitor thickness during evaporation. Iron and nickel films were deposited on both quartz slides and silicon wafers (with the native oxide layer intact). In some cases barrier layers were deposited on the silicon wafers in-between

the silicon and the catalyst. These layers included tungsten, titanium, and aluminum metal films. In the case of aluminum, the substrate was exposed to air before catalyst deposition, forming a thin alumina layer upon which iron was evaporated. When used, these barrier layers were typically between 10nm and 100nm thick.

Using e-beam evaporation also allows the potential to deposit catalyst material in desired patterns. Electron-beam sensitive resist was spun on a silicon wafer substrate, with the spin speed and resist viscosity determining the resulting resist thickness. Using NPGS (the Nanometer pattern generation system), the beam in a SEM was controlled to raster over regions defined through simple CAD designs. Following this exposure and the development of the resist, a metal catalyst film was then evaporated over the wafer surface. The remaining resist (and any metal on the resist) was washed away, leaving behind only the catalyst material deposited directly on the substrate (on regions defined by the exposure pattern in the SEM). Alternately, this lithography step could be bypassed through the use of a simple mask during evaporation. With this method, various TEM grids (Ted Pella, SPI Supplies) were attached to the substrate and metal was evaporated over and through these masks, with only metal that was deposited through the holes in the grids remaining after the grids were lifted off.

The evaporation of thin metal catalyst films on substrates was the most commonly used techniques for the thermal CVD growth of carbon nanotubes in this work. However, two other methods of substrate preparation were also employed, which produced a coating of discrete catalyst particles on the substrate surface, rather

than a film. The first and simpler of these techniques involved the use of nano-scale metal particles. Both nickel (Quantum Sphere Inc.) and titanium powders were used, with particle sizes ranging from 10nm to roughly 50nm. This powder was simply spread over a quartz slide surface or held in a ceramic crucible during growth. Alternately, quartz slides previously used for floating catalyst CVD could be re-used, and residual metal on the surface (in the form of small metal oxide particles) could catalyze nanotube growth. The second method produced nano-scale metal particles by evaporating catalyst-containing solutions on substrates. A number of solutions were used, several of which were very similar to those used for floating catalyst CVD growth (Section 3.1.1). Metal chloride, nitrate, and acetate solutions were made in a given concentration (often between 0.1 wt.% and 1.0 wt.%) by dissolving a quantity of the metal salt in alcohol (typically ethanol). Ferrocene solutions of varying concentrations (in benzene or an alcohol) could also be used. While a number of solutions were made, an iron solution (either iron nitrate or ferrocene in ethanol) and a bi-metallic cobalt and molybdenum acetate solution were used most often. Substrates were either dipped in these solutions or drops of the solution were deposited on the substrate. The alcohol solvent was then allowed to evaporate, leaving a residue consisting of small nano-scale particles of the particular metal. Solutions with higher concentrations could be used and the evaporation process could be repeated to increase the amount of catalyst material deposited on the substrate.

Prior to nanotube growth in some experiments, the prepared substrates (whether by the thin film or solution evaporation techniques) were heat treated in air at

between 400°C and 500°C to form metal oxide particles. After substrate preparation was complete, the samples were loaded into the tube furnace and the thermal CVD process would then be started. While the substrate, reaction tube, and furnace remained the same, the configuration of the rest of the CVD equipment was changed depending on if a liquid or gaseous carbon source was used.

3.1.3 Thermal CVD with a liquid carbon source

The first thermal CVD experiments conducted during this work used a liquid carbon source, and the experimental set-up used was very similar to that used for floating catalyst CVD. A catalyst coated substrate was loaded into the reaction tube and positioned in the center of the furnace. The tube ends were sealed with rubber stoppers with small openings for inlet and exhaust gases as described above. As with the floating catalyst CVD method, a liquid hydrocarbon source was held inside a syringe and introduced to the reaction tube through a small diameter needle. A gravity feed was used, with the reactant introduction rate determined as a function of the height of the liquid column above the needle in the syringe and the needle diameter. Typical feed rates were ~0.3 ml/min with 25 gauge needles (0.305mm inner diameter) and ranged between 0.1 ml/min and 0.15 ml/min with 27 gauge needles (0.203mm inner diameter). Alternately, the carbon source could be held in a beaker and the reaction gases could either be bubbled through or passed over the liquid. This allowed for slower carbon introduction rates; however, the syringe and needle method was found to be preferable in most cases, as more precise control was possible. The carbon source used in the majority of these growth runs was benzene, although some

other liquid sources (other hydrocarbons, alcohols, acetone, etc., see Section 5.2) were also attempted. Unlike floating catalyst CVD, no catalyst material was added to the carbon source, and the only catalyst present during growth was that pre-deposited on the substrate. Initial attempts used only argon as the environmental gas (similar to floating catalyst growth); however, large amounts of amorphous carbon were deposited and nanotube production was very poor. To inhibit the build-up of unwanted carbon byproducts, gas mixtures (ammonia or occasionally hydrogen mixed with argon) with a range of concentrations were used. Overall gas flow rates were typically less than 500 sccm, and growth temperatures were between 800°C and 900°C. Total synthesis time was between 10 and 60 minutes. A schematic for this thermal CVD growth is shown in Figure 3-2, with commonly used reaction parameters (carbon source, gas mixtures and flow rate, catalyst material and film thickness, etc.).

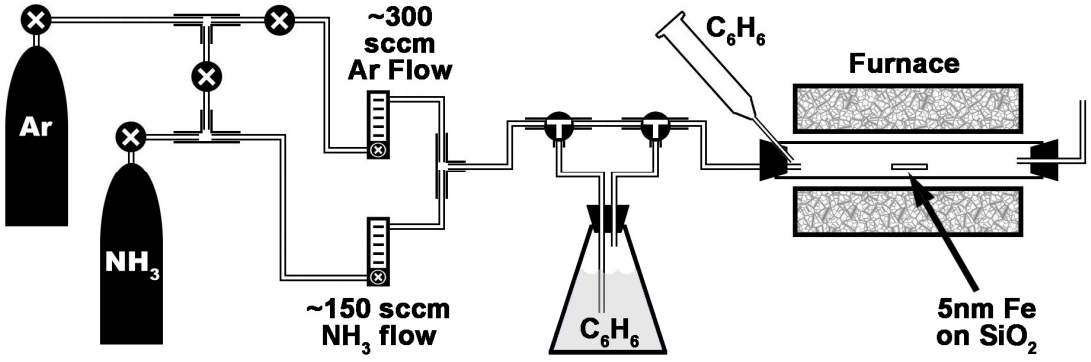

Figure 3-2: Schematic for thermal CVD nanotube growth with a liquid hydrocarbon source. Typical reaction parameters are given, and either bubbling or the needle/syringe method was used for hydrocarbon introduction.

3.1.4 Thermal CVD with a gaseous carbon source

The equipment arrangement required for the use of gaseous hydrocarbon sources is slightly different from the experimental set-ups described above (which use a needle and syringe to dispense a liquid hydrocarbon into the reaction). With a gaseous carbon source, no opening is needed to allow liquid introduction, and only an inlet for reaction gas entry is required through the stopper sealing the tube entrance. This arrangement is very similar to that used when a liquid carbon source is evaporated into the carrier gas via the bubbling method (Section 3.1.3), as in this case the hydrocarbon is also gaseous when it enters the reaction tube. The bubbling process has several drawbacks, such as poor control over the hydrocarbon introduction rate, and for this method much better results were obtained using hydrocarbons initially in a gaseous, rather than liquid state. In this work, two of these carbon sources were investigated, with ethylene (C_2H_4) used predominantly, and acetylene (C_2H_2) used for some earlier experiments. The complete arrangement allowed for the use of up to three gases: an inert gas (argon), the hydrocarbon, and an optional gas to inhibit amorphous carbon formation (hydrogen or ammonia). Through the use of flowmeters, these gases could be mixed in any desired ratio and total flow rates were often between 300 sccm and 600 sccm, with up to 250 sccm hydrocarbon content. Similar to thermal CVD growth with liquid hydrocarbons, total synthesis times were often between 10 and 60 minutes. Due to the lower self-pyrolysis temperatures of ethylene and acetylene (see Section 2.4.1), the growth temperatures were lower than those used previously, and ranged from roughly 650°C to 800°C. Recently, water

vapor has also been shown to effectively inhibit catalyst poisoning and prolong growth, and is added to the reaction in small quantities (20-500 ppm [231]). The measured water content in the argon gas used for growth was relatively high (typically >2000 ppm), so this gas was passed through a desiccant (Drierite, $CaSO_4$) which dropped the water concentration to between 40 ppm and 150 ppm (measured in-line by an Ametek 303B moisture meter). In some cases, a bubbler apparatus (as shown in Figure 3-2) was used to introduce small, controlled amounts of other liquids to the reaction (including de-ionized water or ammonium hydroxide). A schematic of this complete thermal CVD equipment set-up is shown in Figure 3-3.

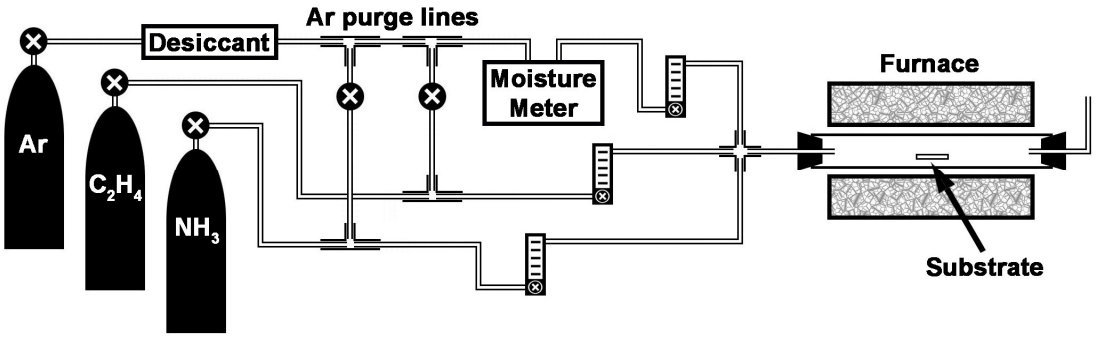

Figure 3-3: Complete thermal CVD set-up for growth using gaseous carbon sources and real-time monitoring of water content

3.2 Product Collection and Analysis

Once the desired growth duration had been reached and the furnace cooled in an inert argon environment, the nanotube covered substrates were removed and analyzed. For SEM analysis, substrates were typically placed directly onto a 12mm carbon conductive tab (Ted Pella, part #16084-1) attached to a SEM pin mount (Ted Pella part #16111). With larger samples, nanotubes were removed from the surface

and mounted as described above, or larger SEM specimen supports were used that accommodated the entire sample. Prior to imaging, aligned mats of carbon nanotubes were often scratched to expose a surface normal to the growth direction of the carbon nanotubes, giving a "side-view" that was useful for height measurements. Scanning electron microscopy analysis was performed on a Philips XL-20 SEM, with an accelerating voltage of between 5.0 and 20.0kV and at a working distance of between roughly 10 and 15mm. For some samples, an Oxford Instruments light element EDS detector was used to perform energy dispersive x-ray analysis of the nanotubes. Transmission electron microscope samples were prepared by scraping a Formvar coated, 200 mesh copper TEM grid (Electron Microscopy Sciences, part #FF200-Cu) across the sample, transferring a small quantity of carbon nanotubes to the grid. Several different TEM models were used in this work, including a Philips EM420 TEM (LaB_6 filament at 120kV) and a Hitachi HD-2000 STEM (200kV, which could also be used to obtain secondary electron images). Following this sample preparation, either the remaining product was scraped from the substrate and collected, or the entire sample (substrate-supported nanotubes) was stored for future analysis.

In addition to the SEM and TEM imaging, qualitative analysis was performed using Raman spectroscopy on a Renishaw Raman spectrometer with a 514.5nm Ar laser. Scan durations were selected to provide a sufficient ratio between the peak intensities and background noise (typically either 10 or 30 second scans). Following acquisition, individual peaks were fitted using the Lorentzian distribution, given by

Equation (3-1), where I is the peak intensity, γ is the peak half width at half maximum, and x_0 is the peak center.

$$f(x; x_0, \gamma, I) = I\left[\frac{\gamma^2}{(x - x_0)^2 + \gamma^2}\right] \qquad (3\text{-}1)$$

A simple computer code was written to perform this fitting automatically, and the heights, widths, and locations of eight different peaks were found for each Raman spectra. In addition to the prominent D, G, and 2D peaks (at roughly 1350 cm^{-1}, 1580 cm^{-1}, and 2700 cm^{-1}, respectively), smaller T and G-shoulder peaks, as well as several second order peaks were also fit. For most scans, a very good fit was obtained, with an average error of less than 1-2% of the intensity value of the larger G-peak. From these fits, comparisons can be made between spectra from different nanotube samples by analyzing peak height ratios, width ratios, areas, and positions. An example of the results from this fitting process is shown in Figure 3-4, with the three most prominent peaks labeled (see Section 2.6).

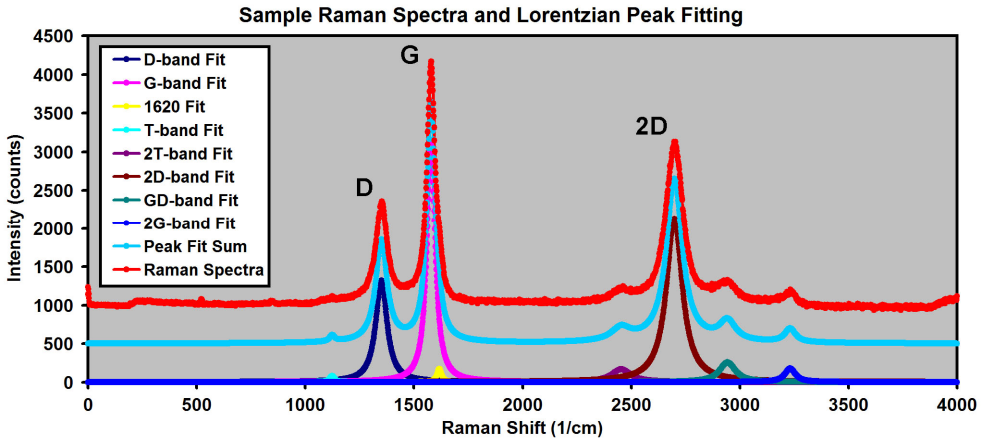

Figure 3-4: Sample carbon nanotube Raman spectra, with individual peak fits and peak fit sum, showing good agreement with Raman data

4. Results and Discussion

The research performed during this work can be divided into several main topics, spanning synthesis, characterization, and applications. Two distinct growth methods were used (floating catalyst CVD and thermal CVD), and comparisons were made between samples produced by each of these techniques (representative nanotube samples are shown in Figure 4-1). Various process parameters have been studied, and methods for control over nanotube morphology, structure, length, and diameter have been investigated. Mats grown using different CVD procedures have then been characterized using several methods. These methods include Raman spectroscopy (to look at the carbon bonding within samples), mechanical testing using two distinct approaches, and thermal, optical, and electrical characterization. Finally, several nanotube-based applications have been explored, including a sensor design (realized during the course of the mechanical testing), as well as potential methods for producing bulk samples exploiting the high strength and stiffness of carbon nanotubes.

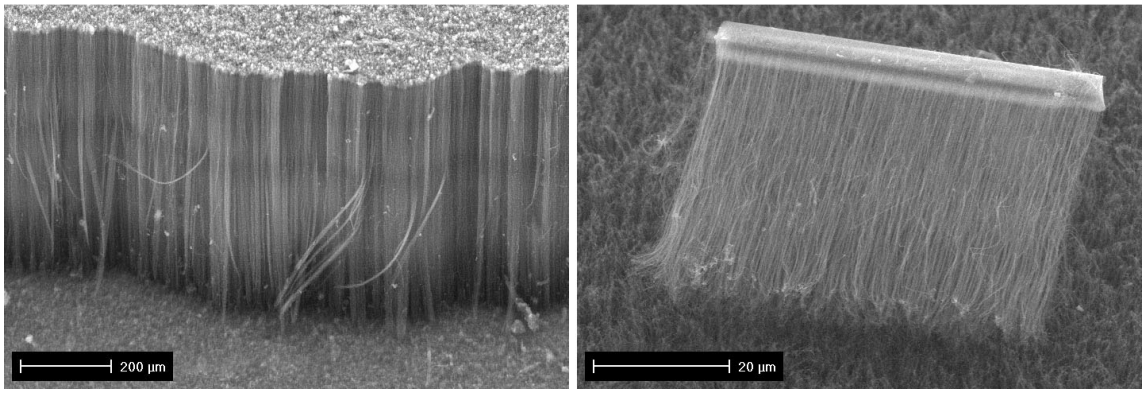

Figure 4-1: Examples of aligned carbon nanotube mats grown via floating catalyst CVD (left) and via thermal CVD (right)

5. Nanotube Growth and Characterization

Due to the wide range of carbon nanotube synthesis methods that have been reported, the many possible CVD growth variations, and the large number of process parameters that can influence nanotube production, an understanding and optimization of nanotube growth is very important. Several CVD-based synthesis techniques were evaluated in this work, and a number of significant process variables studied. These experiments focused on optimizing growth, investigating the effects of catalyst and substrate materials, and variations in reaction gas composition.

One of the most important ways to evaluate different carbon nanotube growth methods is to measure how effective a particular method is at synthesizing nanotubes (both in terms of rapid production and efficient use of reactant materials). To study this, a series of growth runs were performed for a range of reaction durations, with other growth parameters held constant. Following these tests, scanning electron microscopy was used to measure the heights of the resulting nanotube mats. This sequence of experiments not only indicates the ultimate length to which nanotubes can be grown under various conditions, but also reveals changes in growth rate that can occur as a function of growth time. Specifically, in this work nanotube growth using floating catalyst CVD was compared to growth using thermal CVD methods. Significant differences were found between extended growth runs using these two CVD methods, due to the differences in catalyst introduction. For thermal CVD (with a limited catalyst supply), poisoning was observed to limit growth, and different reaction gases were used to prevent this detrimental effect.

In addition, for each synthesis method studied, the growth mechanism was determined in order to investigate the catalyst-substrate interactions. With a base growth mechanism, the catalyst particles would be expected to remain on the substrate surface during growth, while a tip growth mechanism would be active if the particles were found to lift away from this surface. Several approaches were used to determine the active growth methods, including manipulation of the CVD growth process and examination of nanotube products using electron microscopy.

Beyond understanding nanotube growth rates to determine tube lengths, it was also important to control other properties of the nanotubes being produced. The influence of several process parameters on nanotube diameter was studied, and adjustments to reaction conditions and substrate preparation were identified to provide independent control over nanotube inner and outer diameters. Furthermore, continued work on reaction gas effects led to the ability to affect nanotube morphology through the use of nitrogen, producing tubes with either straight walls or compartmentalized bamboo walls. The effects of these structural changes on synthesis were examined, and several methods were identified to produce nanotubes with this bamboo structure.

5.1 Floating Catalyst CVD Growth

The first growth method used during this research was floating catalyst CVD. This synthesis method was quite versatile, and carbon nanotubes could be produced using a wide range of carbon sources, catalyst materials, and substrates. In addition, other reaction parameters, such as growth temperature and argon flow rate, could be

varied over a significant range, while still yielding nanotube products. A summary of these parameters, which resulted in successful nanotube growth, is given in Table 5-1.

Table 5-1: Parameters used for Floating Catalyst CVD carbon nanotube growth

Parameter	Value or Range
Catalyst Metal	Fe, Ni, Co
Catalyst Compound	Metalocenes ($M(C_5H_5)_2$) Chlorides (MCl_x) Nitrates ($M(NO_3)_x$)
Carbon Source	Benzene (C_6H_6) Xylene (C_8H_{10}) MeOH, EthOH, ButOH
Substrate	Quartz (SiO_2) Metals (Ti 6-4) Minerals (HAP)
Temperature	Typically 800°C -900°C
Argon Flow Rate	100-500 sccm (standard) 10^4-10^5 sccm (spray pyrolysis)

Typical growth produced thick mats of nanotubes (tens of microns up to several millimeters long), with growth oriented normal to the substrate surfaces and having good alignment within the mats. Nanotube diameters ranged from less than 50nm to roughly 100nm, in agreement with the catalyst particle sizes expected for the synthesis temperatures used in this work [409, 559]. Multiple catalyst particles were also observed encapsulated within the nanotube walls. Examples of this growth are shown in Figure 5-1.

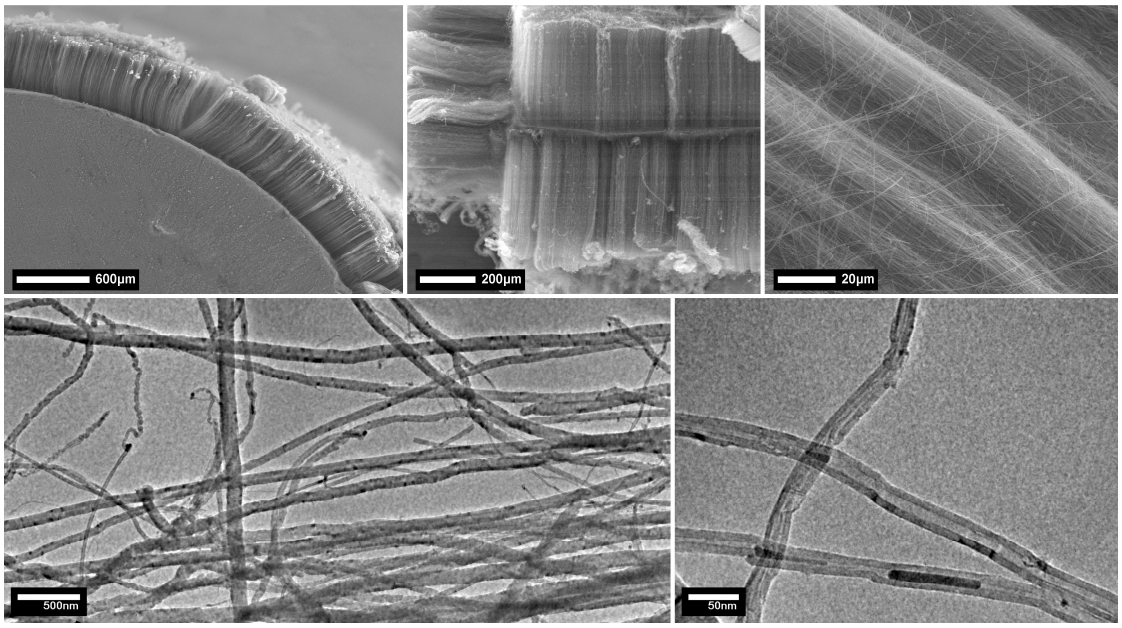

Figure 5-1: Examples of floating catalyst CVD growth of aligned carbon nanotube mats using ferrocene and benzene, SEM and TEM imaging

Raman spectroscopy was used to investigate these samples, and nanotubes grown using this CVD method typically had very prominent G- and 2D-peaks, with large peak height ratios relative to the disorder induced D-peak (Figure 5-2).

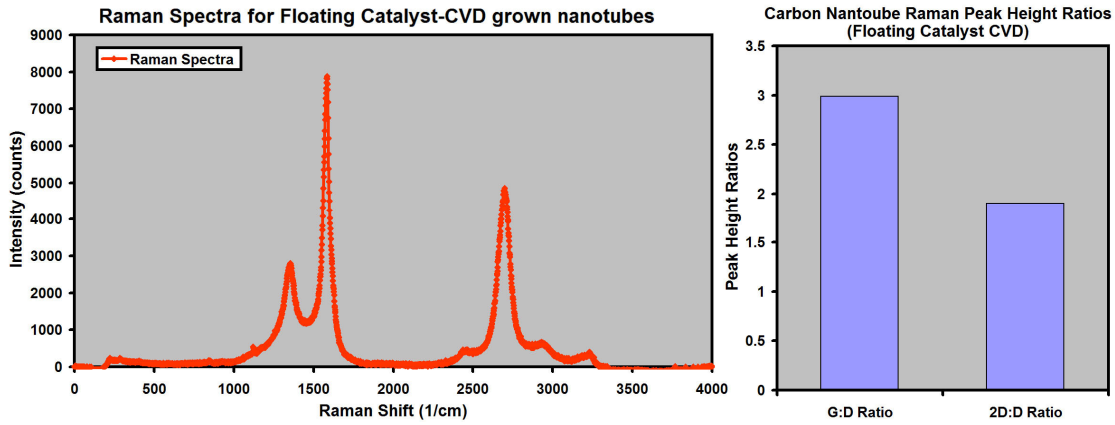

Figure 5-2: Typical Raman spectra for nanotubes grown using floating catalyst CVD

As indicated in Table 5-1, a wide range of process parameters could be used to successfully synthesize carbon nanotubes with this CVD method. Iron (in the form of

ferrocene) was the most commonly used catalyst material, but other metals (Ni and Co) and other compounds (chlorides and nitrates) could also be used. In addition, a range of substrate materials could support growth, including certain metals and minerals (Figure 5-3).

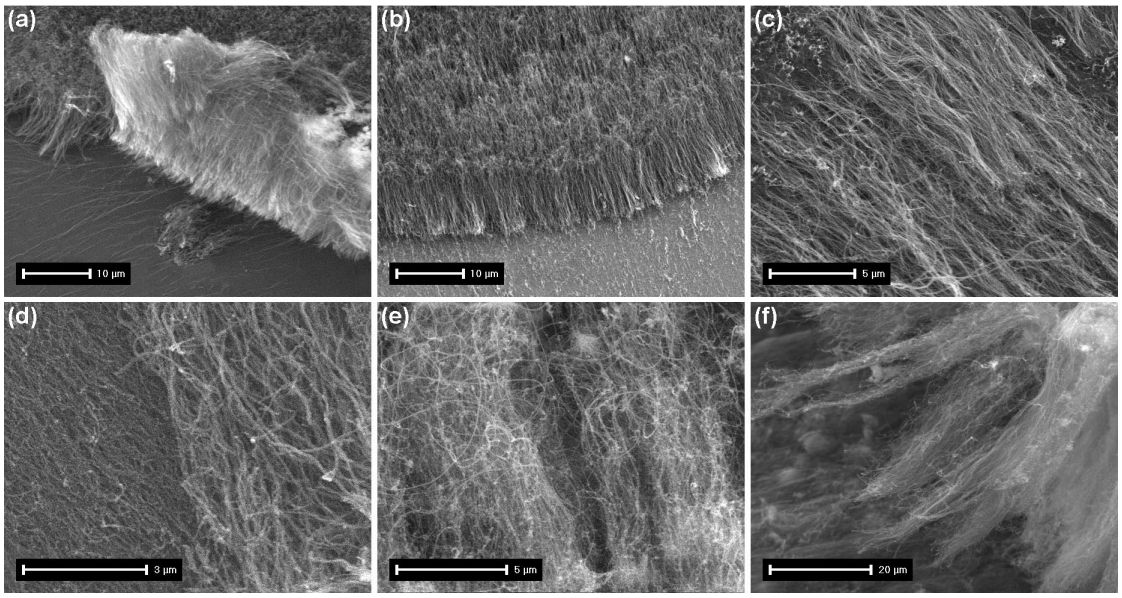

Figure 5-3: Examples of nanotubes grown under alternate conditions (a,b) growth with Nickelocene and Cobaltocene, (c,d) growth with $FeCl_2$ and $CoCl_2$ and alcohol, (e) growth on Hydroxyapatite, (f) growth on Ti 6-4 foils

5.1.1 Growth Rates

Although nanotubes were produced using many different materials and synthesis recipes, certain conditions were found to be more effective than others. In particular, while the spray pyrolysis variation of the floating catalyst growth procedure was able to successfully produce carbon nanotubes, this technique provided very low yields when compared to the more conventional floating catalyst growth used. For this reason the spray pyrolysis approach was not included in this comparison of

nanotube growth methods. Similarly, the best results (highest yields and longest mats) were obtained when ferrocene and benzene were used as reactants, with nanotube products deposited on quartz substrates, and growth optimization was performed using these conditions.

Using these parameters, conventional floating catalyst CVD (described in Section 3.1.1) was used to synthesize nanotubes using a range of growth reaction durations. All other reaction conditions (catalyst solution concentration, temperature, argon flow rate, etc.) were held constant, and are summarized in Table 5-2.

Table 5-2: Summary of Floating Catalyst CVD Growth parameters used

Growth parameter	Value
Carbon Source	Benzene
Catalyst Source	Ferrocene
Catalyst Concentration	~5.0 wt.%
Introduction rate	~0.10 ml/min
Argon flow rate	~200sccm
Reaction Temperature	800°C
Substrate	SiO_2
Reaction Duration	Varied

Following growth, scanning electron microscopy was used to measure the heights of the synthesized nanotube mats; these results are shown in Figure 5-4, plotted as both total length and growth rate as a function of reaction time.

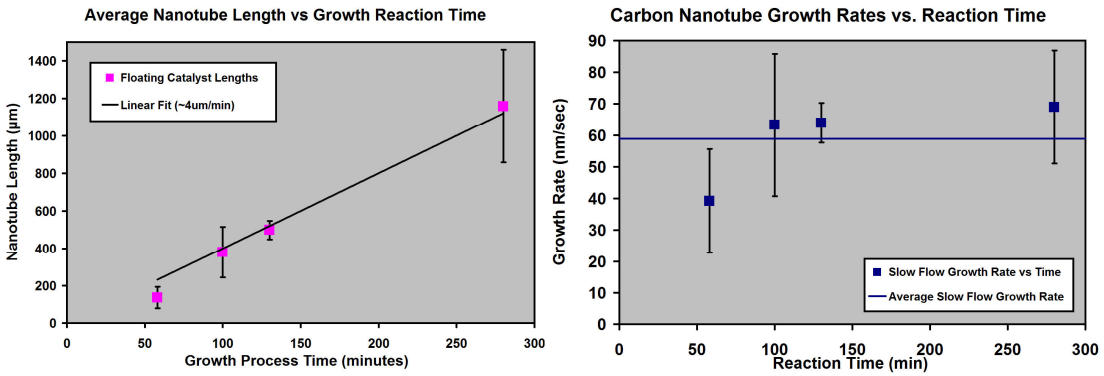

Figure 5-4: Carbon nanotube mat length and growth rate as a function of reaction time for floating catalyst CVD synthesis

With floating catalyst CVD, a roughly linear relationship is observed between nanotube mat length and reaction time (for durations up to roughly 5 hours). Correspondingly, the growth rates of these mats are nearly constant, with the mats lengthening at approximately 60-70nm/second. Due to this near-constant growth rate, the length of these nanotube mats could be controlled through careful selection of the synthesis reaction duration. This allowed the growth of ultra-long mats with lengths reaching several thousand microns; examples of ~1mm and ~6mm mats are seen in Figure 5-5.

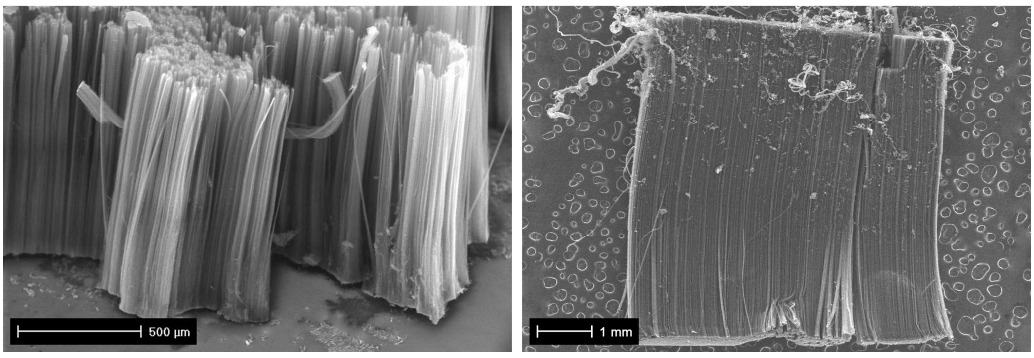

Figure 5-5: Long carbon nanotube mats grown using floating catalyst CVD, ~1mm length (left) and ~6mm length (right)

5.1.2 Growth Mechanism

Floating catalyst CVD growth differs significantly from other common chemical vapor deposition methods in that additional catalyst material is supplied throughout the duration of the synthesis reaction. This catalyst material is carried into the furnace by the movement of the reaction gases and then subsequently forms into metal particles upon heating [409]. Due to this introduction method (as opposed to starting with a catalyst film on the substrate), classification of the growth method into either base or tip growth is not as simple as in thermal CVD. First, the surfaces upon which these metal catalyst particles deposit must be identified, and then once these particles have settled, their movement during subsequent growth (either remaining on the surface or lifting off) can be determined.

With this CVD method, the reaction will begin with the initiation of nanotube growth when catalyst particles start to collect on the substrates (or other surfaces within the reaction chamber) [560]. However, once a sufficient quantity of nanotubes have been produced (forming an aligned mat), deposition is possible on two available surfaces as additional catalyst material is introduced to the reaction. These particles (carried into the chamber by the reaction gases) can either deposit on the growing nanotube mat (on the upper surface or within the mat) or can diffuse through the mat to reach the original substrate surface. In this first case, additional growth will occur from the top of and within the nanotube mat and in the latter case growth will occur on the substrate, pushing the existing mat upwards.

One method to conclusively identify the active mechanism for continuing growth is to interrupt synthesis to form a “break” in the nanotube mat. Following additional growth, the position of this “break” along the mat height can be used to determine if new nanotube growth is occurring from the top of the mat or from its base. A mat of nanotubes was grown using an initial floating catalyst CVD run, allowed to cool, and a portion of this mat was then scraped away. These samples (partially covered with some remaining nanotubes) were then put through a second floating catalyst CVD reaction; the results of this growth are shown in Figure 5-6.

The nanotube layer, which formed during the second floating catalyst growth run, has clearly grown underneath the portion of the mat remaining from the initial synthesis (pushing it upwards); this demonstrates that additional catalyst material accumulates on the original substrate, and not at the tops of existing nanotube mats (no identifiable new growth is observed on the upper mat surfaces). These results suggest that the nanotube mats can continue to grow as long as ferrocene is added (and decomposes to form small nano-scale catalyst particles), and as long as this additional catalyst and carbon material can penetrate the base of the mat and reach the substrate surface.

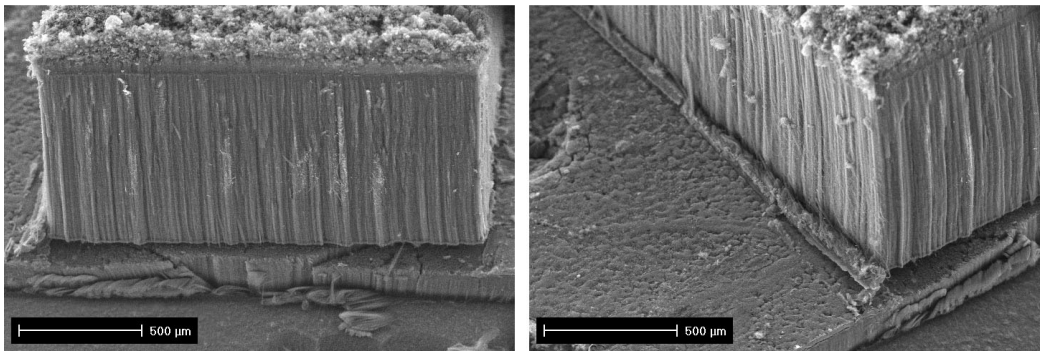

Figure 5-6: Results of sequential vapor phase CVD growth runs, the taller region was grown in the 1st run, shorter mat at base was produced by the 2nd run

In these CVD growth runs, rather than completely stopping the growth reaction (the method used in Figure 5-6), the nanotube samples could also be kept at the growth temperature and atmosphere, and reactant solutions added in an incremental drop-wise manner to the furnace (rather than at a steady rate). Under certain circumstances, when drops of catalyst-rich and catalyst-deficient solutions were alternated at sufficiently long intervals (greater than roughly thirty seconds), separations appeared in the resulting mats. Shorter drop intervals and tests with other variations to the reactant introduction sequence did not produce these interruptions along the length of the nanotube mat. Using this pulsed reactant introduction process, the time between successive doses could be adjusted to allow the growth of one layer to reach a desired height and then to cease prior to the next reactant injection. Nanotube mats composed of many layers (greater than 100) could be produced using this method. In addition, the catalyst used could be varied from one layer to the next. Examples of the products grown using these techniques can be found in Figure 5-7. This sort of layered growth has also been reported by other groups, and these layered structures can be synthesized under a range of conditions [559].

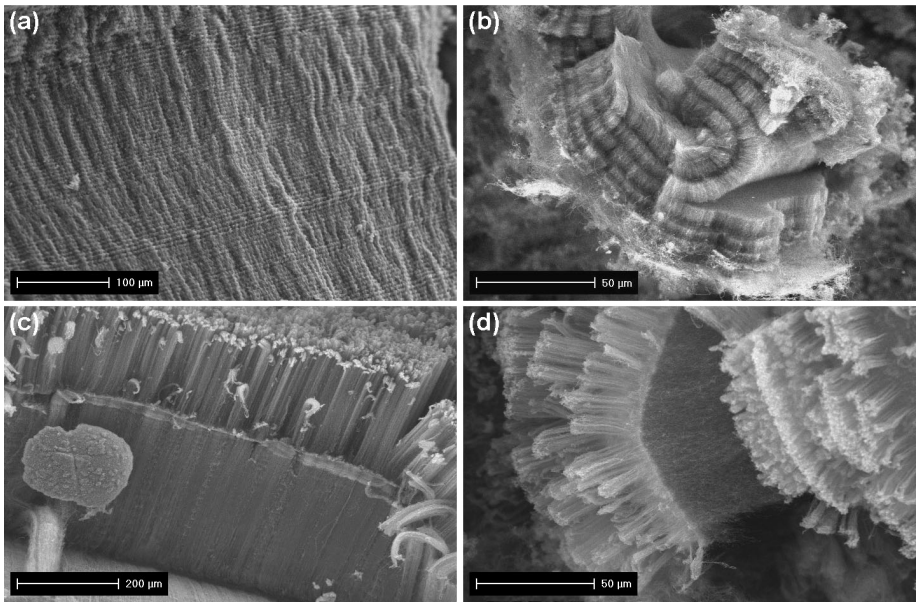

Figure 5-7: (a,b) Multi-layered CNT mat, produced by pulsing reactants, (c) Bi-layered CNT mat produced by varying catalyst material, upper layer (grown first) was catalyzed using nickelocene, lower layer with ferrocene, (d) Bi-layer nanotube structure using cobalt and iron catalysts

While these experiments demonstrate that growth originates from the substrate surface (at the bottom of the nanotube mat rather than from the upper surface of the nanotube mat), this does not reveal the motion of the catalyst particle once growth has started or the corresponding growth mechanism. The determination of the active method during nanotube growth is governed by the interfacial strength between the catalyst particle and the substrate. In base growth, the catalyst particle is strongly attached to the substrate, and remains fixed during growth, with the nanotube growing up, away from both the catalyst and the substrate. Carbon diffusion into the catalyst occurs at any exposed regions of the metal particle or through the substrate. In tip-growth, the catalyst particle is weakly bonded to the substrate, and this contact is broken as nanotube growth begins. As the nanotube lengthens, the catalyst remains at its tip, and is carried away from the substrate.

During longer (several hour) floating catalyst CVD runs, it was not uncommon for several grams of ferrocene to be consumed during the reaction. If this total quantity of iron deposited on the substrate and reaction chamber surfaces (and not on the growing nanotube mats, as indicated by Figure 5-6), and then remained on these surfaces throughout the reaction (as would occur according to a base growth mechanism), then the iron used would be sufficient to form a layer several microns thick over all the chamber surfaces. The catalytic activity of these metal particles depends not only on their composition (carbon saturated metals), but also on their size and shape (metal sheets will lead to graphite formation; large particles can lead to fiber or filament production). It is likely that not all the catalyst material used is deposited, as some metal may remain at the furnace entrance after reactant evaporation and some may be exhausted from the furnace. Even accounting for this, if only some of the deposited metal remained on the substrate surfaces, particle coalescence would cause a metal film to form that would not effectively catalyze nanotube growth (typical metal film thicknesses used during thermal CVD were only 5-10nm). As growth can continue at a steady growth rate for extended durations (see Figure 5-4), it is not likely that this occurs. In addition, EDS studies of carbon nanotube mats grown using floating catalyst CVD reveal significant catalyst concentration distributed throughout the mat height (between 1at.% and 5at.%), contrary to what would be expected for base growth (catalysts remaining on the substrate surface).

However, while base growth is not likely, certain features are also observed in these floating catalyst CVD nanotubes that are not consistent with the tip growth

mechanism. In tip growth, the upper end of the nanotube is capped by the catalyst particle and the base remains attached to the substrate surface; as a result, the inside of the tube is sealed off. TEM examination of these nanotubes revealed many instances of catalyst particles encapsulated within nanotubes, away from tube ends (an extreme example from a run using a high catalyst concentration is shown in Figure 5-8a, which also shows some catalyst particles deposited on the outside of tubes). In addition, while nanotube inner and outer diameters should remain constant according to the traditional formation theory for growth with a single catalyst particle, this is not always observed. Different nanotube inner diameters have been found on opposite sides of an encapsulated catalyst particle (within a single tube), and in some cases growth direction has also changed at a catalyst particle location (Figure 5-8b).

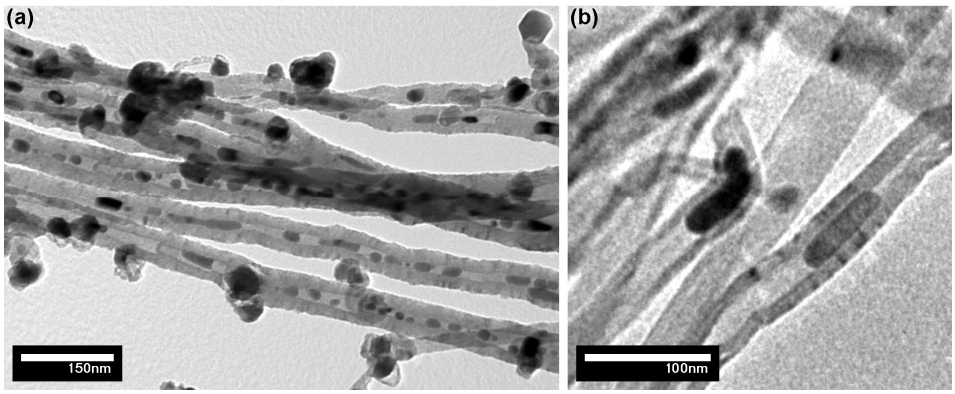

Figure 5-8: Examples of (a) catalyst particles encapsulated within CNT walls and (b) diameter or growth direction changes occurring at catalyst particles

This suggests that growth during floating catalyst CVD cannot be simply classified as either base- or tip-growth. Recent work has indicated that substrate supported catalyst particles can interact and coalesce during growth due to forces caused by variations in reaction gas flow [359]. The distribution of catalyst particles

within the nanotubes in Figure 5-8 could be explained by this catalyst particle interaction mechanism or through interactions between catalyst particles and growing nanotubes [561]. Newly deposited catalyst particles can interact and combine with existing particles, resulting in changes to the growth direction or catalyst size (causing a difference in nanotube diameters before and after this interaction). Nanotubes growing from newly deposited catalyst particles will lift up existing tubes, separating them from the substrate when the van der Waals forces between neighboring tubes can overcome the interaction between the tube and catalyst with the substrate. Once nanotubes separate from the substrate, interactions between the catalyst particles and inner tube walls could draw the particles inside the tubes and encapsulate them.

5.2 Thermal CVD Growth

Thermal chemical vapor deposition is one of the most versatile and most common methods of carbon nanotube production used today. Rather than a continuous addition of catalyst material, thermal CVD separates the metal particle introduction and nanotube growth steps, and a fixed amount of catalyst material is deposited on the substrate surface prior to the growth reaction. This catalyst was most commonly deposited by evaporating a thin metal film on an appropriate substrate, typically quartz slides or silicon wafers coated with a layer of silica or alumina. As with floating catalyst CVD, this approach was very versatile, and nanotubes were grown using several variations to the basic process. A list of the range of synthesis parameters studied is given in Table 5-3.

Table 5-3: Reaction parameters used for thermal CVD nanotube growth

Parameter	Value or Range
Catalyst Metal	Fe, Ni, Co/Mo, TiC
Catalyst Form	Thin films, Particles
Carbon Source	Benzene (C_6H_6) Xylene (C_8H_{10}) Ethylene (C_2H_4) Acetylene (C_2H_2) Acetone (C_3H_6O) Ethanol (C_2H_6O)
Substrate	Quartz slides Oxides (SiO_2, Al_2O_3) Metals films (Ti, Ti/W)
Temperature	600°C -900°C
Argon Flow Rate	100-500 sccm
Other Reaction Gases	Ammonia (NH_3) Hydrogen (H_2)

As with floating catalyst CVD, thermal CVD could be used to produce well-aligned mats of nanotubes. However, these nanotube forests were not able to reach the same heights (millimeter lengths) as those grown using floating catalyst CVD (due to the limited catalyst material), and nanotube lengths typically ranged between 10μm and 100μm. Despite the lower mat heights, the separation of the catalyst deposition and nanotube growth steps did provide several advantages compared to floating catalyst CVD growth; notably, the catalyst could be patterned to control the nanotube growth locations and the nanotubes that did grow spanned the entire mat height (rather then producing long mats composed of numerous shorter, intertwined tubes). Nanotubes were grown with a range of diameters, and were observed to have two distinct morphologies, either with straight walls or with a compartmentalized, bamboo structure. Typical products are shown in Figure 5-9.

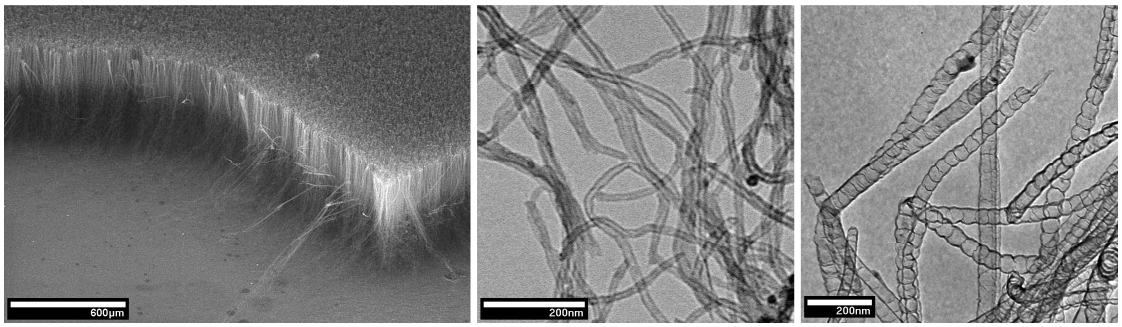

Figure 5-9: Examples of thermal CVD nanotube growth, TEM images show straight-walled and bamboo morphologies

These products were also examined using Raman spectroscopy, and the results tended to fall into two categories, depending on the morphology (Figure 5-10). While the G-peak to D-peak height ratios were similar for most thermal CVD nanotubes (between 1.0 and 1.4), the 2D-peak to D-peak height ratios varied, with very small ratios observed in bamboo tubes (typically less than 0.3) and larger ratios (closer to 1.0) for straight walled samples. The differences between samples with these morphologies are investigated in more detail in Sections 5.3.2 and 5.4.

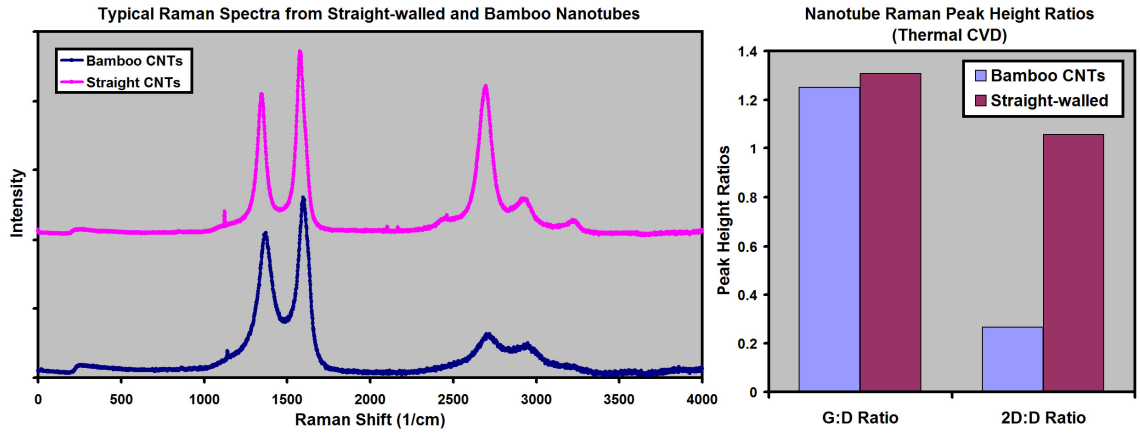

Figure 5-10: Typical Raman spectra for straight-walled and bamboo nanotubes grown via thermal CVD

As with floating catalyst CVD, thermal CVD is a versatile and robust process, and nanotubes could be grown using a number of variations to the standard processes. In addition to synthesis using ethylene and benzene, other carbon sources were attempted, and grow was also conducted at temperatures outside the commonly used ranges (such as growth using benzene at 700°C, well below the typical 850°C-900°C reaction temperatures). Figure 5-11 shows examples of these experiments.

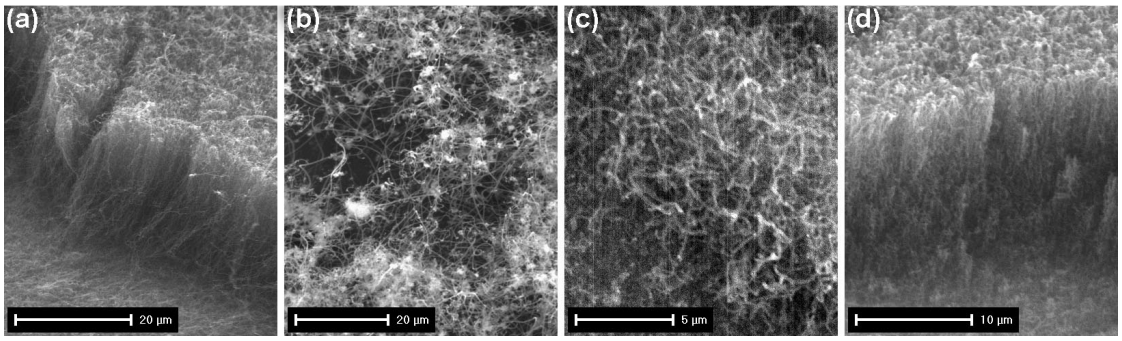

Figure 5-11: Thermal CVD growth with 5nm Fe film catalysts and various carbon sources: (a) acetone, (b) ethanol, (c) acetylene, and (d) xylene

Catalyst material was most often deposited in the form of thin (3-10nm) films on quartz slides or silicon wafer substrates. However, other catalyst metals could be used to grow carbon nanotubes, and metal-containing solutions could also be used as a source of catalyst material. These solutions were typically made by dissolving low concentrations of metal chlorides, nitrates, or acetates in alcohol. In these cases, a dip-coating procedure was used to deposit catalyst material on substrates, and this process could be repeated (with the solvent allowed to evaporate after each step) to increase the amount of catalyst material on the substrate surface. Alternately, for metals or metal-carbides, where nanometer-scale particles could be obtained directly (rather

than from solution), these particles were simply dispersed on substrates as catalysts. Results from these variations are shown in Figure 5-12.

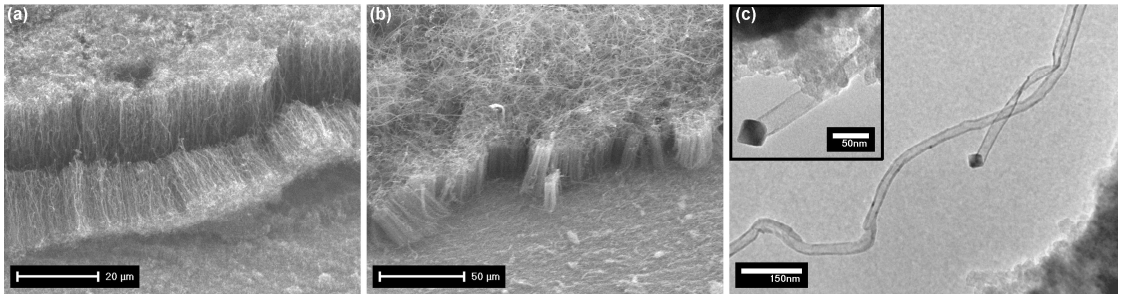

Figure 5-12: (a) Growth using catalysts from cobalt-molybdenum acetate solutions, (b) catalysts from $Fe(NO_3)_3$ solutions, (c) TiC powder catalysts

During metal catalyst coating (via e-beam evaporation), masks could be used to control the regions exposed to metal deposition, leading to the growth of nanotubes in defined patterns. These masks could be as simple as a TEM grid placed over the substrate or more complicated patterns could be defined using electron-beam lithography (Figure 5-13a,b). Alternate growth substrates were also attempted using thermal CVD. In addition to quartz slides and silica and alumina films (deposited on silicon wafers), carbon nanotubes were successfully grown on the surface of metal contacts. In these experiments, iron or nickel catalyst films were deposited over titanium or titanium/tungsten layers supported by a silicon wafer (Figure 5-13c,d). Although nanotubes were successfully grown on these surfaces, delamination was often observed between this tungsten layer and the supporting silicon wafer.

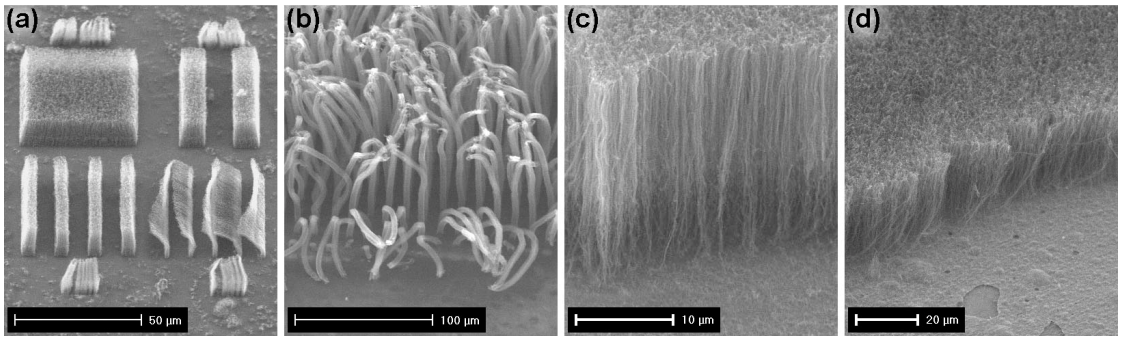

Figure 5-13: Thermal CVD growth on various substrates (a) patterned using e-beam lithography, (b) TEM grid mask patterning, (c) 10nm Ni catalyst on 40nm Ti, (d) 10nm Ni catalyst on 20nm Ti on 90nm W

5.2.1 Growth Rates

Similar to the work done with floating catalyst CVD, a parametric study was performed to study the thermal CVD procedures described in Sections 3.1.3 and 3.1.4. Benzene was used as a liquid carbon source and ethylene was used as a gaseous carbon source to grow nanotubes on both iron (3-10nm thick) and nickel (3-10nm thick) catalyst films (which had been evaporated onto silicon, quartz, and alumina substrates prior to synthesis). Similar trends of nanotube growth speed with time were observed, even with variations in the carbon source used, reaction temperature, catalyst metal and thickness, and substrate material.

A sequence of growth runs differentiated by total reaction durations was performed with the gaseous ethylene carbon source. For these tests, iron films were used as a catalyst material and were deposited on thin alumina layers on silicon wafers. As described in Section 3.1.4, ethylene was found to successfully produce carbon nanotubes at relatively low temperatures compared to nanotubes synthesized using other CVD methods studied, and growth in these experiments was conducted at

750°C. In addition, while the addition of ammonia was found necessary to reduce deposition of amorphous carbon using benzene, this was not required with ethylene, and clean tubes were produced with a mixture of just ethylene and argon. A list of the reaction conditions used during this study is found in Table 5-4.

Table 5-4: Summary of Thermal CVD Growth parameters, gaseous carbon source

Growth parameter	Value
Carbon Source	Ethylene
Carbon feed rate	~200 sccm
Catalyst material	Iron
Catalyst thickness	~5nm
Argon flow rate	~225 sccm
Reaction Temperature	750°C
Substrate	~15nm Al_2O_3 on Si
Reaction Duration	Varied

Using these identical reaction conditions, growth was allowed to continue for several different reaction durations, and nanotube lengths were subsequently measured using SEM. These results are plotted in Figure 5-14, and show an initial period of rapid growth, which slows with increasing reaction time. While in this sequence of growth runs only iron catalysts were used, similar trends (growth rates decreasing with time) would also be expected for nickel catalysts under these synthesis conditions.

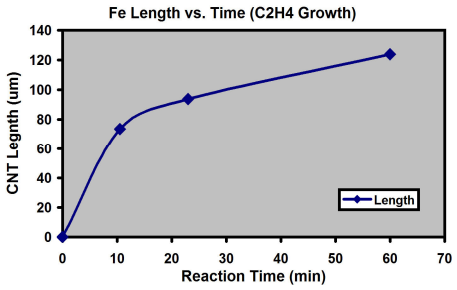

Figure 5-14: Nanotube length as a function of reaction duration, thermal CVD with ethylene carbon source and Fe catalyst

This experimental sequence was also performed for synthesis runs using the benzene carbon source. This growth differed in a number of aspects; most notably two important growth parameters were changed. Benzene was not found to successfully produce carbon nanotubes at lower temperatures (at those temperatures where nanotubes were synthesized with ethylene); as a consequence, CVD using benzene was performed at 900°C, rather than the 750°C used with ethylene. In addition, ammonia was mixed with the argon carrier gas in a roughly 1:1 ratio to limit amorphous carbon formation (see Sections 2.4.4 and 5.3.2). Both nickel and iron catalysts were used in this series of experiments; a summary of the reaction parameters used is given in Table 5-5.

Table 5-5: Summary of synthesis conditions for Thermal CVD, liquid carbon source

Growth parameter	Value
Carbon Source	Benzene
Introduction rate	~0.13 ml/min
Catalyst material	Iron, Nickel
Catalyst thickness	~5nm (Fe), ~10nm (Ni)
Argon flow rate	~225 sccm
Ammonia flow rate	~200 sccm
Reaction Temperature	900°C
Substrate	SiO_2/Si (Fe), SiO_2 (Ni)
Reaction Duration	Varied

As before, synthesis reactions were allowed to proceed for a series of different times, and nanotube lengths were measured as a function of growth duration. Results from this synthesis are shown in Figure 5-15; for both metal catalysts rapid growth was observed at the beginning of the reaction, which then slowed as the synthesis progressed.

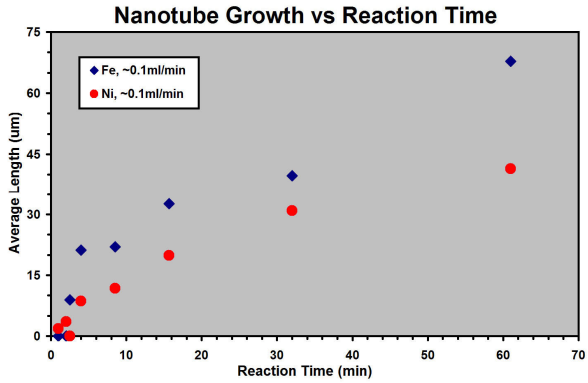

Figure 5-15: Nanotube growth length as a function of reaction time, thermal CVD with Fe and Ni catalysts and a benzene carbon source

In addition to investigating growth as a function of time for two different metal catalysts, different benzene introduction rates were also studied. A benzene introduction rate of ~0.1ml/min was typically used (achieved using a 27 gauge needle). A similar series of synthesis tests were then performed using a 25 gauge needle which provided a ~0.3 ml/min benzene introduction rate. The reaction conditions used were identical to those listed in Table 5-5 with the exception of the increased benzene flow rate. A comparison of these two growth series is shown in Figure 5-16 for iron-catalyst nanotubes, similar results were obtained with nickel catalyzed growth.

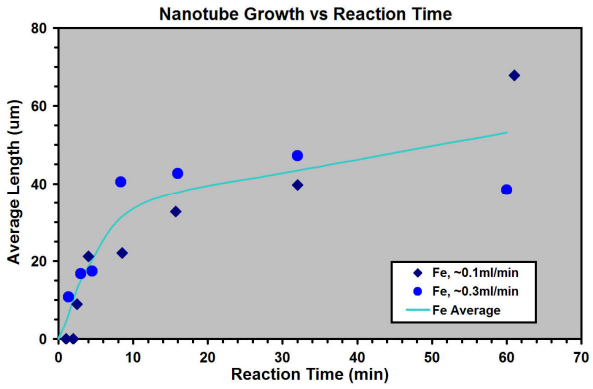

Figure 5-16: Comparison of growth with two carbon introduction rates (Fe thin film catalyst and thermal CVD synthesis)

With both carbon introduction rates, a region of rapid initial growth is first observed, which then slows with time. With slower benzene introduction rates (~0.1ml/min) carbon nanotube growth was found to continue (although at greatly reduced rates) even after relatively long reaction durations (up to 60 minutes). With increased carbon introduction (0.3ml/min) initial growth was very slightly enhanced; however, growth termination occurred much sooner (at roughly 10 minutes), after which no additional lengthening was observed. This observation suggests catalyst poisoning is occurring sooner (at the 0.3ml/min benzene feed rate) due to excessive amorphous carbon formation caused by the higher introduction rate. In these experiments, the reduced carbon feed rate (~0.1ml/min) provides a better compromise between rapid growth and extended catalyst activity (by limiting production of unwanted carbon by-products). Similar trends were also found for the nickel catalyst growth studies. Initially, the tubes lengthened rapidly; however, after roughly ten minutes of synthesis the growth rate began to slow, and length increases became very small with increasing reaction durations. For extended reaction times, growth would

stop completely, and the nanotubes would not grow beyond some ultimate length (determined as a function of specific reaction conditions). This pattern can be more clearly visualized by plotting growth rate against reaction time, as illustrated in Figure 5-17a (data points represent the average length measured from both carbon introduction rates at each given time). Figure 5-17b shows the same growth rate trends for nanotube synthesis using ethylene thermal CVD growth (from the data presented in Figure 5-14).

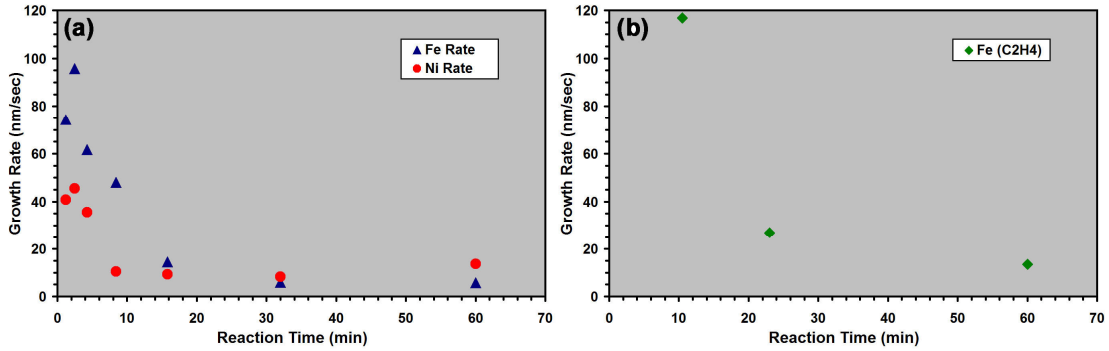

Figure 5-17: Growth rate as a function of thermal CVD reaction time for (a) Fe and Ni catalyst films using benzene, and (b) Fe catalyst films with ethylene

While both catalyst metals and samples from both benzene and ethylene catalyzed growth showed rapid initial growth, which slowed as the reaction progressed, the actual growth rates were not equal for these different synthesis conditions. When comparing growth with the same iron catalyst but different carbon sources, faster peak synthesis rates are observed with the ethylene-based growth. In addition, significant growth occurs for a longer duration with an ethylene carbon sources (growth rates are over twice those of benzene-grown tubes after twenty minutes of synthesis). In both cases, however, growth still slows greatly and has

nearly stopped after a one hour reaction. Nanotube formation theory suggests that carbon diffusion through the catalyst particle can limit growth. Even though the samples used in this comparison all used iron as a catalyst material, the reaction temperature, reaction gas composition, and substrate material were not identical, and these variations can affect amorphous carbon deposition rates and catalyst particles sizes (which can in turn affect carbon diffusion lengths through the particle). The different growth rates observed between these CVD variations are thought to be due to the differences in catalyst particles sizes (this relationship is investigated in more detail in Section 5.3.1).

For tubes grown with the same carbon source (benzene) and at the same reaction temperature, the starting growth rates were not equal, with iron-catalyzed nanotubes lengthening at roughly twice the rate of those using a nickel catalyst. According to the accepted nanotube formation theory (Section 2.4.4), growth can be limited as a result of several factors, the most common of which are restricted carbon availability at the catalyst particle and diffusion limited transport of carbon through the catalyst particle. Due to the similar initial growth rates observed using different carbon introduction rates (Figure 5-16), it is believed that carbon availability is not limiting the potential growth speeds in these experiments. As a result, it is expected that growth rates (before any catalyst poisoning has occurred), would be governed by carbon diffusion through the metal catalyst particles. The activation energy for carbon diffusion through iron has been found to be roughly half that of carbon diffusion through nickel (16.1 kcal/mol compared to 34.7 kcal/mol, see Table 2-3); as the initial

nickel growth rates were roughly half those of iron, this suggests that carbon diffusion rates are the growth limiting factor during the early stages of synthesis. These results can also be compared with the growth rate findings for floating catalyst CVD. During the initial stages of synthesis, iron-catalyzed nanotube growth rates are fairly similar for thermal CVD growth with benzene and for floating catalyst CVD growth with benzene (60-90 nm/sec vs. 60-70 nm/sec). The slightly faster initial growth for the thermal CVD experiments can be attributed to the higher reaction temperatures used (faster carbon diffusion at 900°C vs. 800°C). Beyond roughly ten minutes of growth, however, the thermal CVD growth rates begin to drop due to catalyst poisoning.

Just as an upper carbon introduction rate can be identified (beyond which excessive amorphous carbon deposition can limit growth, as suggested by Figure 5-16), a lower limit can also be experimentally determined. Under growth conditions with very slow carbon introduction, the presence of this reactant can become the rate limiting step during synthesis, rather than carbon diffusion through the metal catalyst particle. To investigate this, a series of growth experiments were performed with benzene introduction rates varying over two orders of magnitude (from less than 0.01 ml/min up to ~1.0 ml/min), with a fixed reaction duration. Following growth nanotube lengths were measured and are plotted as a function of reactant introduction rate in Figure 5-18. At high carbon introduction rates, nanotube lengths were roughly equal, indicating that carbon availability was not limiting and that other factors, such as diffusion rates or catalyst poisoning controlled growth. At very low benzene introduction rates (below ~0.05 ml/min), growth was still be achieved in some trials;

however, nanotube length was considerably reduced, suggesting reactant availability was limiting growth in these slow introduction cases.

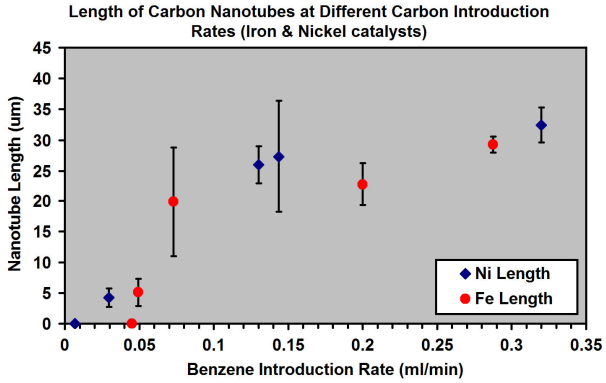

Figure 5-18: Nanotube length as a function of benzene introduction rate (Fe and Ni catalysts, constant reaction duration)

The effects of varying carbon introduction rates can be further studied through the use of Raman spectroscopy (Section 2.6), which can give an indication of the amount of disorder in each sample (induced by amorphous carbon, defects, etc.). With faster carbon introduction rates catalyst poisoning is expected to occur earlier during the reaction. Additional carbon introduction after this point can result in deposition of amorphous carbon on nanotube walls as well as other exposed surfaces. As these deposits would be disordered in nature, the quality of the resulting nanotube product would be decreased and this would be measurable using Raman spectroscopy. This unwanted deposition could be avoided by using very small carbon introduction rates; however (as shown in Figure 5-18), with very slow introduction, carbon availability can be rate limiting and greatly reduce growth. An optimal carbon introduction rate (allowing rapid growth while limiting unwanted amorphous by-products) can be identified by comparing the Raman G-peak and D-peak height ratios as a function of

benzene introduction rates. Higher G:D-peak ratios indicate better structure in nanotubes, as the G-peak is due to vibrations only found in sp^2-bonded carbon (graphitic bonding), and the D-peak arises due to the presence of defects and amorphous carbon in a sample. Results for nickel catalyst films are given in Figure 5-19, and show that benzene introduction rates of roughly 0.1ml/min provide sufficiently rapid growth (not limited by reactant availability) and still maintain high G:D-peak ratios (limited amorphous carbon formation). Synthesis with iron catalysts showed similar trends, and an optimal benzene introduction rate of ~0.1ml/min was identified (matching that found with nickel catalysts). The agreement between these optimal carbon introduction rates is expected, as the introduction rate (along with the growth temperature and specific hydrocarbon used) strongly affects the formation of amorphous carbon, while the catalyst material would have a much smaller influence.

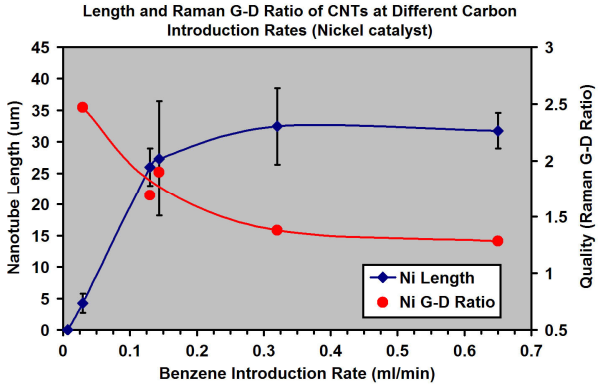

Figure 5-19: Nanotube length and Raman G:D peak ratios as a function of benzene introduction rates for Ni-catalyzed thermal CVD nanotube growth, error bars represent standard deviation in length measurements

Using the optimal growth parameters identified in the previous studies, growth to lengths nearing 200μm was achieved using both the benzene-ammonia process and the ethylene process (Figure 5-20). While this growth represented a significant

improvement over earlier growth runs, this is still significantly less than the longest tubes currently described in the literature (see Figure 2-36). These reports differ from our growth in several respects. Many groups use iron catalyst films deposited over an alumina layer on silicon wafers, similar to those used in this work; however, in reports of very long growth, the iron film thicknesses tend to be significantly thinner (0.5-2nm) [218, 301]. This leads to smaller catalyst particles, which promote the formation of single and double walled tubes with fast growth rates. These small catalysts can also be susceptible to rapid poisoning, and conditions within the reaction must be precisely controlled to prolong growth to produce long tubes. Impurities within the reaction gases have been identified as detrimental, and high purity gases are often used [218, 332]. Water vapor concentrations must be maintained within a small range for optimal growth; in low concentrations, water can selectively oxidize amorphous carbon deposits. In higher concentrations, water can damage nanotubes and can be insufficient to prevent poisoning in very low concentrations [231]. For optimal growth conditions, the water concentration should be roughly 0.1% of the ethylene concentration, and very small increases or decreases to the water content (relative to the ethylene) can have significant detrimental effects on growth [340]. While the reaction chamber used in the present work was quite versatile, allowing for growth using several variations of the CVD process, the flowmeters used were not capable of the extremely precise control required to synthesize very fast growing small diameter tubes. Furthermore, while water content could be monitored during the reaction, this parameter could not be finely adjusted. Typical water concentrations were between

50ppm and 150ppm, which corresponds to roughly 0.01-0.03% of the ethylene used. Although the nanotubes grown using thermal CVD during this research did not approach the millimeter-scale lengths reported by some groups, the nanotubes were sufficiently long (100-200μm) for the mechanical testing performed (Section 6.2.1), and these long lengths were not required for the flexural rigidity and fluid flow measurements (which used shorter, 30-60μm tubes, see Section 6.2.4).

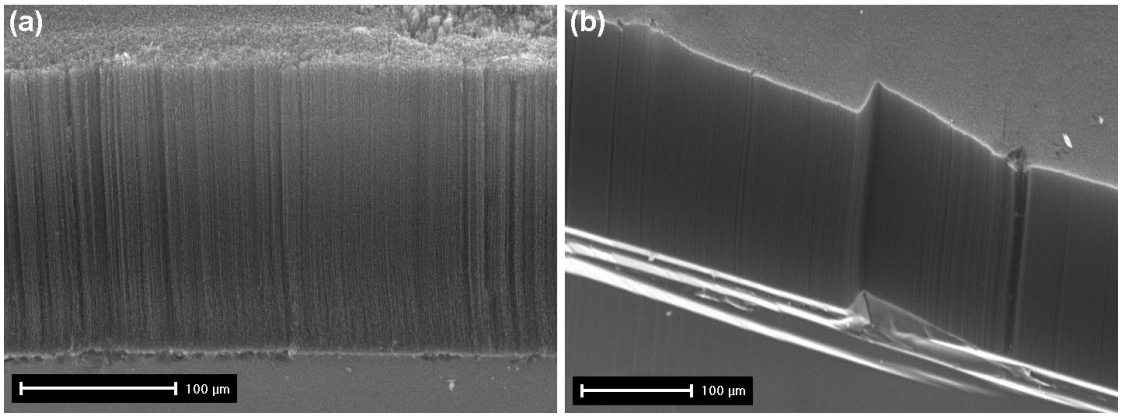

Figure 5-20: Long thermal CVD nanotubes: (a) ~190μm long nanotubes grown using benzene with ammonia (b) ~200μm nanotube grown using ethylene

5.2.2 Growth Mechanism

Due to the method of catalyst introduction in thermal CVD growth (compared to floating catalyst CVD), it is easier to definitively identify the growth mechanism acting for the thermal CVD synthesis of carbon nanotubes. The active growth mechanism will depend on the substrate and catalyst particle interaction, so the selection of substrate material and catalyst metal will influence the mechanism, with certain combinations leading to predominantly tip growth and others, which result in predominantly base growth. In this work, two particular catalyst-substrate

combinations were studied: nickel catalysts on quartz and iron catalysts on silicon wafer-supported alumina films (these were combinations, which were commonly used throughout this research).

To investigate these growth mechanisms, an experiment similar to that used to characterize floating catalyst CVD growth (Section 5.1.2) was performed. Nanotube mats were grown from thin nickel films on quartz slide substrates, and then roughly half of the mat was carefully removed, using a razor blade applied with very little force to scrape away a region of nanotubes. This process would presumably remove any catalyst particles at the tips of the tubes (as would occur in tip-growth), while leaving particles strongly affixed to the substrate behind (as would occur in base-growth). A second thermal CVD reaction was then performed on the sample and the results observed using SEM. Following this, a base-growth mechanism would be confirmed if re-growth occurred in the scraped region (from catalyst particles, which remained affixed to the substrate); if no growth occurred, then tip-growth would be indicated (catalyst particles removed with the nanotubes). The results are shown in Figure 5-21; no re-growth was observed from this nickel catalyst on a quartz substrate, suggesting that this thermal CVD growth is by the tip-growth mechanism.

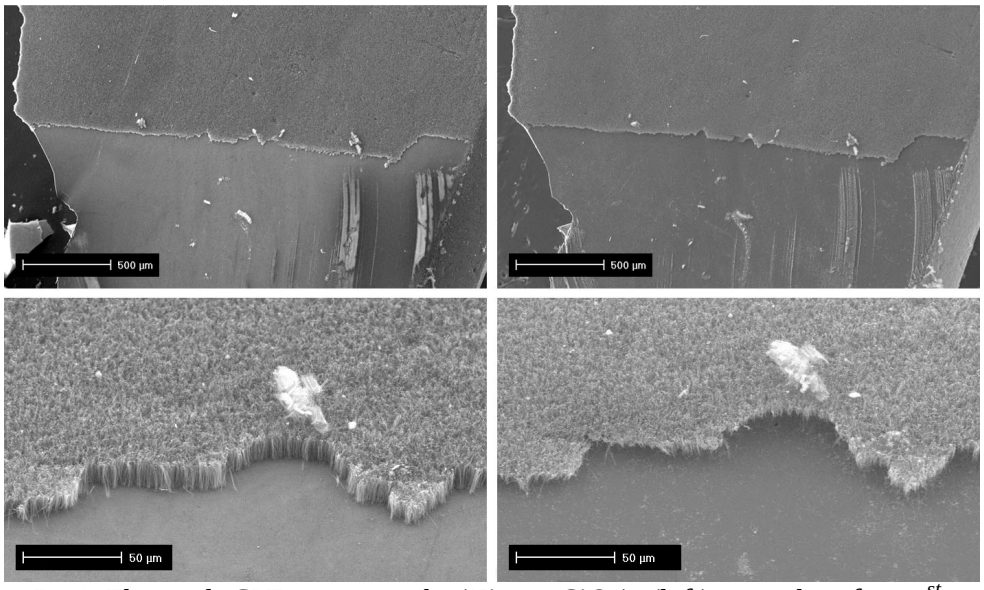

Figure 5-21: Thermal CVD re-growth (Ni on SiO_2) (left) sample after 1st growth process and partially removed, (right) sample after 2nd growth process

A variation to this interrupted growth process was also used to study iron catalysts on alumina surfaces. Similar to the results obtained with floating catalyst CVD (Figure 5-7), this interrupted process was used to produce layered structures with a thermal CVD growth procedure. Growth was carried out using the standard thermal CVD recipe (Table 5-5) with iron catalysts; however, the benzene introduction was interrupted a single time during synthesis. In order to provide further evidence to the growth method (tip vs. root) acting for this CVD method, the interruption in benzene flow was timed to occur early in the run (roughly 20 minutes into a 1 hour run). During this pause, ammonia and trace water vapor (~70ppm) in the reaction atmosphere etched away both amorphous carbon deposits and the region of the nanotube-catalyst junction. Growth then continued following the re-introduction of benzene; these results are shown in Figure 5-22.

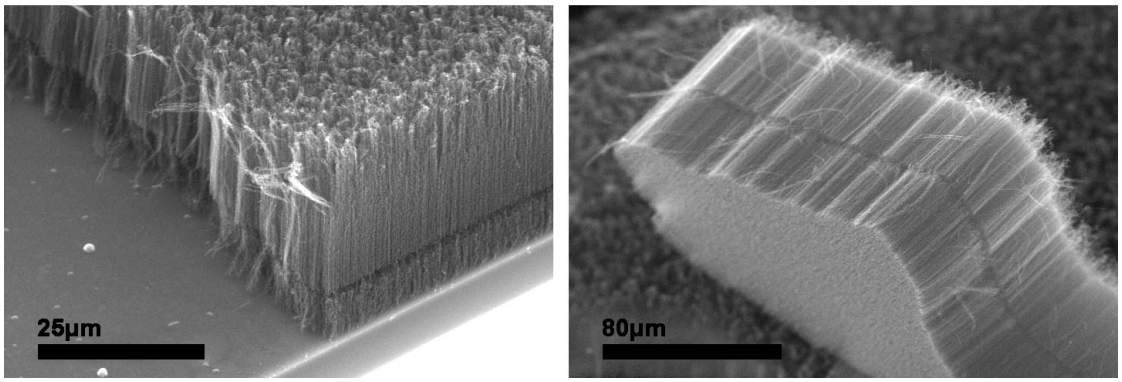

Figure 5-22: Layered nanotube mats grown using 3nm (left) and 10nm (right) iron films on alumina on silicon substrates

This method of pausing growth to allow for etching and the removal of amorphous carbon has been reported before, and the results have varied depending on the active growth mechanism. For tip-growth (using nickel catalysts), all new growth following the etching step continued from the Ni particles already at the tube tips, simply restarting growth of existing tubes [330]. Under condition where base growth is active, this etching step attacks the interface between the nanotubes and the catalyst particles, separating them. When growth is restarted, new tubes will start to form from the substrate-attached particles, pushing the previously formed nanotube layer upwards [199]. These layered structures have been reported by other groups (also using iron catalysts on alumina or silica substrates), and give a clear indication that this synthesis occurs through the base-growth mechanism [189, 197, 209, 324].

While the re-growth attempt with nickel catalysts on quartz and the layered structure obtained with iron catalyst on alumina strongly suggest tip- and base-growth, respectively, an examination at the nanometer-scale (rather than the micron-scale) can provide conclusive evidence regarding the growth mechanism. Careful preparation

allowed the mat alignment to be preserved in electron microscopy samples. By maintaining this structure, the forest base could be identified (regions where many nanotube ends are found along the same line), and catalyst particles could be observed predominantly at either the tube tips or base (using either high resolution SEM or TEM). Figure 5-23 shows nanotubes grown using nickel catalyst films on silica-coated silicon wafer substrates; the catalyst positions clearly indicate tip-growth (supporting the indication of tip-growth given by the re-growth experiment).

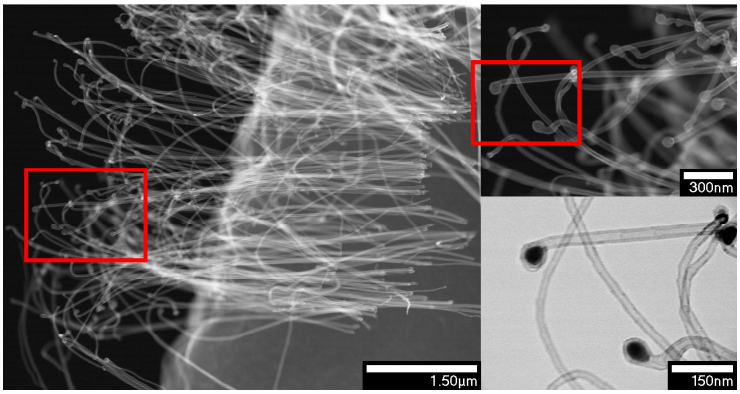

Figure 5-23: Location of catalyst particles at tube ends for growth via tip growth with nickel catalysts on silicon wafer substrates

The appearance of disordered carbon around the catalyst particle can help determine if synthesis is by the tip- or base-growth mechanism. A particle almost completely encapsulated by amorphous carbon suggests tip growth (as in Figure 5-23), as particles are exposed at the nanotube tips to carbon deposition during the reaction. Catalysts attached to the substrate (base-growth), however, can only receive a limited coating of amorphous carbon, as the contact area with the substrate and the region enclosed by the growing nanotubes are protected from exposure to the reaction. If these tubes are firmly scraped away from the substrate, the catalyst can separate from

the surface and remain affixed to the nanotube, and these base-growth particles will have a characteristic appearance, which is distinct from carbon-coated tip-growth catalysts. TEM examination of some nanotube products has revealed the presence of both these types of particles within a single sample, suggesting that both mechanisms can be active simultaneously. As these samples are grown during a single run, many parameters, such as temperature, carbon introduction rate, gas flow rate and composition, and substrate and catalyst material are identical. However, within any sample there is some distribution to the nanotube diameters, and a correlation was observed between tube diameters and the apparent growth mechanism (Figure 5-24).

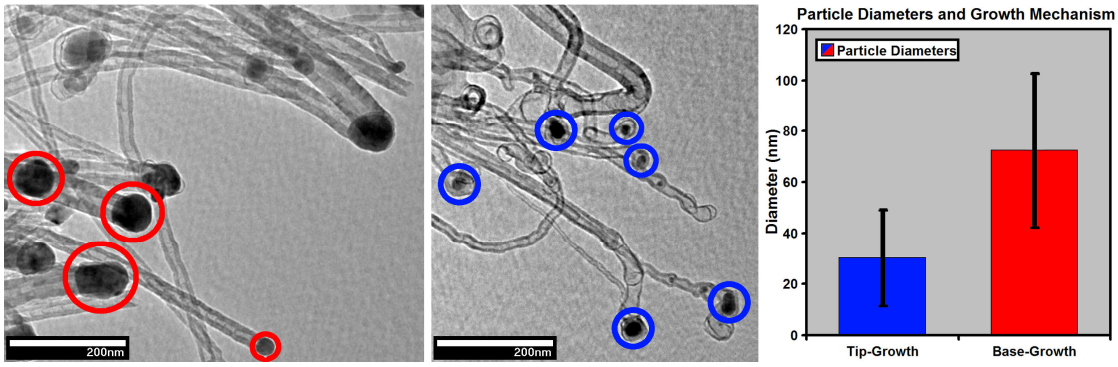

Figure 5-24: Relation between catalyst particle size and observed growth mechanism (Ni catalyst on quartz, single thermal CVD run)

The distinction between tip- and base-growth mechanisms depends on the interaction between the catalyst particle and both the substrate and inner nanotube walls (if the nanotube-catalyst interaction is stronger, the particle will be lifted from the surface via tip-growth). The catalyst and substrate material will strongly influence this; however, the interaction area will also affect the relative interaction strengths. The interfacial area between a catalyst particle and the inner nanotube wall surface

will increase linearly with the particle size (~r), while the catalyst-substrate interface area increases with the square of the catalyst size (~r^2). Therefore, larger particles will have increased interaction areas with the substrate surface and higher relative interaction strengths than smaller particles (greater substrate interaction than interaction with the inner tube wall surfaces). As a result, even for the same substrate-catalyst combination, there can be some quantity of nanotubes growing via the tip mechanism and some amount growing via the base mechanism within the same sample. With greater amounts of catalyst material (promoting larger particles, such as with thicker catalyst films), or with catalyst-substrate combinations, which have greater relative interaction energies, a larger fraction of the tubes will grow via base growth.

This same particle diameter-dependent distribution of growth mechanisms would also be expected to occur for iron catalyst films on alumina surfaces. However, this metal-substrate combination is already expected to have stronger interactions (relative to the nickel-quartz system) resulting in predominantly base-growth (as suggested by the interrupted growth experiment, Figure 5-22). Iron catalysts were rarely observed in these samples; consequently, it was difficult to make a similar growth mechanism classification as with the nickel catalysts. However, the limited number of catalysts observed (relative to nickel) would be expected when strong interaction between the catalyst and substrate would prevent the removal of metal particles during TEM sample preparation.

Based on these results, we observe both base-growth and tip-growth in nanotubes grown via thermal CVD. The growth mechanism depends on the catalyst-substrate combination, and on the catalyst particle size. Due to the diameter distributions found within each sample, tip-growth and base-growth can occur simultaneously on different nanotubes within the same sample (as observed for nickel-catalyzed growth on quartz). The different interaction energies between certain metal-substrate combinations will also influence the growth mechanism, with nickel-quartz samples predominantly growing through tip-growth and iron-alumina samples growing via base growth.

The strength of the catalyst-substrate bond depends on the nature of the interaction, which varies between nickel and iron, and between aluminum oxide and silicon oxide substrates. Nickel has shown high catalytic activity towards the dissociation of hydrogen, and the generation of hydrogen atoms can partially reduce the oxide in the substrate. This can lead to strong metal-support interaction (SMSI), caused by negative charge transfer between the metal cation sites on the substrate and the catalyst particle [206, 562]. However, alumina and silica substrates exhibit this strong metal support interaction to only a limited extent [313, 563], and correspondingly, the interaction between nickel and these substrates is not as strong. Iron is not as effective as nickel in catalyzing the dissociation of hydrogen, and in these cases, the oxygen on the substrate surfaces can act as Lewis base sites, transferring a negative change to the metal catalyst particle. The bonding in alumina is more ionic in nature than that in silica [564, 565], and due to this, the interaction

between the catalyst particles and these Lewis base sites would therefore be increased in alumina. This would result in greater substrate-catalyst interaction and lead to growth predominantly occurring via the base-mechanism. In addition to determining the growth mechanism, these interactions also influence the particle size and corresponding carbon nanotube diameter (Section 5.3.1).

For both iron and nickel catalysts and by both the base- and tip-growth mechanisms observed, nanotubes grew in well-aligned forests. As no external means were used to control this alignment (such as applied electric fields), this alignment occurs via the crowding mechanism (Section 2.4.5). With careful sample preparation, clumps of nanotube forests can be transferred to TEM grids and imaged without disturbing their structure; variations in nanotube orientations from the mat base to tip reveal the development of alignment through the crowding mechanism. Figure 5-25 shows an iron-catalyzed nanotube sample (grown on alumina), and alignment is observed to improve towards the base of the mat compared to the top of the mat. In base-growth (expected for this catalyst-substrate combination), the bottom of the mat will be the region most recently formed within the sample, and the regions of the nanotube towards the top will be those grown at the beginning of the reaction. When growth starts, nanotube alignment will be random, and the crowding mechanism will not begin to influence the tube growth direction until the nanotubes have reached a sufficient length to interact with adjacent tubes. This crowding effect will become more pronounced as growth continues, producing improved alignment in the regions of newest growth, as observed in Figure 5-25. In base growth, this initially misaligned

region (formed at the very start of the reaction) will be pushed upwards (at the top surface of the mat) as the tubes continue to lengthen.

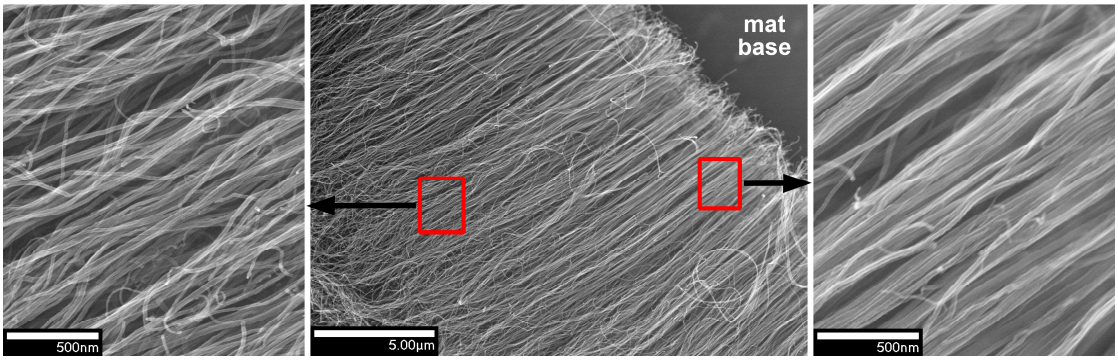

Figure 5-25: Improvement in nanotube alignment from the top of the mat to the base

5.2.3 Growth Termination

Floating catalyst CVD has been observed to produce long (several mm) mats of nanotubes with roughly constant growth rates due to the continuous addition of catalyst material. As a result, while individual tubes will stop growing during the reaction as the metal particle catalyzing nanotube formation becomes poisoned, the entire mat will continue to grow and lengthen. In thermal CVD; however, the poisoning of individual catalysts has a much larger impact on the nanotube production, as these catalyst particles are not replenished during synthesis. As a disordered carbon coating begins to deposit on the catalyst surfaces, diffusion of carbon through the particle and into the nanotube slows and eventually ceases, resulting in a decreasing growth speed as the reaction continues (see Figure 5-17). It was observed that growth in some thermal CVD attempts (with benzene at 800-900°C) was very poor, with thick, disordered carbon fibers forming due to rapid amorphous carbon deposition and

catalyst poisoning. The addition of ammonia to the reaction was found to prevent this problem, resulting in a distinct change in morphology (Figure 5-26) and showing that the reactant gas is an important parameter in the CVD-production of carbon nanotubes. While gas flow rates can affect the yield of nanotubes (with low yields observed for high flow rate, spray pyrolysis reactions, Section 5.1), the composition of the gas is very important for prolonging growth with thermal CVD.

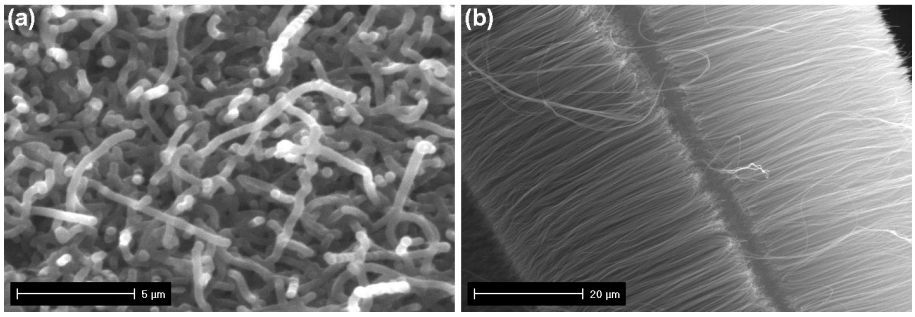

Figure 5-26: Influence of ammonia on CNT growth via thermal CVD, (a) growth without ammonia and (b) growth with ~35% ammonia

In these tests, results, which produced thicker tubes with large amounts of amorphous carbon, tended to have tangled fibers near the substrate, while results with cleaner tubes free from amorphous coatings tended to have a much higher degree of alignment and grow nearly perpendicularly from the substrate surface. This aligned growth (in the absence of any electric fields or other means of controlling growth direction) has been attributed to a "crowding" effect, where relatively tightly packed nanotubes help to support each other during growth, achieving good alignment (see Sections 2.4.5 and 5.2.2). In addition, van der Waals forces exist between tubes due to the small separation gaps; these forces hold tubes together and also contribute to alignment. In order for these effects to produce an aligned product, the lengths of the

tubes must be significantly longer than the average gap distance between adjacent tubes (to allow the tubes to come into close proximity and interact with each other during growth).

In the absence of ammonia (with other reaction parameters, such as catalyst film thickness held constant), thick, randomly aligned carbon fibers are formed (as these fibers cannot reach lengths sufficient to create alignment due to crowding). The lack of alignment and short length of these tubes suggests that their growth (as nanotubes) was quickly terminated due to catalyst poisoning. Subsequent carbon introduction (in the form of benzene at ~0.1 ml/min) results in amorphous carbon deposition on the tube walls, thickening them to diameters of several hundred nanometers. The addition of ammonia during growth clearly helps produce a much more well-ordered nanotube product, as the inhibition of amorphous carbon deposition and catalyst poisoning allows tubes to be grown longer, with better alignment, and smaller diameters.

In addition to potential growth termination due to catalyst poisoning, there is also a possibility of slowing growth due to increasing diffusion lengths for reactants to reach the catalyst particles. However, it seems extremely unlikely that this effect limits growth at all in these thermal CVD growth runs, as growth termination is observed even under conditions where tip-growth occurs (where catalyst particles do not remain on the mat surface and the diffusion distance does not change as the nanotubes lengthen). Furthermore, upon examination of mat cross-sections in base-growth samples, a dependence of height relative to position on the substrate is

sometimes observed, but the findings do not support any diffusion limitations. Rather than finding longer tubes at the edge of the substrate and shorter tubes at the center (as would be expected for diffusion limited growth), the opposite is observed, as shown in Figure 5-27. This confirms that diffusion of reactants (carbon) to the catalyst sites is not a limiting factor in the thermal CVD nanotube growth performed in this study, and that growth termination is a consequence of amorphous carbon deposition and catalyst poisoning.

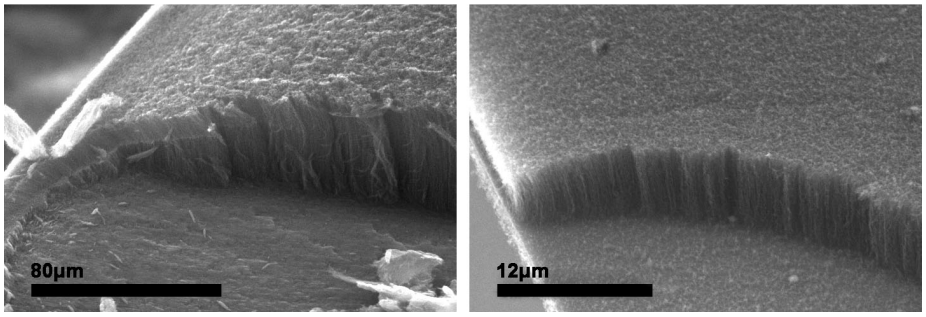

Figure 5-27: Mats of nanotubes grown via thermal CVD showing reduced nanotube height within close proximity to the substrate edge

As the benzene introduction rate remains constant during synthesis, and other parameters (temperature, etc.) do not change, it can be assumed that amorphous carbon deposition rates are roughly uniform throughout the reaction. For tubes grown without ammonia (producing short, disordered mats) lengths can be measured, and, using the growth rates previously determined for different catalyst films (Figure 5-17), the growth time prior to catalyst poisoning can be estimated. Additionally, by measuring tube wall thickness compared to wall thicknesses of nanotube grown with ammonia (using TEM), both the amorphous layer thickness and deposition rates can be determined (using known reaction durations). Finally, with these rough estimates

of amorphous carbon deposition rate and the time required for catalyst poisoning to occur, the thickness of a carbon layer, which is sufficient to poison the catalyst and stop growth can be determined.

Several misaligned, carbon fiber samples were analyzed in this fashion (Figure 5-28), and a hollow inner tube (the original nanotube grown from a catalyst particle) could be seen in many of these fibers. This structure was coated in a thick layer of amorphous carbon, leading to larger average outer diameters ranging between ~192nm and ~426nm. The original inner and outer diameters were also measured, with average inner diameters of 45 to 50nm and very thin walls. Wall thickness of the amorphous carbon sheaths were therefore found to range from ~74nm to ~188nm (for growth durations from 43 to 51 minutes), corresponding to amorphous carbon deposition rates ranging from roughly 1.5nm per minute to 4.4nm per minute. Measurement of nanotube lengths in these samples via SEM was difficult due to the tangled nature of these fibers; however, a rough estimate gave lengths of ~6µm and ~10µm. Based on growth rates previously determined (Section 5.2.1), catalyst poisoning is thought to be complete in these samples within one to two minutes. This indicates that an amorphous carbon layer of just 3 to 6nm on the catalyst surface is sufficient to completely terminate nanotube growth.

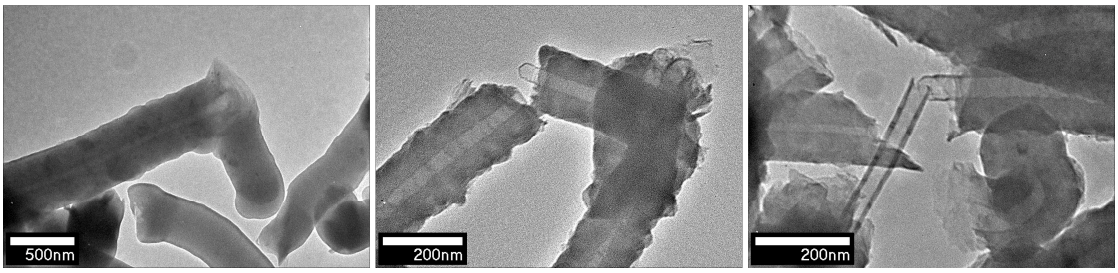

Figure 5-28: TEM images of nanotubes grown without NH_3 showing thick amorphous carbon sheaths coating a thin-walled inner nanotube

5.3 Nanotube Characterization

Carbon nanotubes were successfully produced using several variations of a chemical vapor deposition procedure (Sections 5.1 and 5.2). However, in some cases, these methods produced nanotubes with substantially different characteristics, and small alterations of synthesis reaction parameters could result in significant changes to the nanotube products.

SEM observation of the nanotubes produced using both vapor phase CVD and thermal CVD revealed a similar appearance at the micron-scale. However, the similarities in micro-structural appearance did not carry over to the nanometer-scale, as revealed by TEM analysis. Carbon nanotubes produced using vapor phase CVD typically had a rougher outer surface and showed many defects within the walls. Thermal CVD nanotubes could have either straight walls or distinct bamboo morphology, and tended to have smoother walls and narrower diameter distributions than the vapor phase CVD products. Representative images of these nanotubes are presented in Figure 5-29.

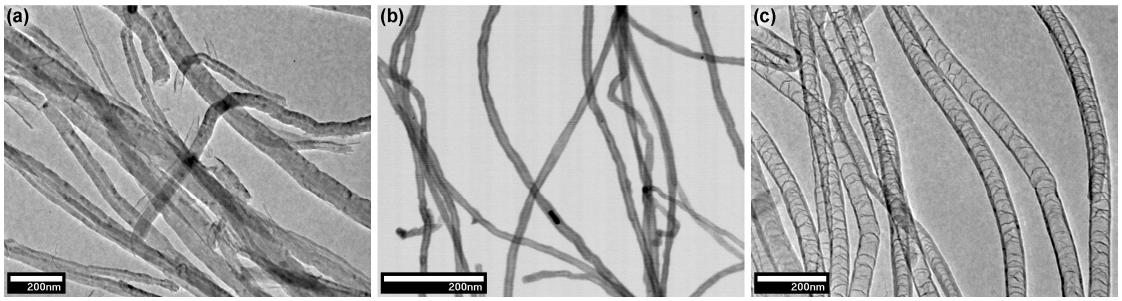

Figure 5-29: TEM images of carbon nanotubes grown via (a) floating catalyst CVD and (b,c) thermal CVD

5.3.1 Control of Carbon Nanotube Diameter

It has been shown that the length of carbon nanotubes can be largely controlled through the synthesis reaction duration, with the exact growth rate determined by growth parameters (see Sections 5.1.1 and 5.2.1). The diameter of a carbon nanotube is also a very important dimension, and differences in diameters can affect mechanical and electrical properties. Nanotube diameter is influenced by many more synthesis parameters than nanotube length, and the effects of these various parameters must be understood. In this study, several reaction parameters were varied (within a range that produced nanotubes in every case), which allowed the effects on nanotube diameters to be examined. While both thermal CVD and floating catalyst CVD growth procedures were used in this work to produce carbon nanotubes, some specific reaction parameters could be more carefully controlled using thermal CVD methods, and this study of diameter control was therefore limited to nanotubes produced using only thermal CVD growth. However, as the general mechanism of nanotube formation is the same for both thermal and floating catalyst CVD methods, the trends observed in this work are expected to also apply to nanotubes synthesized using

floating catalyst chemical vapor deposition. Although there are numerous parameters, which must be controlled during carbon nanotube growth, the study to examine the influence of different parameters on carbon nanotube diameters was limited to the following: catalyst film thickness, substrate material, hydrocarbon introduction rate, and synthesis reaction temperature. These parameters were found to affect the inner diameter of the tube, the tube wall thickness (and resulting outer diameter), or influence both of these dimensions.

It has been widely reported that the carbon nanotube diameter is determined by the size of the catalyst particle (assuming the catalyst particle is within the size range from which nanotubes can be successfully synthesized, see Section 2.4) [152-154]. Accordingly, an increase in the amount of catalyst material available would be expected to result in the formation of larger catalyst particles [566] and correspondingly larger nanotubes. This was observed for both nickel and iron catalyst films, on various substrates, and for thermal CVD growth with both liquid (Section 3.1.3) and gaseous carbon sources (Section 3.1.4). Results for CVD with benzene are shown in Figure 5-30a. In addition to an increase in average tube diameter with film thickness, a slight increase in the standard deviation of the diameter values is also observed. This is expected, as both the mean particle size and the particle size distribution will increase with increasing film thicknesses. Based on these results, diameter control between roughly 20nm and 80nm can be achieved simply by varying the amount of catalyst material deposited prior to growth.

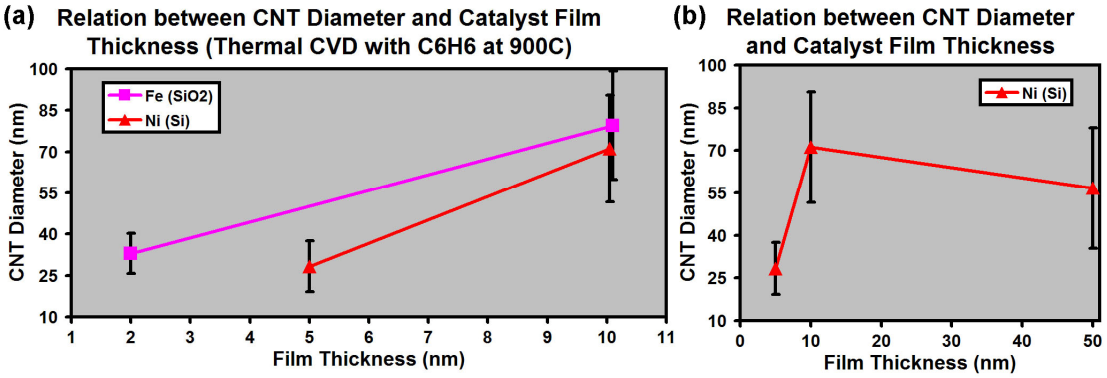

Figure 5-30: Relation between catalyst film thickness and carbon nanotube diameter

Catalytic synthesis of carbon nanotubes requires catalyst particles to be within a certain size range (larger particles will form carbon fibers and filaments) [148, 155]. Due to this, an upper nanotube diameter limit is expected to be reached with increasing film thickness. This was tested by attempting growth with a thicker (50nm) film of nickel catalyst (Figure 5-30b). Unlike the previous samples, the nanotube diameter from this sample did not follow the same trend (increasing with increasing catalyst thickness), and average diameters dropped slightly, from 71±19nm to 57±21nm. For these samples with thicker catalyst films, there is a distribution of metal particle sizes (as found in thinner film samples); however, some portion of these particles will be an appropriate size to catalyst the growth of carbon nanotubes, and the introduction of additional metal may form particles too large to support nanotube growth. Although thicker films will coalesce into a higher percentage of particles that are too large, the catalysts that do lead to growth will be similarly sized compared to those from thinner films (the larger particles self-exclude themselves from growth). As catalyst films exceed the thickness at which a significant percentage of particles are

too large for nanotube growth, a decrease in tube diameters could be expected, as those particles, which would catalyze very large tubes, would become too large for growth.

While thicker catalyst films will lead to larger particles (and more particles too large for nanotube growth), this excess metal still remains in the sample. Nanotube mats were examined using EDS to identify how the catalyst material was distributed within the nanotube forests, and tubes grown from thicker catalyst films were found to have excess metal throughout the height of the mat (Figure 5-31a). In the case of nickel, a nearly uniform increase in catalyst material concentration was observed for the bulk of the mat (approximately four times higher in a 50nm nickel film than in a 10nm film). Towards the top of the nanotube mat, however, the nickel concentrations increased, and the sample grown using a 50nm catalyst film had roughly eight times the amount of catalyst material on the upper mat surface than the 10nm samples. Nickel catalysts have previously been observed to synthesize nanotubes predominantly via the tip growth mechanism (Section 5.2.2), and the weak interaction between nickel and the substrate allows these excess particles to be carried away from the substrate with the top of the nanotube mat during growth (these particles can be seen in the inset of Figure 5-31a). In other cases, large (micron-scale) metal particles have been found on the substrate, surrounded by a “halo” zone of very poor nanotube growth (Figure 5-31b). These large particles (whether originating from very thick metal films or as contaminants), can deplete the surrounding region of catalyst material as the metal

film is heated and coalesces, resulting in a region devoid of suitable catalysts for nanotube growth.

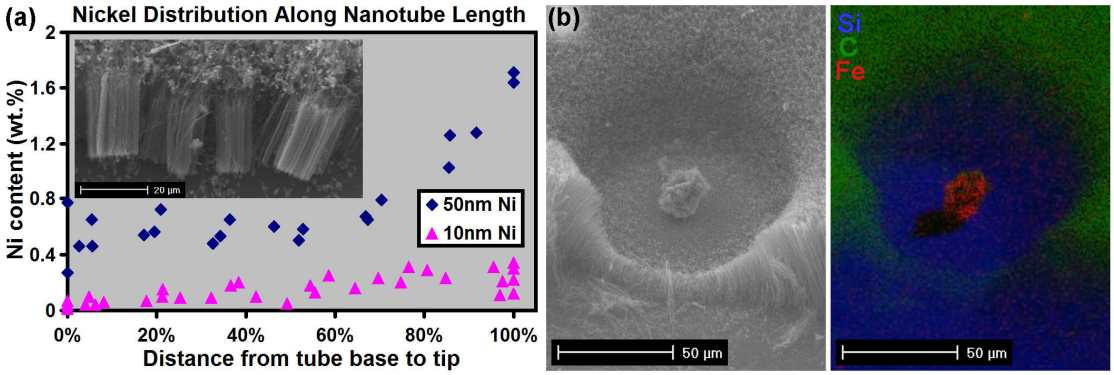

Figure 5-31: (a) Catalyst distribution within a nanotube mat with thick metal films, (b) EDS composition map of a larger metal particle within a nanotube mat

In addition to the amount of catalyst metal used, the substrate material has also been shown to influence the catalyst particle size (and the corresponding nanotube diameters). The interactions between the catalyst metal and substrate surface not only determine the growth mechanism (base- or tip-growth, Section 5.2.2), but stronger catalyst-support interactions can inhibit particle movement and coalescence during heating, resulting in smaller particles and nanotube diameters. In this work (and for most reports of nanotube growth) various oxides are used as substrates (with SiO_2 and Al_2O_3 the most common). Substrate-catalyst interactions can occur through the partial reduction of the substrate by the metal or hydrogen, formation of metal oxides, or the action of Lewis acid and base sites on the surface [206, 311]. Just as metal particles whose sizes are outside a particular range cannot successfully catalyze carbon nanotube growth, substrate-metal interactions, which are either too strong or too weak, can prevent the coalescence of catalyst films into appropriately sized particles. In

cases of very strong interactions, the metal film may wet to the substrate surface and form a continuous overlayer without breaking into discrete islands [311]. Alternatively, very weak interactions can lead to high catalyst particle mobility at the elevated temperatures used during nanotube synthesis, resulting in the formation of large particles that may not be suitable for nanotube growth (through the coalescence of many smaller particles). Substrate surface roughness has also been proposed as a mechanism affecting catalyst particle mobility on the surface [207]; however this is not thought to play a significant role with the supports used in this study (very smooth quartz slides and silicon wafers).

For the two most commonly used substrate materials (Al_2O_3 and SiO_2), alumina is expected to have a higher concentration of Lewis acid and base sites and a correspondingly stronger interaction with metal catalyst particles (the bonding in alumina is more ionic in nature when compared to that of SiO_2 [564, 565]). These interactions will reduce particle mobility on alumina, resulting in less coalescence and therefore smaller metal catalyst islands (leading to smaller nanotube diameters). Thermal CVD was used to grow nanotubes on these two surfaces (with catalyst film thickness, carbon source, growth temperature, and all other reaction parameters held constant), and the average tube diameter on the alumina surface was roughly 40% smaller than those grown on a silica surface (Figure 5-32).

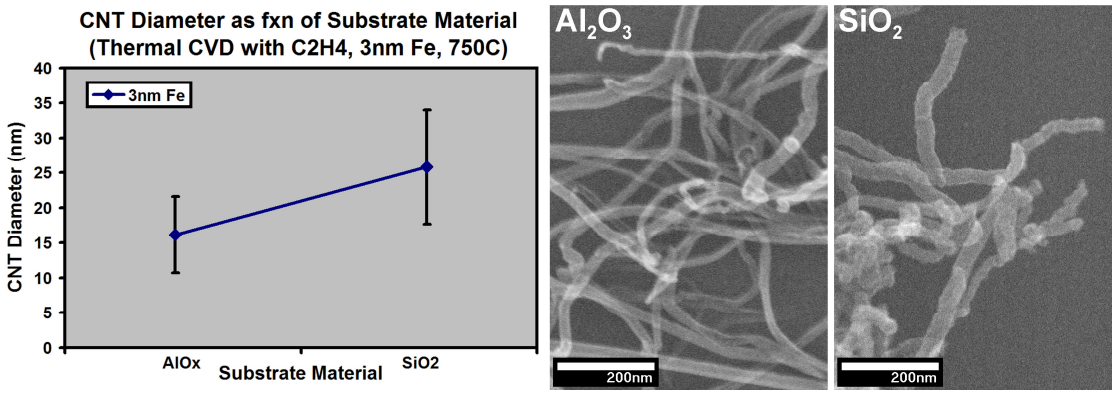

Figure 5-32: Influence of growth substrate on carbon nanotube diameters, 3nm Fe catalyst films with C_2H_4 thermal CVD synthesis, SEM micrographs are at the same magnification

To further investigate the relationship between the catalyst metal and the substrate material, an experiment was designed to separate the nanotube growth step from the annealing of the catalyst film into discrete particles. In this work, a series of AFM scans were performed to examine metal coated substrates after several treatments, including immediately after the metal deposition, and after various heating processes. Iron films (3-10nm thick), were deposited on silicon wafers coated with either a native oxide layer or with a thin (~15nm) film of aluminum, which was allowed to oxidize prior to the iron deposition. These samples were then placed in a furnace, with heating conditions selected to simulate the conditions used for nanotube growth runs. Samples were heated to either 750°C (the temperature most commonly used for thermal CVD growth with ethylene) or 900°C (used for CVD growth with benzene), in environments of either pure argon, or a mixture of roughly 50% ammonia in argon. Once these samples reached the desired temperatures (at which point the hydrocarbon would have been introduced in an actual nanotube growth run), the

furnace was shut off and rapidly cooled. These substrates were then examined using AFM (in close-contact mode). Following heating, the substrate surface roughened significantly, as shown in Figure 5-33.

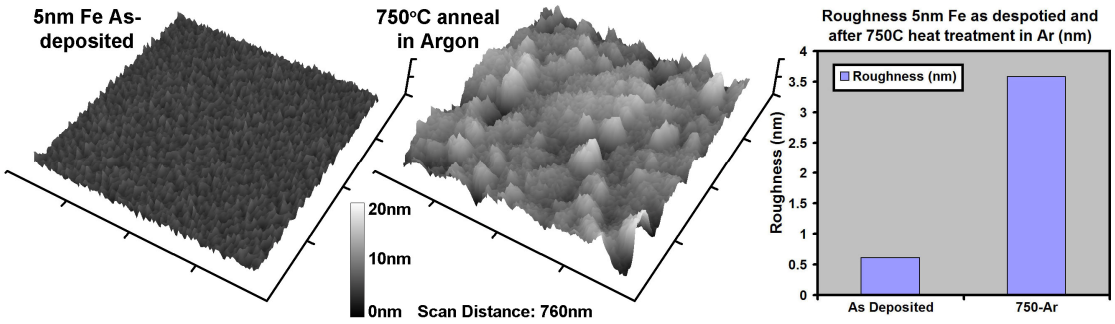

Figure 5-33: AFM scans and roughness measurements of 5nm Fe films as-deposited and after heating to 750C in argon (AFM scan scales are equal)

Unfortunately, while heated and as-deposited samples showed significant changes, AFM examination of various annealed metal films on different substrate materials did not reveal any consistent trends with heat treatments. After heating 5nm iron films (to mimic the two most commonly used nanotube growth conditions of 750°C in argon for ethylene CVD and 900°C with NH_3 for benzene CVD), no discernable trends were observed in either particle height or surface roughness when comparing alumina and silica surfaces (Figure 5-34a). This is not consistent with the diameter results measured in Figure 5-32, where a clear decrease in tube diameter and particles sizes was observed on alumina surfaces (compared to silica substrates). In addition, alumina surfaces with a range of iron film thicknesses (3-10nm) were also imaged using AFM. No correlation was found between film thickness and either surface roughness or particle height (Figure 5-34b), although measured particle width was found to increase with increasing thickness. This was unexpected, as nanotube

diameters were observed to increase with increasing catalyst film thickness (see Figure 5-30a), which suggests that the catalyst particle sizes would also be larger. However, the increasing particle widths observed through AFM could represent a sufficient increase in catalyst size to explain the larger nanotube diameters (and the strong iron-substrate interactions could explain why this increase is only observed in the particle width measurements). In addition, subsequent changes in particle size and shape could occur after the introduction of the hydrocarbon at the start of nanotube growth (this could happen before sufficient nanotube growth has occurred to limit any additional changes), and this AFM study would not be able to measure those variations.

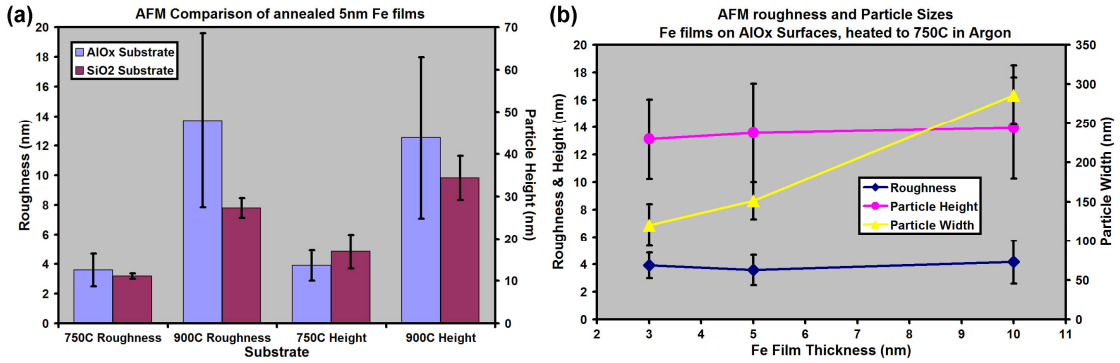

Figure 5-34: AFM surface roughness and particle size trends for 5nm Fe films on different substrate materials (a) and for varying Fe film thicknesses (b)

While AFM imaging did not reveal any clear trends when comparing different substrate surfaces and did not show any correlation between iron film thickness and surface roughness or particle height, a significant difference was observed between those samples annealed at 750°C and 900°C. On both alumina and silica substrates, surface roughness and particle height increased for films annealed at 900°C compared

to 750°C (Figure 5-35a), with a slightly larger increase observed for iron films on alumina (~2.9x for alumina and ~2.2x for silica). Similar increases were also observed for iron films of various thicknesses (Figure 5-35c,d). As with the previous study of catalyst film thicknesses, nanotube diameters grown using these two CVD methods (750°C with ethylene and 900°C with benzene and ammonia) were measured using TEM. The higher temperature (900°C) CVD recipe (with 3nm iron films on alumina surfaces) produced nanotubes with diameters roughly three times larger than those produced using the lower temperature (750°C) ethylene recipe (Figure 5-35b).

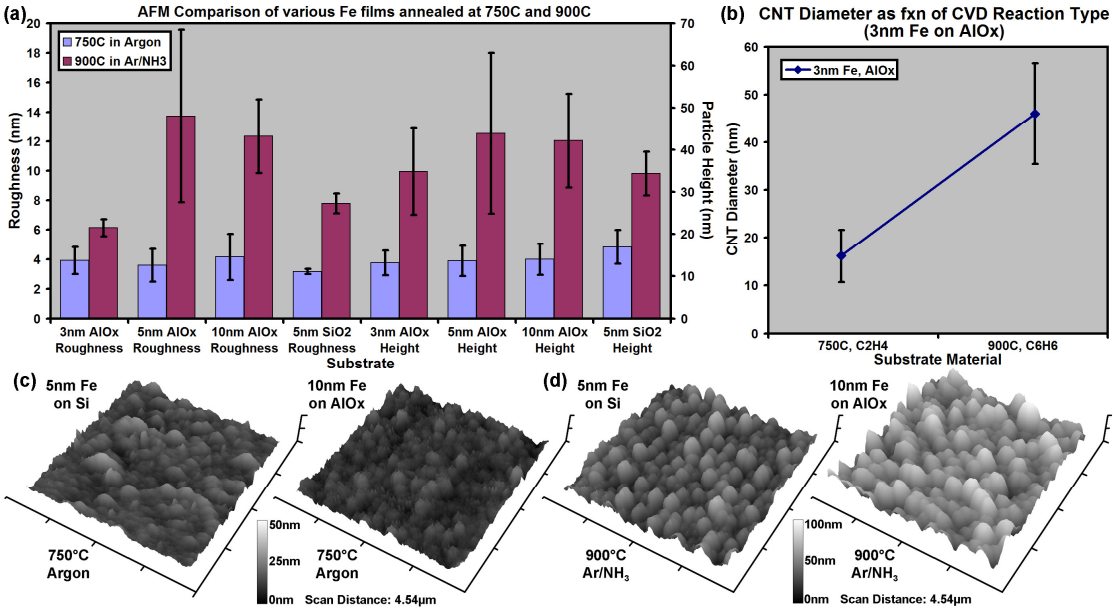

Figure 5-35: (a) AFM surface roughness and particle heights, (b) nanotube diameters using ethylene (750°C) and benzene (900°C), and AFM scans of Fe films after heating to 750°C (c, 50nm scale) and 900°C (d, 100nm scale)

Based on these results, varying reaction temperatures were investigated as a means to control nanotube diameters. Changing reaction temperature can influence nanotubes diameters through two mechanisms. Increased temperatures can lead to

greater particle mobility on the substrate surface, causing metal islands to coalesce into larger catalysts [567-570], and simulations of particle interactions at elevated temperatures have shown that temperature plays a very important role [566]. The temperature at which smaller particles will combine to form larger particles varies with particle size, with smaller metal islands coalescing at lower temperatures. If the particles are in close proximity, this process occurs through the complete coalescence of the particles, while particle growth across larger distances can occur through Ostwald ripening effects. There has been some reported disagreement, however, as to whether this process is limited by the diffusion of metal islands (to come into contact with each other), or by the actual coalescence and sintering of the particles (with some reports suggesting that each of these mechanisms is the rate controlling factor) [571]. In either case, particle coalescence increases with temperature, as does the resulting final particle sizes.

In addition to the catalyst particle coalescence effects, the reaction temperature has to be selected depending on the hydrocarbon used during growth (see Figure 2-19). Nanotubes were grown using ethylene and a range of reaction temperatures; following synthesis, the products were imaged using TEM and nanotube diameters were measured (Figure 5-36).

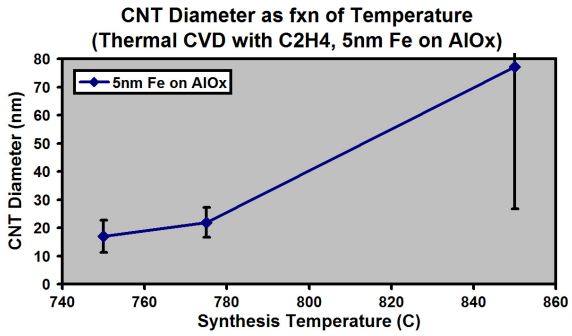

Figure 5-36: Nanotube diameters as a function of reaction temperature (5nm Fe on alumina with ethylene)

For a small temperature range around the optimal growth condition of roughly 750°C (for CVD with ethylene), a small increase in nanotube diameter is observed with increasing temperatures. At temperatures significantly higher than this range, however, a large increase in both nanotube diameter and the standard deviation of the diameters is observed; growth with ethylene at 850°C produces nanotubes with roughly 4 times the diameter and 10 times the deviation in diameter measurements compared to those grown at 750°C or 775°C. At these elevated temperatures, the production of amorphous carbon (from the decomposition of ethylene) is greatly increased (relative to the catalyst-assisted decomposition occurring at lower temperatures). Amorphous carbon can accumulate on many surfaces within the reaction chamber, including the nanotube walls, thickening them through the formation of an amorphous sheath surrounding a graphitic nanotube core (similar to the results shown in Figure 5-28). In addition, the thickness of this amorphous sheath will vary depending on the duration for which the nanotubes are exposed to these conditions. As a result, the nanotube diameter will vary along the length of the nanotube, with the smallest diameters (thinnest amorphous sheath) found in the region

of the tube that was most recently synthesized. Accordingly, tube diameters will be a function of catalyst and substrate properties (influencing inner tube diameters) and of the amorphous carbon deposition rate (affecting the growth time before catalyst poisoning and the outer tube diameter). If catalyst poisoning occurs quickly and prevents any further nanotube lengthening, continued carbon deposition on the tube walls would lead towards thick tubes with smaller diameter variations along their lengths. For reactions in which nanotube growth continues for an extended duration, differences in the amorphous carbon sheath thickness between older and more recently grown regions of the tubes will be more significant, resulting in large deviations of the diameter measurements. The effect of increasing reaction temperature has a much greater influence on the resulting tube outer diameters (through accelerated amorphous carbon deposition) than the tube inner diameters (through larger catalysts due to increased particle coalescence). As a result, the reaction temperature (and carbon source) can be selected to allow the outer diameters of the nanotube product to be controlled relatively independently from the tube inner diameters.

The final reaction parameter studied during this sequence of experiments was the hydrocarbon introduction rate. As shown previously (Figure 5-19), very slow introduction rates can limit nanotube growth, while very fast carbon introduction can reduce the quality of the resulting tubes (observed through reduced Raman G:D peak height ratios). Provided sufficient carbon is present under suitable conditions, nanotube growth speeds will be limited by the diffusion of carbon through the catalyst particles. If carbon is introduced faster than it can be incorporated into nanotube

walls, excess carbon can form amorphous deposits on the reaction chamber surfaces (or it may simply be carried out of the heated zone by the reaction gases and exhausted from the furnace). Similar to the results of increased reaction temperatures, this carbon deposition can poison catalysts and lead to the thickening of the nanotube walls due to amorphous carbon build-up. Increased deposition of this disordered carbon causes the decreased Raman peak ratios observed in Figure 5-19, and also results in an increase in nanotube diameters. As with varying reaction temperatures, this thickening of the tube walls does not affect the inner tube diameter (controlled by the catalyst particle size), and this thickening is also not uniform along the tube length (as there is more time for amorphous carbon to deposit on the regions of the tube that were synthesized first compared to those synthesized nearer to the end of the reaction). An example of this effect is shown in Figure 5-37, for thermal CVD growth with benzene and ammonia. At the fastest benzene introduction rate studied, the outer tube diameter was between three and four times larger than those tubes grown using the slower introduction rates, while the change in the inner tube dimensions was much smaller (less than a thirty percent difference, within the standard deviation). As with the temperature influence study, the deviation in the outer diameter measurements increased with the benzene introduction rates, although this increase was not as pronounced (the deviation roughly doubled at the faster benzene introduction rates compared to a tenfold increase in deviation at the highest temperatures used in Figure 5-36). The use of ammonia in these tests (added to inhibit amorphous carbon

formation with benzene but not needed with the ethylene used in Figure 5-36) is thought to limit this increase by partially removing amorphous carbon as it deposits.

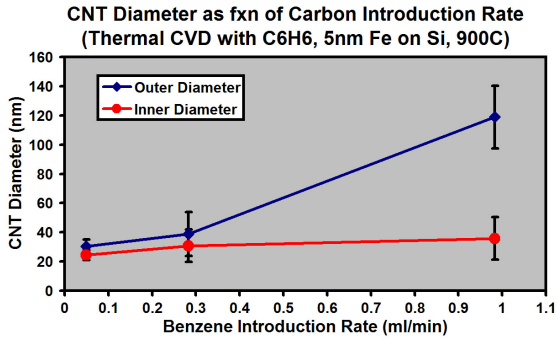

Figure 5-37: Influence of benzene introduction rate on CNT inner and outer diameters

Based on this study of the effects of different reaction parameters on carbon nanotube diameters, several important relations have been identified. In growth environments, which limit the formation of amorphous carbon (lower temperature synthesis with ethylene or ammonia-assisted growth with benzene), the tube diameter can be controlled between roughly 15nm and 85nm, depending on reaction conditions, catalyst film thickness, and substrate material. Larger nanotube diameters were observed with increasing catalyst film thicknesses up to roughly 10nm films; beyond this thickness excess catalyst material accumulated in the nanotube mat, but did not lead to the formation of increasingly larger tube diameters. A substantial difference in average diameters was observed when comparing nanotubes grown using lower temperature methods with ethylene and tubes grown at higher temperatures with benzene and ammonia. This increase occurs through two factors. At higher temperatures metal island mobility on the substrate surface increases, leading to the coalescence of smaller particles into larger catalysts. If the temperature is increased

and the growth conditions are not re-optimized (through the use of ammonia or a different hydrocarbon), the hotter reaction conditions will result in increased amorphous carbon deposition on nanotube walls. A similar result can be obtained by increasing the rate at which the hydrocarbon is introduced. These conditions lead to larger tube outer diameters and wall thicknesses, as well as increased variability in diameters found within a sample. Through selection of a catalyst film thickness and substrate material, the particle size can be influenced, providing control over the inner tube diameters. By adjusting these parameters, along with reaction temperature and carbon introduction rate, the tube inner and outer diameters can then be controlled independently. In addition, while this diameter study was conducted using thermal CVD with thin film catalysts, these trends would also apply to other forms of CVD growth as well. For floating catalyst CVD, the catalyst introduction rate, substrate material, and reaction temperature will influence particle size [146, 409], and high temperatures or carbon introduction rates can increase amorphous carbon deposition.

5.3.2 Ammonia Effects during Growth

For higher temperature thermal CVD growth with benzene, the addition of ammonia (in concentrations of as little as 10-20% in argon by volume) resulted in carbon nanostructures of much smaller diameter than those grown under similar conditions in the absence of ammonia (Figure 5-26). The overall diameter of a carbon nanotube is controlled by a number of factors, including initial catalyst particle size and wall thickness. In order to study the mechanism by which ammonia contributes to smaller diameter carbon nanostructures, thermal CVD was performed with ammonia

introduced at different points during the process. In the first trial, ammonia was introduced only during heating. It is during this step that the thin iron film separates to form discrete catalyst particles, with the size of these particles influencing the resulting nanotube diameters. In the second test, ammonia was introduced only during growth (that is, once temperature was reached and the benzene introduction started). Under these conditions, the effect of ammonia on nanotube wall thickness could be examined. These results were compared to thermal CVD growth with no ammonia and with growth where ammonia was added during both heating and growth. In all these tests, ammonia was added to argon at concentrations of roughly 50 vo.%, and after growth the samples were allowed to cool under pure argon flow. Experiments for growth without ammonia and growth with ammonia only during heating produced very similar results, as did runs with ammonia only during growth and ammonia during both heating and growth. SEM and TEM results for these tests also revealed a significant difference in diameters, and are shown in Figure 5-38.

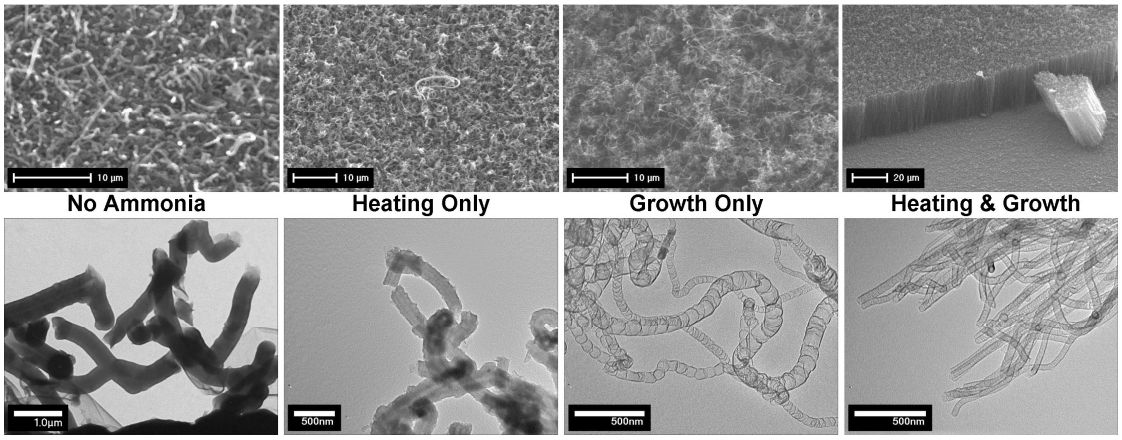

Figure 5-38: SEM and TEM thermal CVD results with ammonia added during different stages of growth

A very thick amorphous carbon layer coating a thin inner nanotube was observed in the results for growth with ammonia only during heating, and this accounts for the large variation in diameter observed between the different samples. The diameter of the inner nanotube in the ammonia during heating only sample is similar to that found in the samples synthesized with ammonia during growth and ammonia during both heating and growth, indicating that the catalyst particles for these runs were of similar size. This suggests that the presence of ammonia during heating has little effect on the particle coalescence and resulting tube diameter. The addition of ammonia during the actual growth (during benzene introduction) is critical and results in a very large reduction in the amount of amorphous carbon byproduct formed on the nanotube surfaces during growth.

A comparison between the Raman spectra for these samples also indicated the strong similarity between growth with no ammonia and growth with ammonia during heating (low G-peak to D-peak widths) and between ammonia only during growth and ammonia during heating and growth (lower G-peak positions), Figure 5-39.

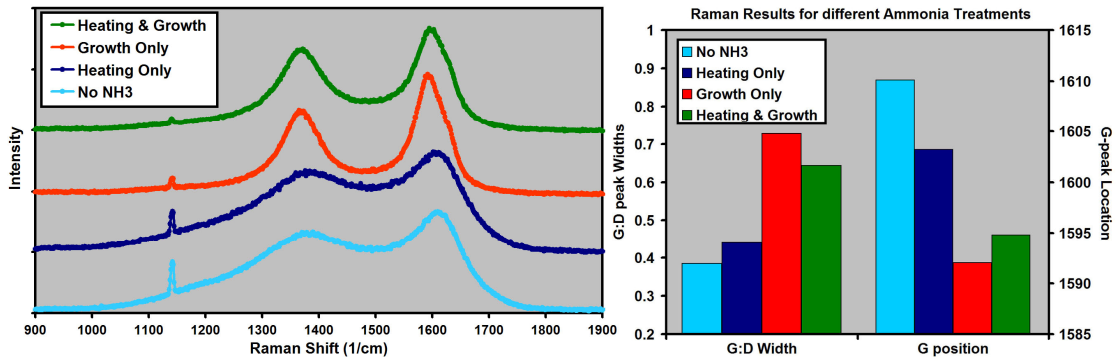

Figure 5-39: Raman spectra for CNTs growth via thermal CVD with no ammonia and ammonia added during different stages of the CVD process

5.3.2.1 Effects of Ammonia Concentration

In addition to studying the effect of ammonia addition at different steps during the reaction procedure, the influence of varying ratios of ammonia to argon was also examined. Thermal CVD tests were performed using a benzene carbon source and with reaction gas mixtures ranging from pure argon to pure ammonia, including several intermediate ratios. Raman spectroscopy was used to characterize the results, and the G:D peak area ratios were then plotted as a function of ammonia concentration, shown in Figure 5-40.

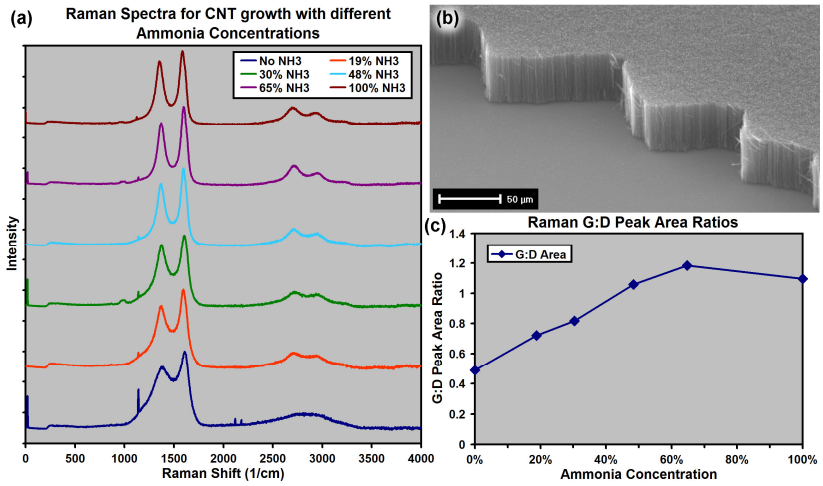

Figure 5-40: (a) Raman Spectra for varying ammonia concentrations, (b) example SEM image of CNT growth at 50% ammonia, (c) Raman G:D: peak area ratios as a function of ammonia concentration

Increasing ammonia concentration (up to ~50%) resulted in increasing G:D peak area ratios, indicating a reduction in amorphous carbon and other impurities and defects. Above 50-65% ammonia, however, no significant further increase in G:D peak area is observed, indicating that above certain levels, excess ammonia provides no additional benefit. SEM examination of the nanotube product grown at the different ammonia levels shows a decrease in length at 100% ammonia compared to

50% and 65% ammonia, suggesting that excess ammonia can be detrimental to nanotube formation.

5.3.2.2 Discussion of Growth Enhancement

The benefits of moderate ammonia concentrations were observed in SEM and TEM analysis and in Raman spectroscopy. In order to examine the mechanism by which ammonia acts to reduce the formation of amorphous carbon, the evolution of ammonia gas in the presence of nano-scale iron or nickel particles at high temperature must be considered. Both iron and nickel can serve as catalysts in either the synthesis or decomposition of ammonia. In the decomposition reaction (under higher ammonia partial pressure relative to N_2 or H_2), ammonia is decomposed on the surface of the catalyst; this leads to the formation of metal nitrides and both nitrogen and hydrogen gas [367]. Experiments were then performed studying the effectiveness of nitrogen and hydrogen on inhibiting the formation of amorphous carbon.

The effect of nitrogen carrier gas was studied first, with thermal CVD growth (benzene carbon source) performed under both pure nitrogen and pure argon atmospheres. These processes produced a very similar product (unaligned, very large diameter carbon fibers), shown in Figure 5-41, suggesting that nitrogen was not the agent responsible for the improvement in nanotube growth. Tests performed with a mixture of nitrogen and ammonia gases produced well aligned mats of nanotubes.

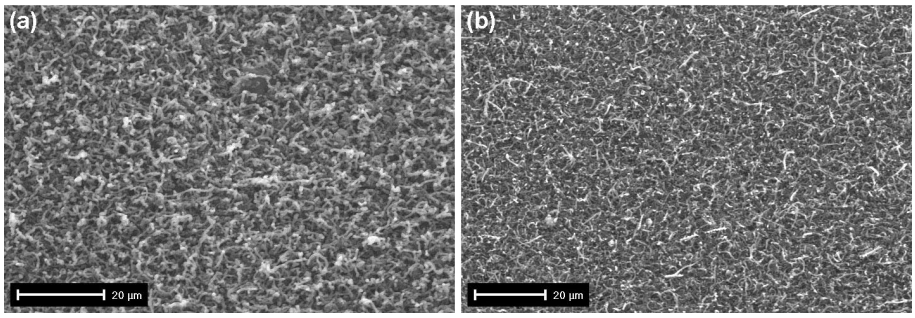

Figure 5-41: Thermal CVD results without ammonia, and with (a) nitrogen carrier gas, and (b) argon carrier gas

The effect of hydrogen was then considered. Mixtures of low concentrations (less than 20vo.%) hydrogen or ammonia in argon were used to grow nanotubes on 5nm iron films on silicon substrates. SEM observation reveals aligned mats of nanotubes produced from the ammonia tests, while the hydrogen tests produced tangled clumps of fibers, Figure 5-42.

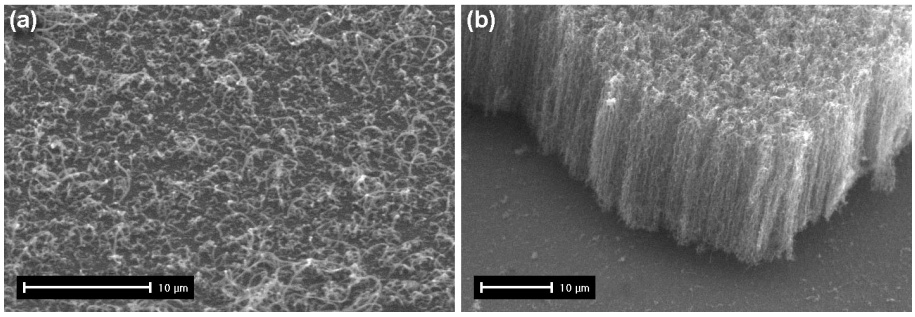

Figure 5-42: Thermal CVD results using a benzene carbon source and an argon reaction gas with low concentrations of (a) hydrogen, and (b) ammonia

Based on the microscopic appearance, the hydrogen added to argon did not appear to improve growth at all. However, these samples were also investigated at the nanometer scale using TEM, and differences between samples grown with low concentrations of hydrogen, ammonia, and pure argon were examined, Figure 5-43. The product formed using thermal CVD with pure argon carrier gas was composed of (relatively) very thick carbon fibers with very poor structure. The hollow core (when

visible) was coated with a thick amorphous coating; as a result of this coating, wall thicknesses approached several hundred nanometers and fiber diameters were roughly 0.5µm. In comparison, the thermal CVD run with small amounts of hydrogen in argon produced much thinner tubes. An amorphous coating was still present on the outer surface of the tubes; however, this coating was much thinner and the average tube diameter was decreased to roughly 100nm. Thermal CVD with even low concentrations of ammonia resulted in a sample, in which nanotubes appeared to be free of any amorphous coating on the surfaces and had distinct bamboo morphology.

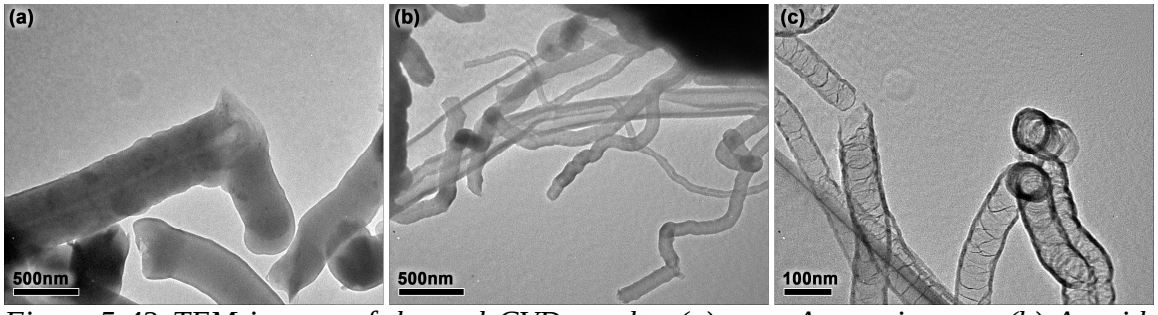

Figure 5-43: TEM images of thermal CVD results, (a) pure Ar carrier gas, (b) Ar with low H_2 concentration, and (c) Ar with low NH_3 concentrations

These results suggest that a small addition of hydrogen to argon is not as effective at eliminating amorphous carbon as a similar small addition of ammonia. However, the significant decrease in amorphous carbon coating thickness observed when comparing samples grown with pure argon and argon with low concentrations of hydrogen (Figure 5-43a,b) indicating that hydrogen does act to suppress the formation of amorphous carbon. The poor results obtained with nitrogen as a carrier gas indicate that nitrogen by itself plays little to no role in etching away amorphous carbon, and the catalytic action of iron or nickel particles on the decomposition of ammonia may result in the more effective etching obtained with ammonia compared to hydrogen.

5.4 Control of Bamboo Morphology

In this work, well-aligned mats of carbon nanotubes have been successfully synthesized using two distinct variations of thermal CVD growth (with both liquid and gaseous carbon sources). Due to the higher temperatures generally used for growth with liquid (C_6H_6) carbon sources, both excessive amorphous carbon deposition and premature catalyst poisoning could occur, and ammonia was used to inhibit these detrimental effects (Sections 5.2.3 and 5.3.2). In addition to reducing nanotube thickening due to amorphous carbon deposition, and prolonging growth to allow aligned mat formation, the use of ammonia was also found to correspond with a distinct change in nanotube morphology. Nanotubes that were grown in an argon environment (by either floating catalyst or thermal CVD methods, using only a carbon and catalyst source) were observed to have straight walls and hollow inner cores, while tubes grown with the addition of ammonia were found to have bamboo morphology, with angled walls and a compartmentalized inner tube structure.

Previous work has indicated that nitrogen can contribute to the formation of this bamboo structure in nanotubes [356-359], and this morphology is clearly observed when nitrogen is added in this work (in the form of ammonia). To verify that nitrogen is the source of this effect, a different nitrogen-containing compound, pyridine (C_5H_5N), was introduced to the synthesis reaction, and the effects of this substance were examined. The use of both pyridine and ammonia was then further investigated to identify how nitrogen contributes to the formation of these bamboo structures, and

experiments were performed to control how this straight walled to bamboo walled morphology change occurred.

5.4.1 Nitrogen introduction via Pyridine

In the previous work, hydrogen was identified as the agent primarily responsible for inhibiting the formation of amorphous carbon. In addition to this major difference, the nanotubes produced with ammonia possessed distinct bamboo morphology, and nitrogen is thought to play a critical role in this process. To further investigate this, nitrogen was introduced in a form other than ammonia; pyridine (C_5H_5N) was added to both thermal and floating catalyst CVD methods, and the morphologies of the resulting nanotubes were studied.

For the first study of nitrogen (introduced as pyridine), a floating catalyst CVD growth approach was used, with a general growth recipe as shown in Table 5-6. In these experiments, pyridine was added in concentrations of 1, 2.5, 5, 10, and 20 percent by volume to a "standard" reactant solution consisting of a mixture of benzene and ~1wt.% ferrocene.

Table 5-6: Floating catalyst CVD growth recipe with Pyridine addition

Growth parameter	Value
Carbon Source	Benzene
Catalyst Source	Ferrocene
Catalyst Concentration	~1.0 wt.%
Nitrogen Source	Pyridine (C_5H_5N)
Pyridine Concentration	0-20 vol.%
Introduction rate	~0.10 ml/min
Argon flow rate	~200sccm
Reaction Temperature	850°C
Substrate	SiO_2

These solutions were then used in floating catalyst CVD processes, and the results were compared to nanotubes grown under similar condition, but without the addition of pyridine. Mats of well aligned nanotubes were produced at all concentrations of pyridine (0-20%), as shown in Figure 5-44.

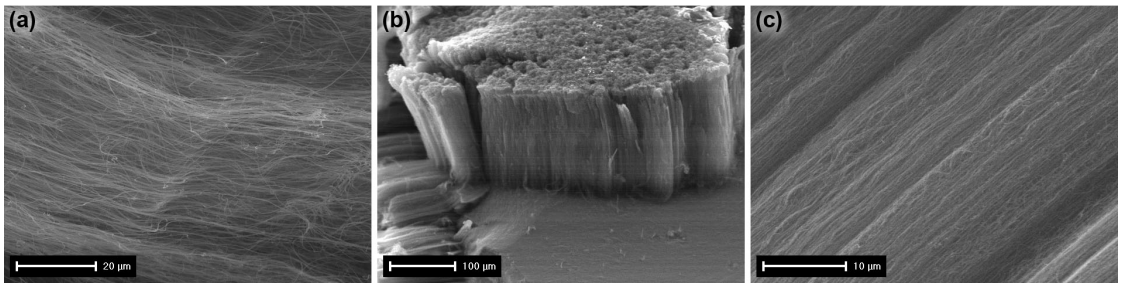

Figure 5-44: (a) Vapor phase CVD growth using benzene with 1wt.% ferrocene, (b) growth with 10vo.% pyridine, and (c) growth with 1vo.% pyridine

Results were similar in appearance at the microscopic level and differences in structure did not become apparent until TEM examination. Nanotubes grown with pyridine had similar diameters to those grown without pyridine; however, the pyridine tubes had bamboo morphology and appeared to have smoother walls, Figure 5-45. The addition of nitrogen (in the form of pyridine) resulted in the formation of tubes having distinct bamboo morphology, which was not observed previously in nanotubes grown via floating catalyst CVD without the addition of nitrogen.

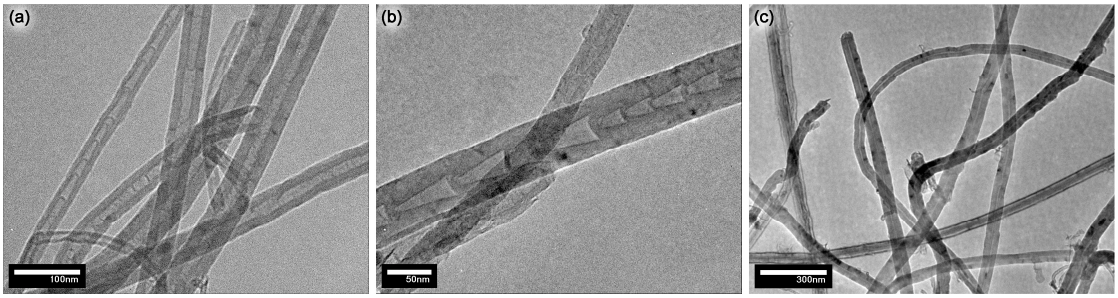

Figure 5-45: TEM images of CNTs grown with ~1wt.% ferrocene and (a) 5% pyridine, (b) 10% pyridine, and (c) nanotubes grown with only benzene

Further TEM examination of these products revealed that the bamboo compartments could be used to determine the nanotube growth direction. In these tubes, the inner compartment walls are angled, forming a triangular shape, and these triangles are all oriented in the same direction along the tube (shown in Figure 5-45b). Through examination of tubes where the catalyst particle could be located, it is clear that these triangular bamboo compartments point towards the growth direction (away from the catalyst particle). Figure 5-46 shows an example of this observation, where the bamboo compartment orientation can be see relative to the catalyst particle position.

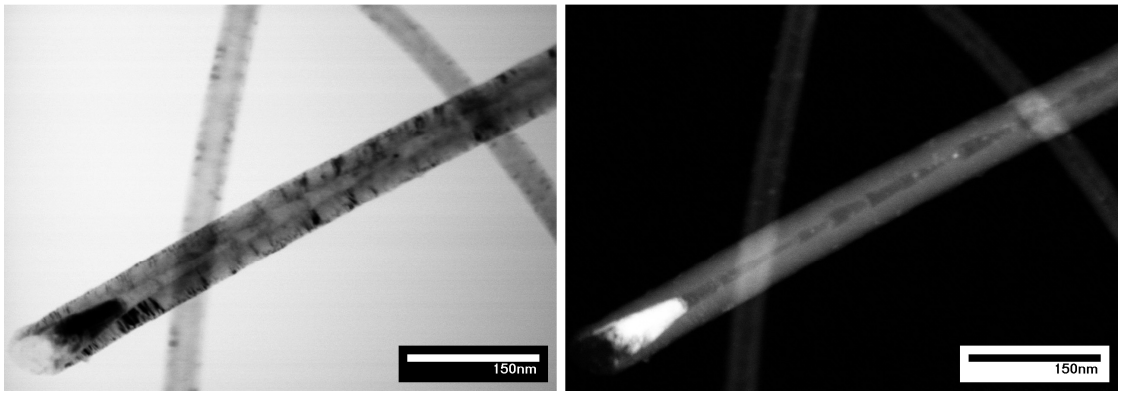

Figure 5-46: Bamboo compartment orientation relative to catalyst particle location: transmission (left) and atomic number-contrast (right) imaging modes.

In addition to this morphology change, a reduction in overall mat length was also observed with the addition of pyridine. There was a significant drop in mat length as the pyridine concentration increased from 0vo.% to 2.5vo.%, but no further reduction was observed with pyridine concentrations ranging from 2.5vo.% to 20vo.% (all other parameters such as reaction time were held equal). In addition to the reduction in length, Raman analysis revealed an abrupt drop in Raman G:D peak

height ratios with even 1% pyridine added; G:D ratios were fairly constant for all runs with some pyridine added (1 to 20%). These results are shown in Figure 5-47.

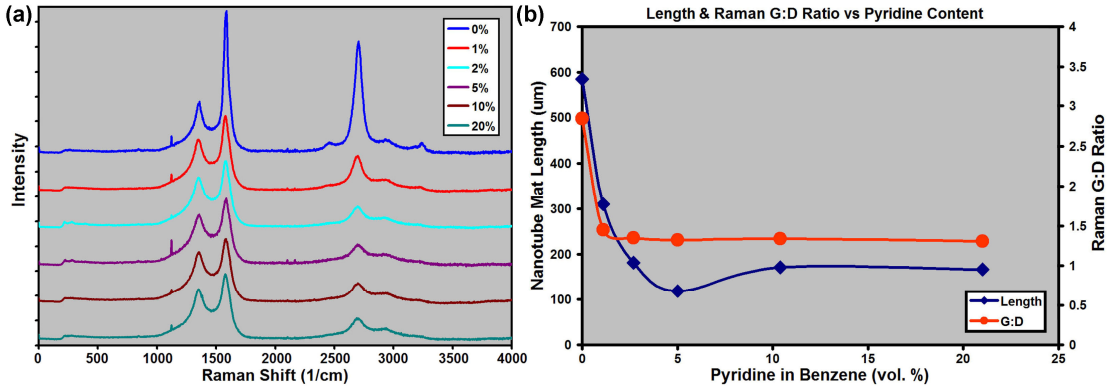

Figure 5-47: (a) Raman spectra for varying pyridine concentrations, (b) Mat length and Raman G:D peak hieght ratio as a function of pyridine concentration

In addition to Raman analysis of the effects of pyridine on nanotubes, temperature-programmed oxidation was also conducted. In these experiments, nanotube samples were heated in a 2% O_2-98% Ar gas mixture, and sample mass was monitored. The burn-off rate was then determined as a function of temperature; these results are plotted in Figure 5-48. Higher burn-off temperatures (increasing stability at elevated temperatures) indicate improved graphitic structure, and, similar to the Raman results, samples grown without pyridine had improved graphitic structure when compared to those grown with pyridine.

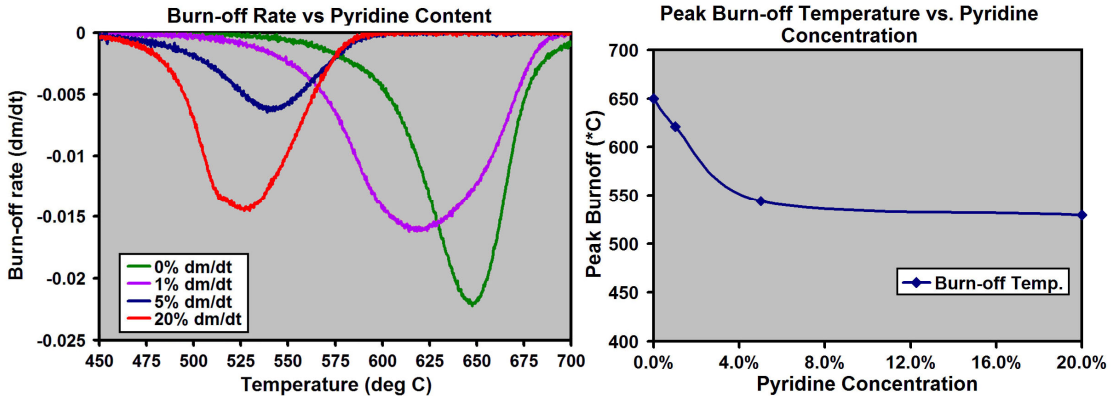

Figure 5-48: Temperature controlled oxidation burn-off rate as a function of temperature and pyridine concentration in reactant solution

The effects of pyridine on nanotube growth for tubes synthesized using thermal CVD methods were also studied. As with the floating catalyst experiments, a general thermal CVD growth recipe was modified through the addition of pyridine; the parameters used are listed in Table 5-7.

Table 5-7: Thermal CVD growth parameters with Pyridine addition

Growth parameter	Value
Carbon Source	Ethylene
Carbon feed rate	~200 sccm
Nitrogen Source	Pyridine (C_5H_5N)
Pyridine feed rate	~0.10 ml/min
Catalyst material	Iron
Catalyst thickness	~5nm
Argon flow rate	~225 sccm
Reaction Temperature	800°C
Substrate	~15nm Al_2O_3 on Si

Similar to the floating catalyst CVD nanotube results, the addition of pyridine to the reaction did not produce any significant changes in appearance at the micron scale. Nanotubes were observed to grow in aligned mats, similar to those grown via thermal CVD (Section 5.2) both with ammonia (synthesis with C_6H_6) and without ammonia (synthesis with C_2H_4), as shown in Figure 5-49.

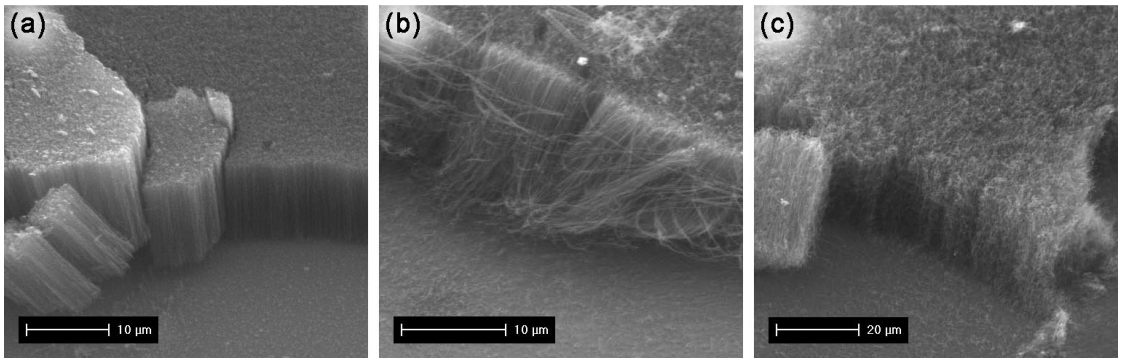

Figure 5-49: Growth of nanotube mats using thermal CVD with C_2H_4 and (a) only argon, (b) argon with ammonia, and (c) argon with pyridine

At the nanometer scale, however (imaged using TEM), the introduction of pyridine led to the formation of nanotubes with distinct bamboo morphology. Although these compartmentalized, bamboo nanotubes could be formed using thermal CVD with the additions of either ammonia or pyridine, the bamboo structure was not identical, as shown in Figure 5-50.

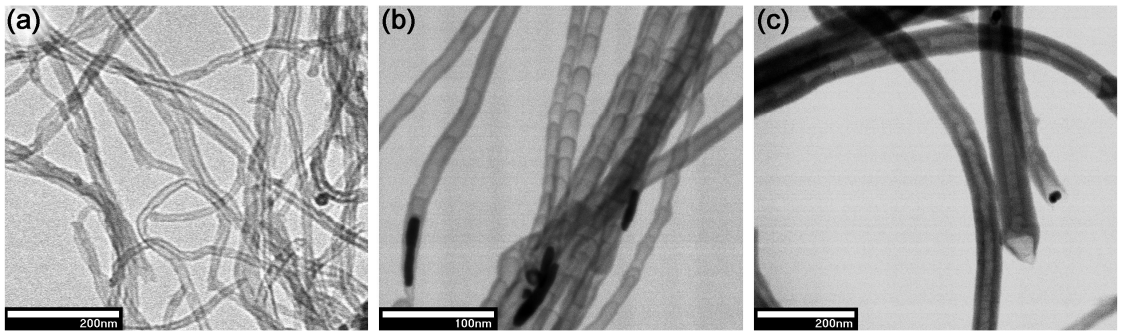

Figure 5-50: Nanotube structures using thermal CVD growth and (a) argon only, (b), argon with ammonia, and (c) argon with pyridine

5.4.1.1 Pyridine and Ammonia Comparison

Nanotubes synthesized with pyridine were found to have thicker walls (wall thickness roughly equal to the inner diameter) for both thermal CVD and floating catalyst CVD methods (Figure 5-51a,b). This is in contrast to those nanotubes

synthesized using thermal CVD with the addition of ammonia, which, while still having a bamboo structure, tended to have much thinner walls (relative to tube inner and outer diameters, Figure 5-51c,d).

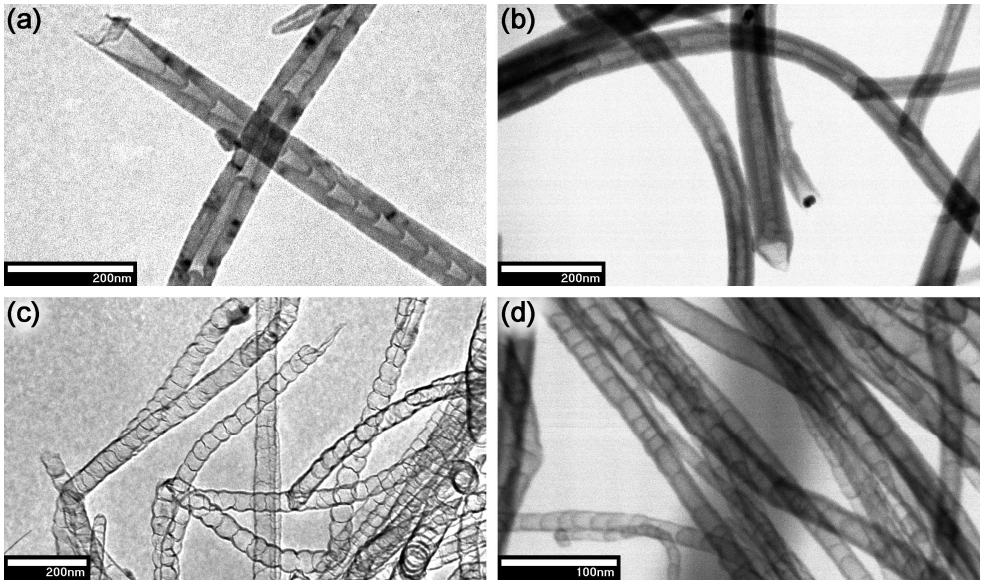

Figure 5-51: Bamboo Nanotubes: (a) floating catalyst CVD with C_6H_6 and pyridine, (b) thermal CVD with C_2H_4 and pyridine, (c) thermal CVD with C_6H_6 and NH_3, and (d) thermal CVD with C_2H_4 and NH_3

The differences observed in the bamboo structures when comparing nanotubes grown with pyridine to those grown using ammonia can be explained by considering the amount of carbon in the reaction. With ammonia, the sole carbon source is the hydrocarbon used (either C_6H_6 or C_2H_4), and only additional hydrogen and nitrogen is introduced (with the nitrogen leading to the formation of bamboo nanotubes, Sections 2.4.6 and 5.4.2). Pyridine, however, also introduces a significant carbon source to the reaction (in addition to nitrogen and hydrogen). Increasing carbon introduction rates have been shown to lead to larger nanotube diameters (Section 5.3.1), and this would likely cause increased diameters as observed with the use of pyridine. In addition,

pyridine decomposes in the same temperature range at which nanotube synthesis occurs, and can produce C_2H_2 as a decomposition byproduct [572-574]. The formation and subsequent decomposition of C_2H_2 at the reaction temperatures used could lead to increased amorphous carbon deposition on the outer tube walls; this would result in the thicker tube walls found when pyridine was included in the nanotube growth reaction.

These thermal CVD results (different bamboo morphologies with ammonia or pyridine) were also checked using floating catalyst CVD. During the initial tests, floating catalyst CVD was shown to produce bamboo nanotubes when pyridine was used as a nitrogen source (Section 5.4.1). Following the thermal CVD synthesis runs, which produced thin-walled bamboo tubes using ammonia and thicker walled bamboo tubes using pyridine, ammonia was also tested with floating catalyst CVD to see if the same wall thickness trends held. Typical floating catalyst CVD growth parameters were used, with ammonia added to form a gas mixture with similar ammonia to argon ratio as used in thermal CVD runs. The growth recipe is detailed in Table 5-8.

Table 5-8: Floating catalyst CVD growth recipe with Ammonia

Growth parameter	Value
Carbon Source	Benzene
Catalyst Source	Ferrocene
Catalyst Concentration	~1.0 wt.%
Introduction rate	~0.10 ml/min
Nitrogen Source	Ammonia (NH_3)
Argon flow rate	~225sccm
Ammonia flow rate	~275sccm
Reaction Temperature	850°C
Substrate	SiO_2

As expected with the addition of ammonia, bamboo nanotubes were formed, and, similar to the trends observed with thermal CVD, the nanotubes synthesized with ammonia had thinner walls than those grown in the presence of pyridine. Typical results from these synthesis runs are shown in Figure 5-52.

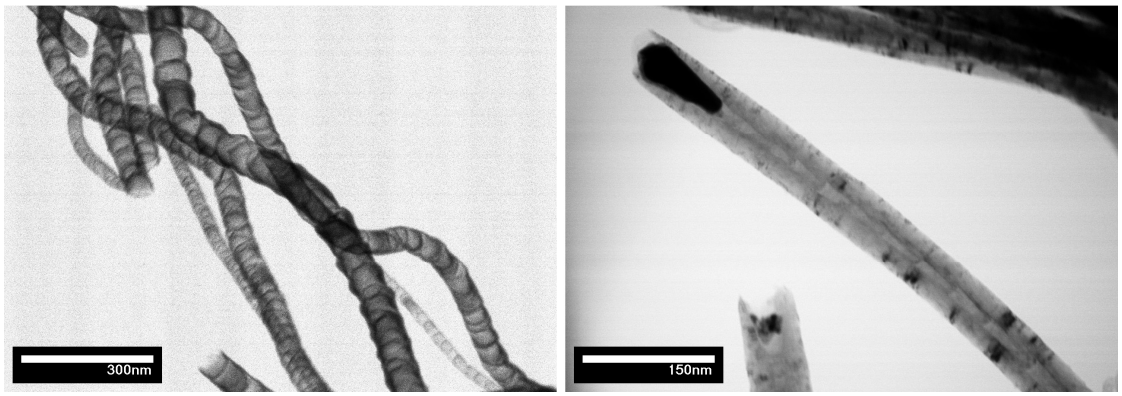

Figure 5-52: Bamboo CNTs grown using floating catalyst CVD with ammonia (left) and pyridine (right)

Using these TEM micrographs, the inner and outer diameters of bamboo tubes grown using either ammonia or pyridine could be measured, and the tubes grown with ammonia were found to have significantly thinner walls (relative to diameter). Ammonia-grown tubes had an average outer to inner diameter ratio of 1.4±0.2 (41.4±12.9nm inner diameters and 56.4±15.5nm outer diameters), while tubes grown with pyridine had diameter ratios of 3.2±0.7 (13.7±4.5nm inner and 43.6±14.8nm outer diameters. These results are plotted in Figure 5-53a.

In addition, the Raman spectra of those tubes grown using these two nitrogen sources can also be evaluated (Figure 5-53b,c). The G-peak to D-peak height ratios were similar for all the pyridine bamboo tubes studied, and the ratio in the ammonia sample was slightly lower still (and all were significantly lower than the ratio for

straight-walled tubes). A similar trend was observed with the 2D- to D-peak height ratios, where tubes grown with between 2vo.% and 20vo.% pyridine had almost equal 2D:D peak height ratios, tubes grown with ammonia had slightly lower ratios, and samples grown with 1vo.% pyridine or no pyridine had higher peak height ratios.

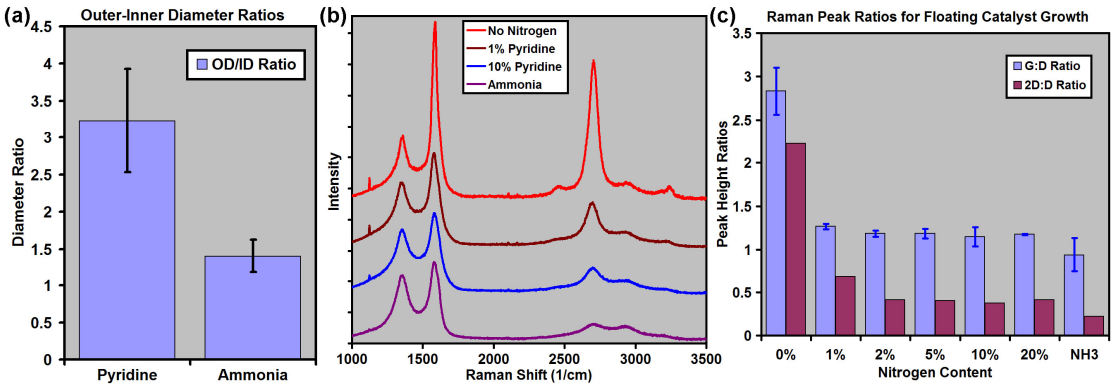

Figure 5-53: (a) Outer diameter-Inner diameter ratios for tubes grown with pyridine and ammonia, (b) Raman spectra for nanotubes grown under various conditions, and (c) Raman G-D and 2D-D peak height ratios

5.4.2 Effects of Nitrogen on Bamboo Morphology

The presence of nitrogen or ammonia has been reported as a key factor leading to formation of nanotubes with bamboo morphology [260, 575, 576]. It has been reported that the determination of nanotube growth with either bamboo or hollow morphology is dependent on the ratio of carbon diffusion over the surface of a catalyst to carbon diffusion through the bulk of the catalyst [211]. Both surface and bulk carbon diffusion can lead to the formation of the outer tube walls; however, high rates of bulk diffusion can produce a graphitic layer on the rear surface of the catalyst particle. This layer will expand and eventually contact the nanotube side walls. It is then “lifted” from the particle by these walls as they grow away from the catalyst; the

process can then start over to form a new bamboo compartment. The presence of nitrogen has been shown to increase carbon diffusion in iron, this would encourage bulk diffusion (and bamboo morphology formation) [369, 370]. The formation of bamboo morphology has also been proposed to occur due to the presence of pentagonal lattice defects in carbon nanotubes (which promote tube closure) [173]. The bond length of carbon-nitrogen is slightly shorter than that of carbon-carbon when comparing benzene and pyridine structures [577]. Nitrogen incorporation into the graphitic lattice could strain the lattice in a similar manner as pentagonal defects, promoting the closure of inner tube layers to form bamboo compartments. These mechanisms are illustrated in Figure 5-54.

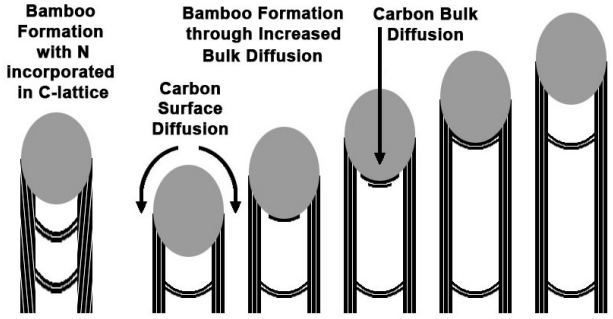

Figure 5-54: Schematics of bamboo compartment formation mechanisms (lattice strain due to nitrogen incorporation and increased bulk carbon diffusion)

In order to investigate the contribution of nitrogen to the formation of bamboo morphology via each of these potential mechanisms, nanotubes grown with various concentrations of nitrogen were examined. Both floating catalyst and thermal CVD methods were studied, with varying pyridine concentrations used for floating catalyst growth, and different ammonia-argon gas mixtures used for thermal CVD. In both

cases, the spacing between subsequent bamboo compartments within the nanotubes was measured.

If the formation of bamboo morphology occurs primarily due to increased bulk diffusion of carbon through nitrogen-containing catalyst particles, then the bamboo spacing would be expected to be relatively independent of nitrogen concentration in the reaction. In this mechanism, the nitrogen in the catalyst particle would reach some solubility limit, and further addition of nitrogen would provide little additional affect once this solubility is reached. Due to the extremely small average size of the catalyst particles used for nanotube growth, solubility would be reach very rapidly even at very low nitrogen concentrations (relative to typical synthesis reaction durations of tens of minutes).

Alternatively, if nitrogen is incorporated into the nanotube walls (inducing strain, which results in the formation of bamboo compartments), then nitrogen would be constantly consumed during the reaction. If this is the dominant mechanism acting during the formation of bamboo morphology, then the presence of nitrogen would be required continuously during growth. Additionally, the nitrogen concentration would be expected to influence the speed at which these bamboo compartments formed. Previously it was observed that increased carbon introduction rates led to increased nanotube growth rates (Section 5.2.1) and increased carbon deposition on tube walls (resulting in thicker tubes, Section 5.3.1). If nitrogen diffuses through the catalyst particle into the nanotube walls, then increased nitrogen concentrations could result in more rapid incorporation of nitrogen into nanotube walls (until diffusion becomes the

limiting factor). Changes in nitrogen diffusion rates would be reflected in changes to the bamboo compartment spacing, as increased nitrogen incorporation into the tube walls result in a decrease in the spacing between adjacent compartments.

Measurements of bamboo compartment spacing were carried out on two series of samples: nanotubes grown via thermal CVD under varying ammonia concentrations (Section 5.3.2.1), and nanotubes grown using floating catalyst CVD with different amounts of pyridine added during synthesis (Section 5.4.1). On average, 85 compartment lengths were measured for each sample, and in all cases a large variation in lengths was observed (particularly for the nanotubes grown using thermal CVD with ammonia). As shown in Figure 5-55, no significant trends were observed between average compartment spacing and the amount of nitrogen used (whether added as ammonia or pyridine).

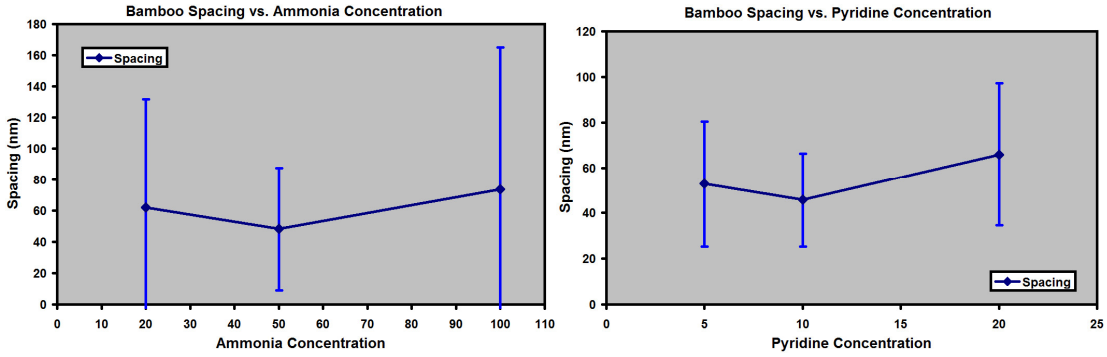

Figure 5-55: Average spacing between adjacent bamboo compartments as a function of ammonia concentration (left) and pyridine concentration (right)

In both proposed mechanisms for the synthesis of nanotubes with bamboo morphology, the catalyst particle size (and corresponding nanotube diameter) can greatly influence the bamboo compartment formation. In the first mechanism, carbon

which diffuses through the bulk of the catalyst particle (rather than around the surface) begins to form a graphitic cap on the catalyst surface inside the tube (shown schematically in Figure 2-35 and Figure 5-54). In order to seal off a section of the inside tube (forming a bamboo compartment), this cap must grow until it contacts the inside nanotube wall, at which point it is pulled away from the catalyst and a new cap can begin to form. The spacing between adjacent bamboo compartments would be a function of the time required for this cap to form (governed by the bulk carbon diffusion rate and the catalyst particle size), and the growth rate of the nanotube (determining the length a nanotube grows during the compartment wall formation process). These inner compartment walls would tend to take longer to form in larger diameter nanotubes (larger inner particle surface to cover), but larger nanotubes also tend to grow at slower rates. For very small tubes growing from very small catalyst particles, the narrow inner diameter may completely prevent the formation of bamboo compartments. In this case, carbon atoms on the small catalyst surface inside the tube could immediately become incorporated into the walls rather than beginning to form a compartment wall.

Bamboo morphology formation under the second mechanism (nitrogen incorporation into tube walls) would also be expected to show a diameter influence. Just as the shorter diffusion distances present in smaller particles generally allow for faster nanotube growth via carbon incorporation into the graphitic wall, nitrogen atoms could also be incorporated into the tubes walls more rapidly. In order to account for the influence of nanotube size, the compartment length values presented in

Figure 5-55 were normalized to the diameters of the tubes being measured. These normalized results are shown in Figure 5-56; however, no significant trends are observed between compartment length and nitrogen concentration.

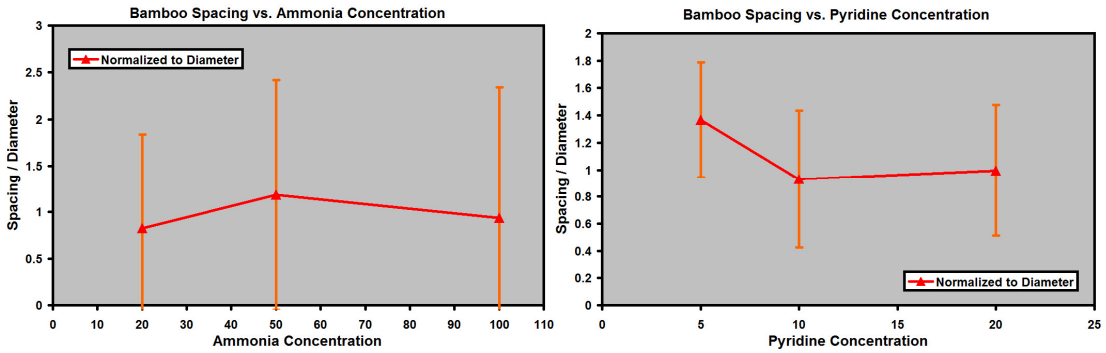

Figure 5-56: Average compartment spacing normalized to tube diameter as a function of ammonia concentration (left) and pyridine concentration (right)

Even when normalized to tube diameter to account for differences in tube size, no correlation is observed between increased nitrogen concentrations (either through ammonia or pyridine addition) and bamboo spacing. Based on these results, it appears that the mechanism acting to produce this compartmentalized structure is not dependent on nitrogen incorporation into the tubes walls (which could be expected to show some concentration dependence), and is instead due to increased carbon diffusion through the bulk of nitrogen-containing catalyst particles.

The bamboo nanotubes grown via thermal CVD using ammonia were typically grown using benzene as a carbon source at relatively high (900°C) temperatures (typical synthesis conditions are listed in Table 5-5). Bamboo nanotubes were also grown by adding ammonia to a thermal CVD reaction using ethylene as a carbon source (Figure 5-51d). The optimal growth temperatures for this thermal CVD

synthesis method were found to be lower than those used with benzene, and this allowed some comparison of the effect of temperature on bamboo morphology formation (although not a direct comparison as the runs were conducted with different carbon sources). Smaller spacing was observed in nanotubes grown at the lower temperature synthesis reaction with ethylene, although a large deviation in the measured compartment lengths was found (similar to the range in spacing distances from the pyridine and ammonia concentration studies above). However, the diameters of nanotubes grown under the cooler, ethylene conditions were substantially smaller than those grown using benzene (15.7±3.5nm vs. 36.9±11.6nm). When normalized to tube diameter, the lower temperature nanotubes show the opposite trend, with larger relative compartment spacing in the smaller diameter tubes (Figure 5-57). As the formation of this bamboo structure is a consequence of greater bulk diffusion (compared to surface diffusion), increased diffusion rates at elevated reaction temperatures could be expected to increase this effect (a more pronounced bamboo structure with more closely spaced compartments). However, as with the comparisons between different ammonia and pyridine concentrations, the large deviations in the bamboo compartment spacing within a given sample make drawing conclusions based on these trends difficult.

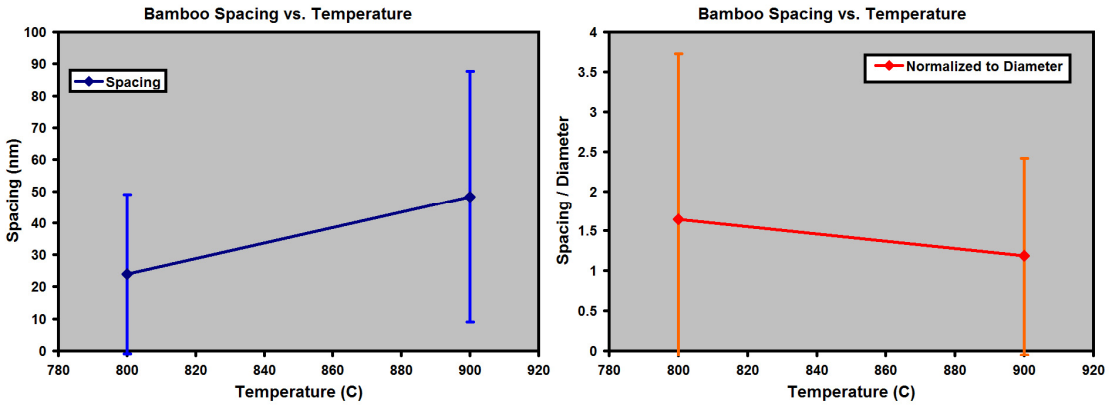

Figure 5-57: Effects of temperature on bamboo spacing (left), spacing normalized to tube diameter (right)

The previous experiments and measurement of compartment sizes revealed no correlation between bamboo spacing and nitrogen concentration (introduced as either ammonia or pyridine). If nitrogen incorporation into the nanotube walls was the mechanism by which these bamboo compartments formed, then a concentration dependent relation could be expected. However, the rate of this nitrogen incorporation could be limited not only by the availability of nitrogen, but by the diffusion of nitrogen through the catalyst particle and into the tube walls. If the range of nitrogen concentrations used on this study was too high to reveal a concentration dependence (if diffusion speed was the rate limiting factor in all tests), then the lack of a correlation between ammonia or pyridine concentration and bamboo spacing would be expected (and the results inconclusive as to identifying the bamboo formation mechanism).

To further investigate these mechanisms (taking into consideration that bamboo formation may be diffusion limited rather than concentration limited), a new experiment was designed to separate the nanotube growth step from nitrogen

introduction step. Silicon wafers were first prepared by coating them with an alumina film followed by a thin layer of iron catalyst (3nm to 10nm, deposited using e-beam evaporation). These samples were heated in an atmosphere of roughly 50% ammonia in argon to 900°C (the reaction temperature commonly used during thermal CVD growth with benzene) and kept at this temperature for approximately twenty minutes. This process was designed to mimic the conditions found during a normal synthesis run just prior to the carbon introduction and allow for nitrogen diffusion into the catalyst particle. Following this gas nitriding process, the furnace was cooled to room temperature in an inert argon environment. After this step, these substrates were used to grow nanotubes using the standard ethylene-based thermal CVD process outlined in Table 5-4. This growth recipe was specifically selected so that synthesis was carried out in an argon environment with no ammonia or pyridine added. Transmission electron microscopy was then used to characterize the products, and bamboo morphology was observed along a continuous length of tube (Figure 5-58).

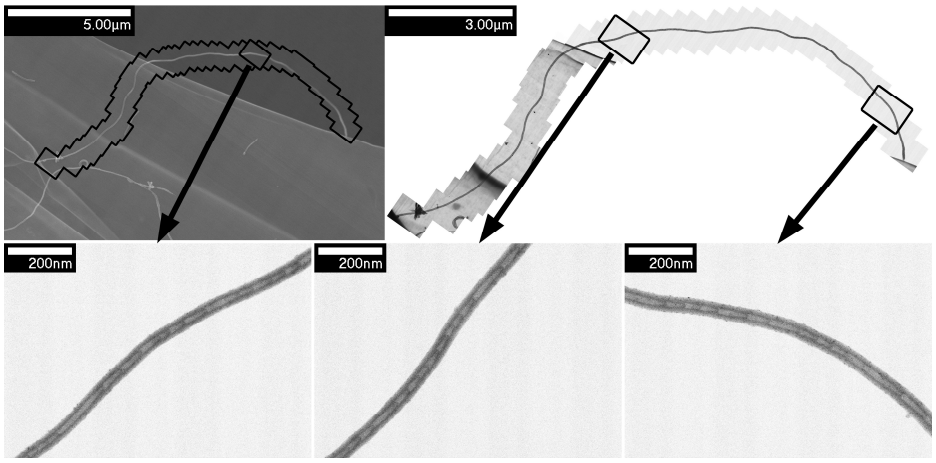

Figure 5-58: SEM and TEM images of a nanotube grown from a nitrogen-containing catalyst particle, magnified views show bamboo morphology

Measurements of bamboo compartment spacing were taken along each tube that could be imaged along a significant portion of its length, and the growth direction of each tube was determined by examining the orientation of the bamboo compartments (as shown in Figure 5-46). Typical results are shown in Figure 5-59, with lower values along the position axis indicating regions of the nanotube further from the catalyst particle (and therefore synthesized earlier during the growth reaction). The bamboo spacing was typically between 50nm and 75nm long, with lengths of occasional compartments reaching several hundred nanometers. While these results were not normalized to diameter as before, the diameters of the tubes studied were similar and very uniform along the tube length (~50-60nm diameter tubes with less than 2nm variation in diameter along their length).

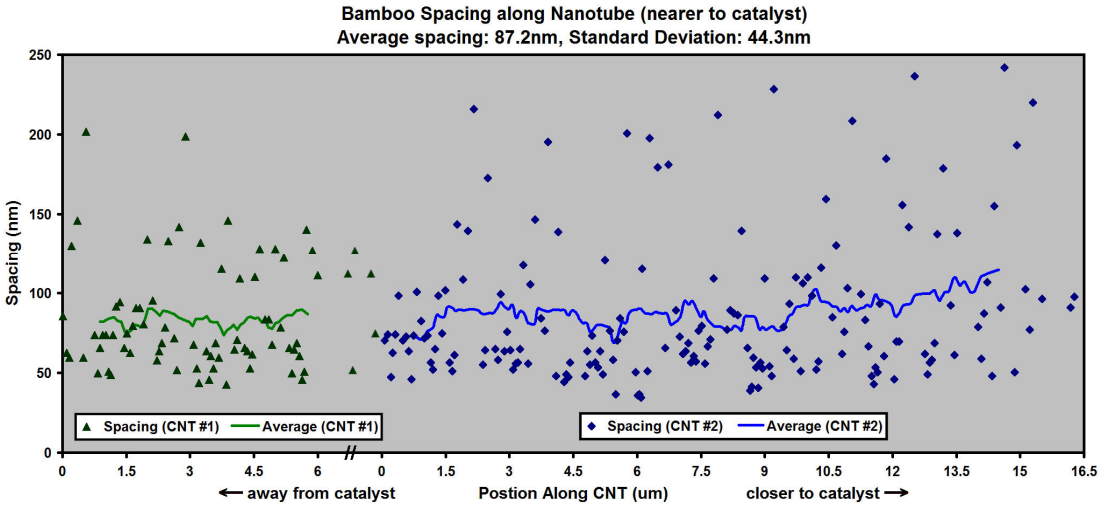

Figure 5-59: Variation of bamboo compartment spacing along nanotube length (measured from nanotubes pictured in Figure 5-58)

When examining the average bamboo spacing along the tube length, no distinct trend is observed (perhaps only a very small increase in spacing when nearing

the catalyst particle in the longer nanotube studied). If nitrogen incorporation into the tube walls was the primary mechanism to form bamboo nanotubes, then the amount of nitrogen remaining in the extremely small volume of the catalyst particle after the nitriding process would be expected to quickly become consumed. In this situation, the nanotubes would begin to grow with a compartmentalized morphology, but as the limited amount of available nitrogen was incorporated into the tube walls, the bamboo spacing would increase and soon transition to a straight walled morphology (once no nitrogen remained in the catalyst particle).

Alternately, if the presence of nitrogen in the catalyst enhances bulk diffusion of carbon through the particle (forming compartments as described in Section 2.4.6), then the bamboo spacing would not change (provided the nitrogen content in the catalyst remained constant). As the data presented in Figure 5-59 indicates no significant trend of increasing bamboo spacing with tube growth in this experiment, it seems that the role of nitrogen in bamboo nanotube synthesis is not related to nitrogen incorporation into nanotube walls. The roughly constant spacing lengths would suggest that nitrogen content in the catalyst particle (and the corresponding carbon diffusion enhancement) remains steady under the growth condition used in this study and for the time period indicated by the length of the nanotube (at least five minutes of growth based on previous results, Section 5.2.1). The slight increase in spacing measured in the second nanotube studied could suggest a small reduction in the nitrogen content as the reaction progressed (perhaps due to nitrogen diffusion into the substrate or tube walls). Some nitrogen diffusion out of the catalyst particle would

likely occur, which, given sufficient time, could change the composition of the catalyst particle enough to influence the morphology of any growing tubes. Based on the current data, however, this trend is not clear enough to draw any substantial conclusions regarding changes in the nitrogen content.

In addition to clarifying the primary mechanism by which nitrogen contributes to the formation of nanotubes with bamboo morphology, these results also hint at significant implications regarding to the nitrogen content of catalysts during nanotube growth. Even without the introduction of any additional nitrogen during growth, it appears that the residual nitrogen content in the catalyst in these experiments was sufficient enough to produce bamboo nanotubes tens of microns long.

5.4.3 Morphological control during growth

We have observed that the addition of nitrogen during the synthesis reaction (either in the form of ammonia or pyridine) can cause the growth of nanotubes with bamboo morphology. In these studies, the nitrogen source was typically held at a constant level throughout the entire growth reaction, producing a sample of tubes with uniform morphology (either a compartmentalized structure in the presence of ammonia or pyridine, or with straight walls in the absence of these substances). Due to the substantial structural differences observed between these morphologies, tubes may exhibit morphologically-dependant material properties. The presence of inner compartment walls could affect the mechanical properties of nanotubes (increased buckling resistance), and the misalignment of the graphitic lattice relative to the tube axis (in bamboo tubes) could affect their electrical and thermal conductivities. Just as

nanotube properties can be influenced through control of diameter, length, chirality, defect concentration, and doping, morphological control could also serve as a means to achieve specific characteristics for potential applications.

In order to further explore this, a series of growth experiments were conducted to attempt to synthesize non-uniform samples containing both straight-walled and bamboo regions. According to the bamboo spacing results (presented in Section 5.4.2), the presence of even a small amount of nitrogen was shown to influence nanotube morphology for a significant duration (with no substantial morphology change over tens of microns of nanotube length). This suggested that a transition from bamboo nanotubes to straight walled tubes would be difficult to achieve, and consequently, these experiments were designed to synthesize straight walled tubes and then transition to growth conditions favoring the formation of bamboo nanotubes.

Experiments were performed using floating catalyst CVD (with the addition of pyridine) and thermal CVD (with either ammonia or pyridine). For floating catalyst CVD, the process for growth with pyridine (Section 5.4.1, summarized in Table 5-6) was modified so that growth was divided into two successive steps. During the first half of the total synthesis duration, only ferrocene and benzene (~0.5 wt.%) reactants were used. At the halfway point of the synthesis, pyridine was added to this solution in a concentration of ~6 vo.%, and the reaction was allowed to continue. The reaction temperature, argon flow rate, and reactant introduction rate was not altered during this transition. Due to the nature of this synthesis method (with continuous catalyst addition), it is difficult to follow a single tube and identify the transition point where

the pyridine was added. However, upon examination of a larger sample of the product generated from individual synthesis runs, tubes were found with both straight-walled and bamboo morphologies (Figure 5-60).

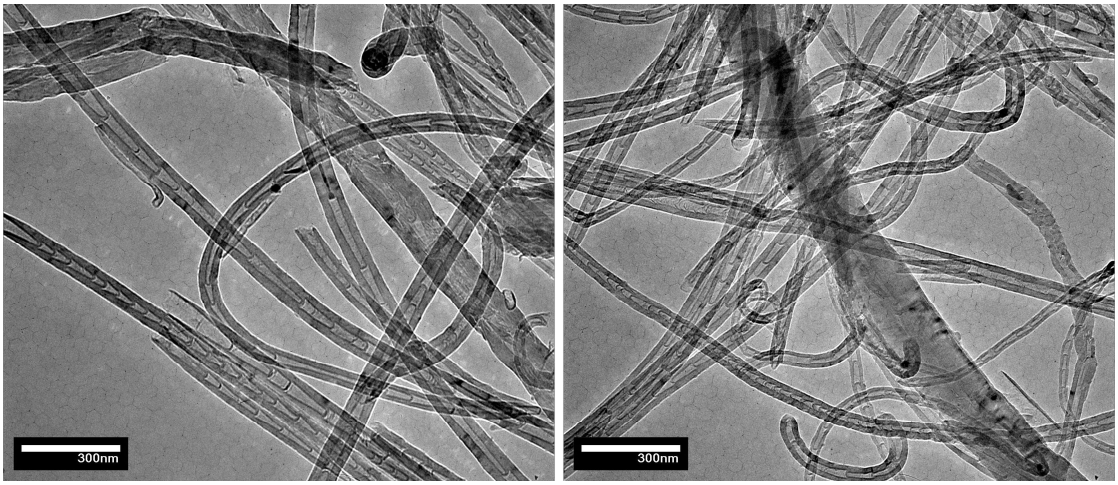

Figure 5-60: Nanotubes grown using floating catalyst CVD with controlled pyridine addition containing tubes with both straight and bamboo morphologies

While this experiment was designed to synthesize straight-walled tubes for some portion of the total reaction time and grow bamboo tubes for the remaining duration, this approach should also work to produce bamboo tube followed by straight-walled tubes, or to alternate between bamboo and straight-walled regions. As additional catalyst material is constantly added with this growth technique, nitrogen-saturated catalyst particles (producing bamboo tubes) can be replenished with nitrogen-free particles as the reaction conditions change (by stopping pyridine introduction, for example). For a short time after this change both bamboo and straight-walled tubes would grow, but as the catalyst particles containing nitrogen became poisoned, only straight-walled tubes would continue to lengthen (and keep growing as more catalyst material is added). Additionally, while only pyridine was

used here, ammonia can also cause the formation of bamboo tubes with floating catalyst CVD (see Figure 5-52); alternating periods of ammonia introduction with periods of growth in pure argon would be expected to produce nanotubes with alternating bamboo and straight-walled morphologies. This approach has been reported previously by Wei *et al.*, where ammonia addition was controlled with floating catalyst growth to produce tubes with alternating bamboo and straight-walled regions [359].

A similar experiment was performed using thermal CVD, where conditions used to grow both straight and bamboo nanotubes were achieved during a single reaction. One of the more successful synthesis recipes for the production of straight walled nanotubes was used for the first part of the reaction, with ethylene as a carbon source, and lower reaction temperatures (775°C). The duration of this phase was kept short (five minutes) to ensure no significant poisoning of the catalyst particles had begun. Following this step, the hydrocarbon source was switched to benzene and the growth condition modified to provide conditions suitable for bamboo nanotube synthesis. Both ammonia and pyridine were used as a nitrogen source for bamboo morphology formation. Ammonia flow (~150sccm) was started as the furnace was heated (to 875°C) and upon reaching the new growth temperature, a ~2 vo.% solution of pyridine in benzene was introduced as a carbon and nitrogen source. TEM examination of the products from this growth recipe revealed both straight-walled and bamboo nanotubes, indicating nanotubes grew in each of the two distinct growth conditions used (Figure 5-61).

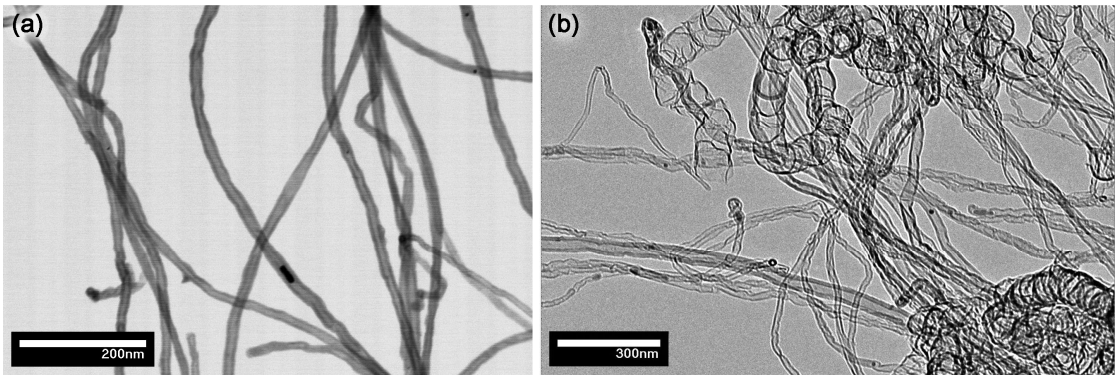

Figure 5-61: (a) straight-walled nanotubes, and (b) a mixture of straight-walled and bamboo nanotubes produced during a single synthesis run

While these results were similar to those observed using the two-stage floating catalyst growth (showing both straight and bamboo nanotubes, Figure 5-60), this thermal CVD process differed in that no additional catalyst was provided. As such, the same nanotubes that began growth with straight walls transitioned to bamboo walls as the growth conditions changed (as nitrogen began to diffuse into the catalyst particles). The synthesis recipe developed succeeded in producing transitions from straight-walled growth to bamboo growth; however, attempts to achieve the reverse (bamboo to straight-walled), or alternating morphologies were not successful, and this is a consequence of the method for catalyst introduction for thermal CVD. Previous work (Figure 5-59) has shown that metal nitride particles will produce bamboo nanotubes even in reaction conditions where no additional source of nitrogen is provided, and that the bamboo spacing does not change substantially during growth. This suggests that switching from bamboo growth to straight-walled growth would only be possible with the addition of new, nitrogen-free catalysts, or by altering the reaction conditions in a way that no nitrogen is present and that the existing nitrogen

in the catalyst particles can be removed. While some methods, such as floating catalyst CVD, could achieve alternating morphologies through the continuous addition of new catalyst material, the thermal CVD approach in this experiment uses only the catalyst present at the beginning of the reaction, and once a sufficient amount of nitrogen has been dissolved in the particles, a transition from bamboo to straight-walled tubes is not possible.

In addition, the two sources of nitrogen (ammonia and pyridine) were added at slightly different times during synthesis, and these have been shown to produce two distinct varieties of bamboo morphology (with thicker and thinner walls, Section 5.4.1.1). As a result, these transitions can be observed within a single tube, as shown in Figure 5-62. The shape and orientation of the bamboo compartments in the thicker walled regions show that these regions grew later in the reaction (they are found closer to the catalyst particle), which is expected, as the ammonia was added prior to the pyridine during growth.

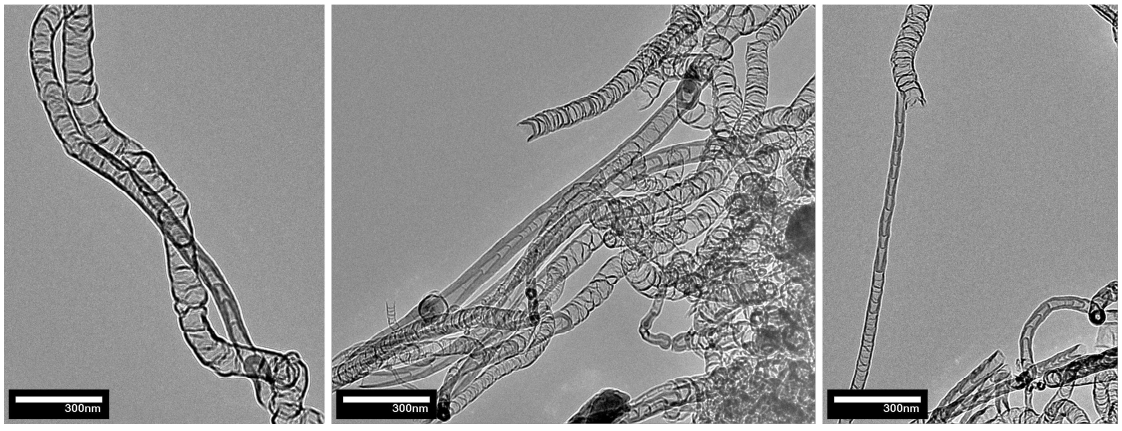

Figure 5-62: Transition from thin walled bamboo morphology (growth with ammonia) to thicker walled bamboo morphology (growth with pyridine) observed along the lengths of individual nanotubes

Raman spectroscopy was then used to characterize nanotube samples containing a mixture of bamboo and straight-walled tubes and to determine if these tubes exhibited Raman characteristics closer to those of pure bamboo or straight-walled samples. For nanotubes grown using thermal CVD procedures, the mixed bamboo and straight-walled sample shown in Figure 5-61 and Figure 5-62 was compared to straight-walled and bamboo nanotube samples using the Raman methods (described in Sections 3.2). Individual peaks were fit to the Raman spectra, and peak height ratios were found, as shown in Figure 5-63.

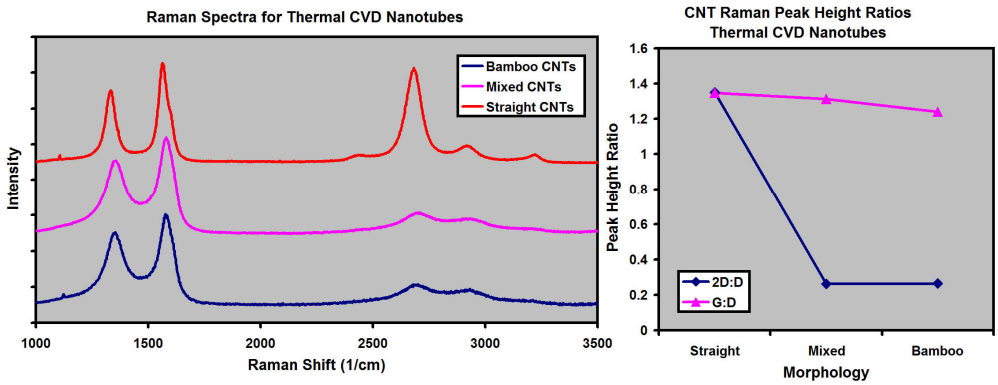

Figure 5-63: Raman spectra comparison between straight-walled, bamboo, and mixed nanotubes grown using thermal CVD

In these samples, the G-peak to D-peak height ratios are observed to slightly decline as the morphology transitions from straight-walled to bamboo walled. A more significant different is observed between the 2D-peak and D-peak heights, where both mixed and bamboo tubes show a much lower ratio than the straight-walled tubes. While the mixed tube sample was expected to show some combination of Raman characteristics of straight and bamboo nanotubes, this mixed spectra appears much more similar to the bamboo spectra (particularly in the 2D:D-peak height ratio). This

similarity can be explained, however, when considering the possible growth mechanism of these samples. Raman spectroscopic measurements were conducted on these samples while the nanotubes were still attached to the substrates (as-grown, in aligned mats). Raman information is only obtained from the top region of these samples, and this region would be either the oldest growth or the most recent growth in the nanotube mat, depending on whether growth was by the base- or tip- growth mechanism (oldest or newest growth, respectively). The mixed morphology sample was grown using conditions producing straight-walled tubes first, followed by conditions for producing bamboo walled tubes (this growth order was also confirmed by examining the compartment alignment, Figure 5-62). If this nanotube sample was synthesized through the tip-growth mechanism, then the most recent growth (growth with bamboo morphology) would be at the top of the mat, and this would be the only region in the sample contributing to the Raman signal. This influence of the growth sequence can explain the similarities between the mixed morphology sample and the pure bamboo nanotube sample. In addition, the exposure to growth conditions promoting straight-walled nanotubes was purposely kept very short (to ensure that the catalyst would not begin to poison before the conditions were changed). As a result, the bamboo synthesis conditions were maintained for a longer time than the straight-walled conditions, possibly leading to a higher ratio of bamboo to straight-walled tubes in the sample.

Raman spectroscopy was also used to compare nanotube samples with different morphologies grown using floating catalyst CVD procedures. This synthesis

method produces a much larger amount of sample during each growth run (as nanotubes are deposited on most surfaces within the reaction chamber, rather than just on catalyst coated substrates). With more sample available, the nanotubes were separated from the substrates and mixed, eliminating any alignment and randomly distributing tubes from the upper and lower portions of the mat. These products were the deposited in thick, un-aligned mats for Raman characterization. As with the thermal CVD samples, nanotubes with straight walls, bamboo walls, and mixed morphology were examined using Raman spectroscopy (Figure 5-64).

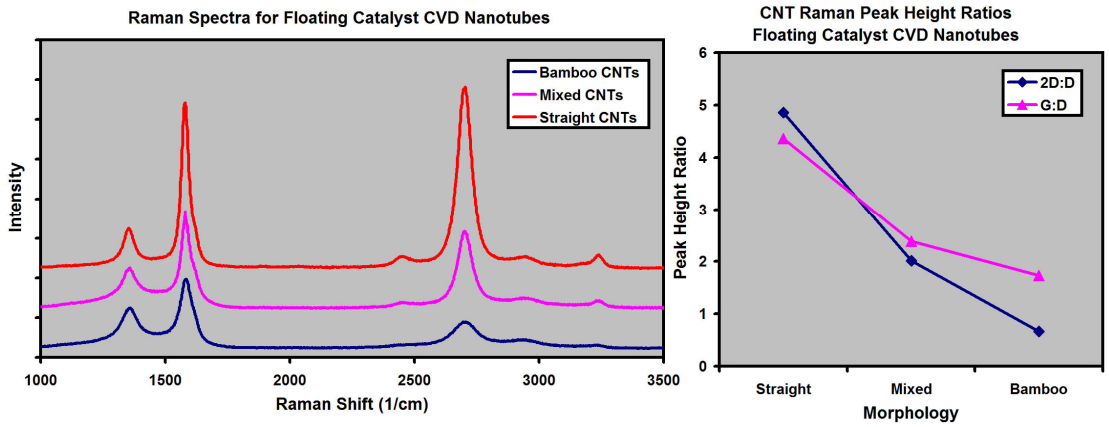

Figure 5-64: Raman spectra comparison between straight-walled, bamboo, and mixed nanotubes grown using floating catalyst CVD

As a result of this preparation method (allowing nanotubes from all regions of the mat to contribute to the Raman signal), the mixed morphology sample showed characteristics (peak ratios, etc.), that were in between those found in the pure straight-walled and pure bamboo samples (Figure 5-64). This approach (comparison to pure samples) could also be used to quantify the ratio of bamboo and straight-walled nanotubes within a mixed sample (for sufficiently randomly-oriented samples). For

example, the mixed morphology nanotubes pictured in Figure 5-60 and whose Raman spectra is shown in Figure 5-64 can be estimated to contain between roughly 25% straight-walled tubes (with roughly 75% bamboo tubes, based on G:D peak ratios) and 32% straight-walled tubes (with 68% bamboo tubes, based on 2D:D peak ratios).

Chapter 5, in part, is a reprint of the material as it appears in:

Deck, C.P., McKee, G.S.B., Vecchio, K.S., “Synthesis Optimization and Characterization of Multiwalled Carbon Nanotubes”, *Journal of Electronic Materials*, v.35, n.2, pp.211-223 (2006)

The dissertation author was the primary investigator and author of this paper.

6. Nanotube Material Properties and Applications

Carbon nanotubes possess excellent material properties (which have been extensively researched, Section 2.3), but these can vary over a wide range depending on many factors, such as the presence of defects, the orientation of the lattice, and the tube dimensions. In order to fully take advantage of nanotubes for their many potential applications, growth must be optimized to reliably produce tubes with specific desired properties. As such, the effects of different synthesis parameters, such as the CVD method used for growth, must be understood. Furthermore, while the properties of individual nanotubes have been widely investigated, other nanotube configurations, such as aligned arrays of as-grown nanotubes, can be important for many applications. In particular, the mechanical properties of nanotube arrays can be markedly different from those of isolated tubes, due to inter-tube forces within the mats, and vary with synthesis method. Properties of larger systems of nanotubes can also vary due to several factors, such as alignment, which are not relevant when characterizing single nanotubes.

In this work, mechanical testing of these nanotube mats was conducted using two distinct approaches (one method used on both floating catalyst- and thermal CVD grown tubes, one only used on thermal CVD tubes). In the first approach, tension and compression tests were performed using a thermal mechanical analyzer (TMA) or a custom-built straining stage for in-situ tests using an SEM. The stiffness of these nanotube forests was measured, and a time-dependent response observed. The second method measured nanotube deflections by monitoring the intensity of a laser beam

transmitted through a nanotube mat exposed to drag forces. This allowed the determination of the flexural rigidity of these mats, as well as provided some information about the optical properties of these tubes. Finally, electrical characterization of tangled nanotube sheets was performed to examine differences between straight-walled and bamboo nanotubes.

6.1 Floating-Catalyst Characterization

Floating catalyst CVD was the first chemical vapor deposition method used in this work and produced large, thick mats of nanotubes (up to several mm thick, see Section 5.1 and Figure 5-5). This size allowed for a number of tests to be conducted, as mat lengths were long enough for tension tests to record measurable displacements, and samples were large enough for testing outside of the SEM.

These samples were tested both in-situ using a SEM and with a Perkin-Elmer Thermo-Mechanical Analyzer (TMA) controlled using Pyris 7^{TM} software. The in-situ procedure was used only for mechanical testing, while the TMA could be adapted to perform several distinct experiments. With the TMA, precise load, position, and temperature measurements could be carried out on small samples.

Compression tests were performed by varying the applied force at a constant temperature. A small initial load was applied, and then the load was increased to a maximum of 1500mN, at rates of 10-50mN.min. With a 3mm probe diameter a stress of only ~0.21MPa could be achieved; this maximum stress could be increased to ~1.9MPa when using a 1mm diameter probe. Nanotube mats were tested with compression applied either parallel or perpendicular to the nanotube axis.

While large mats of nanotubes could be used for compression tests (with test area determined by the probe size), a different procedure was used to prepare samples for tension tests in the TMA. Larger mats were separated from the quartz substrate used during growth, and these were sectioned into smaller pieces with sizes ranging from 3-30mm^2. Rather than the 1mm probe used in compression tests, the top and bottom surfaces of these mats were glued to larger (~15mm diameter) flat, circular supports using very thin layers of glue. The glue layer was kept very thin to avoid wicking of the glue along the long nanotubes. The nanotubes tested in this manner were long enough (>1mm) that the contribution to the stress-strain response by the very thin layer of glue was negligible. These tension experiments were performed with loading applied parallel to the tubes axis; no perpendicular tests were performed. Whether the cross-sectional area being tested was controlled by changing the probe size or the nanotube mat area, the stress-strain response of the nanotube mats could be calculated from the load-position data provided by the thermo-mechanical analyzer. A schematic summarizing the different test procedures used in this work is shown in Figure 6-1.

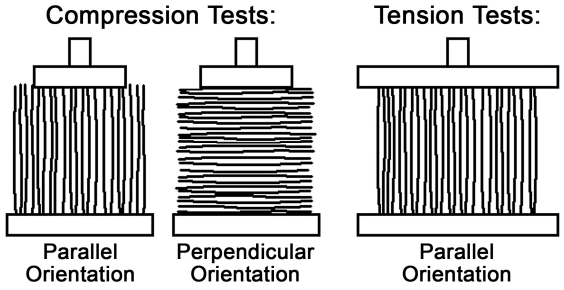

Figure 6-1: Schematic showing compression and tension test configurations, with both parallel & perpendicular orientations

The sample preparation and testing procedures used for in-situ mechanical testing in the SEM were more complicated. Nanotubes were first grown over a substrate area much larger than desired; excess nanotube material was then scraped or "cut" away. An attachment was made to connect to the sample stage within the SEM; this provided a static surface from which the sample could be moved independently. This attachment was designed to hold either a blade (for cutting) or a load cell (for testing) and is shown schematically in Figure 6-2.

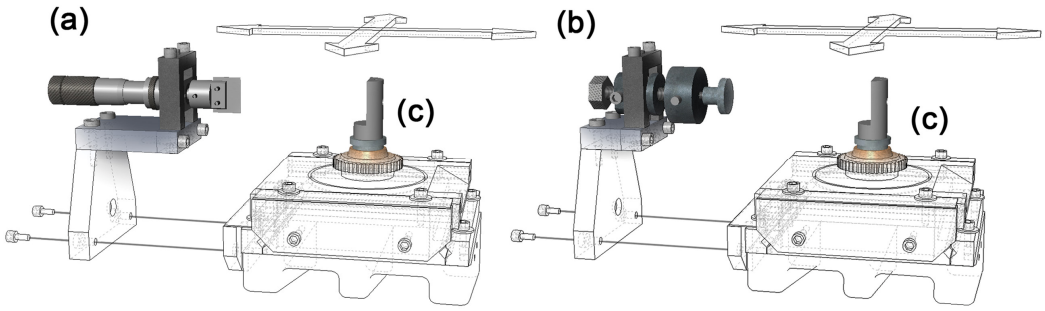

Figure 6-2: SEM Stage Attachment: either the blade attachment (a) or a load cell attachment (b) can be used, sample is held at (c) with rotation and 2-axis motion control independent of blade/load cell attachment

The nanotube mat was first removed from the substrate, transferred to a SEM sample holder, and affixed using a very thin layer of super glue. A rough initial cut was done with a razor blade by hand, and then subsequent, more accurate cuts were done inside the SEM, where the sample was moved against a stationary blade affixed to the stage attachment. The sample was first positioned and then moved into the blade. Once the blade had cut through the entire sample to the substrate, the sample was then dragged laterally away from the blade to remove a portion of the CNT mat. This procedure was repeated for the other side of the sample and then the sample was rotated 90° and two more cuts were made, leaving a rectangular sample of a given

cross-sectional area. Using this procedure, regions were made with dimensions accurate to within ~10µm of the desired size; the cutting sequence used in this process is illustrated in Figure 6-3.

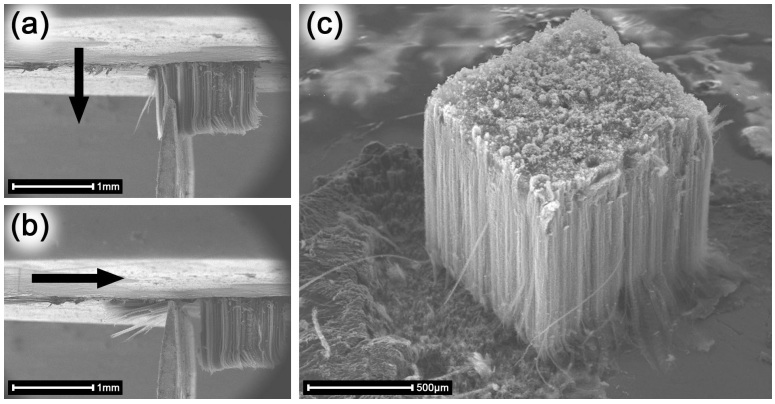

Figure 6-3: Cutting sequence, arrows show sample movement (a) sample is positioned and moved into blade, (b) sample is pulled away from blade, Sectioning off a portion of the CNT mat, (c) example of final cut sample

Once the nanotube mat had been cut to size, the exact cross-sectional area was measured from a SEM image taken looking straight down on the sample. The blade attachment was replaced with a 250g capacity load cell with a flat plate attached to its end, as shown in Figure 6-2b. The sample was then attached to this plate using a thin super glue layer, and strained by manipulating the SEM stage to put the nanotubes in either tension or compression. Calibration of the load cell was achieved by measuring output under a zero load and output under several known loads, and interpolating a linear output-load response. The initial length of the nanotube mats and the compression or elongation at each strain step was measured directly from images taken of the sample in the SEM. This load and position data was then used to generate stress-strain curves.

6.1.1 TMA testing results

Using the TMA, multiple compression tests were performed on the nanotube samples with a 1mm diameter probe, using three testing rates (10, 25, and 50 mN/min) and over a range of loads (200-1500mN). There was very little difference observed between tests run at the three different loading rates, and subsequent tests were all carried out at a single loading rate (25mN/min). Tests were performed with the nanotube samples loaded both parallel and perpendicular to the nanotube axis. From the sample height, probe diameter and load-displacement data, stress-strain curves were calculated.

Nanotubes compressed in the parallel direction typically exhibited an initial linear stress-strain response followed by a region where stress leveled off with increasing strain (Figure 6-4a), while tubes tested in a perpendicular orientation maintained a linear response throughout the entire load range. Results for each orientation were then averaged and the stiffness was obtained; these results are shown in Figure 6-4b.

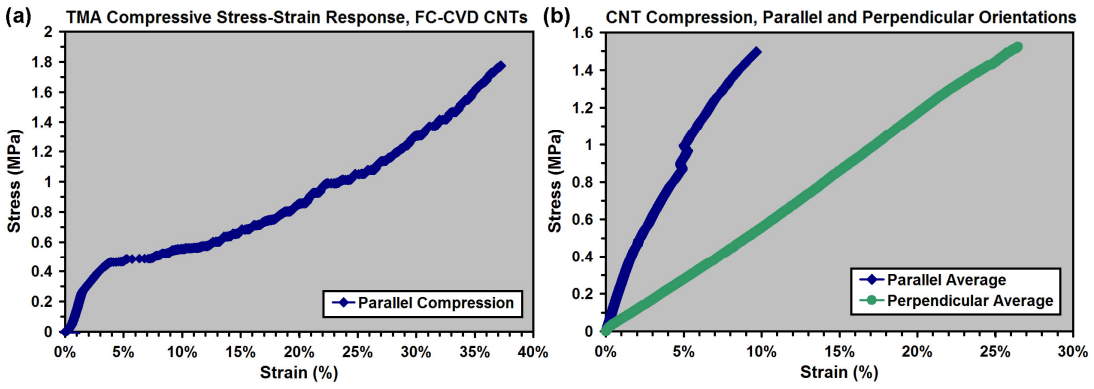

Figure 6-4: (a) Carbon nanotube compressive stress-strain response, loaded parallel to tube axis (b) Average carbon nanotube compressive stress-strain response in both parallel and perpendicular orientations

The stress-strain response of these carbon nanotubes mats was also obtained for tension tests from the load-position data from the TMA, along with the nanotube sample height and surface area. The testing cross-sectional area was dependent on the section of nanotube mat used and thus varied from sample to sample. Multiple tests were run on each sample and were averaged; these results are plotted in Figure 6-5. During the first test with some samples, the initial response showed a very low stiffness, as slack in the system was taken up and kinks in the tubes were straightened. These regions were removed and the beginning of the stiffer response was used as the starting value.

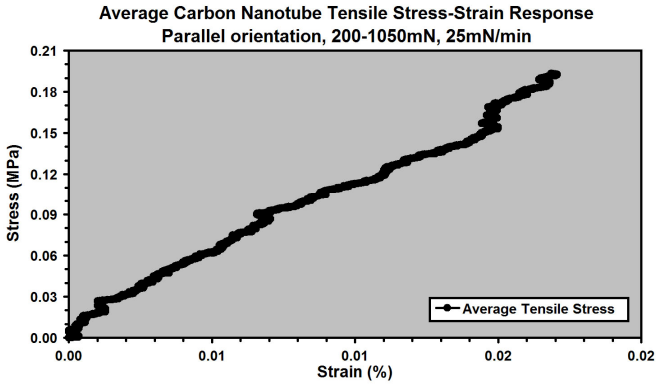

Figure 6-5: Average Nanotube Tensile Stress-Strain response, TMA tests

For both the compression and tension testing done in the TMA, the stress values shown in the plots were calculated using the nominal sample cross-sectional area (either the probe area for compression tests or the sample cross-section for tension tests). However, SEM imaging clearly shows that the nanotube mats are not fully dense, as shown in Figure 6-6a. Measurements based on these SEM images show an estimated spacing of roughly 200nm between centers of adjacent nanotubes. Using this spacing and an average tube outer diameter of 43±20nm and an inner

diameter of ~9.5nm (measured from TEM images, as in Figure 6-6b) the actual tube coverage is ~3% of the measured surface area. This value is in good agreement with volume fractions reported in the literature by other groups, with a 2-3% filling factor found by Yang *et al.* [110] and a 3.6% value reported by Futaba *et al.* [218]. With this correction, the adjusted measured stiffness can be obtained, and was found to be roughly 32.5 GPa, in tension and 750 MPa and 160 MPa in compression (parallel and perpendicular directions). In addition to being much stiffer in tension, these mats were nearly five times stiffer when compressed in the parallel direction compared to the perpendicular direction (750 MPa vs. 160 MPa). Additionally, using a 0.2% offset line, the yield strength of the parallel nanotubes in compression was found to be ~11.5 MPa. A yield strength measurement could not be obtained for the perpendicular tubes, as the stress-strain plot remained linear throughout the entire range (tested up to 44.1 MPa peak stress).

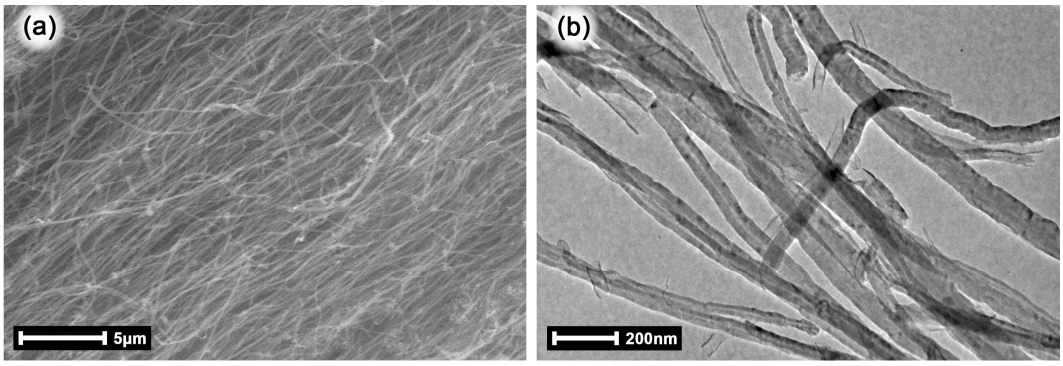

Figure 6-6: (a) SEM image of CNT mat showing low tube density and tube spacing, and (b) TEM micrograph showing tube inner and outer diameter variation

6.1.2 In-Situ testing results

The compression and tension tests were also performed inside the SEM. This allowed for direct observation of the tubes, as well as verification of the TMA results. Strain applied in these tests was controlled by adjusting the micrometers, which positioned the SEM stage. While the micrometer position could be recorded, position measurements could not be read directly from these readings due to slack in the SEM stage, as shown in Figure 6-7. Prior to testing and at each strain step during testing an SEM image was recorded. From the initial image, the starting length was found, and measurements were made at each subsequent step to determine extension or compression strains of the sample.

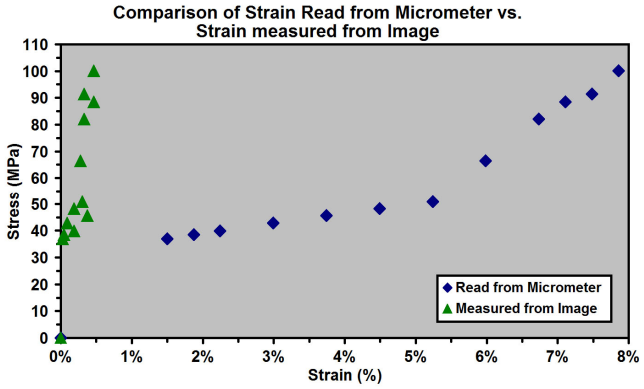

Figure 6-7: Comparison of strain calculated from micrometer position and strain measured directly from nanotube mat sample, tension tests

While this method limited the number of data points obtained, any potential errors arising due to the straining of the glue or slack in the stage were eliminated as only nanotube dimensional changes were measured. The stress-strain response of carbon nanotube mats in both tension and compression is shown in Figure 6-8 (data points from multiple samples are shown in each plot).

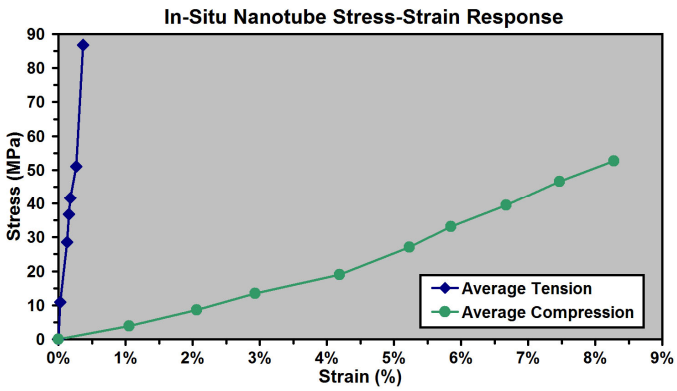

Figure 6-8: In-Situ Carbon Nanotube Tension and Compression Stress-Strain Results (Stresses corrected for actual area)

With both data sets corrected for actual nanotube cross-sectional area (in the same manner as for the TMA mechanical test data), the measured modulus for nanotube mats tested in-situ in the parallel direction is roughly 22.6 GPa in tension and 580 MPa in compression; the results match closely with those results obtained through the TMA (32.5 GPa and 750 MPa), and give average values of 34 GPa and 818 MPa for tension and compression, respectively.

6.1.3 Implications on Mat structure

From the experimental tests performed in this work, material properties of mats of carbon nanotubes in compression and tension were obtained. The stress-strain response of mats of carbon nanotubes was investigated in compression in both parallel and perpendicular orientations, and in tension in the parallel configuration.

In cases where multiple compression tests were run on the same sample, the nanotubes were able to recover a large amount of the strain caused during the previous cycle, indicating that the compression is predominantly elastic. Two samples were subjected to three tests each, and the normalized probe positions at the beginning of

each test are presented in Figure 6-9, showing almost complete recovery of strain for both small and large deformations. A substantial amount of strain (up to 73%) was applied, and even for these large strains the deformation in each preceding test was recovered before the start of the following test. This strain recovery occurs as a result of elastic nanotube buckling, as described previously by Cao *et al.* [78].

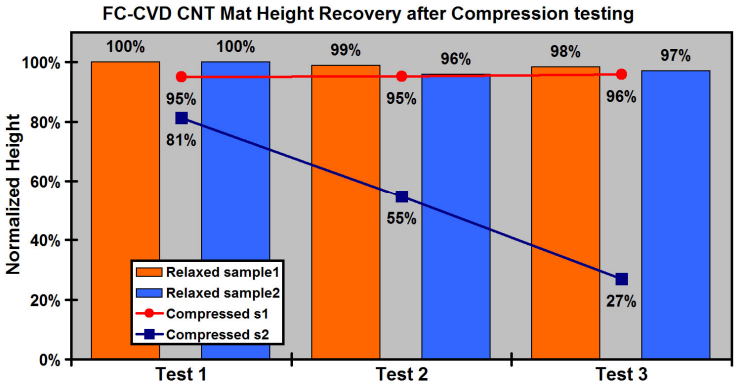

Figure 6-9: Strain recovery in Carbon Nanotube mats between Compression tests, Values next to data points indicate % strain recovered from previous test

The stress-strain results for carbon nanotubes tested in compression in the parallel orientation show a very small stiffness (average combined stiffness in TMA and in-situ tests was ~665 MPa) compared to tensile tests (average of ~27.6 GPa) and to the generally accepted modulus of single-walled nanotubes of ~1TPa, published previously by other groups [50, 51]. This is expected however, as the extremely high aspect ratio of these tubes makes them very susceptible to buckling under compression. The critical Euler buckling load for a pin-ended cylinder with an aspect ratio greater than ~200 is given by Equation (6-1), where P_{cr} is the buckling load, E is the elastic modulus, I is the moment of inertia, and L is the length of the column [578].

The moment of inertia for a thick walled tube is given by Equation (6-2), where r_o and r_i are the outer and inner tube radii, respectively [578].

$$P_{cr} = \frac{\pi^2 EI}{L^2} \qquad (6\text{-}1)$$

$$I_x = \frac{\pi}{4}\left(r_o^4 - r_i^4\right) \qquad (6\text{-}2)$$

Using these Equations, a modulus value of 1TPa, average outer tube diameters of ~40nm, and inner diameters of roughly 10nm (measured in this work and previously [579]), Euler buckling loads were found to be in the order of ~$3*10^{-13}$ N for a single 2mm tube and ~$5*10^{-12}$ N for 0.5mm long tubes. A density of ~25 nanotubes per μm^2 was assumed based on a linear spacing estimate of 5 nanotubes per µm counted on high magnification SEM images as described above. The calculated critical applied load required to buckle a mat of nanotubes under a 1mm diameter probe tip would vary between roughly 0.01mN and 0.1mN (depending on tube length), far, far below the minimum initial applied preload used in these tests. Even with much shorter tubes, the required buckling load is still smaller than the 200mN applied pre-load; 60.6mN would be required to buckle a 1mm diameter mat of 20µm long tubes, for example. These critical values would actually be even lower in the samples used, as the nanotubes tested had some curves along their length and were not perfectly straight. Because the nanotubes begin to buckle before the start of the test, an expected initial stiff region reflecting the actual modulus of the nanotubes themselves (described by Dai *et al.* [464]) is never observed.

The small measured compressive modulus (~580-750 MPa) indicates that the nanotube mats did exhibit some residual strength and resisted additional buckling. Under stresses exceeding the observed yield stress (11.5 MPa) the nanotubes were sufficiently bent that their resistance to further deformation began to decrease. In most cases, the stress levels continued to rise after the yield stress has been exceeded, although a reduced slope was observed. In some samples, however, a stress level was reached where the sample was compressed to very high strain levels with almost no corresponding rise in stress. In these situations, it is believed that this failure is due to large-scale buckling of the entire compressed nanotube mat, rather than the buckling of individual tubes. The results of this large buckling can be seen in Figure 6-10. In these cases, it is believed that with increasing strain a point would be reached where sufficient densification of the mat would occur and the stress would then begin to rise again. However, due to the very low density of these mats, high strains would be required for this to happen, and these strain levels were not reached during this testing.

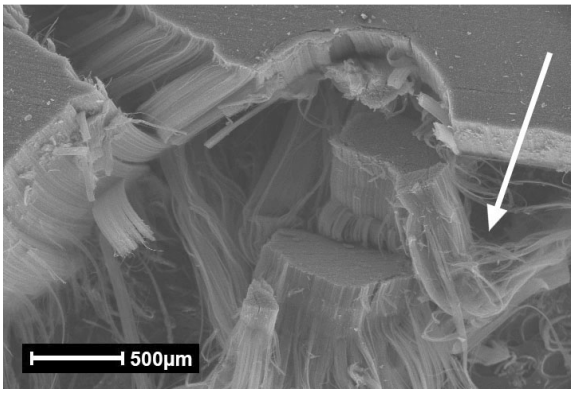

Figure 6-10: Large scale buckling of carbon nanotube mats observed in compression.

While the low observed modulus found in compression tests can be explained by the buckling of these high aspect ratio tubes, this cannot be the cause of the lower

than expected modulus measured in tension. In many cases, the in-situ tension tests ended due to failure in the glue; however, in some tests, the nanotube mats themselves separated. Examples of these types of failure are shown in Figure 6-11(a-b), with an example of glue failure and a sample where the nanotube mat has clearly fractured along its length, rather than at the nanotube-support interface.

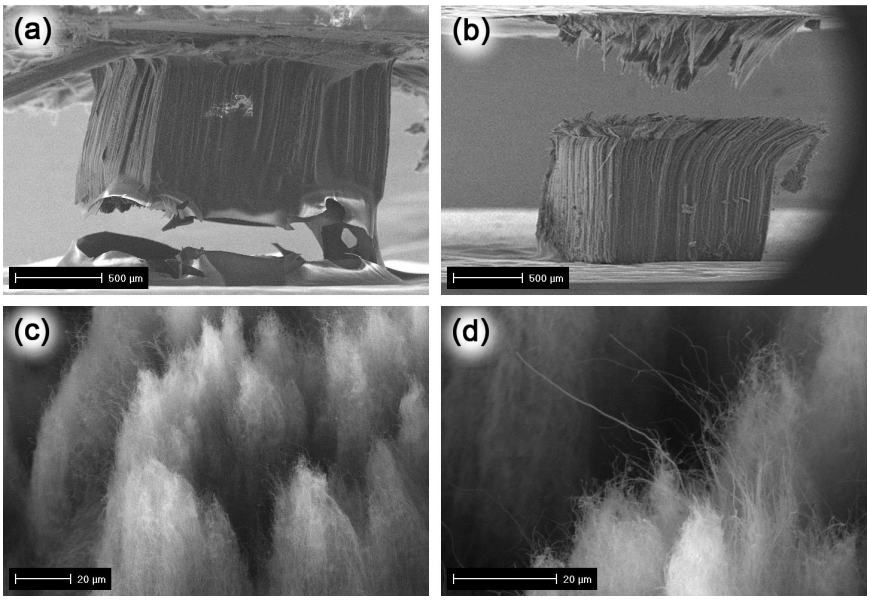

Figure 6-11: (a) SEM micrograph of glue failure, (b) micrograph of nanotube mat after failure under tensile loading, (500 µm scale), (c),(d) failure surface of CNT mat, showing loose nanotube ends caused by nanotube slip and pull-out (20µm scale bars)

The largest stresses applied to these mats during testing was roughly 120 MPa (limited by the capacity of the load cell), far below previously reported values for nanotube tensile strengths (11-63 GPa by Yu *et al.* [57]), suggesting that this failure is caused by another mechanism. A closer examination of the fracture surface of these nanotube mats was conducted and revealed loose nanotube ends, shown in Figure 6-11(c-d). This surface has a similar appearance to failure surfaces of single- and double-walled nanotube bundles loaded in tension, reported previously [196, 580].

Recent work has shown that distinct, separable layers can be formed in the nanotube mat by interrupting reactant flow during the vapor-phase CVD growth process [241, 250]. As these interruptions get shorter and shorter, distinct layers are no longer observed in the product; however, local fluctuations in reactant supply may exist. Very small variations in reactant supply could result in localized growth termination, and while these interruptions would not lead to such obvious layers as observed previously, the nanotubes would still not be continuous along the full length of the mat.

Even assuming a consistent and un-interrupted flow of reactant is provided to the reaction zone inside the furnace, the growth of an individual nanotube can still be terminated due to a loss of catalytic ability in the metal particle. Catalyst assisted nanotube (and nanofiber) growth occurs as carbon continually diffuses into the catalyst particle and is precipitated out in a tube or fiber structure [148, 151]. In order for this process to continue, the carbon diffusion through the catalyst particle must not be interrupted. However, in many CVD growth techniques, an amorphous carbon cap forms a layer on the catalyst particle over time; this process is called “poisoning” of the catalyst and prevents further carbon diffusion [158, 328]. In thermal CVD reactions, where a thin catalyst film is used (with no further catalyst added), the growth rate has been shown to decrease with time and eventually stop, as this amorphous coating builds up [158]. This capping has been observed in the nanotubes grown in this work. However, we have previously shown that relatively constant growth rates are achieved with this method [252]. This suggests that new nanotubes

are continuously nucleating at roughly the same rate as nanotube termination caused by amorphous carbon formation and catalyst poisoning.

As a catalyst becomes poisoned during synthesis, growth of that tube would terminate. However, due to a steady supply of reactants, new tubes would quickly nucleate on the substrate, and would push the earlier tubes up as they grew. This termination and new growth cycle could repeat many times as the nanotube mat grew during the synthesis process. Furthermore, the time required for completion of this cycle would depend on many complicated and uncontrollable factors, such as local reactant supply, local temperature variations, and catalyst particle size (formed from the decomposition of ferrocene or other metal precursors). As a result of these varying factors, there would be a distribution in individual nanotube lengths within the mat.

A nanotube mat composed of many shorter, entangled nanotubes would be considerably more compliant than continuous tubes, as the mat could fail as a result of these shorter tubes sliding past each other and slipping out of the mat. The uneven fracture surface observed in Figure 6-11(c-d) would also be expected for this type of mat structure. In previous work on textiles, broken ends of yarns failing by fiber slippage have been considerably rougher than those of yarns broken by the failure of individual fibers [581]. This discontinuous nanotube mat morphology would also have different mechanical properties than those expected for continuous carbon nanotubes. In these discontinuous mats, stiffness and strength arise from friction and surface forces between tubes, which resist the sliding of adjacent tubes past each other, resulting in a stiffness considerably lower than that of continuous tubes. A better

comparison for the properties measured in this work would be against the properties observed for threads or bundles of many carbon nanotubes, rather than properties of individual tubes. Earlier research on fiber bundles, yarns, and other textiles has shown that failure of these materials takes place in two distinct steps. The yarn is first deformed uniformly until a peak load is reached at the limit of inter-fiber friction. Following this limit, fiber slippage and pull-out begins; these are the primary failure mechanisms in low twist yarns, with fiber breakage increasing relative to pull-out with increasing twist [582, 583]. Additionally, fiber slip in yarns and other textiles plays a greater role at low extension rates (such as those used in these tests); fiber breakage dominates at high strain rates [581]. Several groups have recently reported on the mechanical properties of bundles of nanotubes [196, 580], multi-walled nanotube yarns [213, 263], and nanotube ropes spun into long threads [204]. A modulus of 16 GPa was observed for double-walled nanotube strands [580], 49-77 GPa for single-walled bundles [196], 28 GPa for spun nanotube yarns [204], and a value of 37 GPa for untreated multi-walled nanotube ropes [263]. These values are fairly consistent with the values obtained in this work, ~22.6 GPa for in-situ measurements and ~32.5 GPa for TMA measurements. Tensile strengths were not measured in this work, as either glue failure occurred or the limit of the load cell was reached prior to failure in almost all of the nanotube mats tested. The highest stresses observed were roughly 120 MPa, less than the 460 MPa strengths reported by Zhang *et al.* [204]. It would be expected that the strength of these as-grown mats would be lower than the strength of the spun ropes, as increased twisting angle in yarns has been shown to increase load

transfer between fibers, as well as modulus and strength [515]. However, the modulus values observed in our untwisted mats were close to those reported for twisted ropes; the tangled nature of the nanotubes in our mats (as opposed to the super-aligned mats used for spinning) [263] could perhaps contribute a strengthening mechanism similar to that of twisting.

6.1.4 Time-dependent responses

Due to the nature of this in-situ testing, with strain applied incrementally rather than continuously, time-dependent behavior of these nanotube mats could be observed in between strain steps. The stress on the tubes was found to quickly spike as the strain was applied, and then decrease over the span of a few seconds. This was observed in both compression and tension, as well as during unloading; a plot of these time-dependent responses is shown in Figure 6-12. The time span between strain steps typically ranged between 20 and 30 seconds, during which an SEM image was taken and saved, and the next strain step applied.

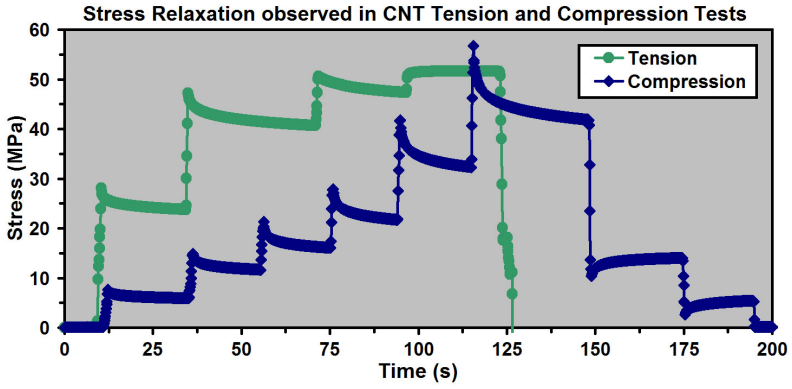

Figure 6-12: Time dependent response of nanotube mats; in the tension test, each strain step is ~0.1% strain, in compression, each strain step is ~2%

The lower observed stiffness in the incremental, in-situ tests compared to the constant strain rate TMA tests has been reported before in a study on the mechanical properties of tendons [584]. Relaxation occurring between incremental strain steps allows for a structural reorganization to better accommodate the load and results in a corresponding drop in stress. Even though relatively low loading rates were used in the TMA testing, the continuous loading was too fast to allow for this reorganization or stress relaxation to occur, and therefore the material behaved stiffer in these tests. The stress relaxation was calculated as a percentage drop from the peak stress for all the in-situ samples, and an average drop of roughly 15% was observed in tension and 22% in compression. To verify the source of this relaxation was actually from the sample, a compression test was run without a nanotube sample (using just the aluminum sample holder); an average relaxation of ~5% was measured, suggesting that while some of this effect may arise from the equipment used, the nanotube mats themselves contribute most of this relaxation. As tests run with continuously increasing loads do not allow any of this relaxation to occur, by removing the effect of this relaxation, a better comparison can be made between data from the incremental and continuous tests. This is accomplished by dividing the peak stresses (from which our stress-strain plots were generated) by the average fraction of stress remaining before each subsequent strain step; a summary of these corrected and the uncorrected values, as well as values from literature are presented in Table 6-1. A small amount of stress relaxation was also observed in the yarns spun and tested by Zhang *et al.*, of roughly 15% of the load, with most of this relaxation taking place in the first 20

minutes [204], and stress relaxation has also been observed in sheets of entangled nanotubes, with a decay of 0.1 MPa [585].

Table 6-1: Summary of modulus results for nanotube mats. Corrected in-situ results have been adjusted to remove stress relaxation effect. Relaxation data has been corrected for the small (~5%) relaxation due to equipment used.

Orientation	Test Procedure	Modulus (GPa)	Relaxation (%)
Tension	In-Situ (Incremental)	22.6	10
	Corrected In-Situ	26.6	…
	TMA (Continuous)	32.5	…
	In-Situ & TMA Average	27.6	…
	From Literature	16-77 [196, 580]	15 [204]
Compression	In-Situ (Incremental)	0.58	17
	Corrected In-Situ	0.74	…
	TMA (Continuous)	0.75	…
	In-Situ & TMA Average	0.67	…

From the time-dependent stress relaxation observed, the relaxation modulus can be calculated for these nanotube mats in both tension and compression using Equation (6-3); this data can then be fit to the Maxwell model [586] used to model polymer deformation responses (time dependent stress is given using Equation *(6-4)* as a function of the time constant).

$$E_r(t) = \frac{\sigma(t)}{\varepsilon_0} \qquad (6\text{-}3)$$

$$\sigma(t) = \sigma_0 e^{-t/T} \qquad (6\text{-}4)$$

Relaxation modulus and Maxwell fits are plotted in Figure 6-13a-c and average modulus and time constants were 28.9 GPa and 5.94s, 266 MPa and 3.72s, and 1.74 MPa and 3.84s, for tension, compression, and unloading, respectively. The small time constant is reasonable, as the stress relaxation occurred very rapidly after each strain step. In addition, the stress relaxation modulus is found to increase as a function of

strain (shown in Figure 6-13d), suggesting that with increased deformation the ability of these nanotube mats to reorganize to accommodate strain is reduced.

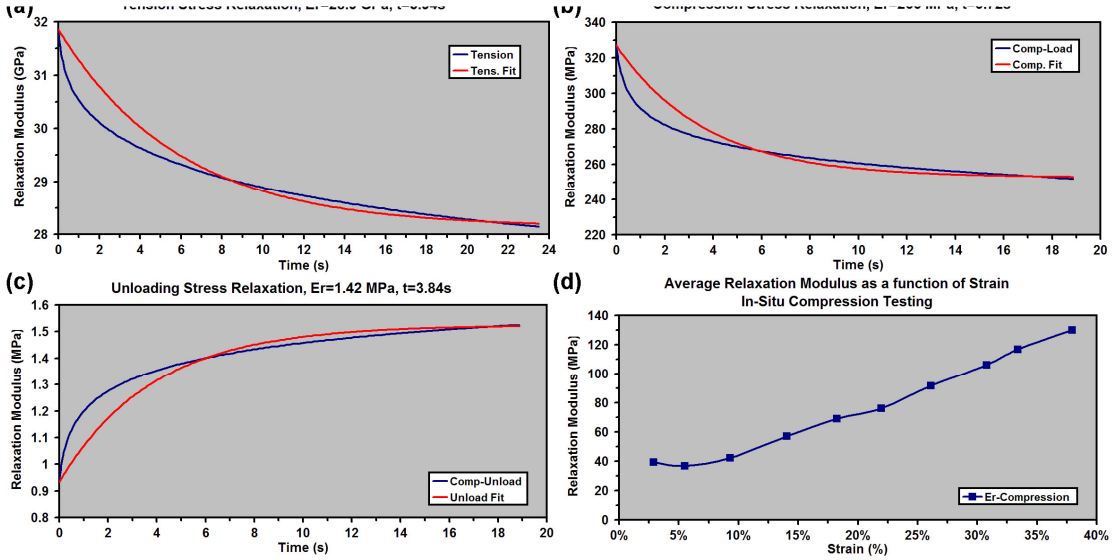

Figure 6-13: (a), (b), and (c) Maxwell Stress relaxation plots for tension, compression, and unloading, (d) Relaxation Modulus plotted against strain for two compression tests

6.1.5 Electrical Resistance of CNT paper

Many of the remarkable material properties of carbon nanotubes are due to their unique bonding, equivalent to a graphene sheet rolled upon itself. For multi-walled nanotubes, properties will be influenced not only by the structure of each concentric shell within the tube, but also by the bonding between shells (equivalent to bonding in the c-direction in the graphitic lattice). In graphite, there are substantial mechanical, thermal, and electrical differences between this in-plane and out-of-plane bonding, with increased stiffness, strength, and electrical conductivity along the in-plane directions. In ideal single-walled carbon nanotubes, this is the only bonding present, and this is the source of the incredible properties reported for this material. In

multi-walled tubes, the weaker bonding between concentric shells can lead to reduced performance, such as failure via the sword-in-sheath mechanism under tensile loading. However, electrical conductivity can still be very high, as well as strength and stiffness, provided loading is carefully applied only to the outer shell. In any type of nanotubes, the presence of defects can reduce these material properties, and these defects can be either naturally occurring or can be induced through artificial means [587]. Careful control over the types and concentrations of defects could be used to tailor the properties of carbon nanotubes for use in specific applications. While post-processing methods for defect introduction were not specifically addressed in this work, the control of the nanotube morphology (for growth of either straight-walled or bamboo nanotubes) was investigated (Sections 5.4 and 5.4.3). In bamboo nanotubes, the in-plane direction of the graphitic lattice is oriented at a slight angle relative to the tube axis (as opposed to a parallel orientation found in straight-walled tubes). For nanotubes with this morphology, control over the material properties could be accomplished using a range of approaches, including the influence of bamboo spacing and lattice angle relative to the tube axis, and through control over tube morphology along the length of the tube (transitioning from straight to bamboo morphologies). In addition to controlling the structure of the nanotubes themselves, the purity of a nanotube sample will also affect the overall properties of any bulk nanotube-based materials. In particular, the presence of high quantities of amorphous carbon or residual catalyst material within a sample could have a detrimental effect on the material properties.

In this investigation of the effects of nanotube structure and purity, nanotubes were processed into nanotube paper samples. The fabrication of these paper materials involved several steps. First, as-grown nanotubes were removed from the reaction substrates, weighed, and mixed with ethanol at a concentration of ~0.32mg/ml. This mixture was then agitated ultrasonically to break-up the aligned nanotube mats and to create a nanotube suspension. The use of ethanol in this process allowed the nanotubes to remain suspended for a sufficient time (as compared with water, where the hydrophobic nanotubes would rapidly clump together). Although nanotubes eventually settled out of these ethanol suspensions, the use of surfactants (such as sodium dodecyl sulfate) which could allow more permanent suspensions (remaining for weeks rather than hours), this approach was avoided, as some surfactant residue could remain in the nanotube paper after fabrication. Once the nanotube suspension had been prepared, it was transferred to a burette and dispensed into a mold consisting of a short, vertical length of pipe (~11mm inner diameter) pressed against a piece of filter paper. The nanotube suspension was then vacuum-filtered through the paper and allowed to dry, leaving a sample consisting of randomly aligned nanotubes supported on a paper substrate (Figure 6-14a,b). The volume of solution used was controlled to produce samples containing a desired mass of nanotubes (ranging from roughly 0.1mg to 3.2mg per sample).

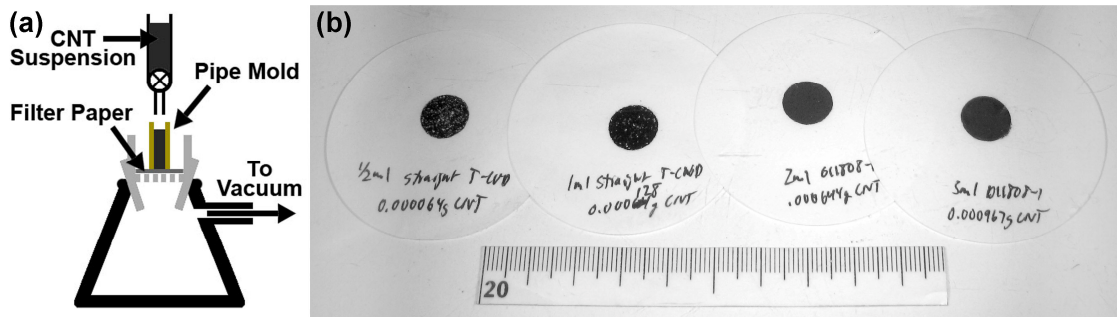

Figure 6-14: (a) Schematic showing fabrication of (b) carbon nanotube paper

Following this process, a simple two-point electrical resistance measurement was taken on each sample (using a similar approach to that described in [109]). Three different measurements were made; first the effects of different probe spacing were examined (to identify the contact resistance), and following this, measurements and comparisons were made between samples with different morphologies and samples that were grown with different catalyst concentrations. The initial test of resistance as a function of probe spacing indicated that there was significant contact resistance, even when the probe spacing was reduced to minimize the path length through the nanotube paper (Figure 6-15). In these cases, contact resistance dominated, rather than actual sample resistance. However, for larger probe spacing (over 7-8mm), inconsistent results were obtained for those samples with very small nanotube contents (below ~0.2mg). Consequently, an intermediate probe spacing of 5mm was selected for the remaining measurements.

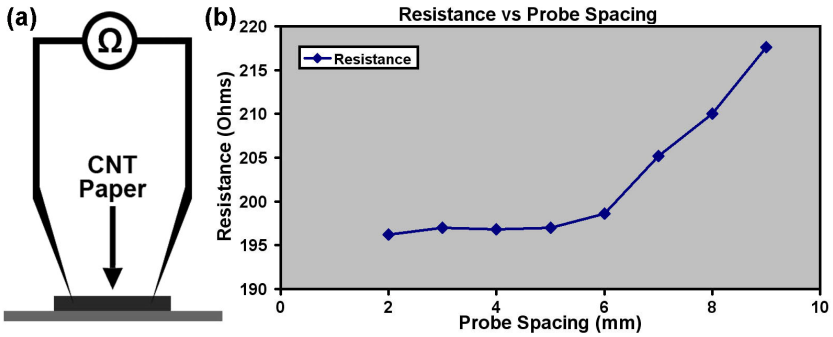

Figure 6-15: (a) Two-point resistance measurement schematic, (b) CNT paper resistance as a function of probe spacing

Once a suitable probe spacing was established, two studies were performed to investigate the effects of iron catalyst concentration and the effects of nanotube morphology. Increasing catalyst concentrations in floating catalyst CVD growth has been shown to result in increased metal content in the sample [588], and increased quantities of non-nanotube material in the products (such as iron particles covered in amorphous carbon shells). These impurities can increase the contact resistance both between the test probes and nanotubes and between adjacent nanotubes within the paper sample (Figure 6-16a,b).

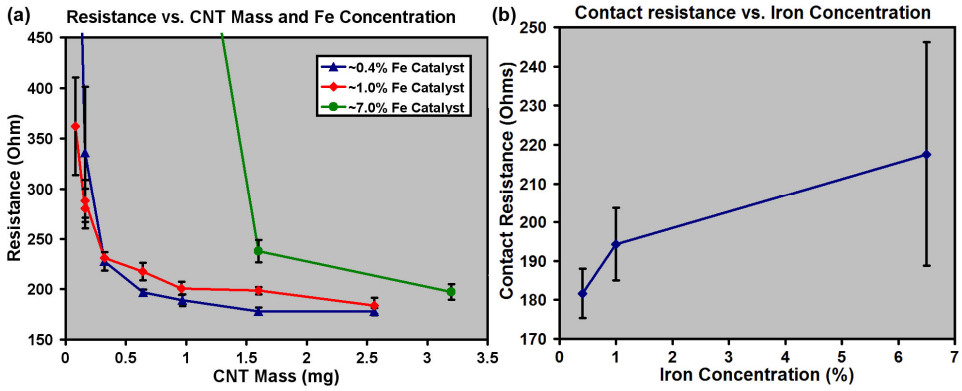

Figure 6-16: (a) CNT paper resistance as a function of nanotube mass and catalyst concentration used during growth (b) contact resistance vs. iron content

Variations to the morphology of the nanotubes are also expected to influence the resistance of the nanotubes. Assuming impurity levels remain similar for samples grown using similar catalyst concentrations, the contact resistance should not change significantly. As a result, the effects of morphology would be more clearly observed in samples with lower nanotube mass, while the resistance of paper samples with higher nanotube content would still be limited by the contact resistance. When comparing samples with straight-walled, bamboo, and mixed morphologies (synthesized using the floating catalyst CVD techniques described in Section 5.4.3), an increase in the misalignment between the graphitic lattice and the nanotube axis is expected to increase the resistance. For samples made from smaller masses of nanotubes (where contact resistance did not dominate), straight-walled nanotube samples were found to have lower resistances than samples made of either bamboo nanotubes or a mixture of bamboo and straight-walled tubes (Figure 6-17a). In graphite, the electrical resistance in the c-direction is roughly four times higher than that in-plane [589]. Consequently, the resistance along a conductive pathway through the length of a nanotube will vary as a function of the lattice angle relative to the tube axis (measured at ~8° for the bamboo nanotubes studied in this work, Figure 6-17b).

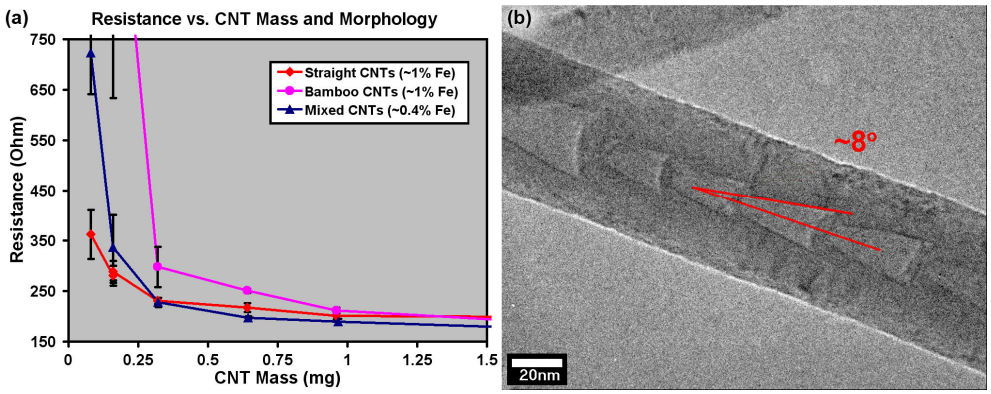

Figure 6-17: (a) Nanotube paper resistance as a function of tube morphology, (b) TEM image of a bamboo nanotube, showing wall angle measurement

These results indicate that control of nanotube morphology could offer an approach towards tailoring the material properties of carbon nanotubes. A related conclusion was reported by Paulson, *et al*., who found that the resistance across the interface of a carbon nanotube lying on a graphite substrate varied as a function of the orientation of the nanotube relative to the surface [590]. Although our current work did not reveal means to control the compartment spacing in bamboo nanotubes (Section 5.4.2), we were able to create transitions from straight-walled nanotubes to bamboo morphologies along the length of individual tubes, and the location along a tube length at which this transition occurred could be adjusted by controlling growth reaction parameters (Section 5.4.3).

6.2 Thermal CVD Characterization

The two chemical vapor deposition techniques used in this work differed significantly in the method of catalyst introduction. For floating catalyst CVD, additional catalyst material was fed into the reaction continuously, in the form of a

metal-hydrocarbon solution, producing long (mm-scale) nanotube mats. Thermal CVD used a pre-deposited catalyst, and this was not replenished during the reaction; as a result growth was limited to ~200μm lengths (see Figure 5-20). However, the heights of these mats were spanned by individual, continuous tubes, rather than by numerous, intertwined tubes, as in floating catalyst growth (identified during the previous mechanical testing, Section 6.1.3).

Due to the different mat dimensions obtained using thermal CVD (rather than floating catalyst CVD), the methods available for mechanical testing were limited. The sample sizes were smaller than those for floating catalyst samples, and challenges in separating the nanotubes from the substrate and handling the samples made tests using the thermal mechanical analyzer approach too difficult to repeat. The nanotube mat heights were also significantly shorter (~20% as tall), resulting in very small displacements (too small to accurately measure) for any tensile strains observed within the load limits of the load cell used. However, in-situ compression testing was carried out, revealing substantial differences in the mechanical response between thermal CVD and floating-catalyst CVD nanotubes (Sections 6.2.1 and 0). In addition, a laser based deflection measurement system was developed, allowing for the flexural rigidity of these samples to be determined (Section 6.2.4).

6.2.1 In-Situ Mechanical Testing

The size of the carbon nanotube mats that were tested mechanically in-situ (described in Section 6.1.2) was limited at both the upper and lower ends. In this process, displacements (under either tension or compression) were measured using an

SEM. At the lowest magnification setting, this instrument was capable of imaging a circular region of ~3.3mm diameter, and as a result, the largest nanotube mats that could be measured were roughly 2mm tall. For shorter nanotube mats, the magnification range of the SEM was not a limitation, as micron-scale regions could be clearly imaged. However, for these smaller samples, the positioning of the testing apparatus within the SEM chamber became more challenging, and the difficulty in precisely centering the sample under the beam limited the minimum nanotube size (the range of motion of the testing apparatus in shown in Figure 6-2). To improve the accuracy of displacement measurements taken during testing, a magnification level was selected to provide a field of view roughly equal in size to the nanotube mat height (providing the best resolution of the actual mat being tested). Smaller samples (which could be up to ~100μm off-center due to difficulties in positioning directly under the beam) could still be imaged during testing; however, lower magnifications were required in order to include the entire nanotube mat height within the field of view, and this reduced the resolution of the sample and the accuracy of displacement measurements.

In addition, while compression testing was done by simply pressing the as-grown nanotube sample between the substrate and the load cell, for tension measurements nanotube mats had to be attached to the testing surface. This was done using superglue, and the glue layer was kept very thin (relative to the nanotube mat thickness) in order to minimize the contribution of this nanotube-glue matrix region to the overall mechanical response of the sample. For thicker nanotube mats this

approach worked well (for >1mm mats grown using floating catalyst CVD, as described in Section 6.1). With thermal CVD nanotube mats were grown to ~200μm lengths (Figure 5-20), and attempts to glue mats of this thickness to testing surfaces resulted in the infiltration of glue into significant portions of the mat. As a result of these limitations, tension testing was not performed on nanotubes grown using thermal CVD methods, and compression testing was only performed on longer nanotube samples (>100μm).

The actual testing process for these thermal CVD nanotubes was very similar to that used for the in-situ compression testing of nanotubes grown using floating catalyst CVD (Section 6.1). However, due to the limited quantity of thermal CVD carbon nanotubes that were of sufficient length for testing, the method used to control the sample cross-sectional area was modified slightly. The process used for floating catalyst nanotubes (cutting down each nanotube mat to a desired cross section, as shown in Figure 6-3) produced only one test sample for each substrate. To allow for multiple tests from a single nanotube sample (to perform one test on each of several locations on the substrate), the load cell was modified with a probe of a known cross-sectional area (~1mm^2). This probe (Figure 6-18) could be used to compress a nanotube sample at several, non-overlapping locations and allowed for up to five tests to be performed on a single nanotube-covered substrate.

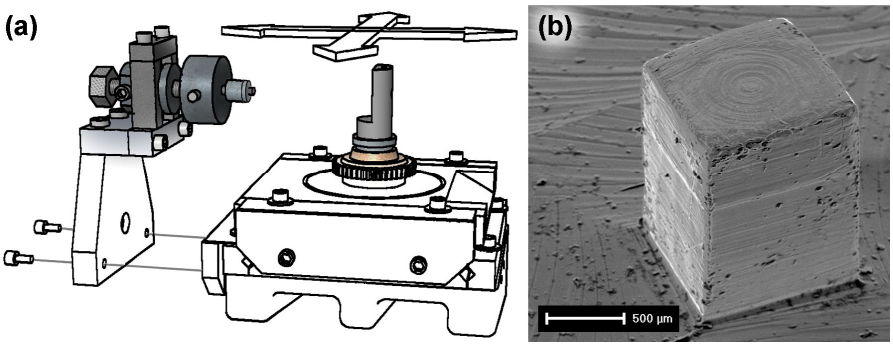

Figure 6-18: (a) Schematic of load cell and straining apparatus used for in-situ compression testing of thermal CVD grown carbon nanotube mats, (b) magnified view of probe tip with ~1mm^2 cross-sectional area

As with the floating catalyst testing described previously (Section 6.1.2), the in-situ testing procedure involved several steps. First, the position of the load cell and compression probe was adjusted to center the probe within the SEM field of view (at the beam center). The nanotube sample was then loading and moved to within a close proximity to the compression probe, using the SEM stage control micrometers. At this point the sample (oriented so that the nanotube axes are perpendicular to the beam) was imaged to allow measurement of an initial reference height. The sample was then moved to come into contact with and press against the compression probe surface, straining the sample. After a small displacement, the sample was held in position while another image was taken. During this entire process, the load cell was used to continuously monitor the applied loads. This sequence was then repeated (using small displacements for each step, ≤12μm), to allow for up to 16 strain steps during loading and up to 10 steps during unloading. As before, displacements were measured from the SEM images obtained at each step, and from these images and the load cell data stress and strain values were calculated. Typical results from these tests

are plotted in Figure 6-19, and these stress values have been adjusted using a nanotube volume fraction correction similar to that used for the floating catalyst CNT testing (obtained using the procedure described in Section 6.1.1).

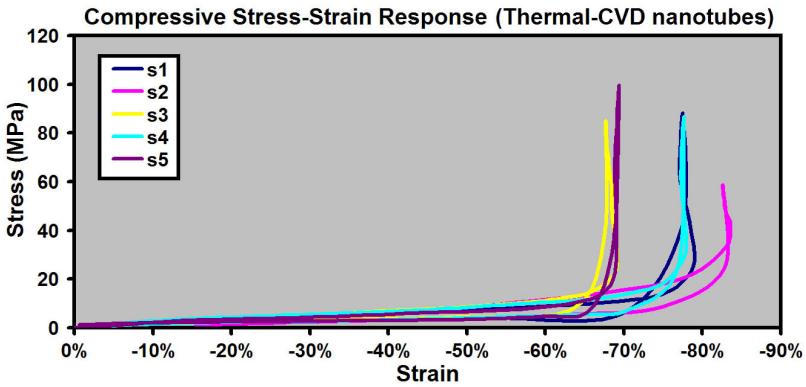

Figure 6-19: Compressive stress-strain response of Thermal CVD grown nanotubes

In these tests, two distinct regions in the stress-strain curves were identified (Figure 6-19). The initial response had a relatively low stiffness (E≈16 MPa), and showed a linear stress-strain relation up to large compressive strains of 65% to 75%. This stiffness is in good agreement with similar compression tests by Cao *et al*., who reported a compressive modulus of 12 MPa during buckling [78]. During this time, long uniform buckles were observed to form in the nanotube mat parallel to the substrate surface (Figure 6-20). Beyond these strains, there is an abrupt transition to a much stiffer behavior (E≈900 MPa), and the stress increases significantly with very little additional strain. This response is similar to that of foam under compression, where a much stiffer region is found at higher strains after densification [591].

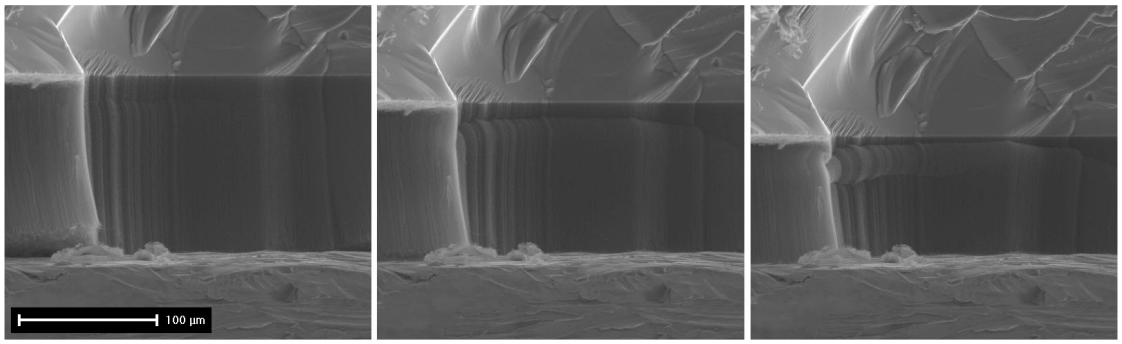

Figure 6-20: Buckle formation during compression of thermal CVD grown nanotubes

Upon unloading, the curve follows a similar pattern, and the heights of unloaded nanotube samples were found to return to almost exactly their initial dimensions, as shown in Figure 6-21 (within the resolution of the displacement measurement made using the SEM).

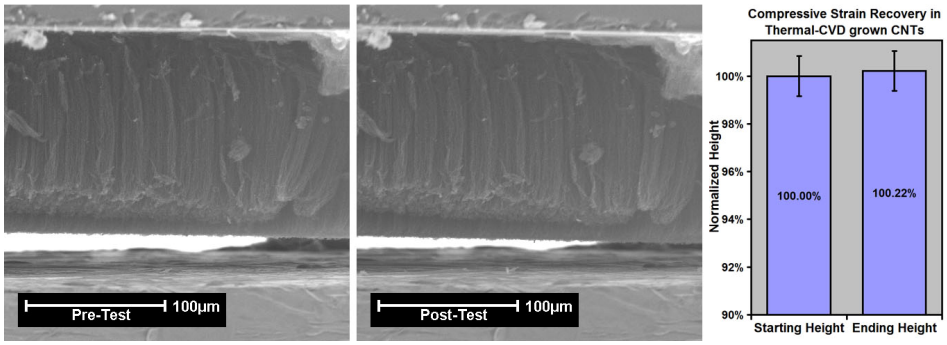

Figure 6-21: Recovery of Thermal CVD nanotubes after compression to 79% strain

At each step in these experiments, SEM images were obtained from which to measure displacements. For some samples, two images were taken at each step, a higher magnification image to measure nanotube mat heights, and a lower magnification image, which showed the entire probe area. The probe in this work (Figure 6-18) was designed to allow multiple compression tests to be performed on different areas on a single nanotube-covered substrate. As a consequence, the

nanotube forest covered the region immediately underneath the probe, as well as the adjacent areas, and the nanotube forest in the vicinity surrounding the probe was observed to deform during testing (Figure 6-22).

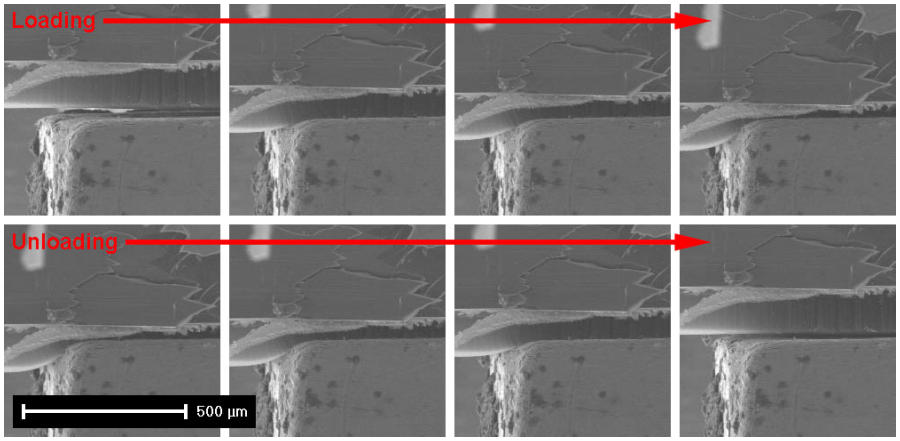

Figure 6-22: Displacement of nanotube mat adjacent to probe indentation

The displacement of the nanotube mat adjacent to the probe was measured as a function of distance away from the probe edge, and strains greater than 60% were observed in regions of the mat close to the probe (<25µm), but under no direct loading. In addition, displacements were measured as far as ~150µm from the probe edge. The van der Waals forces between adjacent tubes in the forest were estimated, as well as the force required to compress a single nanotube to a strain of 60%, in order to investigate the cause of this observed deformation (in tubes not directly loaded by the probe). From SEM imaging, a rough measure of the spacing between nanotubes can be obtained (roughly 15 tubes per µm), and using this spacing and the stress-strain results (Figure 6-19), the force required to achieve a 60% compressive strain in a single nanotube can be estimated (~0.7-1.2nN per tube). The mechanism by which tubes within the mat interact (allowing load transfer from tubes directly underneath the

probe to those adjacent) is expected to be a combination of van der Waals interactions, and possible tangling of tubes within the mat (expected near the mat surface as a consequence of the crowding mechanism of aligned growth). While the contribution from tangled tubes cannot easily be estimated, a rough calculation of the van der Waals interactions between adjacent tubes can be calculated using Equation *(6-5)* ([79], with a Hamaker constant, $A=2.38\times10^{-19}$ J and modified for parallel tubes). For the tube dimensions in this work (~15-20nm diameters with a center-center spacing of 60-75nm), the predicted van der Waals forces (~6-22pN per tube) are much smaller than the forces required to compress a nanotube to 60% strain (~35-190 times smaller). In addition, if van der Waals forces provided the only interactions between adjacent tubes, deformation would be expected only a very short distance away from the probe edge (<1μm), rather than the larger distances (~150μm) observed. This suggests that tangling of tubes within the mat can be significant, and this tangling will result in the deformation observed at distances away from the compression probe edge (Figure 6-23).

$$\frac{f_{vdW}}{\Delta L} = \frac{A}{8\sqrt{2}}\left[\frac{1}{D^{5/2}}\left(\frac{r_2 r_4}{r_2+r_4}\right)^{1/2} - \frac{1}{(D+t)^{5/2}}\left(\frac{r_2 r_3}{r_2+r_3}\right)^{1/2} - \frac{1}{(D+t)^{5/2}}\left(\frac{r_1 r_4}{r_1+r_4}\right)^{1/2} + \frac{1}{(D+2t)^{5/2}}\left(\frac{r_1 r_3}{r_1+r_3}\right)^{1/2}\right] \qquad (6\text{-}5)$$

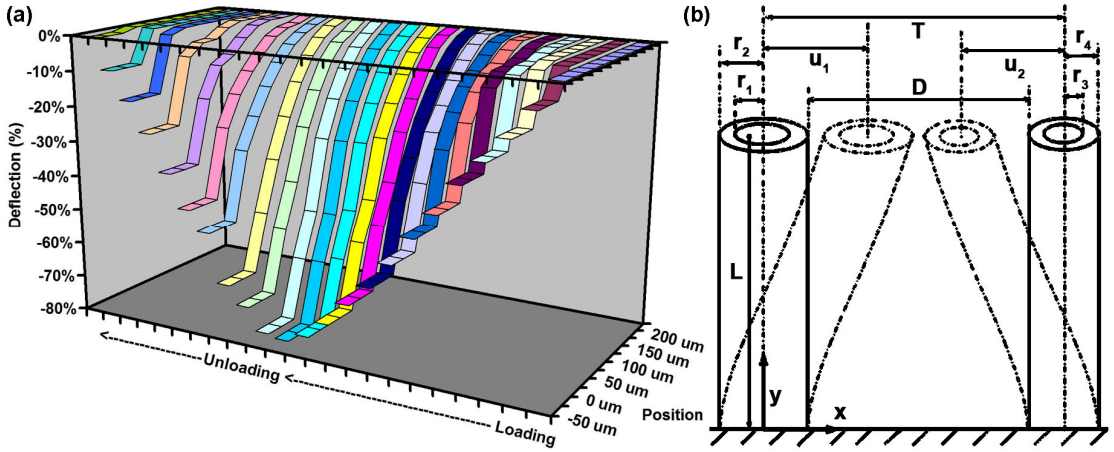

Figure 6-23: (a) Measured deflections of CNT mats as a function of distance from the probe edge for a loading and unloading test sequence, positive positions represent regions of the mat which are not directly compressed and distances are measured away from the probe edge, (b) schematic for calculating van der Waals interaction between adjacent nanotubes [79]

During these experiments, it was noticed that under larger compressive forces (>0.5N), the nanotube mats compressed as expected, but the indentation probe deflected as well (Figure 6-24a,b). In order to identify the source of this additional deflection, the design of the sample holder and load cell support used during these tests was considered. Both of these structures were considered as cantilevers attached at their base to the rigid SEM stage, and deflections under the range of loads typically used during mechanical testing were calculated (Figure 6-24c,d,e). Displacements of the SEM sample holder were found to range between ~25-60μm per Newton of force applied to the nanotube sample, depending on how closely it was attached to the SEM stage. The load cell support was a more rigid structure, but was still predicted to deflect by ~15μm per newton of applied force (peak applied forces during tests did not exceed 2N). These deflections were also observed during the testing of nanotubes grown using floating catalyst CVD (Section 6.1.2), although the greater heights of

those samples made this movement less apparent. However, despite these deflections, the actual displacement and strain in the nanotube sample was still measured accurately, as the sample heights were measured directly from SEM images taken during testing.

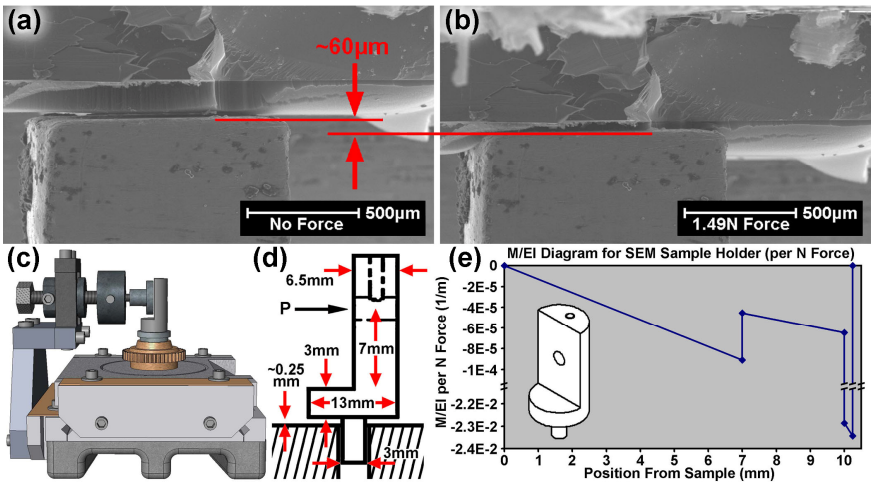

Figure 6-24: (a),(b) SEM images taken during compression testing, showing probe and sample deflections, (c),(d),(e) SEM stage, sample holder dimensions, and M/EI values along sample holder height

Similar to the floating catalyst nanotubes, a time dependent stress relaxation was observed. As described in Section 6.1.4, equations (6-3) and (6-4) were used to calculate the relaxation modulus and fit the data using a Maxwell model [586]. These results are shown in Figure 6-25, and time constants for this relaxation were calculated to be roughly 17.1 seconds for loading and roughly 22.1 seconds for unloading.

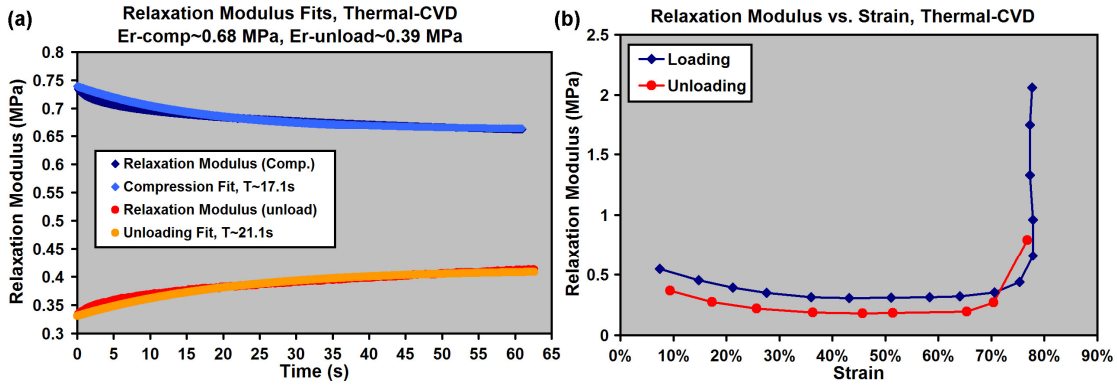

Figure 6-25: (a) Time-dependency observed for the relaxation modulus in thermal CVD nanotubes, (b) variation of relaxation modulus with strain for loading and unloading

6.2.2 Comparison of Thermal and Floating-Catalyst Growth

Although the dimensions of thermal CVD grown nanotubes prevented other mechanical testing from being performed (tension tests and tests using the TMA were not possible), the in-situ compression response (Section 6.2.1) was compared to the behavior of floating-catalyst CVD grown nanotube mats (Section 6.1.2). The variations between the two CVD approaches utilized to grow the samples for these tests can be used to explain the differences between the mechanical responses of these nanotubes.

The typical stress-strain curve of the thermal CVD samples showed two distinct regions; for low to fairly high levels of compressive strain (up to 65%-75% strains) the stresses associated with these strains were very low. With additional loading beyond this point, the response stiffened considerably. This is in contrast to the stress-strain curve observed for floating-catalyst nanotubes, which showed only a single, linear region, with a uniform stiffness. This stiffness was substantially higher

(~40x) than that initially observed with the thermal CVD tubes, although the much higher modulus value found for the second region in the thermal CVD response was comparable to the floating catalyst CVD nanotube modulus value. A comparison of the responses from these nanotube samples is shown in Figure 6-26.

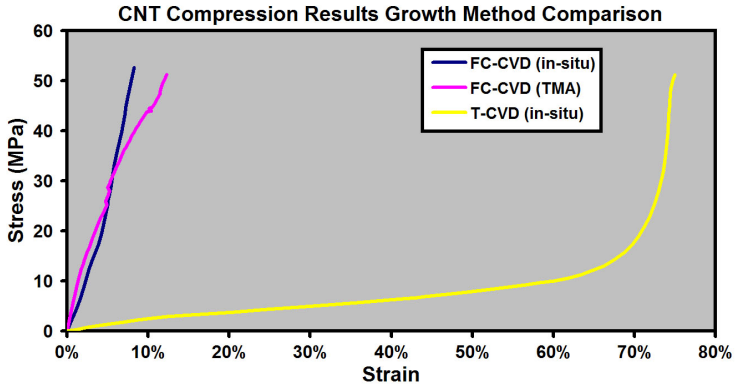

Figure 6-26: Compressive stress-strain reponse of carbon nanotubes grown using floating-catalyst CVD (FC-CVD) and thermal CVD (T-CVD)

The large difference in stress-strain behaviors can be explained by examining the structure of nanotube mats grown by floating-catalyst CVD and by thermal CVD. The nanotubes grown using floating-catalyst methods had larger diameters (over twice those of thermal CVD nanotubes, on average) and mats were composed of many intertwined tubes along the forest height. Buckling will occur towards the center of a tube (rather than near the ends). Due to the more tangled nature of these mats (with tubes beginning and ending at different locations along the mat height), uniform buckling at lower strains is not likely (although uniform buckling was sometimes observed under large strains, see Figure 6-10). For moderate strains, the only indication of buckling occurred at the tip of the mat, where the tube ends appeared to slip on the compression platen surface (Figure 6-27a). As a result, compression and

buckling of tubes within these floating-catalyst mats will occur at a small scale relative to the size of the mat (Figure 6-27b), and a linear stress-strain relation is obtained.

Nanotubes grown using thermal CVD differ in two important ways. These tubes are smaller (average diameters of 15-20nm compared to 40-50nm), and would be expected to buckle under correspondingly lower loads than floating-catalyst nanotubes. More importantly, the mat structure in these samples is composed of individual tubes spanning the entire height. For these well-aligned mats, entire regions can buckle uniformly (Figure 6-27c,d), undergoing high strains at low loads and showing low modulus values. This explains the low compressive modulus observed (these mats do not stiffen until they have undergone considerable densification, at strains of 65-75%). In addition, the location of the buckling within the mat also indicates the alignment and growth mechanism of the nanotubes. This uniform buckling will occur in regions of highly aligned nanotubes (as poor alignment can inhibit uniform buckling, as observed in floating catalyst nanotubes). The thermal CVD nanotubes used in this study were grown using thin iron films as catalysts on alumina-coated silicon surfaces, and this catalyst-substrate combination was found to result in base growth (see Section 5.2.2). According to the crowding mechanism, the initial nanotube growth from the substrate will be poorly aligned, and alignment will improve as the nanotubes lengthen and support each other. The most uniformly aligned part of the nanotube mat will be the region grown immediately prior to the termination of the reaction, and for base growth tubes, this is the area closest to the

substrate (see Figure 5-25). During compression testing, this is the region where the large, uniform buckling was observed to occur (Figure 6-27c).

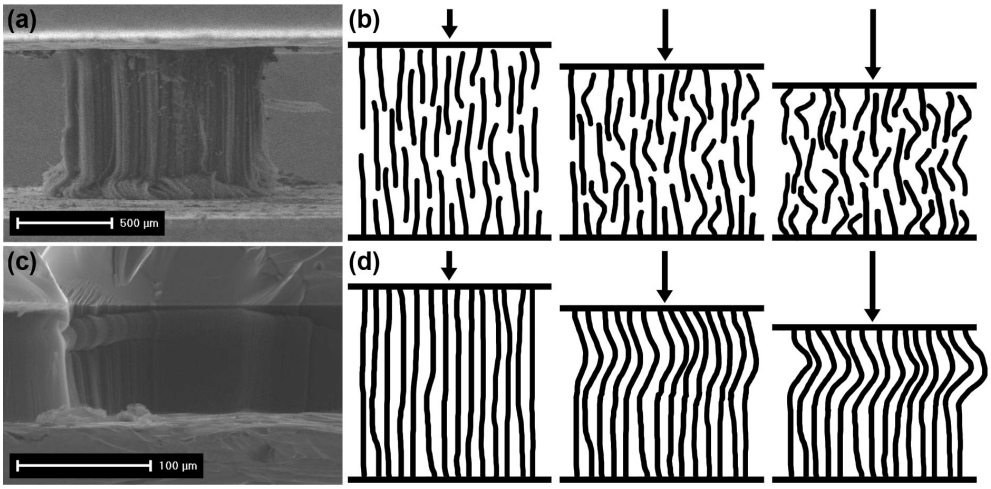

Figure 6-27: (a),(b) SEM image and schematic showing compression and buckling in mats of floating catalyst CVD nanotubes, (c),(d) Compression and buckling in thermal CVD nanotube mats

Time dependent responses were observed for both floating catalyst CVD and thermal CVD grown nanotubes. However, the responses to both compressive loading and unloading differed significantly between the two growth methods, as shown in Figure 6-28 (tension tests were not performed on thermal CVD nanotubes, and are not included in this comparison). Stress relaxation was observed during the pause between successive strain steps for all samples, and the amount of this relaxation was substantially greater for floating catalyst CVD samples than for thermal CVD samples (over twice as high, Figure 6-28a). In addition, stress relaxation occurred fairly rapidly for floating catalyst nanotubes (with a time constant of 3.7 seconds for loading and 1.7 seconds for unloading, compared to 17.1 and 22.1 seconds, respectively, in thermal CVD nanotubes, Figure 6-28b). The structure of these mats (composed of

numerous intertwined nanotubes) allows for a relatively quick reorganization of the mat structure to accommodate strains, as tubes can easily slide past each other. In thermal CVD samples, all nanotubes are supported by the growth substrate at one end (rather than many tubes supported only by van der Waals forces and tangling between tubes, as in floating catalyst samples). Due to this more rigid attachment of nanotubes to the substrate in thermal CVD samples, structural reorganization to accommodate loads is inhibited. As a result, the total relaxation during each step is reduced for thermal CVD nanotubes, and the time constant of this response is considerably longer.

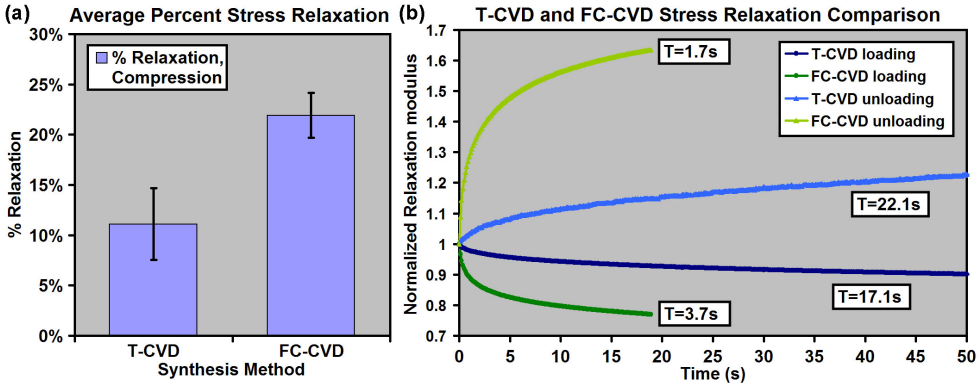

Figure 6-28: Comparison of FC-CVD and thermal CVD nanotubes in compression (a) Average percent stress relaxation during each strain step, (b) Time-dependent variation in relaxation modulus for loading and unloading

In addition to the dissimilar time dependent responses, the recovery measured for each sample (after complete unloading) varied depending on the growth method used. Although all samples were found to recover a large percentage of their initial height, thermal CVD nanotubes were consistently observed to completely recover (100% of their height, within the measurement resolution), even after undergoing significant compressive strains (>75%). Floating catalyst samples did recover a substantial portion of the applied strains; however, a small amount of plastic strain

(~1-3%) remained, and this plastic strain increased with increasing applied strains. This is to be expected, as some rearrangement of the intertwined tubes within the floating catalyst samples could occur during loading. For these floating catalyst samples, the sliding of nanotubes past each other would result in some permanent densification of the sample. Thermal CVD nanotubes, which are composed of continuous tubes along the sample height, are expected to completely recover, as the significant buckling that occurred during compression is reversible. A summary of these results is given in Table 6-2.

Table 6-2: Summary of compressive testing results for floating catalyst and thermal CVD nanotube samples

Property	Floating Catalyst	Thermal CVD
Compressive Modulus	580-750 MPa	16 MPa / 900 MPa
Time Constant	1.7-3.7 seconds	17-22 seconds
Recovery (% Strain)	98.8 ± 2.2%	100.2 ± 0.8%

6.2.3 Optical Properties

The interesting optical properties of carbon nanotubes have been reported by a number of groups previously (see Section 2.3.3). Of particular interest is the anisotropic absorption of light by carbon nanotubes (depending on the light polarization relative to the nanotube axis) and the ability of mats of carbon nanotubes to effectively absorb and scatter light, resulting in a very low intensity ratio between light transmitted through a nanotube mat and the incident light under certain configurations.

To study the interaction of carbon nanotube mats with light, a laser was set up to shine through a mat of thermal CVD grown carbon nanotubes (using Ni film

catalysts on polished SiO_2 substrates). The nanotube mat was held in a gimbal mount support, allowing for rotation in two directions (about the y and z axes). The transmitted laser beam was directed through a polarizer and then into a detector, where the light intensity was monitored. This equipment is shown in Figure 6-29.

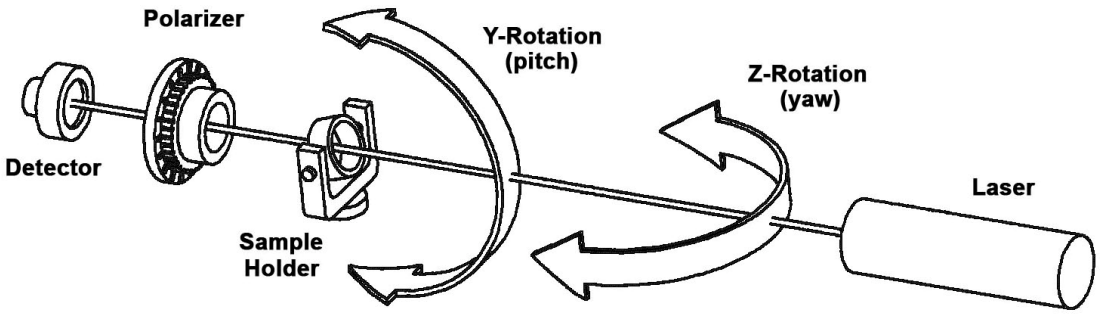

Figure 6-29: Equipment schematic for nanotube light polarization experiments

For each test, a nanotube mat was placed at a fixed position (y and z rotation) and the transmitted laser light intensity was monitored as a function of the polarizer angle. For each measurement (at each polarizer step) the intensity was monitored for 10-15 seconds to provide an average intensity value. Tests were also performed with plain SiO_2 slides and SiO_2 slides coated with thin Ni films (but without any nanotubes) as control samples.

Typical results are shown in Figure 6-30. The green curve (from a control sample without nanotubes) shows a peak in intensity at 90° and 270°, which corresponds to the polarization angle of the initial laser beam. When the laser was passed through a mat of nanotubes, the curve was observed to shift, with the peak moving away from 90°. The minimum measured intensity (relative to the maximum intensity) also increased for light passing through nanotube samples.

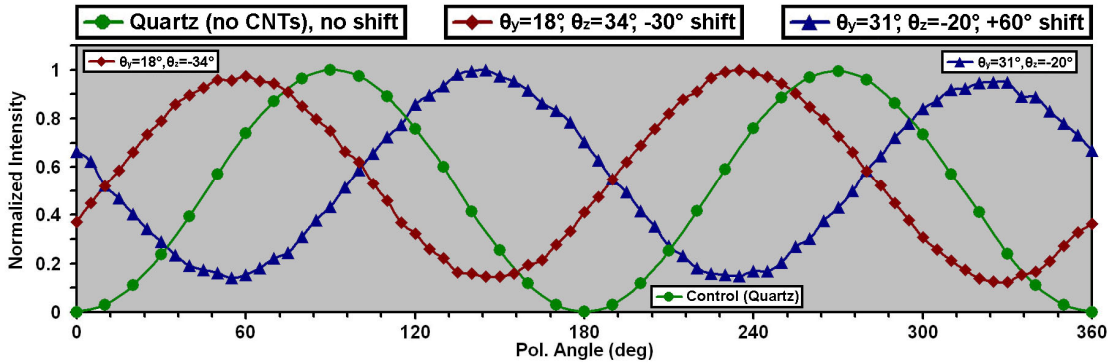

Figure 6-30: Normalized transmitted laser intensity as a function of polarizer angle, green curve shows control sample (no nanotubes), red and blue curves show results for nanotube samples at two different positions.

The position of the nanotube mat axis was calculated as a function of its angle of rotation about the y and z axes. From these angles, an expression for the angle between the nanotube axis and the plane of polarization of the incident laser beam was found; this relation is shown in Equation (6-6). For each nanotube sample, the angle between the tube axis and the plane of polarization of the incident laser was calculated, and these angles were compared to the shift in peak intensity of the transmitted light from the initial peak intensity (90°, 270°) of the incident laser.

$$\theta_{proj.} = a\tan\left(\cot(\theta_y) * \sin(\theta_z)\right) \qquad (6\text{-}6)$$

Using Equation (6-6), the angle between the laser axis and incident laser plane of polarization was found to be ~30° for the transmitted intensity data shown in blue in Figure 6-30 and ~60° for the data shown in red. These match very well compared to the angular difference between the incident laser peak position and the transmitted minimum (nanotubes aligned at 60° from the incident laser polarization plane showed a minimum transmitted intensity offset by 60° from the incident maximum, transmitted intensity from nanotubes aligned at 30° showed a minimum 30° from the

incident laser maximum). A summary of the data points from a series of these tests (along with tests on control samples) is shown in Figure 6-31. A very distinct trend is observed between the nanotube axis orientation and the position of the minimum transmitted intensity (both measured relative to the initial plane of polarization of the laser).

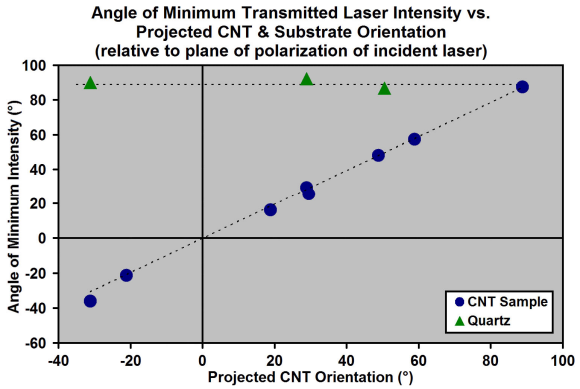

Figure 6-31: Relationship between angle of minimum transmitted intensity and nanotube orientation (relative to the plane of polarization of the incident laser)

These results indicate the component of light polarized in the same plane as the axis of a mat of aligned nanotubes will be absorbed, and light polarized at 90° to the nanotube axis will be transmitted. The transmitted light intensity can be described as a function of the nanotube angle and the peak transmitted intensity; this relationship is given in Equation (6-7) (note that θ gives the CNT axis orientation relative to the incident laser beam polarization, the π/2 represents that maximum intensity is obtained when the CNT axis and laser polarization are offset by 90°).

$$I = I_0 \cos^2(\theta - \frac{\pi}{2}) \qquad (6\text{-}7)$$

The nanotube mats are not perfect polarizers, however. Not only is the peak transmitted intensity far lower than the peak incident laser intensity (a ~20nA signal is measured from an initial 2mA laser transmitted through the CNT mat), but the zero minimum (predicted by Equation (6-7) when the CNT axis is parallel to the laser polarization), is not observed (see the curves shown in Figure 6-30). This indicates that nanotube alignment within the mat is not perfect and that scattering occurs as the light passes through the nanotube sample.

Initial attempts to use this property to develop concepts for measuring nanotube deflection as a function of polarization changes (of laser light transmitted through aligned nanotube mats) proved difficult, as nanotube deflections under lateral loads resembled those of fixed end cantilever beams. However, the very low intensity of light transmitted through the nanotube mats (a 5 order of magnitude drop, ~2mA to ~20nA) led to the development of a revised approach towards measuring small deflections of nanotube in response to lateral loadings (Section 6.2.4).

6.2.4 Flexural Rigidity determination

The in-situ mechanical testing approach described in Sections 6.1.2 and 6.2.1 was used to characterize nanotube samples that were sufficiently long (>100μm) to allow accurate measurements of displacements. However, many of the nanotube samples grown during this study (by the thermal CVD process described in Section 5.2) were too short to allow this testing method to be used. For these nanotube mats, an alternate process was developed to investigate their mechanical properties. This method utilized the optical properties of these nanotube forests (very low transmission

of light through the mats) to determine the flexural rigidity (the product of the modulus and moment of inertia, EI) of these mats.

Accurate independent determination of these values (the stiffness and moment of inertia) for mats of nanotubes is very challenging, due to (a) varying tube-tube distances within the mat, (b) attractive forces between tubes due to van der Waals interactions (as high as nN force per nm CNT length) [79, 81], and (c) sliding of tubes past each other within the mat (requiring smaller forces) [82]. However, for certain different loading conditions, such as deflection (Δ) under shear or critical buckling load (P_{cr}), only the flexural rigidity (EI) is required to determine the mechanical response of nanotubes (as shown in Equations (6-8) and (6-9) [592]).

$$\Delta = \frac{PL^3}{3EI} \qquad (6\text{-}8)$$

$$P_{cr} = \frac{\pi^2 EI}{L^2} \qquad (6\text{-}9)$$

6.2.4.1 Experimental Set-up and Results

To observe the deflection of nanotubes and measure the flexural rigidity of mats of aligned nanotubes in several different configurations, a simple optical method was devised. This approach utilized the very low intensity ratio between light transmitted through a nanotube sample and the incident light (Section 6.2.3). In this work, mats of carbon nanotubes were grown with sufficient height and packing density on a quartz substrate to absorb a large proportion of visible light passing through the mats. Nanotubes were grown using thin iron films evaporated through TEM grid shadow masks of varying dimensions to form catalyst patterns on quartz

substrates. Thermal CVD growth was carried out using the parameters summarized in Table 6-3, see Section 3.1.3 for more details of this process. The growth lengths of the CNTs were determined by controlling the growth period, ranging from 15 to 30 minutes.

Table 6-3: Growth conditions for CNT mats used in flexural rigidity experiments

Growth parameter	Value
Carbon Source	Benzene
Introduction rate	~0.13 ml/min
Catalyst material	Iron
Catalyst thickness	~5-10nm
Argon flow rate	~225 sccm
Ammonia flow rate	~200 sccm
Reaction Temperature	900°C
Substrate	SiO_2 slides
Reaction Duration	15-30 minutes

Several examples of the patterned carbon nanotube arrays produced are shown in Figure 6-32 (showing arrays of 38μm, 19μm, and 5μm pattern sizes using the method described above).

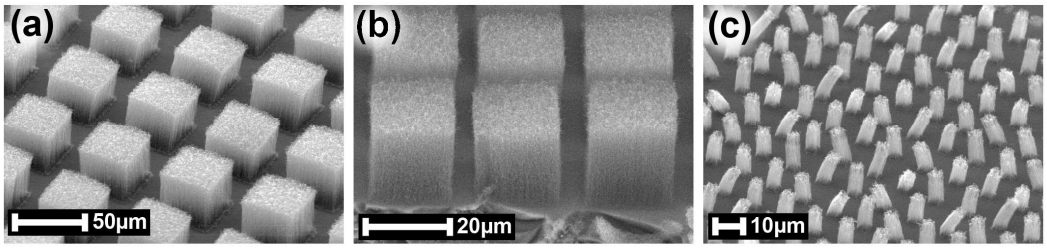

Figure 6-32: (a-c) Patterned nanotube mats, comprising vertically aligned multiwalled nanotubes, with 38μm, 19μm, and 5μm pattern sizes were grown on quartz substrates through chemical vapor deposition.

For monitoring the response of the CNTs to fluid flow, the quartz substrate with the vertically aligned patterned nanotubes was placed inside the experimental apparatus, illustrated in Figure 6-33. The nanotubes were located at the very front

edge of the substrate. The apparatus consisted of a quartz tube with an inner diameter of 6.2 mm connected to a pressurized gas line. The sample was held in place by plastic inserts to prevent sample vibration, and was then exposed to fluid (air) at various velocities, which were calibrated using the flow chamber cross-sectional area and volumetric flow rates measured using a flowmeter.

In our study, two methods were used to monitor the deflection of the CNTs. In the first method, a polarized laser (633nm wavelength) was focused to a roughly 30 μm spot size and positioned over the patterned CNTs). The laser was aligned parallel to the nanotube axis and perpendicular to the substrate, as shown in Figure 6-33, and a photodetector was used to monitor the transmitted intensity at different fluid velocities. In the second method, optical imaging of the CNTs, (with a Sony CCD camera aligned normal to the substrate, 0.25 μm resolution), was used to monitor the deflections of the CNTs as a function of applied fluid velocity.

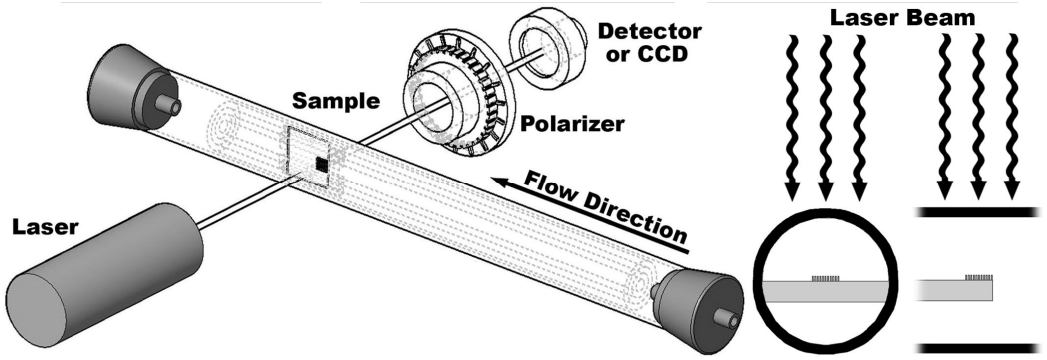

Figure 6-33: A schematic of the experimental set-up for observing the nanotube deflections, during fluid flow, through the transmitted laser intensity variations and CCD image processing.

An immediate issue of using a quartz tube was the poor quality of the transmitted beam and image, resulting from the scattering of light passing through the

quartz due to the curvature of the tube. These refraction and scattering effects result in laser measurements with poor sensitivity and CCD images (taken through the quartz tube) with insufficient resolution. By replacing the quartz tube with a flat quartz plate, the scattering and refraction is greatly reduced without compromising the air seal of the flow chamber (as shown in Figure 6-34).

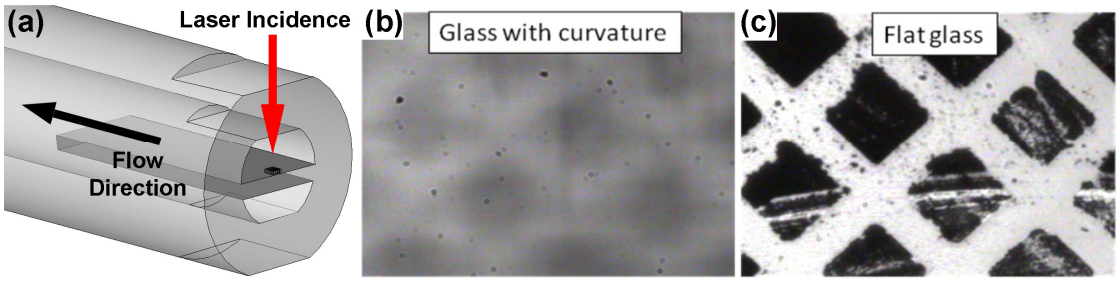

Figure 6-34: (a) Schematic of sample arrangement: The substrate with nanotubes was installed at the center of the quartz tube (b) and (c) show CCD images taken of the sample through the tube (b) and through the flat plate (c)

The incident laser intensity was greatly reduced (by ~10^5) on transmission through a CNT mat, presumably due to scattering and absorption. Consequently, the transmitted laser intensity was calibrated and correlated with the coverage of the nanotubes on the substrate. For example, two masks that were used to pattern CNT growth (one with 90μm squares at a 127μm pitch, one with 38μm squares at a 64μm pitch) have 50% and 35% expected transmission, respectively, and such values were indeed observed experimentally (shown in Figure 6-35).

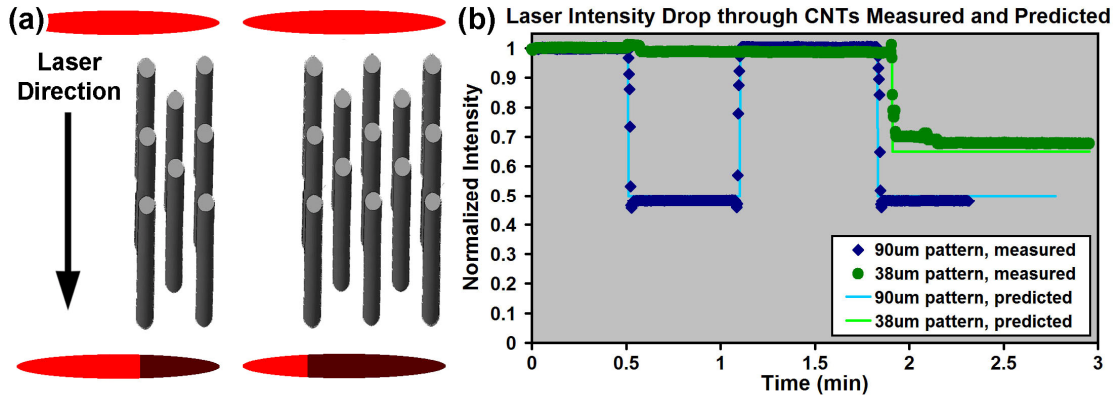

Figure 6-35: (a) Schematic of coverage-related transmitted laser intensity drop, (b) the transmitted laser intensity is reduced by 51.8% and 32.3% when CNTs were arrayed in mesh pattern with 50.2% and 35.2% coverage, respectively. The close agreement of the experimental results with the predicted values was used as a calibration for nanotube deflection.

Nanotube deflections were determined as a function of fluid velocity, and were calculated based on the intensity variations and pattern coverage (for transmitted laser experiments) or by using image processing (for CCD measurements). For each nanotube pattern, the grid was aligned with the leading edge of the substrate, and any deflection would be parallel to both the direction of fluid flow and the pattern rows (Figure 6-36).

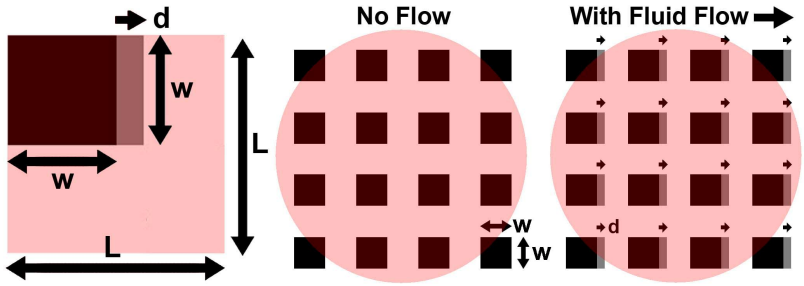

Figure 6-36: Schematic of the CNT arrays shows of the effect of fluid flow on aligned CNT mat patterns. The displacement d is correlated with a measured variation in the transmitted laser intensity. The representative laser spot is colored in red and the dark squares are CNT ensembles.

The transmitted intensity, in the absence of fluid flow is related to the area initially devoid of the CNT mats (Equation (6-10)) and is determined from the geometry of Figure 6-36. When subject to fluid flow, the nanotubes deflect a distance *d*, covering an extra area (*w* x *d*), where *w* is the width of the CNT pattern. The light transmission changes with this additional coverage, and the normalized intensity is given by Equation (6-11), and the deflection *d* can be obtained using Equation (6-12).

$$\frac{I}{I_0} = 1 - \frac{w^2}{L^2} \qquad (6\text{-}10)$$

$$\frac{I}{I_0} = 1 - \frac{\left(w^2 + wd\right)}{L^2} \qquad (6\text{-}11)$$

$$d = \frac{L^2}{w}\left(1 - \frac{I}{I_0}\right) - w \qquad (6\text{-}12)$$

During tests, it was observed that vibration due to fluid flow could cause a variation in the transmitted intensity. Averaging was used to minimize the effect of this variation (by selecting a laser spot size large enough to encompass many CNT arrays), and this vibration has been considered in determining the error.

An excellent correspondence was observed between the transmitted intensity (Figure 6-37a) and the air flow velocity (Figure 6-37b), and this response is attributed to nanotube deflection and subsequent hindrance to the light transmission. Such correlation was observed, very reliably, for many measurements on the patterned CNT arrays, and the constant reference intensity (in the absence of fluid flow), attests to the outstanding mechanical characteristics of CNTs. The changes in transmitted laser intensity can be normalized, and the corresponding deflections can be calculated using Equation (6-12) (shown in Figure 6-37c).

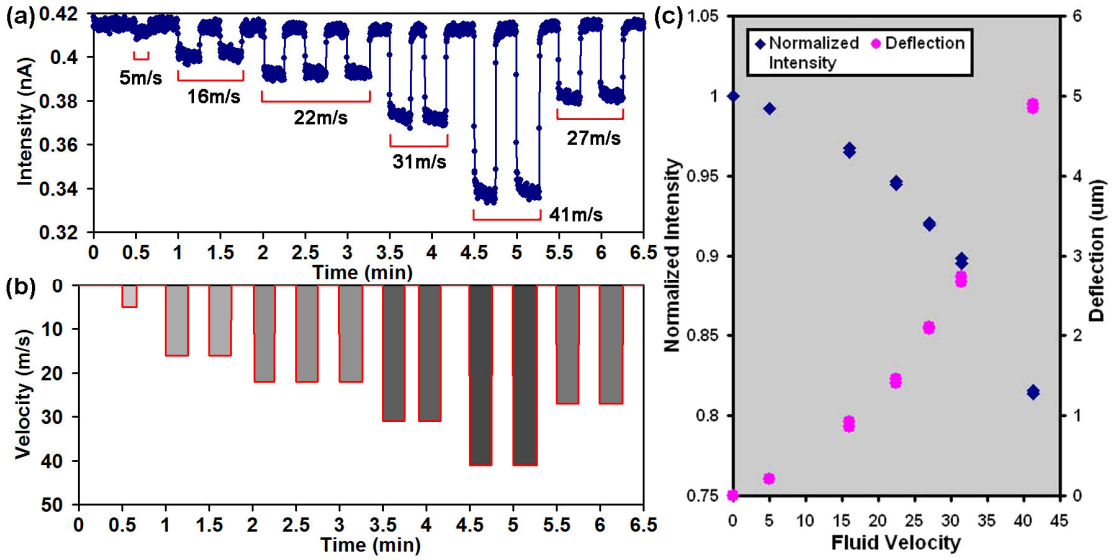

Figure 6-37: (a) The variation in the transmitted laser intensity is a very sensitive function of the fluid velocity, and can be used for (b) digital calibration of the flow. (c) The data points show a decrease in the transmission with increased nanotube deflection caused by fluid motion.

Alternately, CCD images of nanotubes exposed to different fluid flows (as shown in Figure 6-38) gave another calibration in terms of the nanotube deflections. The resolution of the measured deflection was roughly ~ 0.25μm (set by the camera resolution), and images were analyzed by image processing, with the scale of the images calibrated via the known CNT pattern size.

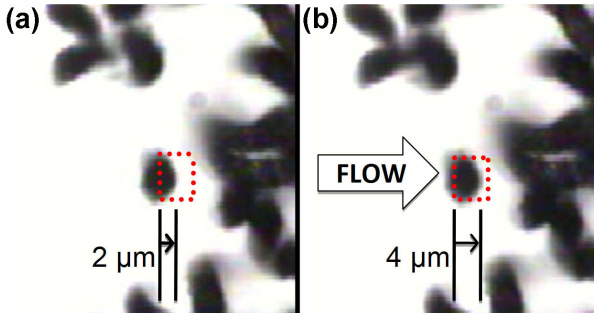

Figure 6-38: The images captured by CCD (from the top of CNT samples, with focal plane at CNT tips) when the flow velocity is (a) 0 m/s and (b) 30 m/s The images show a CNT deflection of ~ 2 μm under the flow.

6.2.4.2 Fluid Flow and Nanotube Deflection modeling

In order to understand the effects of the drag forces induced by fluid flow on the nanotubes (positioned as shown in Figure 6-33 and Figure 6-34), the following methodology was used. Three characteristic length (L) scales are of relevance in considering fluid flow on and around nanotubes, each associated with a Reynolds number (Equation (6-13)).

$$\mathrm{Re} = \frac{\rho UL}{\mu} = \frac{UL}{\nu} \qquad (6\text{-}13)$$

Most tests were carried out with air as the working fluid, and in these cases, the following values were used: υ (kinematic viscosity) ~ 1.5×10^{-5} m^2/s and ρ (density), ~ 1.2 kg/m^3 at 1 atm and 20 °C. In Equation (6-13), U is the fluid velocity and the characteristic length, L, is given in Table 6-4 for each of the three length scales considered.

Table 6-4: Characteristic length scales used to simulate fluid flow through nanotube arrays

For Flow:	Characteristic length (L) is:
Through the pipe	The diameter of the tube (~ 6.2 mm)
Over the flat substrate	The distance from the leading edge of the substrate to the sample, (<1000μm)
Through aligned CNTs	The diameter of the CNTs (~50nm)

The Reynold's number (Re) for the air flow through the cylindrical pipe was found to be in the range of 8,300 – 24,800 (at air velocities 20-60 m/s), clearly in the turbulent regime (Re>2300) [593]. As fluid entrance effects could be significant and make accurate prediction of fluid velocity difficult, we avoided such complications by

placing the sample sufficiently inside the tube (~17 cm), beyond the entrance length (L_e) ~14.7 cm in our set-up for velocities of ~60 m/s (obtained using Equation (6-14)).

$$L_e = 4.4D\left(\mathrm{Re}^{1/6}\right) \qquad (6\text{-}14)$$

Beyond L_e, the fluid flow is considered to be fully developed, and the peak fluid velocity (U_{peak}), at the pipe center, is related to the average velocity (U_a) through Equation (6-15).

$$U_{peak} = \left(1 + \frac{0.722}{\log\left(\mathrm{Re}/6.9\right)}\right) U_{avg} \qquad (6\text{-}15)$$

The mats of vertically-aligned multi-walled carbon nanotubes used in this study were grown close to the leading edge of the quartz substrate (within 1000μm). Due to this small characteristic length, the Re in this region, ~10^2, is much smaller than that for turbulent flow (which is ~10^6), and the fluid flow over the plate can be considered laminar. The boundary layer thickness, δ, at a certain distance, *x*, from the leading edge, was computed using Equation (6-16). The velocity (*u)* profile is considered as a function of the vertical height (*y*), and is given by Equation (6-17) for $y \leq \delta$ and $u=U_{peak}$ for $y > \delta$. For nanotubes positioned within 1000μm of the substrate leading edge, the δ was computed to be ~10-100 μm, depending on position and air velocities (up to ~60m/s). With average CNT heights between 30μm and 60μm, this implies that for many samples, the upper region of the nanotubes was exposed to the full centerline flow ($u=U_{peak}$).

$$\frac{\delta}{x} = \frac{5}{\sqrt{\mathrm{Re}}} \qquad (6\text{-}16)$$

$$u = U_{peak}\left(2\frac{y}{\delta} - \left(\frac{y}{\delta}\right)^2\right) \qquad (6\text{-}17)$$

Due to the small CNT diameters (~50 nm), the Re for flow through/around tubes is very small (~0.2 at an air velocity of 60 m/s). A modified Stokes-Oseen Equation (6-18) is used to predict the drag coefficient at low Re, the first term is related to the drag on a single cylinder, and the second term provides a correction for φ, (the volume fraction) for flow passing through a vertically aligned array of cylinders [594].

$$C_D = \left(\frac{8\pi}{\mathrm{Re}_{S-O}\ln\left(7.4/\mathrm{Re}_{S-O}\right)}\right)\left(\frac{3+2\phi^{5/3}}{3-4.5\phi^{1/3}+4.5\phi^{5/3}-3\phi^2}\right) \qquad (6\text{-}18)$$

The above expression, however, is based on conventional Navier-Stokes continuum mechanics [594], where zero fluid velocity is assumed next to the surface of the object (no-slip boundary condition). At the size scales for flow through CNT mats, the no-slip assumption could no longer be valid and a correction, through the Knudsen number (Kn) must be introduced [595]. Kn is the ratio of the mean free path of molecules (λ) in the fluid to the characteristic length (L) of a system. The no-slip assumption is only considered to be valid for Kn < 10^{-3}. However, for air at standard temperature and pressure, the mean free path is λ ~80nm, and with an average spacing between nanotubes of ~150 nm, the Kn ranges around 0.5. Consequently, slip at surfaces must be considered, and will reduce the effective drag on the object (Equation (6-19)). The incorporation of the slip condition yields Equation (6-20), a comprehensive relation for the drag coefficient (C_D).

$$C_D = \frac{1+4Kn}{1+6Kn} C_{D(cont.)};\ Kn = \frac{\lambda}{L} \qquad (6\text{-}19)$$

$$C_D = \left(\frac{1+4Kn}{1+6Kn}\right)\left(\frac{8\pi}{\mathrm{Re}_{S-O}\ln\left(7.4/\mathrm{Re}_{S-O}\right)}\right)\left(\frac{3+2\phi^{5/3}}{3-4.5\phi^{1/3}+4.5\phi^{5/3}-3\phi^{2}}\right) \qquad (6\text{-}20)$$

Subsequent to the determination of C_D, the drag force per unit length, F_D, was found through Equation (6-21), as a function of fluid velocity, *u*, fluid density, ρ, and the CNT cross-sectional area, A. To account for the varying fluid velocity near the bases of the CNTs (in the boundary layer), we divided the nanotube height into N different segments, each with a step height $\Delta y = h/N$. Fluid velocities were found for each segment (at the corresponding height above the substrate), and the cross-sectional area used was the product of CNT diameter, *d*, and step height Δy. The deflection of carbon nanotubes was modeled by treating the tubes as a fixed end cantilever system, as shown in Figure 6-39.

$$F_D = \frac{1}{2} C_D A \rho V^2 \qquad (6\text{-}21)$$

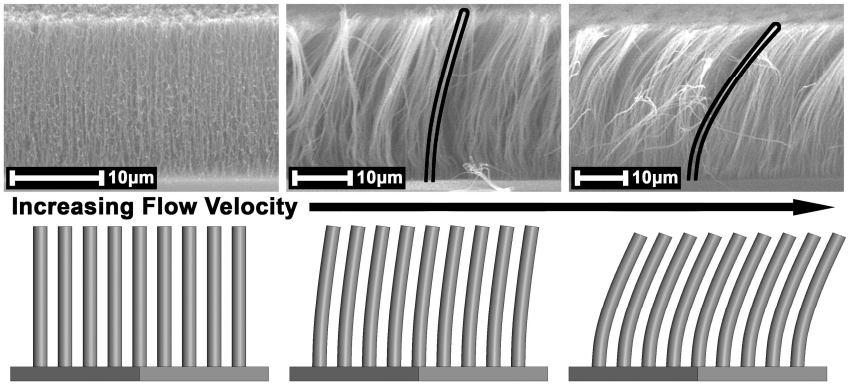

Figure 6-39: The shearing of carbon nanotube arrays, can be modeled as cantilevers through solid mechanics (the outlines depict the close correspondence between the theory and experimentally observed shear)

The horizontal deflection (x), as a function of position in the vertical direction (y), $x(y)$ was determined using a nanotube height dependent, distributed force per unit length w(y) using Equation (6-22), where E is the CNT elastic modulus and I, the moment of inertia.

$$\frac{d^4x}{dy^4} = -\frac{w(y)}{EI} \qquad (6\text{-}22)$$

To obtain the horizontal displacement $x(y)$ as a function of nanotube height and average air velocity, Equation (6-22) is integrated four times; the following boundary conditions were applied (listed in Table 6-5). In this work, the modeled deflections are small enough that the small angle approximation remains valid (dx/dy=tan(θ)≈θ).

Table 6-5: Boundary Conditions used to calculate nanotube deflections

Integration Step	Boundary Condition
1	No shear at the CNT free ends ($d^3x/dy^3 = 0$, at $y = h$)
2	No bending moments at the free end ($d^2x/dy^2 = 0$, at $y = h$),
3	Zero slope at the fixed end of the CNTs ($dx/dy = 0$, at $y = 0$)
4	Zero deflection at the fixed end ($x = 0$, at $y = 0$)

In order to calculate the deflection of a nanotube exposed to fluid flow, a procedure to allow for repeated numerical integration of the distributed load on the side of the tube was developed. The nanotube height was considered as N segments, and for each segment, Δy, the following calculations were performed. The velocity profile in the boundary layer was calculated using Equation (6-17), while above the boundary layer, the velocity was obtained using Equation (6-15). With the determined velocity distribution and given nanotube diameter (~ 50nm) both the Reynolds number (Re) and the drag coefficient (C_D) were then calculated (Equations (6-13) and (6-20))

for each height step. The F_D on each segment (Δy) was then calculated (Equation (6-21)) and this distributed force was then integrated (Equation (6-22)), using the trapezoid rule with appropriate boundary conditions, along the entire nanotube height. Subsequently, the deflection was obtained for each segment along the nanotube height, using Equation (6-22)). Examples of the results obtained from these calculations are seen in Figure 6-40, illustrating the effects of different sample positions and fluid flow velocities.

Figure 6-40a-c shows the effects of moving the patterned nanotubes away from the leading edge of the substrate (from 2μm to 100μm). The boundary layer thickness decreases as the distance to the leading edge of the substrate is reduced; consequently, nanotubes placed closer to this leading edge (at 2 μm vs. 100μm) are exposed to higher flow velocity, leading to a modified velocity profile, drag force, and increased CNT deflection.

The flow velocity and the CNT deflection along the CNT height were also modeled as a function of the input fluid flow velocity (Figure 6-40d-f). At increased velocities, not only do drag forces increase ($F_D \sim u^2$, Equation (6-21)), but the boundary layer height is thinner. This results in larger CNT deflections, and demonstrates that fluid velocity has a much greater influence on deflection than the position of the nanotube on the substrate.

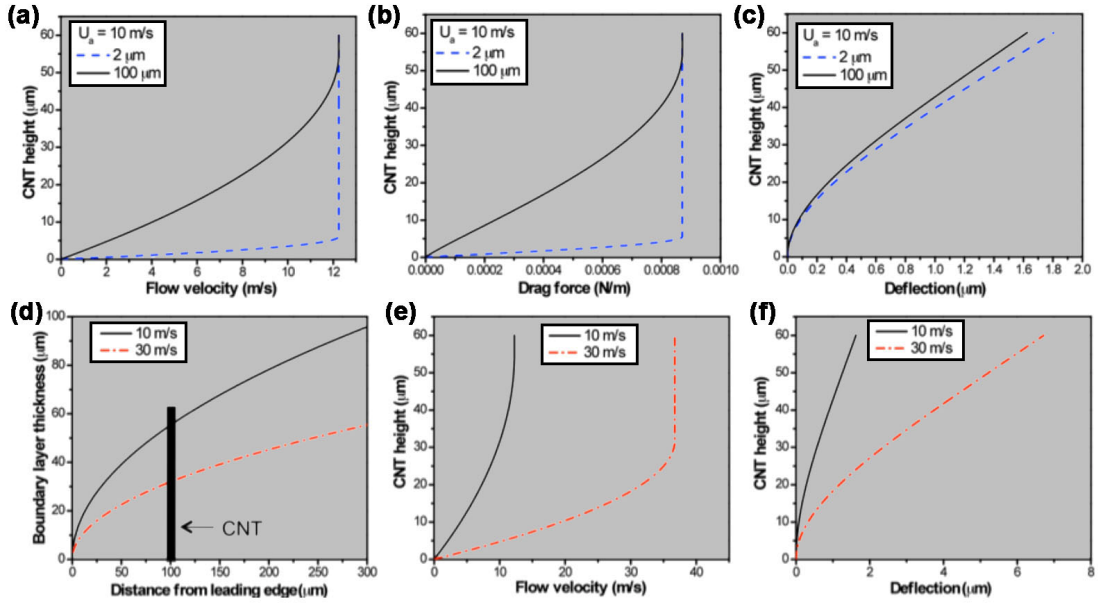

Figure 6-40: (a-c) Simulations of fluid velocity, drag force, and CNT deflection along CNT height for CNTs placed 2 and 100 μm from the leading edge of the substrate. (d-f) Simulations of flow velocities of 10 m/s and 30 m/s, for CNTs 100 μm away from the leading edge.

6.2.4.3 Determination of the Flexural Rigidity

In order to obtain the flexural rigidity of the nanotube mats, the deflections calculated using our simulations were compared to the experimentally measured deflections. Using the two experimental methods (laser intensity measurement and CCD imaging, Figure 6-37 and Figure 6-38), deflections for nine different patterned nanotube samples were measured. These samples had a range of dimensions and were studied under a range of fluid flow velocities, listed in Table 6-6.

Table 6-6: Nanotube sample dimensions, positions on substrate, and velocity ranges used for deflection measurement tests

Sample Number	Measurement technique	CNT Length	Pattern Size	Leading Edge	Velocity Range
1	Laser	40μm	5x5μm	75μm	0-58 m/s
2	Laser	50μm	5x5μm	1000μm	0-51 m/s
3	Laser	50μm	5x5μm	1000μm	0-51 m/s
4	Laser	50μm	5x5μm	1000μm	0-27 m/s
5	Laser	50μm	5x5μm	1000μm	0-50 m/s
6	CCD	40μm	5x5μm	200μm	0-64 m/s
7	CCD	40μm	5x5μm	200μm	0-64 m/s
8	CCD	35μm	7x7μm	1μm	0-58 m/s
9	CCD	60μm	5x5μm	1000μm	0-44 m/s

In order to match the deflections predicted by our simulation to the experimentally observed deflections, the flexural rigidity values were used in the model were varied. The average error between the modeled deflections and the experimental results was obtained for each EI value tested, and the best fit EI value was obtained (the one giving simulated deflections most closely matching the experimentally observed deflections). In order to optimize this fitting process, a broad initial range of EI values was initially tested and a relatively coarse step size between value was used. As this process converged on the best fit flexural rigidity, the range was decreased and the step sizes were further reduced.

Figure 6-41 shows results of this process. Flexural rigidities were obtained using deflections measured via laser intensity variations (Section 6.2.4.1). Data from five different CNT mats (Figure 6-41a) was fit to an *EI* value of ~ 7.9 x 10^{-16} Nm^2. Deflections measured using the CCD method had a best fit *EI* value of ~ 7.0 x10^{-16} Nm^2 (Figure 6-41b). The very close agreement between the *EI* values obtained from two separate experiments again attests to the consistency of the two methods. The

average flexural rigidity for all the measured data points was 7.56 x 10^{-16} Nm^2, and the solid lines in Figure 6-41 represent the deflections predicted as a function of air velocity using our simulation (Section 6.2.4.2) with this EI value.

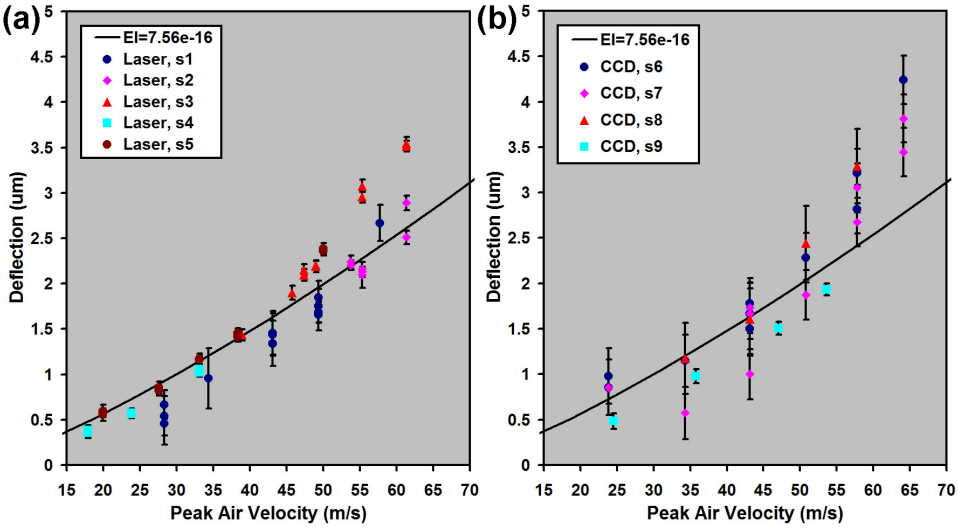

Figure 6-41: (a) Deflections of CNT mats obtained through laser intensity variations, plotted as a function of air velocity, for five different CNT samples (s1-s5). Numerical simulation was used to obtain the EI fit to the data. (b) The deflections were also measured through CCD image processing (s6-s9), and were compared using the same EI value fitted from (a)

The error in the *EI* determination has a very small (~ 10%) contribution from factors such as CNT diameter, length and spacing variation, and mainly arises from the resolution of nanotube deflection, which can be further improved. Further error could arise due to the Logarithmic Overlap Law [596], as the velocity profile close to the wall surface is generally difficult to determine due to the combination of turbulent and laminar stresses. Therefore, we also estimated the errors in *EI*s, fitted from both (i) pure turbulent and (ii) pure laminar velocity profiles. It was seen that the differences of *EI* for cases (i) and (ii) was between 1% and 10%. The exact error depended on the sample position, and increased as the sample position was moved

further away from the leading edge of the substrate (differences between turbulent and laminar flow become more pronounced as the flow developed, i.e. further downstream).

For comparative purposes, we also estimated the flexural rigidity by calculating the value of the moment of inertia, *I*, using the parallel axis theorem (Equation *(6-23)*).

$$I = \sum I_n + A_n d_n^2 \qquad (6\text{-}23)$$

We calculated the moment of inertia for a 5 μm square mat to be ~$5x10^{-24}$ m^4. With a nanotube elastic modulus ~1 TPa, a flexural rigidity of ~$5x10^{-12}$ Nm^2 was calculated, four orders of magnitude higher, than found in the current work. However, the elastic modulus for nanotube mats loaded in compression normal to the tube axes (in the same direction as the drag) was found to be ~0.16 GPa (for tubes grown using floating-catalyst CVD, see Section 6.1.1). While van der Waals forces between the nanotubes within the mats could be operative, sliding between adjacent CNTs is also feasible. Consequently, a nanotube mat could exhibit a much lower resistance to deflection than a rigid array. Using an *E* of 0.16 GPa, an *EI* ~$8x10^{-16}$ Nm^2 is obtained for 5 μm x 5 μm square pattern, in close agreement with our experimental results (7.56 $x10^{-16}$ Nm^2). Flexural rigidity (*EI*) values would be expected to transition from one extreme of a single, isolated nanotube to another extreme of a sufficiently large mat, where increasing mat size would provide no additional resistance to bending, due to the sliding of CNTs.

The modulus of nanotubes grown using thermal CVD (the same process as those used for this fluid flow investigation) was also investigated using in-situ testing methods (Section 6.2.1), however, these samples were only measured in the direction parallel to the tube axis. In this direction, the measured modulus was significantly smaller than that for floating catalyst nanotubes (E~16 MPa, see Section 6.2.1). Using the same moment of inertia estimated above and this thermal CVD modulus value gives a flexural rigidity of only ~8×10^{-17} Nm^2, lower than that measured in this experiment. During the measurement of this modulus value (with loads applied parallel to the tube axis), significant buckling was observed, resulting in the very low calculated stiffness. In this flexural rigidity work, the loading due to drag forces is applied laterally, and for the deflections measured no buckling is expected to occur as a result of these drag forces (the nanotubes behaved like fixed end cantilevers). As a result of the different loading directions, the low modulus value measured for thermal CVD nanotubes in Section 6.2.1 should not be applied towards predicting the flexural rigidity, and would provide an inaccurate, underestimated value due to buckling.

There have been a few theoretical studies on the flow of fluids through nanotube mats, and expressions for the coefficient of drag (determined through these simulations) were fit to a power law expression in the form of Equation (6-24).

$$C_D = \left(\frac{a}{\mathrm{Re}^b} \right) \qquad (6\text{-}24)$$

Walther *et al.* [594] used non-equilibrium molecular dynamics to model water flow past single-walled nanotubes, and report good agreement with the macroscopic

Stokes-Oseen equation. While the flow velocities used were similar to those in our own experiments, both the nanotube diameter and the array density were smaller. In this work, the drag coefficient (C_D) values obtained were fit to Equation (6-24) with a=9.0158 and b=1.0708.

The flow of liquid argon around both single- and double-walled nanotubes was investigated by Tang *et al.* [597], who found that the drag was higher than predicted using continuum equations. Non-equilibrium molecular dynamics were used and the drag results were also fit to Equation (6-24), with a=12.354 and b=0.9887. In another study, Ford and Papavassiliou [598], used computational fluid dynamics (CFD) based simulations to study water flow around an array of nanotubes. The use of CFD allowed larger systems to be studied, and drag coefficient results were presented for simulations of flow through nanotube arrays of different volume fractions, φ. Drag coefficient results from this work were fit to an expression of the form given by Equation (6-25). Using a no-slip assumption, the drag coefficient on the nanotube surface was given by a=86.7 and b=0.287, in Equation (6-25); with a slip assumption the coefficients of the fit were found to be a=39.9 and b=0.175. It is to be noted that C_D in all these cases is inversely proportional to the Reynolds number, Re.

$$C_D = \left(\frac{a}{\mathrm{Re}} \right) \phi^b \qquad (6\text{-}25)$$

It is important to note the differences between these earlier studies and Equation (6-20), that we have used. The model used in this work has assumed infinitely long cylinders (which implies uniform velocity over the entire nanotube

height), and was constructed under the assumption of no-slip on the tube surface. Probing further into these issues, we have taken two additional steps for determining C_D. First, the Knudsen number was used to correct the initial expression (Equation 2) for the coefficient of drag to account for slip conditions on the tube surfaces. Secondly, due to the finite length of our nanotubes, the fluid velocity to which the CNTs are exposed is not constant along the entire height (with lower velocities within the boundary layer). To account for this, our calculations subdivide the nanotube height (h) into N individual segments, each of length, Δy and use the appropriate velocity for each segment (determined using the modeling described in Section 6.2.4.2). For $N \geq 100$, errors in calculated deflections were less than 0.01% (with lower N tending to under-estimate the drag forces). In order to account for the varying velocities along the nanotube heights, while avoiding additional complexity in our model (which would not improve our results), the CNTs were divided into 100 segments along their length in this work. The fluid velocity, drag coefficients, and drag force were calculated for each segment, using the process described in Section 6.2.4.2. With this approach, the Stokes-Oseen equation used (Equation (6-20), with the Knudsen number correction) was seen to be an adequate choice for our experiments.

A close correspondence was observed between the experimental results and drag results given in published non-equilibrium molecular dynamics [597] and computational fluid dynamics simulations [598]. The nanotube deflections were well approximated by Equation (6-20) (Figure 6-42). Using an average flexural rigidity of

$7.56x10^{-16}$ Nm^2 obtained above, nanotube deflections were simulated using the drag model developed in this work, as well as with previous studies of fluid flow past nanotubes reported in the literature.

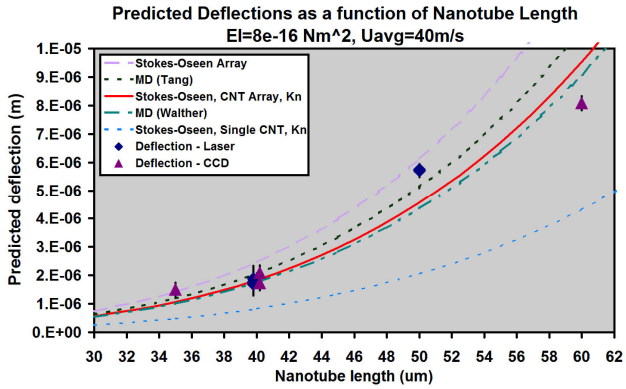

Figure 6-42: Our experimental results are modeled well by considering a Knudsen number (Kn) modified Stokes-Oseen expression and appropriate molecular dynamics and fluid mechanics simulations

6.2.4.4 Flow Sensors and Time-Dependent Response

We propose that our technique can be adapted for a novel CNT based gas flow sensor. To this purpose, the light transmission as a function of flow velocities for both air and argon were measured and are compared in Figure 6-43. The drag forces (Equation (6-21)) on a nanotube exposed to fluid flow are a function of the nanotube dimensions (C_D and A), and the fluid properties (u and ρ). For a given nanotube sample is subjected to flow from two different fluids at the same velocity, the drag forces and corresponding deflections (x) will be vary linearly with the fluid density ($x_1/x_2=\rho_1/\rho_2$). To investigate this, variations in transmitted laser intensities were recorded on the same sample under flows of either argon or air at varying velocities. Under conditions with fixed temperature (T) and pressure (P), the density ($\rho=MP/RT$)

of a gas is proportional to its molecular weight (*M*). As a result, for exposure to a different fluid (argon), the deflection at a given velocity is expected to scale with the ratio of the densities of the two fluids used. A relation was obtained between the measured deflections of the nantoube sample and the air flow velocity; this fit was then scaled by the ratio of the average molecular mass or density of argon to air (~1.37), and was found to be in excellent agreement with the deflections measured under argon flow (Figure 6-43).

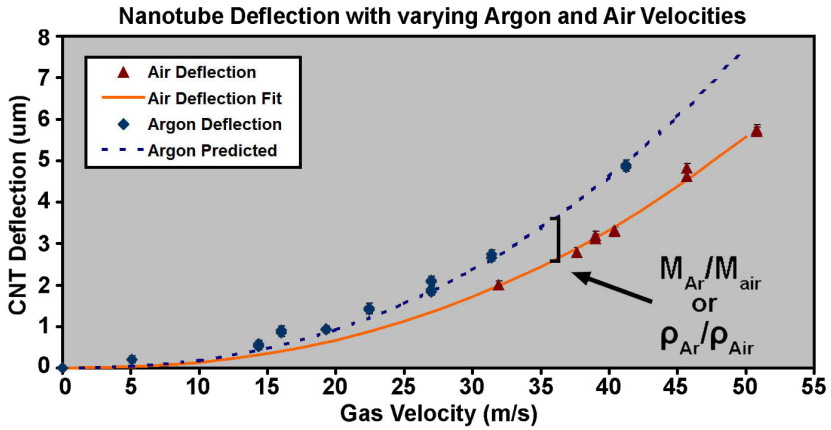

Figure 6-43: Deflections calculated via light transmission as a function of flow velocity of air and Ar were plotted and compared. A fit relating deflection to air velocities was scaled by the ratio of the density of argon to the density of air, and is in excellent agreement to the observed deflections under argon flow. The sample is a 55-μm CNT array and the fitted EI is $7.8 \cdot 10^{-16}$ Nm^2.

Using this same approach, any nanotube sample can be calibrated using a known gas (with the velocity-deflection relation obtained either experimentally or by using our model). With this calibration, the nanotube sample could then be used to accurately measure the velocities of any other fluid by simply scaling the velocity-deflection relation by the density ratio between the reference fluid and the test fluid.

In addition to this versatility, our approach offers excellent spatial resolution and can be used to measure velocities within the boundary layer region. In this work, the laser was focused to a ~30μm spot, and the deflections measured represented an average deflection of the nanotube arrays within that spot. This spot size could be further reduced, and velocity measurements could be taken from different locations on a surface spaced only tens of microns apart (limited by the accuracy with which the laser could be positioned).

When testing the mechanical response of nanotube forests to applied fluid flows, it was noticed that in most cases the measured later intensities returned to their baseline intensity immediately on the termination of fluid flow. However, for high velocity flows, or during tests using fluids with higher densities (argon), a slight time-dependent recovery was observed (Figure 6-44). This response was fit with Equation *(6-26)* (used to model creep responses in polymers [586]), and a time constant of $\tau \approx$ 0.1-0.2 seconds was obtained. This indicates that even under larger deflections, the recovery of these nanotube mats is still fairly quick, and this would allow numerous sequential measurements to be taken in rapid succession (such as for studies of fluid flow variations with time).

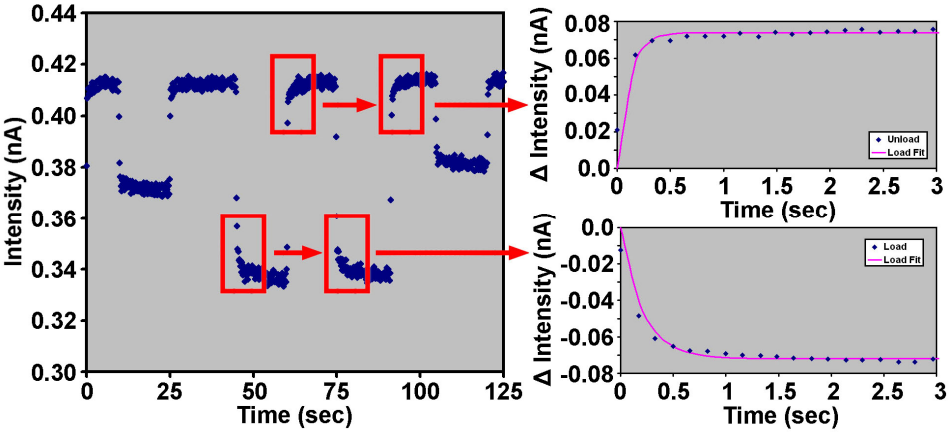

Figure 6-44: Time-dependent recovery observed in aligned carbon nanotube mats subjected to fluid drag forces

$$I(t) = I_0\left(1 - \exp\left(-t/\tau\right)\right) \qquad (6\text{-}26)$$

In this study, two simple and consistent methods were demonstrated for measuring the deflection of patterned arrays of carbon nanotubes subject to drag force, due to fluid flow. By modeling the fluid flow across the nanotubes, numerical values for the flexural rigidity (*EI*) values, a quantity pertinent to mechanical deformation such as buckling and deflections were obtained. Consistent flexural rigidities (with an average value of 7.56×10^{-16} Nm^2) were obtained for a number of different nanotube samples over a range or measurement configurations. The flexural rigidity of carbon nanotube mats has not been widely studied to date (through either simulation or experimental approaches), and in this work we present some of the first ever experimental measurements of this value [599]. In addition, we developed two optical methods that would be suitable for mechanical characterization of carbon nanotubes and other nanostructures.

With flow-deflection calibration (demonstrated in Figure 6-43), the techniques described in this work could also be adapted as the basis for the characterization of

nano-scale flow, and for various applications, including shear force sensors for boundary layer measurements, micro- and nano-fluidics, and high sensitivity tactile sensing and gas sensing, which has been demonstrated in this study. In addition, following an initial calibration, flow measurements could be made with a wide range of fluids with a simple correction for density.

6.3 Production of Bulk nanotube-based materials

An important obstacle that must be overcome for many carbon nanotube-based applications is to ensure that the beneficial properties of individual nanotubes are translated to macroscopic materials. One approach towards retaining the exceptional mechanical properties of carbon nanotubes is the processing of mats of aligned tubes into yarns and sheets of pure nanotubes. This process involves the careful drawing of nanotubes away from the mat in a manner that leads to the pulling away of adjacent tubes. This sequence continues, forming nanotube sheets that can also be twisted and spun into ropes (see Section 2.7.2.2). Although the fabrication of pure nanotube paper materials was demonstrated and reported previously in this work (described in Section 6.1.5), the particular process used for these yarns and sheets results in considerably improved alignment and interactions between nanotubes, resulting in higher strength and reduced tube slippage under tensile loading.

At the beginning of this project (2006), the only thermal CVD method that could consistently produce nanotubes utilized a liquid benzene carbon source (described in sections 3.1.3 and 5.2). These nanotubes (synthesized using this CVD process) were compared to those produced by the groups that had first reported this

spinning process. Under SEM observation, the nanotube mats look similar. However, at the nanometer scale, “spinnable” tubes were found to have straighter walls, smaller diameters, and did not have bamboo morphology, as observed in our product. This is shown in Figure 6-45.

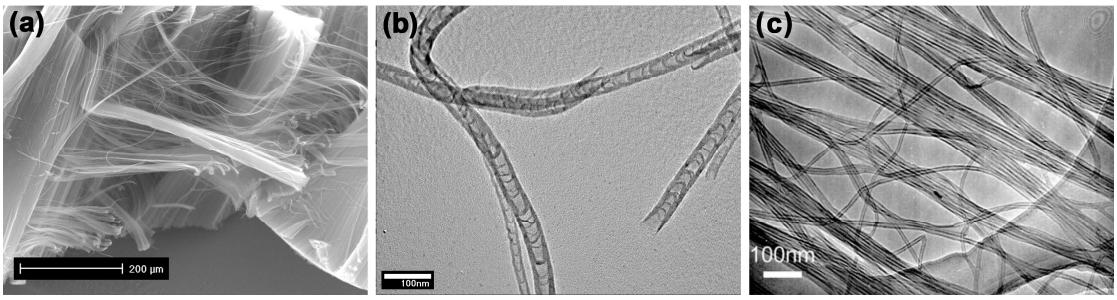

Figure 6-45: (a) SEM image of "spinnable" CNTs, (b) TEM image of bamboo CNTs grown in this work, (c) TEM images of "spinnable” CNTs [263]

To explore the causes for these differences, the growth conditions used by these groups were compared to those used in this work. All groups used similar thermal CVD techniques, and the growth reaction equipment was comparable to that used in the current work, so only the major differences in growth parameters were considered; these are listed in Table 6-7.

Table 6-7: Comparison of important CVD synthesis parameters for reported "spinnable" CNTs and the method used in the current work

Parameter	Jiang, *et al* [213, 263]	Zhang, *et al* [203, 204]	Li, *et al* [189, 201]	2006 Growth Parameters
Catalyst	3.5-5.5nm Fe	~5nm Fe	~1nm Fe	5nm Ni, Fe
Carbon	C_2H_2	C_2H_2	C_2H_4	Benzene
Gas	Ar or H_2	He	Ar, H_2, H_2O	Ar, NH_3
Pressure	Atm. or 2 torr	Atm.	Atm.	Atm.
Temperature	620-700°C	680°C	730-780°C	850-900°C
Substrate	SiO_2 on Si	SiO_2 on Si	Al_2O_3 on Si	SiO_2, Si
Lengths	$\geq 100\mu m$	$\geq 200\mu m$	$\geq 300\mu m$	$\leq 150\mu m$
Spinnable?	Yes	Yes	Yes	No

No major differences are observed in the choice of catalysts (thin Fe films for all groups) and in reaction pressure (spinnable nanotubes have been produced at atmospheric pressure, so low pressure CVD is not a requirement). The choice of inert reaction gas does not appear to play a major role; however, the addition of ammonia in our work (intended to reduce amorphous carbon build-up, discussed previously) is not added in any other group's growth. This difference explains the bamboo morphology observed in our nanotubes but not in the "spinnable" nanotubes (see Section 5.4.2). The most important differences are in the choice of carbon source and the reaction temperature. During most of this study, benzene was used predominantly; the ring structure of benzene is very stable and benzene therefore requires higher temperatures to decompose and provide carbon for nanotube formation. The groups reporting "spinnable" nanotubes have used either acetylene or ethylene as a carbon source. The triple bond in acetylene is fairly unstable compared to other hydrocarbons, and both acetylene and ethylene have optimal growth temperatures which are lower than those used with benzene. This choice of carbon source allows for a significantly reduced reaction temperature, between roughly 620-780°C, rather than the 900°C typically used with benzene in this work.

Also of note is the smaller diameters of nanotubes found in "spinnable" mats. Similar thickness metal catalyst films have been used in all growth methods compared in Table 6-7. Catalyst particle size has been shown to closely relate to nanotube diameter, with smaller particles producing smaller nanotubes [143, 154, 188]. For a given quantity of starting catalyst material (a film of fixed thickness), the number of

discrete catalyst particles formed from this film will be inversely proportional to the volume of the particles. More numerous smaller particles will be packed closer together on the substrate surface; this will lead to a more tightly packed nanotube mat with increased van der Waals forces between adjacent tubes.

6.3.1 CVD Optimization for Spinnable CNTs

Due to poor initial growth attempts with acetylene (see Figure 5-11), ethylene was selected as the carbon source for this nanotube synthesis optimization. In addition, the use of very thin (< 2nm thick) catalyst films was found to result in inconsistent growth. Consequently, the thin iron catalyst films used in this study had thicknesses ranging from 3nm to 5nm, and were deposited on either SiO_2 or AL_2O_3 substrates. The other reaction parameters (atmospheric pressure, 750°C, argon gas with trace water vapor) were selected to mimic those condition used by other groups to grow “spinnable” tubes.

During this optimization process, several reaction variables were adjusted. The results of these experiments have already been presented (in sections 5.2.1, 5.3.1, and 5.4.2), and will just be briefly summarized here. The use of ethylene allowed for growth to be carried out at lower temperatures, and as a consequence of this, the coalescence of smaller catalyst particles into larger ones is reduced (relative to higher temperature reactions such as those using benzene). Nanotube growth rates are slightly increased with smaller catalyst particles and the higher hydrogen to carbon ratio in ethylene (compared to benzene) allows for growth at higher carbon source concentrations and without the use of other reaction gases (such as ammonia). As a

result, growth rates exceeding 100 nm/sec were achieved and this rapid growth continued for a longer duration (relative to the previous synthesis attempts using benzene). Nanotube samples as long as 200µm long were produced (see Figure 5-20), and these nanotube lengths have been reported previously as sufficiently long for spinning nanotubes into ropes.

The next important difference between the tubes grown previously and those synthesized for nanotube spinning is the much larger diameters of those tubes grown earlier in this work. Smaller tube diameters will result in reduced spacing between adjacent tubes, increasing van der Waals interactions between tubes in the mat. Four reaction parameters were found to significantly influence tube diameters (section 5.3.1), and growth was then optimized to produce the smallest nanotubes possible. The starting nanotube diameter is a function of the catalyst particle diameter, and to reduce this dimension, thinner catalyst films were used (3nm and 5nm rather than 10nm) and alumina covered substrates were selected over silica substrates. Iron catalyst on alumina substrates were previously found to grow via the base growth mechanism (section 5.2.2), and the increased catalyst-substrate interactions that lead to base growth could potentially interfere with the spinning process. However, recent reports [189, 201] have described the successful spinning of nanotubes supported on alumina substrates, so this interaction appears to play a minor role during spinning.

In addition to control over the initial catalyst particle sizes, the deposition of amorphous carbon (which can thicken nanotubes during growth) must be limited. Two reaction parameters were optimized to achieve this. First, excessive reaction

temperatures were observed to considerably thicken nanotube products (see Figure 5-36), and a growth temperature of 750°C for ethylene was used to avoid this unwanted deposition. In addition to minimizing the formation of amorphous carbon byproducts, lower temperatures also can slightly reduce the initial catalyst particle sizes by limiting particle movement and coalescence during heating. Secondly, the introduction rate of the carbon source must also be selected to avoid this unwanted carbon buildup. Consequently, the flow ratio of ethylene to argon was always kept below one for the overall volumetric gas flow rates used (300-500 sccm).

The final structural difference between those nanotubes that have been drawn and spun by other groups and the tubes initially produced in this work is the tube morphology. In order to achieve aligned growth of nanotubes with few impurities using benzene, the addition of ammonia gas to the reaction was found to be beneficial. However, earlier studies have demonstrated that while the hydrogen generated through ammonia decomposition inhibits the formation of amorphous carbon (section 5.3.2.2), the nitrogen leads to the growth of bamboo carbon nanotubes. Although it is unknown exactly how the bamboo structure could influence how spinnable carbon nanotubes may be (besides possibly increasing the flexural rigidity of the tubes), all of the reports of spinnable tubes have straight walls. To avoid the growth of nanotubes with bamboo morphology, ammonia was not used in any of these experiments.

The revised ethylene growth recipe was able to produce nanotube products with very similar characteristics to those reported in the literature as being “spinnable” (shown in Figure 6-46 and summarized in Table 6-8).

Table 6-8: Comparison of nanotube properties for spinnable CNTs [189, 201, 203, 204, 263], and nanotubes grown using two different methods in this work

Property	Spinnable CNTs	2006 Recipe	2008 Recipe
Length	> 100-200µm	Often < 150µm	Up to 200µm
Diameter	10-15nm or less	~40-50nm	~15-20nm
Morphology	Straight-walled	Bamboo	Straight-walled

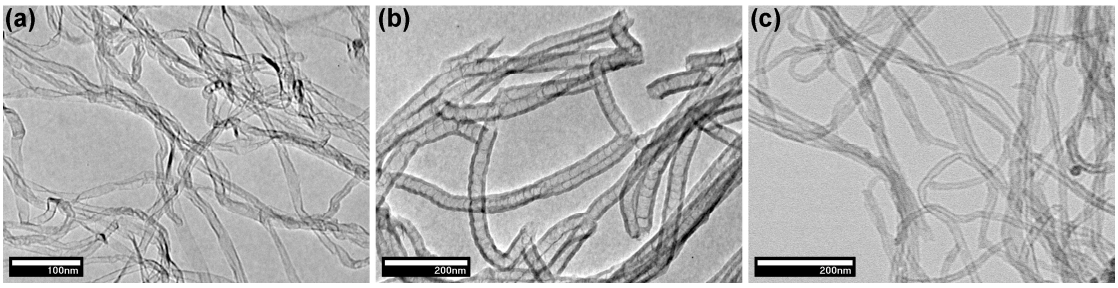

Figure 6-46: (a) "spinnable" carbon nanotubes, (b) thicker, bamboo nanotubes grown using the 2006 CVD recipe, (c) improved growth using the 2008 recipe

6.3.2 Development and Results of Spinning Process

Once the nanotube synthesis process had been refined to allow consistent growth of nanotubes similar to those described in the literature, the actual spinning procedure was studied. As reported, the requirements for this process were relatively simple (Figure 2-49). The draw process is begun by contacting the side of a suitable nanotube mat with an appropriate probe (such as a wooden toothpick [204] or adhesive tape [203]). After contacting the nanotube mat, this probe is drawn away in a direction parallel to the substrate surface (perpendicular to the nanotube axis), although once the process has been initiated, the draw angle (relative to the tube axis) can be adjusted [204]. Nanotube sheet or yarn material can be drawn from the mat a speeds of up to 5 cm/min [201], and rotational speeds of ~2000rpm (provided by a motor, see Figure 2-49) are used to twist the yarn during fabrication. The maximum

possible length that can be achieved is governed by the size of the substrate, with yarns lengths of ~50m consuming roughly a $1cm^2$ area of nanotube mat [204].

In the current work, two devices were built to facilitate this drawing process. The first apparatus could be affixed to the sample stage within the SEM to allow spinning attempts to be made in-situ. The second device consisted of two linear translation stages, and was sized so that it could be operated while viewing the sample using a stereo microscope (to allow for more precise control over sample and probe positioning). In addition, different probes (metal, plastic, wood, or adhesive tape) could be used, and a variable speed dc motor could be attached to introduce a twist in addition to the linear draw. Reports from the literature on this process have indicated that the initial contact between the probe and the nanotubes should occur on the side of the mat (rather than at an angle or at the top). Even with the synthesis refinements described in section 6.3.1, the nanotubes used in this work were no longer than ~200µm, and the accurate positioning of the probe on the mat edge was difficult. To simplify this, both the devices used were designed to allow precise vertical adjustment of the sample (in addition to the linear translation of the probe away from the sample).

The first device built was based on the apparatus used for in-situ tension and compression testing inside the SEM (see section 6.1.2). However, rather than using the SEM stage to position the nanotube sample (against a stationary load cell), the sample was kept stationary, and an attachment was built to affix a dc motor to the SEM stage (Figure 6-47). With this set-up, a probe attached to the motor could be moved relative to the sample, and an electrical feed-through (used previously for the

load cell signal), provided power to the motor. Either plastic or metal probes could be used, and all plastic parts (including those supporting the motor) were sputter-coated with a thin gold layer to prevent charging under the beam.

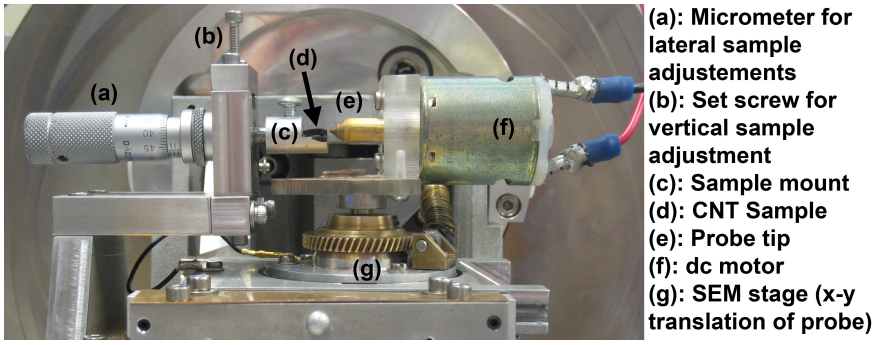

Figure 6-47: Apparatus designed for in-situ nanotube spinning attempts

The motor was found to operate inside the SEM without issue, and the only drawback was relatively blurry imaging due to vibrations and slight misalignment of the probe while the motor was running (Figure 6-48a,b). Each probe was shaped to a sharp point using sandpaper; however, while probe surfaces appeared smooth at a macroscopic level, at the microscopic level they were still fairly rough (Figure 6-48c), and the probe roughness is important for the spinning process [201].

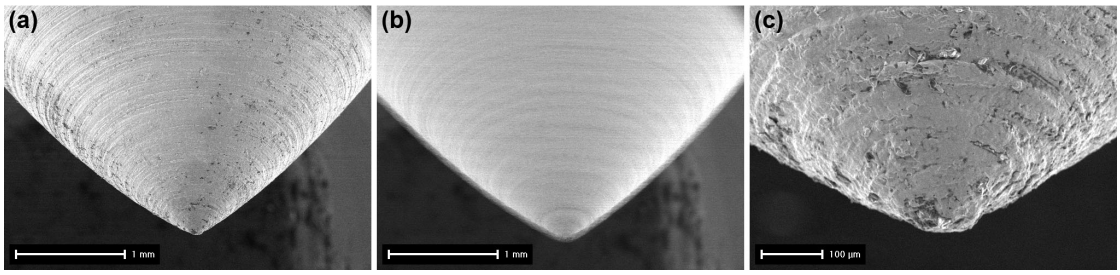

Figure 6-48: (a) low magnification view of metal probe tip, (b) spinning probe, (c) magnified view of probe tip showing roughened surface

Attempts at spinning nanotube sample into ropes using this in-situ device were not successful. One of the main challenges was the accurate vertical positioning of the

nanotube sample and the probe tip. Vibrations (arising due to some compliance in the SEM stage and motor mount) and the difficulties of fabricating the probe point exactly on-center with the motor axis made it hard to achieve controlled contact between the probe tip and the nanotubes for short CNT mats. In many cases, the spinning probe would make contact with the substrate and damage the nanotube mat.

To avoid this, longer floating catalyst nanotube samples were used. However, all spinning attempts on these nanotube mats resulted in the "drilling" of the probe tip into the nanotube mat, with no nanotube material draw away from the mat when the probe was removed (Figure 6-49).

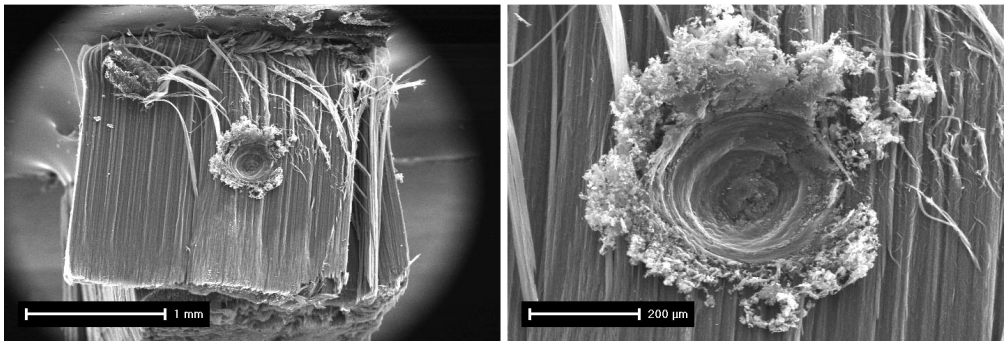

Figure 6-49: In-situ spinning results for floating catalyst CVD nanotubes

While the in-situ approach provided excellent imaging of the nanotube mats before and after spinning attempts, the process for vertically centering the probe on the mat edge was tedious. For each new sample, fine tuning the vertical position involved imaging the sample, venting the SEM chamber and making a fine adjustment in the sample height, then pumping the chamber and imaging the new position. To avoid this process, a new device was designed to give accurate vertical and controlled horizontal translation outside of the SEM (Figure 6-50). Two fixtures were designed

to allow either a motor with a sharpened probe tip or a stationary piece of adhesive to be attached to the horizontal stage.

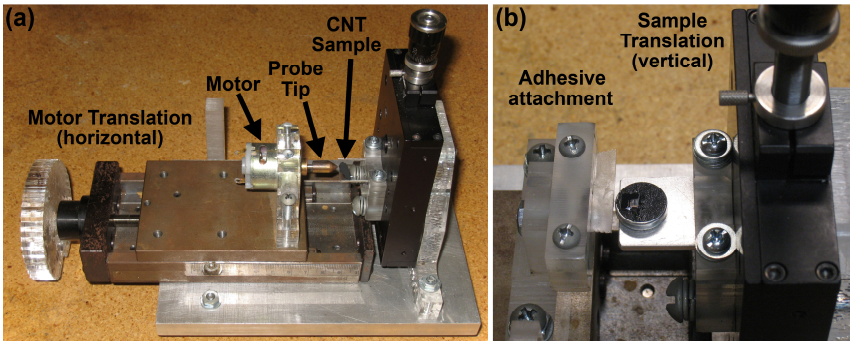

Figure 6-50: Dual linear translation stages used to adjust sample and probe positions during spinning and drawing attempts

Because this device was not constrained to fit within the SEM chamber, a more robust motor support was built, which largely eliminated the vibration problem observed during the in-situ tests. This improvement did not eliminate the issue of centering the sharpened probe tip on the motor axis, and the probe rotation was still slightly eccentric. Nevertheless, attempts were made to spin thermal CVD nanotubes using this apparatus (floating catalyst nanotubes were not considered due to the poor results in the in-situ tests). A cylindrical wooden toothpick (similar to that used in [204]) was attached to the motor for spinning trials, and adhesive scotch tape was used to replicate the nanotube sheet fabrication procedure (described in [203]). In both cases, some nanotube material became attached to the probe or adhesive surface (Figure 6-51); however, none of the attempts was able to produce nanotube yarns or sheets.

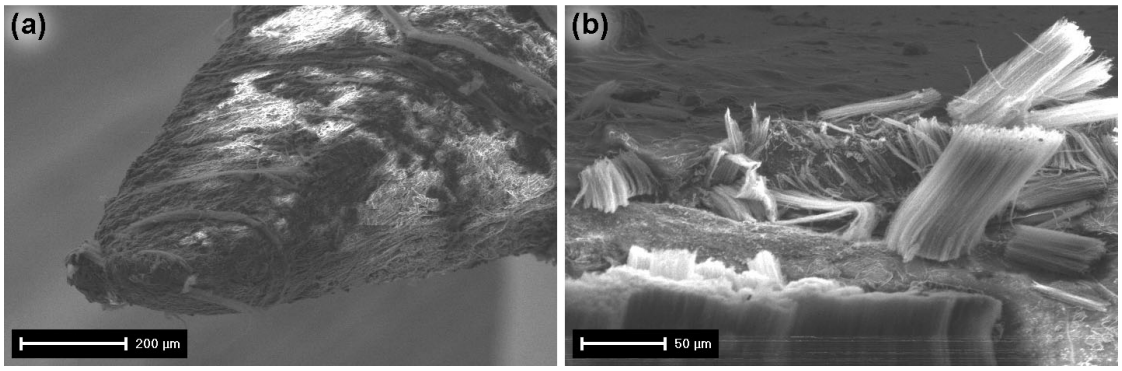

Figure 6-51: Results of spinning and drawing attempts using (a) a wooden toothpick probe, and (b) adhesive tape

Although the nanotube synthesis method used in this work was refined (producing nanotubes similar in appearance to spinnable tubes, Figure 6-46), attempts to produce macroscopic nanotube-based material using the spinning procedures described in the literature were not successful. In these papers, the alignment of nanotubes within the mat and the cleanliness of the tubes have been described as critical factors in spinnable tubes [263]. The literature does not report any measurement of this alignment, and characterization results (such as Raman spectroscopy data to quantify impurity content) are not given. The crowding mechanism has been proposed as the source of this alignment, and tightly packed catalyst particles (on the substrate) have been reported to improve alignment to produce spinnable tubes. However, the mechanism by which these improved catalyst particles are obtained has not been adequately described, and the substrate and catalyst preparation procedures reported in the literature are quite commonplace [263]. While the synthesis conditions used in this work have been optimized to reduce nanotube diameters and to minimize the formation of unwanted byproducts, it appears that

other, unreported reaction parameters play an important role in the growth of spinnable nanotubes.

Chapter 6, in part, is a reprint of the material as it appears in:

Deck, C. P., Flowers, J., McKee, G. S. B., Vecchio, K. S., “Mechanical behavior of ultralong multiwalled carbon nanotube mats”, *Journal of Applied Physics*, v.101, 023512 (2007)

Deck, C., Ni, C., Vecchio, K., Bandaru, P. R., “Optical Determination of the Flexural Rigidity of Carbon Nanotube Ensembles”, *Applied Physics Letters,* v.92, 173106 (2008).

The dissertation author was the primary investigator and author of these papers.

7. Conclusions

In this work, carbon nanotubes were successfully produced using a wide range of reaction conditions, and several approaches were used to optimize this synthesis and to characterize the nanotube products.

The growth methods used in this research differed in two distinct aspects: the manner in which the catalyst material was introduced, and the phase of the carbon source used for growth. In floating catalyst chemical vapor deposition (CVD), the catalyst material was dissolved into a hydrocarbon solution, and these reactants were fed directly into the growth chamber. Long nanotube mats were produced (up to ~6mm length), and growth rates were relatively constant for extended reaction durations. Growth of nanotubes synthesized using this method initiated at the substrate surface, and mats containing numerous distinct layers could be formed by varying the reactant flow.

Thermal chemical vapor deposition growth used catalyst materials which were deposited on the growth substrates prior to synthesis. Nanotubes were produced using several different catalyst metals, and these metals were put down either through thin film deposition or by using a solution approach. Either liquid or gaseous carbon sources could be used with this method, and in both cases, a rapid initial growth rate was observed which slowed as the reaction progressed and the catalytic activity of the metal particles was diminished. This transition occurred due to amorphous carbon build-up on the catalyst particles, and as a result of this poisoning, nanotube growth was limited to ~200μm lengths.

This effect could be reduced by optimizing the reactant gas composition used during synthesis. The introduction of either hydrogen or ammonia was found to reduce the rate of amorphous carbon deposition, and by examining nanotubes grown under different conditions, it was found that an amorphous carbon coating of roughly 3-6nm was sufficient to completely terminate growth.

In addition to optimizing synthesis conditions to produce longer carbon nanotubes, the effects of different reaction parameters on nanotube diameters were studied. Using thermal CVD, nanotubes were grown from catalyst films with thicknesses ranging from 2-50nm. Diameters were found to increase (from ~20nm to ~80nm) with increasing film thickness; however, this trend did not continue for very thick films (50nm). Interactions between the catalyst and substrate surface were observed to influence both nanotube diameter and growth mechanism, with stronger metal-substrate interactions producing smaller tubes which formed via the base growth mechanism. To further investigate this, atomic force microscopy was used to measure surface roughness of several metal-coated substrates, which had been heated to reaction temperatures. A significant dependence of particle size on temperature was observed, and subsequent growth of nanotubes confirmed this relation. Increased reaction temperatures resulted in both increasing particle sizes (controlling the initial nanotube diameters), but also increasing nanotube outer diameters (which thickened due to amorphous carbon deposition). A similar effect was obtained by increasing the introduction rate of the hydrocarbon used during synthesis. Through control of these parameters (catalyst film thickness, substrate material, reaction temperature, and

carbon source introduction), the inner and outer nanotube diameters could be independently controlled.

Another important aspect of synthesis was the reaction gas composition. The use of ammonia had previously been identified as a means to reduce the deposition of amorphous carbon and prolong growth. Tubes grown under these conditions, however, were found to have a distinct compartmentalized structure. The introduction of nitrogen (through the use of ammonia) was identified as the cause of this bamboo morphology, and pyridine (C_5H_5N) was also found to produce a similar effect. Through careful introduction of these substances, nanotube wall thicknesses could be controlled and the tube morphology could be changed during synthesis (from straight-walled to bamboo). A study of the effects of varying ammonia or pyridine concentrations was used to find optimal growth conditions and to identify the exact mechanism by which nitrogen leads to this bamboo morphology.

Following this work to optimize growth and to control nanotube dimensions and morphology, a series of experiments were designed to investigate the material properties of these tubes. The first studies were performed on tubes grown via floating catalyst CVD, as the larger scale (several mm) of these products allowed for a number of characterization methods to be applied. One of the main areas of interest was to determine the mechanical properties of as-grown nanotube mats. In this work, nanotubes were synthesized in the form of well-aligned arrays of tubes supported by the growth substrate. A straining stage was design to fit inside an SEM to allow for in-situ compression and tension testing of these samples. As expected, the observed

modulus was considerably higher in tension (~28 GPa compared to ~670 MPa in compression). These tests also revealed that the mat structure in floating catalyst CVD products is discontinuous, with many separate tubes contributing to the overall mat height. This structure contributed to a distinct time-dependent stress relaxation that was observed during both compression and tension tests.

The relatively large quantities of products obtained from floating catalyst synthesis also allowed some simple electrical testing to be performed. Nanotube samples were grown under a range of synthesis conditions (with both bamboo and straight-walled morphologies and with varying catalyst concentrations) and were processed to form nanotube paper (mats of randomly aligned tubes). Measurements of these samples indicated electrical resistance increased as the catalyst concentration went up (due to accumulation of impurities within the mat), and resistance was also higher in bamboo nanotubes (as a result of misalignment between the graphitic lattice in the tube walls and the nanotube axis). These results, along with the methods that were discovered to produce this bamboo morphology could lead to control over the electrical properties of nanotubes by simply adjusting reaction conditions during growth. While a more complete investigation of the electrical properties of carbon nanotubes was beyond the scope of this work, this is one area where further investigation could help develop this potentially powerful method to control nanotube properties.

Nanotubes produced using the thermal CVD procedure were also characterized using multiple approaches. Although mats of tubes grown using this method were

typically much shorter that those obtained using floating catalyst CVD, compression tests (using the same in-situ approach) were attempted, and two distinct regions were observed in the stress-strain response. Initially the nanotube mats were very compliant, and uniform buckling could be observed. Once the mats had been compressed to large strains (up to ~75%), sufficient densification had occurred and the response became significantly stiffer (the modulus increased over fifty-fold).

The separation of the catalyst deposition and nanotube growth stages in thermal CVD also allowed the catalyst regions to be patterned. The well aligned nanotube mats produce in this work were found to polarize light transmitted through them, although the light intensity was reduced considerably (a drop of ~10^5). An experiment was designed to take advantage of this low light transmission in order to measure the flexural rigidity of carbon nanotube arrays. In this study, patterned nanotubes were subjected to fluid flow, and the resulting drag forces caused the nanotubes to deflect as a function of the applied fluid velocity. This deflection was measured experimentally by monitoring changes in the intensity of a laser passed through these mats. In addition, the deflection was modeled by simulating the fluid flow and drag forces acting on the tubes and then by treating the nanotubes as fixed end cantilever beams to solve for defections. Comparisons between the experimental results and our model led to the determination of the flexural rigidity of these mats, and EI was ~7.5×10^{-16} Nm^2. The experimental set-up used also demonstrated a potential fluid flow or shear force sensor, and consistent measurements were obtained using two different fluids over a range of velocities.

The final part of this work investigated methods to process as-grown nanotubes into macroscopic, nanotube-based, bulk materials. Other groups have reported previously on this topic (spinning mats of tubes into yarns and sheets); however, the tubes used in these studies differed in several important aspects from those synthesized in this work. Towards the goal of successfully producing these bulk materials, the growth conditions used were significantly modified to synthesis tubes that were longer, narrower, and had a straight-walled morphology (matching those reported elsewhere). Two devices were also constructed, to allow for the particular spinning processing conditions to be replicated. However, attempts to produce macroscopic materials out of our nanotube samples were unsuccessful, and further work is needed in this area to identify additional growth parameters and nanotube properties that are critical towards producing these bulk materials.

8. References

1. Kroto, H.W., et al., *C60: Buckminsterfullerene.* Nature, 1985. **318**(6042): p. 162-163.

2. Krätschmer, W., et al., *Solid C60: a new form of carbon.* Nature, 1990. **347**(6291): p. 354-358.

3. Iijima, S., *Helical microtubules of graphitic carbon.* Nature, 1991. **354**(6348): p. 56-58.

4. Monthioux, M. and V.L. Kuznetsov, *Who should be given the credit for the discovery of carbon nanotubes?* Carbon, 2006. **44**(9): p. 1621-1623.

5. Bacon, R., *Growth, Structure, and Properties of Graphite Whiskers.* Journal of Applied Physics, 1960. **31**(2): p. 283-290.

6. Baker, R.T.K., et al., *Nucleation and growth of carbon deposits from the nickel catalyzed decomposition of acetylene.* Journal of Catalysis, 1972. **26**(1): p. 51-62.

7. Baker, R.T.K. and P.S. Harris, *The Formation of Filamentous Carbon,* in *Chemistry and Physics of Carbon,* P.L. Walker and P.A. Thrower, Editors. 1978, Marcel Dekker, Inc.: New York. p. 83-165.

8. Baker, R.T.K., et al., *The formation of filamentous carbon from decomposition of acetylene over vanadium and molybdenum.* Carbon, 1983. **21**(5): p. 463-468.

9. Baker, R.T.K., et al., *Formation of filamentous carbon from iron, cobalt and chromium catalyzed decomposition of acetylene.* Journal of Catalysis, 1973. **30**(1): p. 86-95.

10. Baker, R.T.K., et al., *The production and properties of filamentous carbon.* Carbon, 1975. **13**(3): p. 211-214.

11. Oberlin, A., M. Endo, and T. Koyama, *Filamentous growth of carbon through benzene decomposition.* Journal of Crystal Growth, 1976. **32**(3): p. 335-349.

12. Bethune, D.S., et al., *Cobalt-catalysed growth of carbon nanotubes with single-atomic-layer walls.* Nature, 1993. **363**: p. 605-607.

13. Iijima, S. and T. Ichihashi, *Single-shell carbon nanotubes of 1-nm diameter.* Nature, 1993. **363**: p. 603-605.

14. Buseck, P.R., S.J. Tsipursky, and R. Hettich, *Fullerenes from the Geological Environment.* Science, 1992. **257**(5067): p. 215-217.

15. Daly, T.K., et al., *Fullerenes from a Fulgurite.* Science, 1993. **259**(5101): p. 1599-1601.

16. Becker, L., et al., *Fullerenes in the 1.85-billion-year-old Sudbury impact structure.* Science, 1994. **265**(5172): p. 642-645.

17. Murr, L.E. and P.A. Guerrero, *Carbon nanotubes in wood soot.* Atmospheric Science Letters, 2006. **7**(4): p. 93-95.

18. Reibold, M., et al., *Carbon nanotubes in an ancient Damascus sabre.* Nature, 2006. **444**: p. 286.

19. Murr, L.E., et al., *Chemistry and nanoparticulate compositions of a 10,000 year-old ice core melt water.* Water Research, 2004. **38**: p. 4282–4296.

20. Lau, K.-T. and D. Hui, *The Revolutionary creation of new advanced materials - CNT Composites.* Composites: Part B, 2002. **33**: p. 263-277.

21. Ouyang, M., et al., *Energy Gaps in "Metallic" Single-Walled Carbon Nanotubes.* Science, 2001. **292**: p. 702-705.

22. Lebedkin, S., et al., *Single-wall carbon nanotubes with diameters approaching 6 nm obtained by laser vaporization.* Carbon, 2002. **40**(3): p. 417-423.

23. Li, G.D., et al., *Structural study of the 0.4-nm single-walled carbon nanotubes aligned in channels of AlPO4-5 crystal.* Carbon, 2002. **40**(6): p. 917-921.

24. Li, Y., et al., *Preparation and characterization of junction-like multiwall carbon nanotubes.* Carbon, 2003. **41**(2): p. 380-384.

25. Ding, D. and J. Wang, *Electron irradiation of multi-walled carbon nanotubes with encapsulated Ni particles.* Carbon, 2002. **40**(5): p. 797-799.

26. Gao, G., T. Cagin, and W.A. Goddard III, *Energetics, Structure, Mechanical and Vibrational Properties of single Walled Carbon Nanotubes (SWNT).* Nanotechnology, 1998. **9**: p. 184-191.

27. Dresselhaus, M.S., G. Dresselhaus, and R. Saito, *Physics of carbon nanotubes.* Carbon, 1995. **33**(7): p. 883-891.

28. Nelson, L.S. and N.L. Richardson, *Formation of thin rods of pyrolytic carbon by heating with a focused carbon dioxide laser.* Materials Research Bulletin, 1972. **7**(9): p. 971-975.

29. Oberlin, A., M. Endo, and T. Koyama, *High resolution electron microscope observations of graphitized carbon fibers.* Carbon, 1976. **14**(2): p. 133-135.

30. Lee, C.J., et al., *Large-scale production of aligned carbon nanotubes by the vapor phase growth method.* Chemical Physics Letters, 2002. **359**: p. 109-114.

31. Eres, G., et al., *In situ control of the catalyst efficiency in chemical vapor deposition of vertically aligned carbon nanotubes on predeposited metal catalyst films.* Applied Physics Letters, 2004. **84**(10): p. 1759-1761.

32. Shanov, V. and M. Schulz, *The Longest Carbon Nanotubes You've Ever Seen*. 2007, http://www.nsf.gov/news/news_summ.jsp?cntn_id=108992&org=NSF&from=news.

33. Shanov, V. and M. Schulz, *University of Cincinnati Researchers Grow Their Longest Carbon Nanotube Ever*. 2006, http://www.uc.edu/news/NR.asp?id=4811.

34. Shanov, V. and M. Schulz, *UC Researchers Shatter World Records with Length of Carbon Nanotube Arrays*. 2007, http://www.uc.edu/news/NR.asp?id=5700.

35. Hong, B.H., et al., *Quasi-Continuous Growth of Ultralong Carbon Nanotube Arrays.* Journal of the American Chemical Society, 2005. **127**(44): p. 15336-15337.

36. Zheng, L.X., et al., *Ultralong single-wall carbon nanotubes.* Nature Materials, 2004. **3**: p. 673-676.

37. Dresselhaus, M.S. and G. Dresselhaus, *Nanotechnology in Carbon Materials.* Acta Metallurgica, 1997. **9**: p. 33-42.

38. Rochefort, A., D.R. Salahub, and P. Avouris, *Effects of Finite Length on the Electronic Structure of Carbon Nanotubes.* Journal of Physical Chemistry B, 1999. **103**: p. 641-646.

39. Collins, P.G. and P. Avouris, *Nanotubes for Electronics.* Scientific American, 2000. **283**(6): p. 62-69.

40. Hernandeza, E., et al., *Tight binding molecular dynamics studies of boron assisted nanotube growth.* Journal of Chemical Physics, 2000. **113**(9): p. 3814-3821.

41. Lee, C., et al., *Measurement of the Elastic Properties and Intrinsic Strength of Monolayer Graphene.* Science, 2008. **321**(5887): p. 385 - 388.

42. Liu, F., P. Ming, and J. Li, *Ab initio calculation of ideal strength and phonon instability of graphene under tension.* Physical Review B, 2007. **76**: p. 064120.

43. Blakslee, O.L., et al., *Elastic Constants of Compression-Annealed Pyrolytic Graphite.* Journal of Applied Physics, 1970. **41**(8): p. 3373-3382.

44. Soule, D.E. and C.W. Nezbeda, *Direct Basal-Plane Shear in Single-Crystal Graphite.* Journal of Applied Physics, 1968. **39**(11): p. 5122-5139.

45. Zhao, Q., M.B. Nardelli, and J. Bernholc, *Ultimate strength of carbon nanotubes: A theoretical study.* Physical Review B, 2002. **65**: p. 144105.

46. Hernández, E. and A. Rubio, *Nanotubes: Mechanical and Spectroscopic Properties.* Scientific Highlight of the Month, 1999: p. 48-67.

47. Vaccarini, L., et al., *Mechanical and electronic properties of carbon and boron-nitride nanotubes.* Carbon, 2000. **38**: p. 1681-1690.

48. Hernandez, E., et al., *Elastic properties of single-wall nanotubes.* Applied Physics A, 1999. **68**(3): p. 287-292.

49. Goze, C., et al., *Elastic and mechanical properties of carbon nanotubes.* Synthetic Metals, 1999. **103**(1-3): p. 2500-2501.

50. Krishnan, A., et al., *Young's modulus of single-walled nanotubes.* Physical Review B, 1998. **58**(20): p. 14013-14019.

51. Salvetat-Delmotte, J.-P. and A. Rubio, *Mechanical properties of carbon nanotubes: a fiber digest for beginners.* Carbon, 2002. **40**(10): p. 1729-1734.

52. To, C.W.S., *Bending and shear moduli of single-walled carbon nanotubes.* Finite Elements in Analysis and Design, 2006. **42**: p. 404-413.

53. Demczyk, B.G., et al., *Direct mechanical measurement of the tensile strength and elastic modulus of multiwalled carbon nanotubes.* Materials Science and Engineering A, 2002. **334**: p. 173-178.

54. Ding, W., et al., *Modulus, Fracture Strength, and Brittle vs. Plastic Response of the Outer Shell of Arc-grown Multi-walled Carbon Nanotubes.* Experimental Mechanics, 2007. **47**(1): p. 25-36.

55. Peng, B., et al., *Measurements of near-ultimate strength for multiwalled carbon nanotubes and irradiation-induced crosslinking improvements.* Nature Nanotechnology, 2008. **3**: p. doi:10.1038/nnano.2008.211.

56. Yu, M.-F., et al., *Tensile loading of ropes of single wall carbon nanotubes and their mechanical properties.* Physical Review Letters, 2000. **84**(12): p. 5552-5555.

57. Yu, M.-F., et al., *Strength and Breaking Mechanism of Multiwalled Carbon Nanotubes Under Tensile Load.* Science, 2000. **287**(Jan): p. 637-640.

58. Huang, Y., J. Wu, and K.C. Hwang, *Thickness of graphene and single-wall carbon nanotubes.* Physical Review B, 2006. **74**: p. 245413.

59. Odegard, G.M., et al., *Equivalent-continuum modeling of nano-structured materials.* Composites Science and Technology, 2002. **62**(14): p. 1869-1880.

60. Lu, J.P., *Elastic Properties of Carbon Nanotubes and Nanoropes.* Physical Review Letters, 1997. **79**(7-18): p. 1297-1300.

61. Yakobson, B.I., C.J. Brabec, and J. Bernholc, *Nanomechanics of Carbon Tubes: Instabilities beyond Linear Response.* Physical Review Letters, 1996. **76**(14-1): p. 2511-2514.

62. Salvetat, J.-P., et al., *Elastic Modulus of Ordered and Disordered Multiwalled Carbon Nanotubes.* Advanced Materials, 1999. **11**(2): p. 161-165.

63. Lukic, B., et al., *Elastic modulus of multi-walled carbon nanotubes produced by catalytic chemical vapour deposition.* Applied Physics A, 2005. **80**: p. 695-700.

64. Lukic, B., et al., *Catalytically Grown Carbon Nanotubes of Small Diameter Have a High Young's Modulus.* Nano Letters, 2005. **5**(10): p. 2074-2077.

65. Wang, X.Y. and X. Wang, *Numerical simulation for bending modulus of carbon nanotubes and some explanations for experiment.* Composites: Part B, 2004. **35**: p. 79-86.

66. Liu, J.Z., Q. Zheng, and Q. Jiang, *Effect of bending instabilities on the measurements of mechanical properties of multiwalled carbon nanotubes.* Physical Review B, 2003. **67**: p. 075414.

67. *Material Property Data Search*, in *MatWeb Material Property Data*. 2004, www.matweb.com.

68. Srivastava, D., C. Wei, and K. Cho, *Nanomechanics of carbon nanotubes and composites.* Applied Mechanics Reviews, 2003. **56**(2): p. 215-230.

69. Huang, J.Y., et al., *Superplastic Carbon Nanotubes.* Nature, 2006. **439**: p. 281.

70. Chang, T., W. Guo, and X. Guo, *Buckling of multiwalled carbon nanotubes under axial compression and bending via a molecular mechanics model.* Physical Review B, 2005. **72**: p. 064101.

71. Wang, Q., et al., *Bending instability characteristics of double-walled carbon nanotubes.* Physical Review B, 2005. **71**: p. 045403.

72. Iijima, S., et al., *Structural flexibility of carbon nanotubes.* Journal of Chemical Physics, 1996. **104**(5): p. 2089-2092.

73. Cao, G. and X. Chen, *Buckling of single-walled carbon nanotubes upon bending: Molecular dynamics simulations and finite element method.* Physical Review B, 2006. **73**: p. 155435.

74. Zhou, X., et al., *The structure relaxation of carbon nanotube.* Physica B, 2001. **304**: p. 86-90.

75. Wang, X. and H.K. Yang, *Bending stability of multiwalled carbon nanotubes.* Physical Review B, 2006. **73**: p. 085409.

76. Kuzumaki, T., et al., *Dynamic observation of the bending behavior of carbon nanotubes by nanoprobe manipulation in TEM.* Carbon, 2004. **42**: p. 2343-2345.

77. Suhr, J., et al., *Fatigue resistance of aligned carbon nanotube arrays under cyclic compression.* Nature Nanotechnology, 2007. **2**: p. 417-420.

78. Cao, A., et al., *Super-Compressible Foamlike Carbon Nanotube Films.* Science, 2005. **310**(5752): p. 1307-1310.

79. Wang, G.-W., et al., *Pull-in instability study of carbon nanotube tweezers under the influence of van der Waals forces.* Journal of Micromechanics and Microengineering, 2004. **14**: p. 1119-1125.

80. Dequesnes, M., S.V. Rotkin, and N.R. Aluru, *Calculation of pull-in voltages for carbon-nanotube-based nanoelectromechanical switches.* Nanotechnology, 2002. **13**: p. 120-131.

81. Falvo, M.R., et al., *Nanometre-scale rolling and sliding of carbon nanotubes.* Nature, 1999. **397**: p. 236-238.

82. Akita, S., H. Nishijima, and Y. Nakayama, *Influence of stiffness of carbon-nanotube probes in atomic force microscopy*. Journal of Physics D: Applied Physics, 2000. **33**: p. 2673-2677.

83. Tadmor, R., *The London–van der Waals interaction energy between objects of various geometries.* Journal of Physics: Condensed Matter, 2001. **13**: p. L195-L202.

84. Pan, Z.W., et al., *Tensile tests of ropes of very long aligned multiwall carbon nanotubes.* Applied Physics Letters, 1999. **74**(21): p. 3152-3154.

85. Schönenberger, C. and L. Forró, *Multiwall carbon nanotubes.* Physics World, 2000. **13**: p. 37-41.

86. McEuen, P.L., et al., *Disorder, pseudospins, and backscattering in carbon nanotubes.* Physical Review Letters, 1999. **83**(24): p. 5098-5101.

87. Li, S., et al., *Electrical Properties of 0.4 cm Long Single-Walled Carbon Nanotubes.* Nano Letters, 2004. **4**(10): p. 2003-2007.

88. Frank, S., et al., *Carbon Nanotube Quantum Resistors.* Science, 1998. **280**(5370): p. 1744-1746.

89. Anazawa, K., et al., *High-purity carbon nanotubes synthesis method by an arc discharging in magnetic field.* Applied Physics Letters, 2002. **81**(4): p. 739-741.

90. Berger, C., et al., *Multiwalled carbon nanotubes are ballistic conductors at room temperature.* Applied Physics A, 2002. **74**(3): p. 363-365.

91. Dai, H., *Carbon nanotubes: opportunities and challenges.* Surface Science, 2002. **500**: p. 218-241.

92. McEuen, P.L., M.S. Fuhrer, and H. Park, *Single-Walled Carbon Nanotube Electronics.* IEEE Transactions on Nanotechnology, 2002. **1**(1): p. 78-85.

93. Gao, B., et al., *Four-Point Resistance of Individual Single-Wall Carbon Nanotubes.* Physical Review Letters, 2005. **95**: p. 196802.

94. Zhu, L., et al., *Well-Aligned Open-Ended Carbon Nanotube Architectures: An Approach for Device Assembly.* Nano Letters, 2006. **6**(2): p. 243-247.

95. Zhu, L., et al., *Growth and electrical characterization of high-aspect-ratio carbon nanotube arrays.* Carbon, 2006. **44**: p. 253-258.

96. Ebbesen, T.W., et al., *Electrical conductivity of individual carbon nanotubes.* Nature, 1996. **382**(6586): p. 54-56.

97. Bachtold, A., et al., *Contacting carbon nanotubes selectively with low-ohmic contacts for four-probe electric measurements.* Applied Physics Letters, 1998. **73**(2): p. 274-276.

98. Avouris, P., *Carbon Nanotube Electronics.* Chemical Physics, 2002. **281**: p. 429-445.

99. Chiu, P.W., et al., *Electrical Transport through Carbon Nanotube Junction,* in *Electronic Properties of Molecular Nanostructures,* e.a. H. Kuzmany, Editor. 2001, American Institure of Physics. p. 368-371.

100. Collins, P.G., et al., *Current Saturation and Electrical Breakdown in Multiwalled Carbon Nanotubes.* Physical Review Letters, 2001. **86**(14): p. 3128-3131.

101. Collins, P.G. and P. Avouris, *Multishell conduction in multiwalled carbon nanotubes.* Applied Physics A, 2002. **74**(3): p. 329-332.

102. Rochefort, A., et al., *Electrical and mechanical properties of distorted carbon nanotubes.* Physical Review B, 1999. **60**(19): p. 13824-13830.

103. Bolton, K., et al. *Changes in carbon nanotube electronic properties by collisions with inert gases*. in *Electronic Properties of Synthetic Nanostructures*. 2004.

104. Collins, P.G., M.S. Arnold, and P. Avouris, *Engineering Carbon Nanotubes and Nanotube Circuits Using Electrical Breakdown.* Science, 2001. **292**: p. 706-709.

105. Martel, R., et al., *Single- and multi-wall carbon nanotube field-effect transistors.* Applied Physics Letters, 1998. **73**(17): p. 2447-2449.

106. Derycke, V., et al., *Carbon Nanotube Inter- and Intramolecular Logic Gates.* Nano Letters, 2001. **1**(9): p. 453-456.

107. Martel, R., et al. *Carbon Nanotube Field-Effect Transistors and Logic Circuits*. in *39th Design Automation Conference*. 2002. New Orleans, LA: Association for Computing Machinery.

108. Bockrath, M., et al., *Chemical doping of individual semiconducting carbon-nanotube ropes.* Physical Review B, 2000. **61**(16): p. R10606-R10608.

109. Hu, L., D.S. Hecht, and G. Gruner, *Percolation in Transparent and Conducting Carbon Nanotube Networks.* Nano Letters, 2004. **4**(12): p. 2513-2517.

110. Yang, Z.-P., et al., *Experimental Observation of an Extremely Dark Material Made By a Low-Density Nanotube Array.* Nano Letters, 2008. **8**(2): p. 446-451.

111. Murakami, Y., et al., *Polarization dependent optical absorption properties of single-walled carbon nanotubes and methodology for the evaluation of their morphology.* Carbon, 2005. **43**: p. 2664-2676.

112. Reed, B.W. and M. Sarikaya, *Electronic properties of carbon nanotubes by transmission electron energy-loss spectroscopy.* Physical Review B, 2001. **64**(19): p. 195404.

113. Li, Z.M., et al., *Polarized Absorption Spectra of Single-Walled 4 Å Carbon Nanotubes Aligned in Channels of an AlPO4-5 Single Crystal.* Physical Review Letters, 2001. **87**(12): p. 127401-1 to 127401-4.

114. Venghaus, H., *Redetermination of the Dielectric Function of Graphite.* Physica Status Solidi B, 1975. **71**(2): p. 609-614.

115. Murakami, Y., et al., *Polarization Dependence of the Optical Absorption of Single-Walled Carbon Nanotubes.* Physical Review Letters, 2005. **94**(8): p. 087402.

116. Kataura, H., et al., *Optical Properties of Single-Wall Carbon Nanotubes.* Synthetic Metals, 1999. **103**: p. 2555-2558.

117. Torrens, F., *Effect of type, size and deformation on the polarizability of carbon nanotubes from atomic increments.* Nanotechnology, 2004. **15**: p. 8259-8264.

118. Torrens, F., *Effect of size and deformation on polarizabilities of carbon nanotubes from atomic increments.* Future Generation Computer Systems, 2004. **20**: p. 763-772.

119. Bubke, K., et al., *Optical anisotropy of dispersed carbon nanotubes induced by an electric field.* Applied Physics Letters, 1997. **71**(14): p. 1906-1908.

120. Murakami, Y., et al., *Polarization dependence of resonant Raman scattering from vertically aligned single-walled carbon nanotube films.* Physical Review B, 2005. **71**: p. 085403-1 to 085403-8.

121. Rao, A.M., et al., *Polarized Raman Study of Aligned Multiwalled Carbon Nanotubes.* Physical Review Letters, 2000. **84**(8): p. 1820-1823.

122. Gommans, H.H., et al., *Fibers of aligned single-walled carbon nanotubes: Polarized Raman spectroscopy.* Journal of Applied Physics, 2000. **88**(5): p. 2509-2514.

123. Jorio, A., et al., *Polarized resonant Raman study of isolated single-wall carbon nanotubes: Symmetry selection rules, dipolar and multipolar antenna effects.* Physical Review B, 2002. **65**(121402): p. 121402-1 to 121402-4.

124. Ren, W., F. Li, and H.-M. Cheng, *Polarized Raman analysis of aligned double-walled carbon nanotubes.* Physical Review B, 2005. **71**: p. 115428-1 to 115428-5.

125. Osman, M.A. and D. Srivastava, *Temperature dependence of the thermal conductivity of single-wall carbon nanotubes.* Nanotechnology, 2001. **12**: p. 21-24.

126. Che, J., T. Cagin, and W.A. Goddard III, *Thermal conductivity of carbon nanotubes.* Nanotechnology, 2000. **11**: p. 65-69.

127. Berber, S., Y.-K. Kwon, and D. Tománek, *Unusually High Thermal Conductivity of Carbon Nanotubes.* Physical Review Letters, 2000. **84**(20): p. 4613-4616.

128. Yang, D.J., et al., *Thermal conductivity of multiwalled carbon nanotubes.* Physical Review B, 2002. **66**: p. 165440.

129. Hone, J., et al., *Thermal properties of carbon nanotubes and nanotube-based materials.* Applied Physics A, 2002. **74**: p. 339-343.

130. Brown, E., et al. *Thermal Measurements on Multi-wall Nanotubes*. in *American Institute of Physics Proceedings - Electronic Properties of Synthetic Nanostructures*. 2004.

131. Xu, Y., et al., *Thermal properties of carbon nanotube array used for integrated circuit cooling.* Journal of Applied Physics, 2006. **100**: p. 074302.

132. Wang, H., et al., *Synthesis of Aligned Carbon Nanotubes on Double-Sided Metallic Substrate by Chemical Vapor Deposition.* Journal of Physical Chemistry C, 2007. **111**: p. 12617-12624.

133. Riley, D.P., *The Thermal Expansion of Graphite: Part II. Theoretical.* Proc. Phys. Soc., 1945. **57**: p. 486-495.

134. Nelson, J.B. and D.P. Riley, *The Thermal Expansion of Graphite From 15"C to 800"C: Part I. Experimental.* Proc. Phys. Soc., 1945. **57**: p. 477-486.

135. Kwon, Y.-K., S. Berber, and D. Tomanek, *Thermal Contraction of Carbon Fullerenes and Nanotubes.* Physical Review Letters, 2004. **92**(1): p. 015901.

136. Maniwa, Y., et al., *Thermal expansion of single-walled carbon nanotube SWNT bundles: X-ray diffraction studies.* Physical Review B, 2001. **64**: p. 241402-1-3.

137. De Bokx, P.K., et al., *The formation of filamentous carbon on iron and nickel catalysts I. Thermodynamics.* Journal of Catalysis, 1985. **96**(2): p. 454-467.

138. Schmidt, F.A. and J.C. Warner, *Diffusion of carbon, nitrogen and oxygen in vanadium between 60 and 1825 degrees C.* Journal of the Less-Common Metals, 1972. **26**(2): p. 325-326.

139. Yudasaka, M., et al., *Behavior of Ni in carbon nanotube nucleation.* Applied Physics Letters, 1997. **70**(14): p. 1817-1818.

140. Yudasaka, M., et al., *Specific conditions for Ni catalyzed carbon nanotube growth by chemical vapor deposition.* Applied Physics Letters, 1995. **67**(17): p. 2477-2479.

141. Yudasaka, M., et al., *Graphite formation on Ni film by chemical vapor deposition.* Thin Solid Films, 1996. **280**(1-2): p. 117-123.

142. Wei, Y.Y., et al., *Effect of catalyst film thickness on carbon nanotube growth by selective area chemical vapor deposition.* Applied Physics Letters, 2001. **78**(10): p. 1394-1396.

143. Kukovitsky, E.F., et al., *Correlation between metal catalyst particle size and carbon nanotube growth.* Chemical Physics Letters, 2002. **355**: p. 497-503.

144. Jang, Y.-T., et al., *Effect of NH3 and thickness of catalyst on growth of carbon nanotubes using thermal chemical vapor deposition.* Chemical Physics Letters, 2003. **372**: p. 745-749.

145. Li, D.-C., et al., *Structure and growth of aligned carbon nanotube films by pyrolysis.* Chemical Physics Letters, 2000. **316**: p. 349-355.

146. Hou, H., et al., *Large-Scale Synthesis of Aligned Carbon Nanotubes Using FeCl3 as Floating Catalyst Precursor.* Chemistry of Materials, 2003. **15**: p. 580-585.

147. Zhou, Z., et al., *Controllable growth of double wall carbon nanotubes in a floating catalytic system.* Carbon, 2003. **41**(2): p. 337-342.

148. Sinnott, S.B., et al., *Model of carbon nanotube growth through chemical vapor deposition.* Chemical Physics Letters, 1999. **315**: p. 25-30.

149. Wagner, R.S. and W.C. Ellis, *Vapor-Liquid-Solid Mechanism of Single Crystal Growth.* Applied Physics Letters, 1964. **4**(5): p. 89-90.

150. Derbyshire, F.J., A.E.B. Presland, and D.L. Trimm, *Graphite formation by the dissolution—precipitation of carbon in cobalt, nickel and iron.* Carbon, 1975. **13**(2): p. 111-113.

151. Baker, R.T.K., *Catalytic growth of carbon filaments.* Carbon, 1989. **27**(3): p. 315-323.

152. Andrews, R., et al., *Continuous production of aligned carbon nanotubes: a step closer to commercial realization.* Chemical Physics Letters, 1999. **303**(5-6): p. 467-474.

153. Li, Y., et al., *Growth of Single-Walled Carbon Nanotubes from Discrete Catalytic Nanoparticles of Various Sizes.* Journal of Physical Chemistry B, 2001. **105**: p. 11424-11431.

154. Ding, F., A. Rosen, and K. Bolton, *Molecular dynamics study of the catalyst particle size dependence on carbon nanotube growth.* Journal of Chemical Physics, 2004. **121**(6): p. 2775-2779.

155. Teo, K.B.K., et al., *Catalytic Synthesis of Carbon Nanotubes and Nanofibers,* in *Encyclopedia of Nanoscience and Nanotechnology*, H.S. Nalwa, Editor. 2003, American Scientific Publishers. p. 665-686.

156. Ding, F., K. Bolton, and A. Rosen, *Nucleation and Growth of Single-Walled Carbon Nanotubes: A Molecular Dynamics Study.* Journal of Physical Chemistry B, 2004. **108**: p. 17369-17377.

157. Ding, F. and K. Bolton, *The importance of supersaturated carbon concentration and its distribution in catalytic particles for single-walled carbon nanotube nucleation.* Nanotechnology, 2006. **17**: p. 543-548.

158. Puretzky, A.A., et al., *In situ measurements and modeling of carbon nanotube array growth kinetics during chemical vapor deposition.* Applied Physics A, 2005. **81**: p. 223-240.

159. Ding, F., K. Bolton, and A. Rosen, *Molecular dynamics study of SWNT growth on catalyst particles without temperature gradients.* Computational Materials Science, 2006. **35**: p. 243-246.

160. Ding, F., A. Rosen, and K. Bolton, *The role of the catalytic particle temperature gradient for SWNT growth from small particles.* Chemical Physics Letters, 2004. **393**: p. 309-313.

161. Ding, F., A. Rosén, and K. Bolton, *Size dependence of the coalescence and melting of iron clusters: A molecular-dynamics study.* Physical Review B, 2004. **70**: p. 075416-1 to 075416-6.

162. Hafner, J.H., et al., *Catalytic growth of single-wall carbon nanotubes from metal particles.* Chemical Physics Letters, 1998. **296**: p. 195-202.

163. Robertson, D.H., D.W. Brenner, and J.W. Mintmire, *Energetics of nanoscale graphitic tubules.* Physical Review B, 1992. **45**(21): p. 12592-12595.

164. Smalley, R.E. and B.I. Yakobsonb, *The Future of the Fullerenes.* Solid State Communications, 1998. **107**(11): p. 597-606.

165. Kwon, Y.-K., et al., *Morphology and stability of growing multiwall carbon nanotubes.* Physical Review Letters, 1997. **79**(11): p. 2065-2068.

166. Nardelli, M.B., C. Roland, and J. Bernholc, *Theoretical bounds for multiwalled carbon nanotube growth.* Chemical Physics Letters, 1998. **296**: p. 471-476.

167. Bernholc, J., et al., *Theory of growth and mechanical properties of nanotubes.* Applied Physics A, 1998. **67**: p. 39-46.

168. Maiti, A., et al., *Theory of Carbon Nanotube Growth.* Physical Review B, 1995. **52**(20): p. 14850-14858.

169. Ajayan, P.M., T. Ichihashi, and S. Iijima, *Distribution of pentagons and shapes in carbon nano-tubes and nano-particles.* Chemical Physics Letters, 1993. **202**(5): p. 384-388.

170. Krishnan, A., et al., *Graphitic cones and the nucleation of curved carbon surfaces.* Nature, 1997. **388**: p. 451-454.

171. Lee, Y.H., S.G. Kim, and D. Tomanek, *Catalytic growth of single-wall carbon nanotubes: An ab initio study.* Physical Review Letters, 1997. **78**(12): p. 2393-2396.

172. Zhou, L.G. and S.Q. Shi, *Adsorption of foreign atoms on Stone-Wales defects in carbon nanotube.* Carbon, 2003. **41**(3): p. 613-615.

173. Iijima, S., P.M. Ajayan, and T. Ichihashi, *Growth model for carbon nanotubes.* Physical Review Letters, 1992. **69**(21): p. 3100-3103.

174. Endo, M., et al., *The Production and Structure of Pyrolytic Carbon Nanotubes (PCNTs).* Journal of Physics & Chemistry of Solids, 1993. **54**(12): p. 1841-1848.

175. Wong, T.S., et al., *Carbon nanotube growth by rapid thermal processing.* Diamond and Related Materials, 2001. **10**: p. 1810-1813.

176. Ugarte, D., *Curling and closure of graphitic networks under electron-beam irradiation.* Nature, 1992. **359**(6397): p. 707-709.

177. Yamamoto, K., et al., *New method of carbon nanotube growth by ion beam irradiation.* Applied Physics Letters, 1996. **69**(27): p. 4174-4175.

178. Guo, T., et al., *Catalytic growth of single-walled nanotubes by laser vaporization.* Chemical Physics Letters, 1995. **243**(1-2): p. 49-54.

179. Eres, G., et al., *Molecular Beam-Controlled Nucleation and Growth of Vertically Aligned Single-Wall Carbon Nanotube Arrays.* Journal of Physical Chemistry B, 2005. **109**: p. 16684-16694.

180. Zhagfarov, F.G., N.A. Grigorrsquoeva, and A.L. Lapidus, *New Catalysts of Hydrocarbon Pyrolysis.* Chemistry and Technology of Fuels and Oils, 2005. **41**(2): p. 141-145.

181. Cassell, A.M., et al., *Large Scale CVD Synthesis of Single-Walled Carbon Nanotubes.* Journal of Physical Chemistry B, 1999. **103**: p. 6484-6492.

182. Takenaka, S., et al., *Ni/SiO2 catalyst effective for methane decomposition into hydrogen and carbon nanofiber.* Journal of Catalysis, 2003. **217**(1): p. 79-87.

183. Wang, Y., N. Shah, and G.P. Huffman, *Simultaneous production of hydrogen and carbon nanostructures by decomposition of propane and cyclohexane over alumina supported binary catalysts.* Catalysis Today, 2005. **99**: p. 359-364.

184. Ting, J.-M. and N.Z. Huang, *Thickening of chemical vapor deposited carbon fiber.* Carbon, 2001. **39**: p. 835-839.

185. Tibbetts, G.G., *Lengths of Carbon Fibers Grown from Iron Catalyst Particles in Natural Gas.* Journal Of Crystal Growth, 1985. **73**: p. 431-438.

186. Hart, A.J., A.H. Slocum, and L. Royer, *Growth of conformal single-walled carbon nanotube films from Mo/Fe/Al2O3 deposited by electron beam evaporation.* Carbon, 2006. **44**: p. 348-359.

187. Kong, J., A.M. Cassell, and H. Dai, *Chemical vapor deposition of methane for single-walled carbon nanotubes.* Chemical Physics Letters, 1998. **292**: p. 567-.

188. Yamada, T., et al., *Size-selective growth of double-walled carbon nanotube forests from engineered iron catalysts.* Nature Nanotechnology, 2006. **1**: p. 131-135.

189. Li, Q., et al., *Sustained Growth of Ultralong Carbon Nanotube Arrays for Fiber Spinning.* Advanced Materials, 2006. **18**: p. 3160-3163.

190. Becker, A. and K.J. Hüttinger, *Chemistry and kinetics of chemical vapor deposition of pyrocarbon - II pyrocarbon deposition from ethylene, acetylene and 1,3-butadiene in the low temperature regime.* Carbon, 1998. **36**(2): p. 177-199.

191. Zheng, B., Y. Li, and J. Liu, *CVD synthesis and purification of single-walled carbon nanotubes on aerogel-supported catalyst.* Applied Physics A, 2002. **74**: p. 345-348.

192. Yu, Z., S. Li, and P.J. Burke, *Synthesis of Aligned Arrays of Millimeter Long, Straight Single-Walled Carbon Nanotubes.* Chem. Mater., 2004. **16**: p. 3414-3416.

193. Ren, Z.F., et al. *Large Arrays of Well-Aligned Carbon Nanotubes*. in *Proceedings of 13th International Winter School on Electronic Properties of Novel Materials*. 1999. Kirchberg/Tirol, Austria.

194. Juang, Z.Y., et al., *On the kinetics of carbon nanotube growth by thermal CVD method.* Diamond and Related Materials, 2004. **13**: p. 2140-2146.

195. Wei, B.Q., et al., *Growing pillars of densely packed carbon nanotubes on Ni-coated silica.* Carbon, 2002. **40**(1): p. 47-51.

196. Zhu, H.W., et al., *Direct Synthesis of Long Single-Walled Carbon Nanotube Strands.* Science, 2002. **296**: p. 884-886.

197. Zhu, L., et al., *The growth of carbon nanotube stacks in the kinetics-controlled regime.* Carbon, 2007. **45**: p. 344-348.

198. Zhu, L., D.W. Hess, and C.P. Wong, *Monitoring Carbon Nanotube Growth by Formation of Nanotube Stacks and Investigation of the Diffusion-Controlled Kinetics.* Journal of Physical Chemistry B, 2006. **110**(11): p. 5445-5449.

199. Zhu, L., et al., *Aligned Carbon Nanotube Stacks by Water-Assisted Selective Etching.* Nano Letters, 2005. **5**(12): p. 2641-2645.

200. Zheng, L., et al., *Carbon-Nanotube Cotton for Large-Scale Fibers.* Advanced Materials, 2007. **19**: p. 2567-2570.

201. Zhang, X., et al., *Ultrastrong, Stiff, and Lightweight Carbon-Nanotube Fibers.* Advanced Materials, 2007. **19**: p. 4198-4201.

202. Zhang, X., et al., *Strong Carbon-Nanotube Fibers Spun from Long Carbon-Nanotube Arrays.* Small, 2007. **3**(2): p. 244-248.

203. Zhang, M., et al., *Strong, Transparent, Multifunctional, Carbon Nanotube Sheets.* Science, 2005. **309**: p. 1215-1219.

204. Zhang, M., K.R. Atkinson, and R.H. Baughman, *Multifunctional Carbon Nanotube Yarns by Downsizing an Ancient Technology.* Science, 2004. **306**: p. 1358-1361.

205. Ward, J.W., B.Q. Wei, and P.M. Ajayan, *Substrate effects on the growth of carbon nanotubes by thermal decomposition of methane.* Chemical Physics Letters, 2003. **376**: p. 717-725.

206. Vander Wal, R.L., T.M. Ticich, and V.E. Curtis, *Substrate-support interactions in metal-catalyzed carbon nanofiber growth.* Carbon, 2001. **39**(15): p. 2277-2289.

207. Shanov, V.N., et al. *Substrate and Process Interplay During Synthesis of Millimeter Long Multi-Wall Carbon Nanotube Arrays*. in *Sixth IEEE Conference on Nanotechnology*. 2006. Cincinnati , Ohio: IEEE.

208. Su, D.S. and X.-W. Chen, *Natural Lavas as Catalysts for Efficient Production of Carbon Nanotubes and Nanofibers.* Angewandte Chemie, 2007. **46**(11): p. 1823-1824.

209. Liu, K., et al., *A growth mark method for studying growth mechanism of carbon nanotube arrays.* Carbon, 2005. **43**: p. 2850-2856.

210. Li, Q., et al., *Structure-Dependent Electrical Properties of Carbon Nanotube Fibers.* Advanced Materials, 2007. **19**: p. 3358-3363.

211. Lee, C.J. and J. Park, *Growth Model for Bamboolike Structured Carbon Nanotubes Synthesized Using Thermal Chemical Vapor Deposition.* Journal of Physical Chemistry B, 2001. **105**: p. 2365-2368.

212. Lee, C.J., T.J. Lee, and S.C. Lyu, *Growth of Vertically Aligned Bamboo-Shaped Carbon Nanotubes.* Journal of the Korean Physical Society, 2001. **39**: p. S59-S62.

213. Jiang, K., Q. Li, and S. Fan, *Spinning continuous carbon nanotube yarns.* Nature, 2002. **419**: p. 801.

214. Huang, S., X. Cai, and J. Liu, *Growth of Millimeter-Long and Horizontally Aligned Single-Walled Carbon Nanotubes on Flat Substrates.* J. Am. Chem. Soc., 2003. **125**: p. 5636-5637.

215. Hinds, B.J., et al., *Aligned Multiwalled Carbon Nanotube Membranes.* Science, 2004. **303**: p. 62-65.

216. Hafner, J.H., et al., *High-Yield Assembly of Individual Single-Walled Carbon Nanotube Tips for Scanning Probe Microscopies.* Journal of Physical Chemistry B, 2001. **105**(4): p. 743-746.

217. Geohegan, D.B., et al., *In situ growth rate measurements and length control during chemical vapor deposition of vertically aligned multiwall carbon nanotubes.* Applied Physics Letters, 2003. **83**(9): p. 1851-1853.

218. Futaba, D.N., et al., *84% Catalyst Activity of Water-Assisted Growth of Single Walled Carbon Nanotube Forest Characterization by a Statistical and Macroscopic Approach.* Journal of Physical Chemistry B, 2006. **110**: p. 8035-8038.

219. Endo, M., et al., *'Buckypaper' from coaxial nanotubes.* Nature, 2005. **433**: p. 476.

220. Dai, H., et al., *Controlled Chemical Routes to Nanotube Architectures, Physics, and Devices.* Journal of Physical Chemistry B, 1999. **103**: p. 11246-11255.

221. Christen, H.M., et al., *Rapid Growth of Long, Vertically Aligned Carbon Nanotubes through Efficient Catalyst Optimization Using Metal Film Gradients.* Nano Letters, 2004. **4**(10): p. 1939-1942.

222. Cheung, C.L., J.H. Hafner, and C.M. Lieber, *Carbon nanotube atomic force microscopy tips: Direct growth by chemical vapor deposition and application to high-resolution imaging.* Proceedings of the National Academy of Sciences, 2000. **97**(8): p. 3809-3813.

223. Huang, Z.P., et al., *Growth of large periodic arrays of carbon nanotubes.* Applied Physics Letters, 2003. **82**(3): p. 460-462.

224. Chen, Y., et al., *Aligned conical carbon nanotubes.* Journal of Materials Science, 2000. **35**: p. 5517-5521.

225. Zhang, G., et al., *Ultra-high-yield growth of vertical single-walled carbon nanotubes: Hidden roles of hydrogen and oxygen.* Proceedings of the National Academy of Sciences, 2005. **102**(45): p. 16141-16145.

226. Park, K.H., et al., *Advanced nanosphere lithography for the areal-density variation of periodic arrays of vertically aligned carbon nanofibers.* Journal of Applied Physics, 2005. **97**: p. 024311.

227. Merkulov, V.I., et al., *Alignment mechanism of carbon nanofibers produced by plasma-enhanced chemical-vapor deposition.* Applied Physics Letters, 2001. **79**(18): p. 2970-2972.

228. Journet, C., et al., *Contact angle measurements on superhydrophobic Carbon Nanotube Forests: effect of fluid pressure.* Europhysics Letters, 2005. **71**(1): p. 104-109.

229. Pan, Z.W., et al., *Very Long Carbon Nanotubes.* Nature, 1998. **394**: p. 631-632.

230. Xiong, G.-Y., D.Z. Wang, and Z.F. Ren, *Aligned millimeter-long carbon nanotube arrays grown on single crystal magnesia.* Carbon, 2006. **44**: p. 969-973.

231. Hata, K., et al., *Water-Assisted Highly Efficient Synthesis of Impurity-Free Single-Walled Carbon Nanotubes.* Science, 2004. **306**: p. 1362-1364.

232. Gruneis, A., et al., *High quality double wall carbon nanotubes with a defined diameter distribution by chemical vapor deposition from alcohol.* Carbon, 2006. **44**: p. 3177-3182.

233. Motta, M., et al., *Mechanical Properties of Continuously Spun Fibers of Carbon Nanotubes.* Nano Letters, 2005. **5**(8): p. 1529-1533.

234. Cao, A., P.M. Ajayan, and G. Ramanath, *Assembly of mm-scale macrobridges with carbon nanotube bundles.* Applied Physics Letters, 2003. **83**(2): p. 356-358.

235. Wei, B.Q., et al., *Assembly of Highly Organized Carbon Nanotube Architectures by Chemical Vapor Deposition.* Chemistry of Materials, 2003. **15**(8): p. 1598-1606.

236. Vajtai, R., et al., *Building carbon nanotubes and their smart architectures.* Smart Materials and Structures, 2002. **11**: p. 691-698.

237. Li, X., et al., *Bottom-Up Growth of Carbon Nanotube Multilayers: Unprecedented Growth.* Nano Letters, 2005. **5**(10): p. 1997-2000.

238. Motta, M., et al., *High Performance Fibres from 'Dog Bone' Carbon Nanotubes.* Advanced Materials, 2007. **19**: p. 3721-3726.

239. Li, Y.-L., I.A. Kinloch, and A.H. Windle, *Direct Spinning of Carbon Nanotube Fibers from Chemical Vapor Deposition Synthesis.* Science, 2004. **304**: p. 276-278.

240. Koziol, K., et al., *High-Performance Carbon Nanotube Fiber.* Science, 2007. **318**: p. 1892-1895.

241. Deck, C.P. and K.S. Vecchio, *Growth of Well-Aligned Carbon Nanotube Structures in Successive Layers.* Journal of Physical Chemistry B, 2005. **109**: p. 12353-12357.

242. Kamalakaran, R., et al., *Synthesis of thick and Crystalline nanotube arrays by Spray Pyrolysis.* Applied Physics Letters, 2000. **77**(21): p. 3385-3387.

243. Harutyunyan, A.R., et al., *Evolution of catalyst particle size during carbon single walled nanotube growth and its effect on the tube characteristics.* Journal of Applied Physics, 2006. **100**: p. 044321.

244. Zhu, H., et al., *A new method for synthesizing double-walled carbon nanotubes.* Carbon, 2002. **40**(11): p. 2023-2025.

245. Yan, H., et al., *Possible tactics to improve the growth of single-walled carbon nanotubes by chemical vapor deposition.* Carbon, 2002. **40**(14): p. 2693-2698.

246. Huang, S., et al., *Oriented Long Single Walled Carbon Nanotubes on Substrates from Floating Catalysts.* Journal of Physical Chemistry B Letters, 2003. **107**(48): p. 13251-13254.

247. Lupo, F., et al., *Pyrolytic synthesis of long strands of large diameter single-walled carbon nanotubes at atmospheric pressure in the absence of sulphur and hydrogen.* Chemical Physics Letters, 2005. **410**: p. 384-390.

248. Cheng, H.M., et al., *Large-scale and low-cost synthesis of single-walled carbon nanotubes by the catalytic pyrolysis of hydrocarbons.* Applied Physics Letters, 1998. **72**(25): p. 3282-3284.

249. Vander Wal, R.L. and L.J. Hall, *Carbon nanotube synthesis upon stainless steel meshes.* Carbon, 2003. **41**(4): p. 659-672.

250. Pinault, M., et al., *Evidence of Sequential Lift in Growth of Aligned Multiwalled Carbon Nanotube Multilayers.* Nano Letters, 2005. **5**(12): p. 2394-2398.

251. Endo, M., et al., *Pyrolytic carbon nanotubes from vapor-grown carbon fibers.* Carbon, 1995. **33**(7): p. 873-881.

252. Deck, C.P., G.S.B. McKee, and K.S. Vecchio, *Synthesis Optimization and Characterization of Multiwalled Carbon Nanotubes.* Journal of Electronic Materials, 2006. **35**(2): p. 211-223.

253. Nikolaev, P., et al., *Gas-phase catalytic growth of single-walled carbon nanotubes from carbon monoxide.* Chemical Physics Letters, 1999. **313**: p. 91-97.

254. Bronikowski, M.J., et al., *Gas-phase production of carbon single-walled nanotubes from carbon monoxide via the HiPco process: A parametric study.* Journal of Vacuum Science and Technology A, 2001. **19**(4): p. 1800-1805.

255. Cao, A., et al., *Silicon oxide thickness-dependent growth of carbon nanotubes.* Applied Physics Letters, 2004. **84**(1): p. 109-111.

256. Jung, Y.J., et al., *Mechanism of Selective Growth of Carbon Nanotubes on SiO2/Si Patterns.* Nano Letters, 2003. **3**(4): p. 561-564.

257. Wei, B.Q., et al., *Organized assembly of carbon nanotubes.* Nature, 2002. **416**: p. 495-496.

258. Talapatra, S., et al., *Direct growth of aligned carbon nanotubes on bulk metals.* Nature Nanotechnology, 2006. **1**(2): p. 112-116.

259. Sato, S., et al., *Growth of diameter-controlled carbon nanotubes using monodisperse nickel nanoparticles obtained with a differential mobility analyzer.* Chemical Physics Letters, 2003. **382**: p. 361-366.

260. Cui, H., O. Zhou, and B.R. Stoner, *Deposition of aligned bamboo-like carbon nanotubes via microwave plasma enhanced chemical vapor deposition.* Journal of Applied Physics, 2000. **88**(10): p. 6072-6074.

261. Wei, J., et al., *Large-Scale Synthesis of Long Double-Walled Carbon Nanotubes.* Journal of Physical Chemistry B, 2004. **108**: p. 8844-8847.

262. *NIST Chemistry WebBook*, in *NIST Standard Reference Database, n.69*. 2005, NIST: http://webbook.nist.gov/chemistry/.

263. Zhang, X., et al., *Spinning and Processing Continuous Yarns from 4-Inch Wafer Scale Super-Aligned Carbon Nanotube Arrays.* Advanced Materials, 2006. **18**: p. 1505-1510.

264. Xu, Y.-Q., et al., *Effects of atomic hydrogen and active carbon species in 1 mm vertically aligned single-walled carbon nanotube growth.* Applied Physics Letters, 2006. **89**: p. 123116.

265. Mukai, S.R., et al., *Dominant Hydrocarbon Which Contributes To The Growth Of Vapor Grown Carbon Fibers.* Carbon, 1996. **34**(5): p. 645-648.

266. Benzinger, W., A. Becker, and K.J. Hüttinger, *Chemistry and kinetics of chemical vapour deposition of pyrocarbon: I. Fundamentals of kinetics and chemical reaction engineering.* Carbon, 1996. **34**(8): p. 957-966.

267. Xu, X. and P.D. Pacey, *Interactions between acetylene and carbon nanotubes at 893 and 1019 K.* Carbon, 2001. **39**(12): p. 1835-1847.

268. Becker, A. and K.J. Hüttinger, *Chemistry and kinetics of chemical vapor deposition of pyrocarbon - III pyrocarbon deposition from propylene and benzene in the low temperature regime.* Carbon, 1998. **36**(2): p. 201-211.

269. Hart, A.J., L.v. Laake, and A.H. Slocum, *Desktop Growth of Carbon-Nanotube Monoliths with In Situ Optical Imaging.* Small, 2007. **3**(5): p. 772-777.

270. Becker, A. and K.J. Hüttinger, *Chemistry and kinetics of chemical vapor deposition of pyrocarbon - IV pyrocarbon deposition from methane in the low temperature regime.* Carbon, 1998. **36**(2): p. 213-224.

271. Becker, A. and K.J. Hüttinger, *Chemistry and kinetics of chemical vapor deposition of pyrocarbon - V influence of reactor volume/deposition surface area ratio.* Carbon, 1998. **36**(2): p. 225-232.

272. Kukovitsky, E.F., et al., *CVD growth of carbon nanotube films on nickel substrates.* Applied Surface Science, 2003. **215**: p. 201-208.

273. Hirahara, K., et al., *Boron-catalyzed multi-walled carbon nanotube growth with the reduced number of layers by laser ablation.* Chemical Physics Letters, 2000. **324**: p. 224-230.

274. Xu, Y.-Q., et al., *Vertical Array Growth of Small Diameter Single-Walled Carbon Nanotubes.* Journal of the American Chemical Society, 2006. **128**(20): p. 6560-6561.

275. Zhang, W.D., et al., *Synthesis of vertically aligned carbon nanotubes on metal deposited quartz plates.* Carbon, 2002. **40**(11): p. 1981-1989.

276. Lian, L., C.X. Su, and P.B. Armentrout, *Collision-induced dissociation of Fe-n+ (n=2–19) with Xe: Bond energies, geometric structures, and dissociation pathways.* Journal of Chemical Physics, 1992. **97**(6): p. 4072-4083.

277. Benissad, F., et al., *Formation de fibres de carbone a partir du methane II: Germination du carbone et fusion des particules catalytiques.* Carbon, 1988. **26**(4): p. 425-432.

278. Kukovitsky, E.F., S.G. L'vov, and N.A. Sainov, *VLS-growth of carbon nanotubes from the vapor.* Chemical Physics Letters, 2000. **317**: p. 65-70.

279. Hussain, A., *Ferric-sulfate-catalysed hot filament chemical vapour deposition carbon nanotube synthesis.* Nanotechnology, 2003. **14**: p. 925-930.

280. Jung, M., et al., *Effect of NH3 environmental gas on the growth of aligned carbon nanotube in catalystically pyrolizing C2H2.* Thin Solid Films, 2001. **398-399**: p. 150-155.

281. Saito, Y., et al., *Carbon nanocapsules and single-layered nanotubes produced with platinum-group metals (Ru, Rh, Pd, Os, Ir, Pt) by arc discharge.* Journal of Applied Physics, 1996. **80**(5): p. 3062-3067.

282. Kwok, K. and W.K.S. Chiu, *Growth of carbon nanotubes by open-air laser-induced chemical vapor deposition chemical vapor deposition.* Carbon, 2005. **43**: p. 437-446.

283. Kwok, K. and W.K.S. Chiu, *Continuous deposition of carbon nanotubes on a moving substrate by open-air laser-induced chemical vapor deposition.* Carbon, 2005. **43**: p. 2571-2578.

284. Yoon, S.-H., et al., *A conceptual model for the structure of catalytically grown carbon nano-fibers.* Carbon, 2005. **43**(9): p. 1828-1838.

285. Osvath, Z., et al., *Arc-grown Y-branched carbon nanotubes observed by scanning tunneling microscopy (STM).* Chemical Physics Letters, 2002. **365**: p. 338-342.

286. Bethune, D.S., *Carbon and metals: a path to single-wall carbon nanotubes.* Physica B, 2002. **323**: p. 90-96.

287. Alvarez, W.E., et al., *Characterization of Single-Walled Carbon Nanotubes (SWNTs) Produced by CO Disproportionation on Co-Mo Catalysts.* Chemistry of Materials, 2002. **14**(4): p. 1853-1858.

288. Kitiyanan, B., et al., *Controlled production of single-wall carbon nanotubes by catalytic decomposition of CO on bimetallic Co–Mo catalysts.* Chemical Physics Letters, 2000. **317**: p. 497-503.

289. Herrera, J.E., et al., *Relationship between the Structure/Composition of Co–Mo Catalysts and Their Ability to Produce Single-Walled Carbon Nanotubes by CO Disproportionation.* Journal of Catalysis, 2001. **204**: p. 129-145.

290. Alvarez, W.E., et al., *Synergism of Co and Mo in the catalytic production of singlewall carbon nanotubes by decomposition of CO.* Carbon, 2001. **39**: p. 547-558.

291. Zheng, B., et al., *Efficient CVD Growth of Single-Walled Carbon Nanotubes on Surfaces Using Carbon Monoxide Precursor.* Nano Letters, 2002. **2**(8): p. 895-898.

292. Harutyunyan, A.R., et al., *CVD Synthesis of Single Wall Carbon Nanotubes under "Soft" Conditions.* Nano Letters, 2002. **2**(5): p. 525-530.

293. Nishino, H., et al., *Growth of amorphous carbon nanotube from poly(tetrafluoroethylene) and ferrous chloride.* Carbon, 2003. **41**: p. 2819-2823.

294. Alexandrescu, R., et al., *Synthesis of carbon nanotubes by CO2-laser-assisted chemical vapour deposition.* Infrared Physics & Technology, 2003. **44**: p. 43-50.

295. Boellaard, E., et al., *The formation of filamentous carbon on iron and nickel catalysts III. Morphology.* Journal of Catalysis, 1985. **96**(2): p. 481-490.

296. Kock, A.J.H.M., et al., *The formation of filamentous carbon on iron and nickel catalysts II. Mechanism.* Journal of Catalysis, 1985. **96**(2): p. 468-480.

297. Arcos, T.d.l., et al., *The Influence of Catalyst Chemical State and Morphology on Carbon Nanotube Growth.* Journal of Physical Chemistry B, 2004. **108**: p. 7728-7734.

298. Takenaka, S., et al., *Decomposition of methane over supported-Ni catalysts: effects of the supports on the catalytic lifetime.* Applied Catalysis A: General, 2001. **217**(1-2): p. 101-110.

299. Wright, A.C., et al., *The influence of the substrate on the growth of carbon nanotubes from nickel clusters—an investigation using STM, FE-SEM, TEM and Raman spectroscopy.* Materials Science & Engineering C, 2003. **23**: p. 279-283.

300. Seidel, R., et al., *Chemical Vapor Deposition Growth of Single-Walled Carbon Nanotubes at 600°C and a Simple Growth Model.* Journal of Physical Chemistry B, 2004. **108**: p. 1888-1893.

301. Noda, S., et al., *Millimeter-Thick Single-Walled Carbon Nanotube Forests: Hidden Role of Catalyst Support.* Japanese Journal of Applied Physics, 2007. **46**(17): p. L399-L401.

302. Su, M., B. Zheng, and J. Liu, *A scalable CVD method for the synthesis of single-walled carbon nanotubes with high catalyst productivity.* Chemical Physics Letters, 2000. **322**: p. 321-326.

303. Kazmerski, L.L. and D.M. Racine, *Growth, environmental, and electrical properties of ultrathin metal films.* Journal of Applied Physics, 1975. **46**(2): p. 791-795.

304. Venables, J.A., G.D.T. Spiller, and M. Hanbucken, *Nucleation and growth of thin films.* Reports on Progress in Physics, 1984. **47**: p. 399-459.

305. Kukta, R.V. and L.B. Freund, *Minimum energy configuration of epitaxial material clusters on a lattice-mismatched substrate.* Journal of the Mechanics and Physics of Solids, 1997. **45**(11-12): p. 1835-1860.

306. Eaglesham, D.J. and M. Cerullo, *Dislocation-free Stranski-Krastanow growth of Ge on Si(100).* Physical Review Letters, 1990. **64**(16): p. 1943-1946.

307. Daudin, B., et al., *Stranski-Krastanov growth mode during the molecular beam epitaxy of highly strained GaN.* Physical Review B, 1997. **56**(12): p. R7069-R7072.

308. Wang, Y., et al., *Effect of supporting layer on growth of carbon nanotubes by thermal chemical vapor deposition.* Applied Physics Letters, 2006. **89**(18): p. 183113.

309. Schwarz-Selinger, T., et al., *Surface mass transport and island nucleation during growth of Ge on laser textured Si(001).* Physical Review B, 2002. **65**: p. 125317.

310. Teo, K.B.K., et al., *Preferential Growth of Carbon Nanotubes/Nanofibers Using Lithographically Patterned Catalysts.* Materials Research Society Conference Proceedings, 2001. **675**: p. W9.1.1-6.

311. Diebold, U., J.-M. Pan, and T.E. Madey, *Ultrathin metal film growth on TiO2 (110) - an overview.* Surface Science, 1995. **331-333**: p. 845-854.

312. Merkulov, V.I., et al., *Patterned growth of individual and multiple vertically aligned carbon nanofibers.* Applied Physics Letters, 2000. **76**(24): p. 3555-3557.

313. Arai, M., et al., *Effects of metal-support interaction and temperature on the sintering of Pt and Ag particles supported on inorganic solids.* Journal of Colloid and Interface Science, 1984. **97**(1): p. 254-265.

314. Chhowalla, M., et al., *Growth process conditions of vertically aligned carbon nanotubes using plasma enhanced chemical vapor deposition.* Journal of Applied Physics, 2001. **90**(10): p. 5308-5317.

315. Bower, C., et al., *Nucleation and growth of carbon nanotubes by microwave plasma chemical vapor deposition.* Applied Physics Letters, 2000. **77**: p. 2767-2769.

316. Siegal, M.P., D.L. Overmyer, and P.P. Provencio, *Precise control of multiwall carbon nanotube diameters using thermal chemical vapor deposition.* Applied Physics Letters, 2002. **80**: p. 2171-2173.

317. Delzeit, L., et al., *Multilayered metal catalysts for controlling the density of single-walled carbon nanotube growth.* Chemical Physics Letters, 2001. **348**: p. 368-374.

318. Chow, T.S., *Wetting of rough surfaces.* Journal of Physics: Condensed Matter, 1998. **10**: p. 445-454.

319. Huang, Z.P., et al., *Effect of nickel, iron and cobalt on growth of aligned carbon nanotubes.* Applied Physics A, 2002. **74**: p. 387-391.

320. Ding, F., A. Rosén, and K. Bolton. *MD Simulations of Catalytic Carbon Nanotube Growth: Important Features of the Metal-Carbon Interactions*. in *Electronic Properties of Synthetic Nanostructures*. 2004.

321. Fan, S., et al., *Self-Oriented Regular Arrays of Carbon Nanotubes and Their Field Emission Properties.* Science, 1999. **283**(5401): p. 512-514.

322. Nardelli, M.B., et al., *Lip-Lip Interactions and the Growth of Multiwalled Carbon Nanotubes.* Physical Review Letters, 1998. **80**(2): p. 313-316.

323. Chakrabarti, S., et al., *Growth of Super Long Aligned Brush-Like Carbon Nanotubes.* Japanese Journal of Applied Physics, 2006. **45**(28): p. 720-722.

324. Zhang, C., et al., *Growth of aligned millimeter-long carbon nanotube by chemical vapor deposition.* Diamond and Related Materials, 2008. **17**: p. 1447-1451.

325. Zhang, L., Y. Tan, and D.E. Resasco, *Controlling the growth of vertically oriented single-walled carbon nanotubes by varying the density of Co-Mo catalyst particles.* Chemical Physics Letters, 2006. **422**(1-3): p. 198-203.

326. Deal, B.E. and A.S. Grove, *General Relationship for the Thermal Oxidation of Silicon.* Journal of Applied Physics, 1965. **36**(12): p. 3770-3778.

327. Zhang, Y., et al., *Imaging as-grown single-walled carbon nanotubes originated from isolated catalytic nanoparticles.* Applied Physics A, 2002. **74**: p. 325-328.

328. Meyyappan, M., et al., *Carbon nanotube growth by PECVD: a review.* Plasma Sources Science and Technology, 2003. **12**: p. 205-216.

329. Ago, H., et al., *Gas-Phase Synthesis of Single-wall Carbon Nanotubes from Colloidal Solution of Metal Nanoparticles.* Journal of Physical Chemistry B, 2001. **105**(43): p. 10453-10456.

330. AuBuchon, J.F., L.-H. Chen, and S. Jin, *Control of Carbon Capping for Regrowth of Aligned Carbon Nanotubes.* Journal of Physical Chemistry B Letters, 2005. **109**: p. 6044-6048.

331. Kowalczyk, Z., et al., *Effect of Potassium on the Kinetics of Ammonia Synthesis and Decomposition over Fused Iron Catalyst at Atmospheric Pressure.* Journal of Catalysis, 1997. **169**: p. 407-414.

332. Hart, A.J. and A.H. Slocum, *Rapid Growth and Flow-Mediated Nucleation of Millimeter-Scale Aligned Carbon Nanotube Structures from a Thin-Film Catalyst.* Journal of Physical Chemistry B, 2006. **110**: p. 8250-8257.

333. Kim, T.-Y., et al., *Carbon nanotube growth enhanced by nitrogen incorporation.* Chemical Physics Letters, 2003. **372**: p. 603-607.

334. Lee, C.J., et al., *Synthesis of aligned carbon nanotubes using thermal chemical vapor deposition.* Chemical Physics Letters, 1999. **312**(5-6): p. 461-468.

335. Choi, G.S., et al., *Carbon nanotubes synthesized by Ni-assisted atmospheric pressure thermal chemical vapor deposition.* Journal of Applied Physics, 2002. **91**(6): p. 3847-3854.

336. Choi, K.S., et al., *Effects of ammonia on the alignment of carbon nanotubes in metal-assisted thermal chemical vapor deposition.* Journal of the European Ceramic Society, 2001. **21**(10-11): p. 2095-2098.

337. Jung, M., et al., *Growth of carbon nanotubes by chemical vapor deposition.* Diamond and Related Materials, 2001. **10**(3-7): p. 1235-1240.

338. Murakami, Y., et al., *Characterization of single-walled carbon nanotubes catalytically synthesized from alcohol.* Chemical Physics Letters, 2003. **374**(1-2): p. 53-58.

339. Maruyama, S., et al., *Low-temperature synthesis of high-purity single-walled carbon nanotubes from alcohol.* Chemical Physics Letters, 2002. **360**(3-4): p. 229-234.

340. Futaba, D.N., et al., *Kinetics of Water-Assisted Single-Walled Carbon Nanotube Synthesis Revealed by a Time-Evolution Analysis.* Physical Review Letters, 2005. **95**: p. 056104.

341. Patole, S.P., et al., *Water-assisted synthesis of carbon nanotubes: Acetylene partial pressure and height control.* European Physical Letters, 2008. **81**: p. 38002.

342. Suekane, O., et al., *Rapid Growth of Vertically Aligned Carbon Nanotubes.* Japanese Journal of Applied Physics, 2004. **43**(9): p. L1214-L1216.

343. Zhu, L., et al., *A Rapid Growth of Aligned Carbon Nanotube Films and High-Aspect-Ratio Arrays.* Journal of Electronic Materials, 2006. **35**(2): p. 195-199.

344. Lee, Y.T., et al., *Temperature-Dependent Growth of Vertically Aligned Carbon nanotubes in the Range 800-1100 °C.* Journal of Physical Chemistry B, 2002. **106**: p. 7614-7618.

345. Singh, C., et al., *Towards the production of large-scale aligned carbon nanotubes.* Chemical Physics Letters, 2003. **372**: p. 860-865.

346. Wang, H., Z. Xu, and G. Eres, *Order in vertically aligned carbon nanotube arrays.* Applied Physics Letters, 2006. **88**: p. 213111.

347. Shin, Y.M., et al., *Influence of morphology of catalyst thin film on vertically aligned carbon nanotube growth.* Journal of Crystal Growth, 2004. **271**: p. 81-89.

348. Sattler, M.G., *Bundles of carbon nanotubes generated by vapor-phase growth.* Applied Physics Letters, 1994. **64**(6): p. 710-711.

349. Avigal, Y. and R. Kalish, *Growth of aligned carbon nanotubes by biasing during growth.* Applied Physics Letters, 2001. **78**(16): p. 2291-2293.

350. Hayashi, Y., T. Negishi, and S. Nishino, *Growth of well-aligned carbon nanotubes on nickel by hot-filament assisted dc plasma chemical vapor deposition in a CH4/H2 plasma.* Journal of Vacuum Science and Technology, 2001. **19**(4): p. 1796-1799.

351. Moser, J., et al., *Individual free-standing carbon nanofibers addressable on the 50 nm scale.* Journal of Vacuum Science and Technology B, 2003. **21**(3): p. 1004-1007.

352. Merkulov, V.I., et al., *Effects of spatial separation on the growth of vertically aligned carbon nanofibers produced by plasma-enhanced chemical vapor deposition.* Applied Physics Letters, 2002. **80**: p. 476-478.

353. AuBuchon, J.F., et al., *Multiple Sharp Bendings of Carbon Nanotubes during Growth to Produce Zigzag Morphology.* Nano Letters, 2004. **4**(9): p. 1781-1784.

354. Audier, M., A. Oberlin, and M. Coulon, *Study of biconic microcrystals in the middle of carbon tubes obtained by catalytic disproportionation of CO.* Journal of Crystal Growth, 1982. **57**(3): p. 5224-534.

355. Blank, V.D., et al., *Nanocarbons formed in a hot isostatic pressure apparatus.* Thin Solid Films, 1999. **346**(1-2): p. 86-90.

356. Liu, J., R. Czerw, and D.L. Carroll, *Large-scale synthesis of highly aligned nitrogen doped carbon nanotubes by injection chemical vapor deposition methods.* Journal of Materials Research, 2005. **20**(2): p. 538-543.

357. Liu, J., S. Webster, and D.L. Carroll, *Highly aligned coiled nitrogen-doped carbon nanotubes synthesized by injection-assisted chemical vapor deposition.* Applied Physics Letters, 2006. **88**: p. 213119.

358. Lu, Y., et al., *Formation of bamboo-shape carbon nanotubes by controlled rapid decomposition of picric acid.* Carbon, 2004. **42**: p. 3199-3207.

359. Wei, D., et al., *A New Method to Synthesize Complicated Multibranched Carbon Nanotubes with Controlled Architecture and Composition.* Nano Letters, 2006. **6**(2): p. 186-192.

360. Lin, M., et al., *Dynamical Observation of Bamboo-like Carbon Nanotube Growth.* Nano Letters, 2007. **7**(8): p. 2234-2238.

361. Tu, Y., et al., *Growth of aligned carbon nanotubes with controlled site density.* Applied Physics Letters, 2002. **80**(21): p. 4018-4020.

362. Li, W.Z., J.G. Wen, and Z.F. Ren, *Effect of temperature on growth and structure of carbon nanotubes by chemical vapor deposition.* Applied Physics A, 2002. **74**(3): p. 397-402.

363. Li, W.Z., et al., *Effect of gas pressure on the growth and structure of carbon nanotubes by chemical vapor deposition.* Applied Physics A, 2001. **73**(2): p. 259-264.

364. lijima, S., T. Ichihashi, and Y. Ando, *Pentagons, heptagons and negative curvature in graphite microtubule growth.* Nature, 1992. **356**(6372): p. 776-778.

365. Lee, C.J. and J. Park, *Growth model of bamboo-shaped carbon nanotubes by thermal chemical vapor deposition.* Applied Physics Letters, 2000. **77**(21): p. 3397-3399.

366. Ding, F., K. Bolton, and A. Rosen, *Molecular Dynamics Study of Bamboo-Like Carbon Nanotube Nucleation.* Journal of Electronic Materials, 2006. **35**(2): p. 207-210.

367. Arabczyk, W. and J. Zamynny, *Study of the ammonia decomposition over iron catalysts.* Catalysis Letters, 1999. **60**: p. 167-171.

368. Raghavan, V., *C-Fe-N (carbon-iron-nitrogen).* Journal of Phase Equilibria and Diffusion, 1993. **14**(5): p. 620.

369. Lin, C.H., et al., *The role of nitrogen in carbon nanotube formation.* Diamond and Related Materials, 2003. **12**: p. 1851-1857.

370. Gyulikhandanov, E.L. and V.I. Shapochkin, *Kinetics of Saturation of Steel by Nitrogen and Carbon in High-Temperature Carbonitriding with High Nitrogen Potential.* Metal Science and Heat Treatment, 1994. **36**(3-4): p. 183-188.

371. Grobert, N., et al., *A novel route to aligned nanotubes and nanofibres using laser-patterned catalytic substrates.* Applied Physics A, 2000. **70**: p. 175-183.

372. Wang, J.N., L.F. Su, and Z.P. Wu, *Growth of Highly Compressed and Regular Coiled Carbon Nanotubes by a Spray-Pyrolysis Method.* Crystal Growth and Design, 2008. **8**(5): p. 1741-1747.

373. Luo, T., et al., *Synthesis of helically coiled carbon nanotubes by reducing ethyl ether with metallic zinc.* Carbon, 2005. **43**: p. 755-759.

374. Boehm, H.P., *Carbon from carbon monoxide disproportionation on nickel and iron catalysts: Morphological studies and possible growth mechanisms.* Carbon, 1973. **11**(6): p. 583-586.

375. Fonseca, A., et al., *Growth mechanism of coiled carbon nanotubes.* Synthetic Metals, 1996. **77**(1-3): p. 235-242.

376. Wen, Y. and Z. Shen, *Synthesis of regular coiled carbon nanotubes by Ni-catalyzed pyrolysis of acetylene and a growth mechanism analysis.* Carbon, 2001. **39**(15): p. 2369-2374.

377. Gothard, N., et al., *Controlled Growth of Y-Junction Nanotubes Using Ti-Doped Vapor Catalyst.* Nano Letters, 2004. **4**(2): p. 213-217.

378. Bandaru, P.R., et al., *Novel electrical switching behaviour and logic in carbon nanotube Y-junctions.* Nature Materials, 2005. **4**: p. 663-666.

379. Liu, B.C., et al., *Synthesis of well-aligned carbon nanotubes with open tips.* Carbon, 2005. **43**: p. 1341-1346.

380. AuBuchon, J.F., et al., *Multibranching Carbon Nanotubes via Self-Seeded Catalysts.* Nano Letters, 2006. **6**(2): p. 324-328.

381. Otsuka, K., et al., *Synthesis of carbon nanotubes on Ni/carbon-fiber catalysts under mild conditions.* Carbon, 2004. **42**: p. 727-736.

382. Tsai, S.-H., et al., *Tubes on tube--a novel form of aligned carbon nanotubes.* Carbon, 2002. **40**(9): p. 1597-1600.

383. Shao, M., et al., *Benzene-thermal route to carbon nanotubes at a moderate temperature.* Carbon, 2002. **40**(15): p. 2961-2963.

384. Vander Wal, R.L., *Flame synthesis of Ni-catalyzed nanofibers.* Carbon, 2002. **40**(12): p. 2101-2107.

385. Yuan, L., et al., *Nanotubes from methane flames.* Chemical Physics Letters, 2001. **340**(3-4): p. 237-241.

386. Matveev, A.T., et al., *Synthesis of carbon nanotubes below room temperature.* Carbon, 2001. **39**: p. 155-158.

387. Yamashita, J., et al., *Growth of a single-wall carbon nanotube in the gap of scanning tunneling microscope.* Applied Physics Letters, 1999. **74**(17): p. 2450-2452.

388. Rao, A.M., et al., *Structural characterization of heat-treated activated carbon fibers.* Journal of Materials Research, 1992. **7**(7): p. 1788-1794.

389. Deck, C., et al., *Mechanical Behavior of Ultralong Multiwalled Carbon Nanotube Mats.* Journal of Applied Physics, 2007. **101**(2): p. 023512.

390. Huang, S., et al., *Ultralong, Well-Aligned Single-Walled Carbon Nanotube Architectures on Surfaces.* Advanced Materials, 2003. **15**(19): p. 1651-1655.

391. Zhong, G., et al., *Growth Kinetics of 0.5 cm Vertically Aligned Single-Walled Carbon Nanotubes.* Journal of Physical Chemistry B, 2007. **111**(8): p. 1907-1910.

392. Endo, M., et al., *Structural characterization of carbon nanofibers obtained by hydrocarbon pyrolysis.* Carbon, 2001. **39**(13): p. 2003-2010.

393. Chopra, N., et al., *Control of Multiwalled Carbon Nanotube Diameter by Selective Growth on the Exposed Edge of a Thin Film Multilayer Structure.* Nano Letters, 2002. **2**(10): p. 1177-1181.

394. Kichambare, P.D., et al., *Thin film metallic catalyst coatings for the growth of multiwalled carbon nanotubes by pyrolysis of xylene.* Carbon, 2002. **40**(11): p. 1903-1909.

395. Emmenegger, C., et al., *Synthesis of carbon nanotubes over Fe catalyst on aluminium and suggested growth mechanism.* Carbon, 2003. **41**(3): p. 539-547.

396. Soneda, Y., L. Duclaux, and F. Beguin, *Synthesis of high quality multi-walled carbon nanotubes from the decomposition of acetylene on iron-group metal catalysts supported on MgO.* Carbon, 2002. **40**(6): p. 965-969.

397. Fazle Kibria, A.K.M., et al., *Synthesis of narrow-diameter carbon nanotubes from acetylene decomposition over an iron-nickel catalyst supported on alumina.* Carbon, 2002. **40**(8): p. 1241-1247.

398. Zhu, S., et al., *Carbon nanotube growth on carbon fibers.* Diamond and Related Materials, 2003. **12**: p. 1825-1828.

399. Li, Z., et al., *Catalytic synthesized carbon nanostructures from methane using nanocrystalline Ni.* Carbon, 2002. **40**(3): p. 409-415.

400. Franklin, N.R., et al., *Patterned growth of single-walled carbon nanotubes on full 4-inch wafers.* Applied Physics Letters, 2001. **79**(27): p. 4571-4573.

401. Lee, C.J., et al., *Growth and field emission of carbon nanotubes on sodalime glass at 550°C using thermal chemical vapor deposition.* Chemical Physics Letters, 2001. **337**: p. 398-402.

402. Park, J.-B., et al., *Characterization of Fe-catalyzed carbon nanotubes grown by thermal chemical vapor deposition.* Journal of Crystal Growth, 2002. **244**: p. 211-217.

403. Lee, C.J., et al., *Low-temperature growth of carbon nanotubes by thermal chemical vapor deposition using Pd, Cr, and Pt as co-catalyst.* Chemical Physics Letters, 2000. **327**: p. 277-283.

404. Lee, K.-H., et al., *Silicon enhanced carbon nanotube growth on nickel films by chemical vapor deposition.* Solid State Communications, 2004. **129**: p. 583-587.

405. Maohui, G. and K. Sattler, *Vapor-condensation generation and STM analysis of fullerene tubes.* Science, 1993. **260**(5107): p. 515-518.

406. Liu, X.-Y., B.-C. Huang, and N.J. Coville, *The Fe(CO)5 catalyzed pyrolysis of pentane carbon nanotube and carbon nanoball formation.* Carbon, 2002. **40**(15): p. 2791-2799.

407. Harutyunyana, A.R., G. Chen, and P.C. Eklund, *Self-assembled growth of single-walled carbon nanotubes by pyrolysis of metalorganic precursor.* Applied Physics Letters, 2003. **82**(26): p. 4794-4796.

408. Cao, A., et al., *Macroscopic Three-Dimensional Arrays of Fe Nanoparticles Supported in Aligned Carbon Nanotubes.* Journal of Physical Chemistry B, 2001. **105**: p. 11937-11940.

409. Kuwana, K. and K. Saito, *Modeling CVD synthesis of carbon nanotubes: Nanoparticle formation from ferrocene.* Carbon, 2005. **43**: p. 2088-2095.

410. Singh, C., M.S.P. Shaffer, and A.H. Windle, *Production of controlled architectures of aligned carbon nanotubes by an injection chemical vapour deposition method.* Carbon, 2003. **41**(2): p. 359-368.

411. Ren, Z.F., et al., *Synthesis of Large Arrays of Well-Aligned Carbon Nanotubes on Glass.* Science, 1998. **282**: p. 1105-1107.

412. Chen, M., C.-M. Chen, and C.-F. Chen, *Preparation of high yield multi-walled carbon nanotubes by microwave plasma chemical vapor deposition at low temperature.* Journal of Materials Science, 2002. **37**: p. 3561-3567.

413. Huang, Z.P., et al., *Growth of highly oriented carbon nanotubes by plasma-enhanced hot filament chemical vapor deposition.* Applied Physics Letters, 1998. **73**(26): p. 3845-3847.

414. Kurt, R., J.-M. Bonard, and A. Karimi, *Morphology and field emission properties of nano-structured nitrogenated carbon films produced by plasma enhanced hot filament CVD.* Carbon, 2001. **39**: p. 1723-1730.

415. Chen, J.H., et al., *Electrochemical synthesis of polypyrrole/carbon nanotube nanoscale composites using well-aligned carbon nanotube arrays.* Applied Physics A, 2001. **73**: p. 129-131.

416. Wal, R.L.V., T.M. Ticich, and V.E. Curtis, *Diffusion flame synthesis of single-walled carbon nanotubes.* Chemical Physics Letters, 2000. **323**: p. 217-223.

417. Height, M.J., et al., *Flame synthesis of single-walled carbon nanotubes.* Carbon, 2004. **42**: p. 2295-2307.

418. Chen, Z., et al. *Fabrication of Self-Organized Carbon nanotubes on Si Substrates Using nano-Template by Flame Synthesis Technique*. in *International Semiconductor Device Research Symposium*. 2001. Piscataway, NJ, USA: IEEE.

419. Farhat, S., et al., *Diameter control of single-walled carbon nanotubes using argon-helium mixture gases.* Journal of Chemical Physics, 2001. **115**(14): p. 6752-6759.

420. Saito, Y. and S. Uemura, *Field emission from Carbon Nanotubes and its application to Electron Sources.* Carbon, 2000. **38**: p. 169-182.

421. Tang, D.S., et al., *Evidence for an open-ended nanotube growth model in arc discharge.* Carbon, 2000. **38**: p. 480-483.

422. Ebbesen, T.W. and P.M. Ajayan, *Large-scale synthesis of carbon nanotubes.* Nature, 1992. **358**(6383): p. 220-222.

423. Gamaly, E.G. and T.W. Ebbesen, *Mechanism of carbon nanotube formation in the arc discharge.* Physical Review B, 1995. **52**(3): p. 2083-2089.

424. Cadek, M., et al., *Optimisation of the arc-discharge production of multi-walled carbon nanotubes.* Carbon, 2002. **40**(6): p. 923-928.

425. Jung, S.H., et al., *High-yield synthesis of multi-walled carbon nanotubes by arc discharge in liquid nitrogen.* Applied Physics A, 2003. **76**(2): p. 285-286.

426. Kiang, C.-H., et al., *Carbon nanotubes with single-layer walls.* Carbon, 1995. **33**(7): p. 903-914.

427. Journet, C. and P. Bernier, *Production of carbon nanotubes.* Applied Physics A, 1998. **67**(1): p. 1-9.

428. Braidy, N., M.A. El Khakani, and G.A. Botton, *Effect of laser intensity on yield and physical characteristics of single wall carbon nanotubes produced by the Nd:YAG laser vaporization method.* Carbon, 2002. **40**(15): p. 2835-2842.

429. Puretzky, A.A., et al., *Dynamics of single-wall carbon nanotube synthesis by laser vaporization.* Applied Physics A, 2000. **70**: p. 153-160.

430. Scott, C.D., et al., *Growth mechanisms for single-wall carbon nanotubes in a laser-ablation process.* Applied Physics A, 2001. **72**(5): p. 573-580.

431. Kokai, F., et al., *Laser ablation of graphite-Co/Ni and growth of single-wall carbon nanotubes in vortexes formed in an Ar atmosphere.* Journal of Physical Chemistry B, 2000. **104**(29): p. 6777-6784.

432. Bolshakova, A.P., et al., *A novel CW laser-powder method of carbon single-wall nanotubes production.* Diamond and Related Materials, 2002. **11**(3-6): p. 927-930.

433. Kokai, F., et al., *Growth dynamics of single-wall carbon nanotubes synthesized by CO2 laser vaporization.* Journal of Physical Chemistry B, 1999. **103**(21): p. 4346-4351.

434. Yudasaka, M., et al., *Formation of single-wall carbon nanotubes: comparison of CO2 laser ablation and Nd:YAG laser ablation.* Journal of Physical Chemistry B, 1999. **103**(18): p. 3576-3581.

435. Puretzky, A.A., et al., *Investigations of single-wall carbon nanotube growth by time-restricted laser vaporization.* Physical Review B, 2002. **65**: p. 245425.

436. Eklund, P.C., et al., *Large-scale production of single-walled carbon nanotubes using ultrafast pulses from a free electron laser.* Nano Letters, 2002. **2**(6): p. 561-566.

437. Yudasaka, M., T. Ichihashi, and S. Iijima, *Roles of laser light and heat in formation of single-wall carbon nanotubes by pulsed laser ablation of Cx Niy Coy targets at high temperature.* Journal of Physical Chemistry B, 1998. **102**(50): p. 10201-10207.

438. Maser, W.K., et al., *Production of high-density single-walled nanotube material by a simple laser-ablation method.* Chemical Physics Letters, 1998. **292**(4-6): p. 587-593.

439. Rinzler, A.G., et al., *Large-scale purification of single-wall carbon nanotubes: process, product, and characterization.* Applied Physics A, 1998. **67**(1): p. 29-37.

440. Thess, A., et al., *Crystalline ropes of metallic carbon nanotubes.* Science, 1996. **273**(5274): p. 483-487.

441. Guo, T., et al., *Self-Assembly of Tubular Fullerenes.* Journal of Physical Chemistry A, 1995. **99**(27): p. 10694-10697.

442. Jost, O., et al., *Diameter grouping in bulk samples of single-walled carbon nanotubes from optical absorption spectroscopy.* Applied Physics Letters, 1999. **75**(15): p. 2217-2219.

443. Chattopadhyay, D., I. Galeska, and F. Papadimitrakopoulos, *Complete elimination of metal catalysts from single wall carbon nanotubes.* Carbon, 2002. **40**(7): p. 985-988.

444. McKee, G.S.B. and K.S. Vecchio, *Thermogravimetric analysis of synthesis variation effects on CVD generated multiwalled carbon nanotubes.* Journal of Physical Chemistry B, 2006. **110**(3): p. 1179-1186.

445. Eklund, P.C., J.M. Holden, and R.A. Jishi, *Vibrational modes of carbon nanotubes; Spectroscopy and theory.* Carbon, 1995. **33**(7): p. 959-972.

446. Dresselhaus, M.S., et al., *Raman spectroscopy on isolated single wall carbon nanotubes.* Carbon, 2002. **40**(12): p. 2043-2061.

447. Jorio, A., et al., *Characterizing carbon nanotube samples with resonance Raman scattering.* New Journal of Physics, 2003. **5**: p. 139.1-17.

448. Chieu, T.C., M.S. Dresselhaus, and M. Endo, *Raman studies of benzene-derived graphite fibers.* Physical Review B, 1982. **26**(10): p. 5867-5877.

449. Tan, P., Y. Deng, and Q. Zhao, *Temperature-dependent Raman spectra and anomalous Raman phenomenon of highly oriented pyrolytic graphite.* Physical Review B, 1998. **58**(9): p. 5435-5439.

450. Leung, S.Y., M.S. Dresselhaus, and G. Dresselhaus, *Infrared and Raman Spectroscopy of Graphite Intercalation Compounds.* Physica, 1981. **105B**: p. 375-380.

451. Maultzsch, J., et al., *Raman characterization of boron-doped multiwalled carbon nanotubes.* Applied Physics Letters, 2002. **81**(14): p. 2647-2649.

452. Shimada, T., et al., *Origin of the 2450 cm-1 Raman bands in HOPG, single-wall and double-wall carbon nanotubes.* Carbon, 2005. **43**: p. 1049-1054.

453. Kawashima, Y. and G. Katagiri, *Fundamentals, overtones, and combinations in the Raman spectrum of graphite.* Physical Review B, 1995. **52**(14): p. 10053-10059.

454. Pimenta, M.A., et al., *The Anomalous Dispersion of the Disorder-Induced and the Second-Order Raman Bands in Carbon Nanotubes.* Brazilian Journal of Physics, 2000. **30**(2): p. 423-427.

455. Antunes, E.F., et al., *Comparative study of first- and second-order Raman spectra of MWCNT at visible and infrared laser excitation.* Carbon, 2006. **44**: p. 2202-2211.

456. Peigney, A., et al., *Specific surface area of carbon nanotubes and bundles of carbon nanotubes.* Carbon, 2001. **39**: p. 507-514.

457. Qu, L., et al., *Carbon Nanotube Electroactive Polymer Materials: Opportunities and Challenges.* MRS Bulletin, 2008. **33**: p. 215-224.

458. Kong, J., et al., *Nanotube Molecular Wires as Chemical Sensors.* Science, 2000. **287**(5453): p. 622-625.

459. Romero, H.E., et al., *Atom Collision–Induced Resistivity of Carbon Nanotubes.* Science, 2005. **307**: p. 89-93.

460. Qu, L. and L. Dai, *Polymer-masking for controlled functionalization of carbon nanotubes.* Chemical Communications, 2007. **37**: p. 3859-3861.

461. Wei, C., et al., *Multifunctional Chemical Vapor Sensors of Aligned Carbon Nanotube and Polymer Composites.* Journal of the American Chemical Society, 2006. **128**(5): p. 1412-1413.

462. Zhao, G.-C., et al., *Myoglobin on multi-walled carbon nanotubes modified electrode: direct electrochemistry and electrocatalysis.* Electrochemistry Communications, 2003. **5**(9): p. 825-829.

463. Gao, M., L. Dai, and G.G. Wallace, *Biosensors Based on Aligned Carbon Nanotubes Coated with Inherently Conducting Polymers.* Electroanalysis, 2003. **15**(13): p. 1089-1094.

464. Dai, H., et al., *Nanotubes as nanoprobes in scanning probe microscopy.* Nature, 1996. **384**(6605): p. 147-150.

465. Wong, S.S., et al., *Carbon Nanotube Tips: High-Resolution Probes for Imaging Biological Systems.* Journal of the American Chemical Society, 1998. **120**: p. 603-604.

466. Wong, S.S., et al., *Covalently functionalized nanotubes as nanometresized probes in chemistry and biology.* Nature, 1998. **394**: p. 52-55.

467. Stampfer, C., et al., *Fabrication of Single-Walled Carbon-Nanotube-Based Pressure Sensors.* Nano Letters, 2006. **6**(2): p. 233-237.

468. Grow, R.J., et al., *Piezoresistance of carbon nanotubes on deformable thin-film membranes.* Applied Physics Letters, 2005. **86**: p. 093104.

469. Hierold, C., et al., *Nano electromechanical sensors based on carbon nanotubes.* Sensors and Actuators A, 2007. **136**: p. 51-61.

470. Laxminarayana, K. and N. Jalili, *Functional Nanotube-based Textiles: Pathway to Next Generation Fabrics with Enhanced Sensing Capabilities.* Textile Research Journal, 2005. **75**(9): p. 670-680.

471. Wood, J.R. and H.D. Wagner, *Single-wall carbon nanotubes as molecular pressure sensors.* Applied Physics Letters, 2000. **76**(20): p. 2883-2885.

472. Wood, J.R., et al., *Mechanical Response of Carbon Nanotubes under Molecular and Macroscopic Pressures.* Journal of Physical Chemistry B, 1999. **103**: p. 10388-10392.

473. Wood, J.R., et al., *Carbon nanotubes: From molecular to macroscopic sensors.* Physical Review B, 2000. **62**(11): p. 7571-7575.

474. Lourie, O. and H.D. Wagner, *Evaluation of Young's modulus of carbon nanotubes by micro-Raman spectroscopy.* Journal of Materials Research, 1998. **13**(9): p. 2418-2422.

475. Gao, R., et al., *Nanomechanics of Individual Carbon Nanotubes from Pyrolytically Grown Arrays.* Physical Review Letters, 2000. **85**(3): p. 622-625.

476. Král, P. and M. Shapiro, *Nanotube Electron Drag in Flowing Liquids.* Physical Review Letters, 2001. **86**(1): p. 131-134.

477. Ghosh, S., A.K. Sood, and N. Kumar, *Carbon Nanotube Flow Sensors.* Science, 2003. **299**: p. 1042-1044.

478. Liu, J., L. Dai, and J.W. Baur, *Multiwalled carbon nanotubes for flow-induced voltage generation.* Journal of Applied Physics, 2007. **101**: p. 064312.

479. Wallenberger, F.T. and P.C. Nordine, *Strong, Pure, and Uniform Carbon Fibers Obtained Directly from the Vapor Phase.* Science, 1993. **260**(5104): p. 66-68.

480. Jacobsen, R.L., et al., *Mechanical properties of vapor-grown carbon fiber.* Carbon, 1995. **33**(9): p. 1217-1221.

481. Qian, D. and E.C. Dickey, *In situ transmission electron microscopy studies of polymer-carbon nanotube composite deformation.* Journal of Microscopy, 2001. **204**(1): p. 39-45.

482. Stephan, C., et al., *Characterization of singlewalled carbon nanotubes-PMMA composites.* Synthetic Metals, 2000. **108**: p. 139-149.

483. McCarthy, B., et al., *Complex nano-assemblies of polymers and carbon nanotubes.* Nanotechnology, 2001. **12**: p. 187-190.

484. Cooper, C.A., et al., *Distribution and alignment of carbon nanotubes and nanofibrils in a polymer matrix.* Composites Science and Technology, 2002. **62**: p. 1105-1112.

485. An, J.W., D.H. You, and D. S. Lim, *Tribological properties of hot-pressed alumina–CNT composites.* Wear, 2003. **255**: p. 677-681.

486. Vigolo, B., et al., *Macroscopic Fibers and Ribbons of Oriented Carbon Nanotubes.* Science, 2000. **290**: p. 1331-1334.

487. Miaudet, P., et al., *Thermo-electrical properties of PVA-nanotube composite fibers.* Polymer, 2007. **48**: p. 4068-4074.

488. Miaudet, P., et al., *Hot-Drawing of Single and Multiwall Carbon Nanotube Fibers for High Toughness and Alignment.* Nano Letters, 2005. **5**(11): p. 2212-2215.

489. Poulin, P., B. Vigolo, and P. Launois, *Films and fibers of oriented single wall nanotubes.* Carbon, 2002. **40**(10): p. 1741-1749.

490. Haquea, A., A. Ramasettya, and S. Shamsuzzohab, *Characterization of Carbon Nanotube-Reinforced Polymer Composites.* 2002.

491. Cooper, C.A., et al., *Detachment of nanotubes from a polymer matrix.* Applied Physics Letters, 2002. **81**(20): p. 3873-3875.

492. Watts, P.C.P., et al., *Fe-filled carbon nanotube-polystyrene: RCL composites.* Chemical Physics Letters, 2002. **366**: p. 42-50.

493. Sennett, M., et al., *Dispersion and alignment of carbon nanotubes in polycarbonate.* Applied Physics A, 2003. **76**: p. 111-113.

494. Jia, Z., et al., *Study on poly(methyl methacrylate):carbon nanotube composites.* Materials Science & Engineering A, 1999. **271**: p. 395-400.

495. Shaffer, M.S.P. and A.H. Windle, *Fabrication and Characterization of Carbon Nanotube/Poly(vinyl alcohol) Composites.* Advanced Materials, 1999. **11**(11): p. 937-941.

496. Dong, S.R., J.P. Tu, and X.B. Zhang, *An investigation of the sliding wear behavior of Cu-matrix composite reinforced by carbon nanotubes.* Materials Science & Engineering A, 2001. **313**: p. 83-87.

497. Xia, Z., et al., *Direct observation of toughening mechanisms in carbon nanotube ceramic matrix composites.* Acta Materialia, 2004. **52**(4): p. 931-944.

498. Ajayan, P.M., et al., *Single-Walled Carbon Nanotube-Polymer Composites: Strength and Weakness.* Advanced Materials, 2000. **12**(10): p. 750-753.

499. Cooper, C.A., et al., *Detachment of Nanotubes from a polymer matrix.* Applied Physics Letters, 2002. **81**(20): p. 3873-3875.

500. Bower, C., et al., *Deformation of carbon nanotubes in nanotube–polymer composites.* Applied Physics Letters, 1999. **74**(22): p. 3317-3319.

501. Schadler, L.S., et al., *Nanotube Reinforced Polymer Composites - Tailoring the Interface for Improved Mechanical Properties.* 2003: p. 1-9.

502. Qian, D., et al., *Load transfer and deformation mechanisms in carbon nanotube-polystyrene composites.* Applied Physics Letters, 2000. **76**(20): p. 2868-2870.

503. Thostenson, E.T. and T.-W. Chou, *Aligned multi-walled carbon nanotube-reinforced composites: processing and mechanical characterization.* Journal of Physics D: Applied Physics, 2002. **35**: p. L77-L80.

504. Andrews, R., et al., *Nanotube composite carbon fibers.* Applied Physics Letters, 1999. **75**(9): p. 1329-1331.

505. Xia, Z., W.A. Curtin, and B.W. Sheldon, *Fracture toughness of highly ordered carbon nanotube/alumina nanocomposites.* Journal of Engineering Materials and Technology, 2004. **126**(3): p. 238-244.

506. Lim, D.-S., J.-W. An, and H.J. Lee, *Effect of carbon nanotube addition on the tribological behavior of carbon/carbon composites.* Wear, 2002. **252**: p. 512-517.

507. Jin, Z., et al., *Dynamic mechanical behavior of melt-processed multi-walled carbon nanotube/poly(methyl methacrylate) composites.* Chemical Physics Letters, 2001. **337**: p. 43-47.

508. Chen, M., et al., *Characterization of Single-walled Carbon Nanotube Fibers and Correlation with Stretch Alignment.* Materials Research Society Conference Proceedings, 2005. **858E**: p. HH4.11.

509. Bryning, M.B., et al., *Thermal conductivity and interfacial resistance in single-wall carbon nanotube epoxy composites.* Applied Physics Letters, 2005. **87**: p. 161909-1 to 161909-3.

510. Kymakis, E., I. Alexandou, and G.A.J. Amaratunga, *Single-walled Carbon Nanotube-Polymer Composites: Electrical, Optical, and Structural Investigation.* Synthetic Metals, 2002. **127**: p. 59-62.

511. Wei, C., D. Srivastava, and K. Cho, *Thermal Expansion and Diffusion Coefficients of Carbon Nanotube-Polymer Composites.* Nano Letters, 2002. **2**(6): p. 647-650.

512. Bin, Y., et al., *Morphology and mechanical and electrical properties of oriented PVA–VGCF and PVA–MWNT composites.* Polymer, 2006. **47**: p. 1308-1317.

513. Gao, Y., et al., *Effects of Surface Modification, Carbon Nanofiber Concentration, and Dispersion Time on the Mechanical Properties of Carbon-Nanofiber–Polycarbonate Composites.* Journal of Applied Polymer Science, 2007. **103**(5): p. 3792-3797.

514. Ericson, L.M., et al., *Macroscopic, Neat, Single-Walled Carbon Nanotube Fibers.* Science, 2004. **305**: p. 1447-1450.

515. Hearle, J.W.S., P. Grosberg, and S. Backer, *Structural Mechanics of Fibers, Yarns, and Fabrics*. Vol. 1. 1969, New York: Wiley-Interscience. 255-306.

516. Lashmore, D.S., et al., *Systems and Methods for Formation and Harvesting of Nanofibrous Materials*. 2007: United States.

517. *Nanocomp Technologies Inc.* 2008: www.nanocomptech.com.

518. Atkinson, K.R., et al., *Multifunctional carbon nanotube yarns and transparent sheets: Fabrication, properties, and applications.* Physica B, 2007. **394**: p. 339-343.

519. Liu, K., et al., *Controlled Growth of Super-Aligned Carbon Nanotube Arrays for Spinning Continuous Unidirectional Sheets with Tunable Physical Properties.* Nano Letters, 2008. **8**(2): p. 700-705.

520. Wei, Y.Y. and G. Eres, *Direct fabrication of carbon nanotube circuits by selective area chemical vapor deposition on pre-patterned structures.* Nanotechnology, 2000. **11**: p. 61-64.

521. Wei, Y.Y. and G. Eres, *Directed assembly of carbon nanotube electronic circuits.* Applied Physics Letters, 2000. **76**(25): p. 3759-3761.

522. Lee, Y.-H., et al., *Direct nano-wiring carbon nanotube using growth barrier: A possible mechanism of selective lateral growth.* Journal of Applied Physics, 2002. **91**(9): p. 6044-6050.

523. Tans, S.J., R.M. Verschueren, and C. Dekker, *Room temperature transistor based on a single carbon nanotube.* Nature, 1998. **393**(6680): p. 49-52.

524. Wind, S.J., et al., *Fabrication and electrical characterization of top gate single-wall carbon nanotube field-effect transistors.* Journal of Vacuum Science and Technology B, 2002. **20**(6): p. 2798-2801.

525. Rochefort, A., M.D. Ventra, and P. Avouris, *Switching behavior of semiconducting carbon nanotubes under an external electric field.* Applied Physics Letters, 2001. **78**(17): p. 2521-2523.

526. Postma, H.W.C., et al., *Carbon nanotube single-electron transistors at room temperature.* Science, 2001. **293**(5527): p. 76-79.

527. Kong, J., et al., *Chemical profiling of single nanotubes: Intramolecular p-n-p junctions and on-tube single-electron transistors.* Applied Physics Letters, 2002. **80**(1): p. 73-75.

528. Wu, Z., et al., *Transparent, Conductive Carbon Nanotube Films.* Science, 2004. **305**: p. 1273-1276.

529. Serp, P., M. Corrias, and P. Kalck, *Carbon nanotubes and nanofibers in catalysis.* Applied Catalysis A: General, 2003. **253**(2): p. 337-358.

530. Jang, J.E., et al. *Nanoscale Capacitors based on Metal-Insulator-Carbon Nanotube-Metal (MICNM) Structures*. in *Proceedings of ESSDERC*. 2005. Grenoble, France: IEEE.

531. Zhang, B., et al., *Electric double-layer capacitors using carbon nanotube electrodes and organic electrolyte.* Materials Letters, 2001. **51**: p. 539-542.

532. Flicker, J. and J. Ready, *Simulations of absorbance efficiency and power production of three dimensional tower arrays for use in photovoltaics.* Journal of Applied Physics, 2008. **103**(11): p. 113110.

533. Cheng, H.-M., Q.-H. Yang, and C. Liu, *Hydrogen storage in carbon nanotubes.* Carbon, 2001. **39**: p. 1447-1454.

534. Zuttel, A., et al., *Hydrogen storage in carbon nanostructures.* International Journal of Hydrogen Energy, 2002. **27**(2): p. 203-212.

535. Nijkamp, M.G., et al., *Hydrogen storage using physisorption-materials demands.* Applied Physics A, 2001. **A72**(5): p. 619-623.

536. Daenen, M., et al., *The Wondrous World of Carbon Nanotubes (Unpublished)*. 2003: Eindhoven University of Technology.

537. Rajalakshmi, N., et al., *Electrochemical investigation of single-walled carbon nanotubes for hydrogen storage.* Electrochimica Acta, 2000. **45**(27): p. 4511-4515.

538. Fazle Kibria, A.K.M., et al., *Electrochemical hydrogen storage behaviors of CVD, AD and LA grown carbon nanotubes in KOH medium.* International Journal of Hydrogen Energy, 2001. **26**(8): p. 823-829.

539. Zuttel, A., et al., *Hydrogen sorption by carbon nanotubes and other carbon nanostructures.* Journal of Alloys & Compounds, 2002. **330**: p. 676-682.

540. Li, X., et al., *Hydrogen uptake by graphitized multi-walled carbon nanotubes under moderate pressure and at room temperature.* Carbon, 2001. **39**(13): p. 2077-2079.

541. Yang, F.H. and R.T. Yang, *Ab initio molecular orbital study of adsorption of atomic hydrogen on graphite: Insight into hydrogen storage in carbon nanotubes.* Carbon, 2002. **40**(3): p. 437-444.

542. Levesque, D., et al., *Monte Carlo simulations of hydrogen storage in carbon nanotubes.* Journal of Physics-Condensed Matter, 2002. **14**(40): p. 9285-9293.

543. Hirscher, M., et al., *Hydrogen storage in carbon nanostructures.* Journal of Alloys & Compounds, 2002. **330**: p. 654-658.

544. Chernozatonskii, L.A., et al., *Electron field emission from nanofilament carbon films.* Chemical Physics Letters, 1995. **233**(1-2): p. 63-68.

545. de Heer, W.A., A. Chatelain, and D. Ugarte, *A carbon nanotube field-emission electron source.* Science, 1995. **270**(5239): p. 1179-1180.

546. Rinzler, A.G., et al., *Unraveling nanotubes: field emission from an atomic wire.* Science, 1995. **269**(5230): p. 1550-1553.

547. Jo, S.H., et al., *Effect of length and spacing of vertically aligned carbon nanotubes on field emission properties.* Applied Physics Letters, 2003. **82**(20): p. 3520-3522.

548. Bonard, J.M., et al., *Field emission properties of multiwalled carbon nanotubes.* Ultramicroscopy, 1998. **73**(1-4): p. 7-15.

549. Bonard, J.M., et al., *Field emission from carbon nanotubes: The first five years.* Solid State Electronics, 2001. **45**(6): p. 893-914.

550. Pirio, G., et al., *Fabrication and electrical characteristics of carbon nanotube field emission microcathodes with an integrated gate electrode.* Nanotechnology, 2002. **13**: p. 1-4.

551. Lee, O.-J. and K.-H. Lee, *Fabrication of flexible field emitter arrays of carbon nanotubes using self-assembly monolayers.* Applied Physics Letters, 2003. **82**(21): p. 3770-3772.

552. Kim, J.M., et al., *Field emission from carbon nanotubes for displays.* Diamond and Related Materials, 2000. **9**: p. 1184-1189.

553. Lee, S.B., et al., *Fabrication of carbon nanotube lateral field emitters.* Nanotechnology, 2003. **14**: p. 192-195.

554. Kim, H.J., et al., *Fabrication of field emission triode using carbon nanotubes.* Materials Science & Engineering C, 2001. **16**: p. 27-30.

555. Bonard, J.-M., et al., *Carbon nanotube films as electron field emitters.* Carbon, 2002. **40**(10): p. 1715-1728.

556. Sohn, J.I. and S. Lee, *Micropatterned vertically aligned carbon-nanotube growth on a Si surface or inside trenches.* Applied Physics A, 2002. **74**: p. 287-290.

557. Lazic, S., *Microcrystalline hydroxyapatite formation from alkaline solutions.* Journal of Crystal Growth, 1995. **147**(1-2): p. 147-154.

558. Brown, P.W., N. Hocker, and S. Hoyle, *Variations in solution chemistry during the low-temperature formation of hydroxyapatite.* Journal of the American Ceramic Society, 1991. **74**(8): p. 1848-1854.

559. Zhang, H., et al., *Layered growth of aligned carbon nanotube arrays by pyrolysis.* Physica B, 2003. **337**: p. 10-16.

560. Pinault, M., et al., *Growth of multiwalled carbon nanotubes during the initial stages of aerosol-assisted CCVD.* Carbon, 2005. **43**: p. 2968-2976.

561. Aguilar-Elguezabal, A., et al., *Study of carbon nanotubes synthesis by spray pyrolysis and model of growth.* Diamond and Related Materials, 2006. **15**: p. 1329-1335.

562. Borowiecki, T., *Effect of the support on the coking of nickel catalysts in hydrocarbon steam reforming.* Journal Reaction Kinetics and Catalysis Letters, 1987. **33**(2): p. 429-434.

563. Kunimori, K., et al., *Metal-support interaction in alumina-supported Pt catalysts.* Journal of Catalysis, 1983. **79**(1): p. 185-195.

564. Shchipalov, Y.K., *Surface energy of crystalline and vitreous silica.* Glass and Ceramics, 2000. **57**(11-12): p. 374-377.

565. Lodziana, Z., N.-Y. Topsoe, and J.K. Norskov, *A negative surface energy for alumina.* Nature Materials, 2004. **3**(5): p. 289-293.

566. Tian, D.-X. and X.-Y. Guo, *Coalescence kinetics of free and supported metal clusters.* Computational Materials Science, 2005. **34**: p. 14-21.

567. Phillips, W.B., E.A. Desloge, and J.G. Skofronick, *A Mechanism to Account for Observed Morphological Changes in Discontinuous Gold Films following Deposition.* Journal of Applied Physics, 1968. **39**(7): p. 3210.

568. Jensen, P., *Growth of nanostructures by cluster deposition: Experiments and simple models.* Reviews of Modern Physics, 1999. **71**(5): p. 1695-1731.

569. Kashchiev, D., *Kinetics of thin film coalescence due to crystallite surface migration.* Surface Science, 1976. **55**(2): p. 477-493.

570. , et al., *Morphological Changes in Discontinuous Gold Films following Deposition.* Journal of Applied Physics, 1967. **38**(12): p. 4791-4796.

571. Ruckenstein, E. and B. Pulvermacher, *Growth kinetics and the size distributions of supported metal crystallites.* Journal of Catalysis, 1973. **29**(2): p. 224-245.

572. Houser, T.J., et al., *Kinetics of formation of HCN during pyridine pyrolysis.* International Journal of Chemical Kinetics, 1980. **12**(8): p. 569-574.

573. Houser, T.J., M.E. McCarville, and T. Biftu, *Kinetics of the thermal decomposition of pyridine in a flow system.* International Journal of Chemical Kinetics, 1980. **12**(8): p. 555-568.

574. Alexiou, A. and A. Williams, *Soot formation in shock-tube pyrolysis of pyridine and toluene-pyridine mixtures.* Fuel, 1994. **73**(8): p. 1280-1283.

575. Jang, J.W., et al., *Structural study of nitrogen-doping effects in bamboo-shaped multiwalled carbon nanotubes.* Applied Physics Letters, 2004. **84**(15): p. 2877-2879.

576. Wang, Y.Y., et al., *Experimental studies of the formation process and morphologies of carbon nanotubes with bamboo mode structures.* Diamond and Related Materials, 2004. **13**: p. 1287-1291.

577. Schomaker, V. and L. Pauling, *The Electron Diffraction Investigation of the Structure of Benzene, Pyridine, Pyrazine, Butadiene-l,3, Cyclopentadiene, Furan, Pyrrole, and Thiophene.* Stuctures of Some Similar Ring Compounds, 1939. **61**: p. 1769-1780.

578. Ugural, A.C. and S.K. Fenster, *Advanced Strength and Applied Elasticity*. 3rd ed. 1995, Upper Saddle River, NJ: Prentice Hall. 570.

579. Deck, C.P. and K.S. Vecchio, *Growth Mechanism of Vapor-phase CVD-grown Multi-walled Carbon Nanotubes.* Carbon, 2005. **43**(12): p. 2608-2617.

580. Li, Y., et al., *Tensile properties of long aligned double-walled carbon nanotube strands.* Carbon, 2005. **43**: p. 31-35.

581. Ghosh, A., S.M. Ishtiaque, and R.S. Rengasamy, *Analysis of Spun Yarn Failure. Part I: Tensile Failure of Yarns as a Function of Structure and Testing Parameters.* Textile Research Journal, 2005. **75**(10): p. 731-740.

582. Shao, X., Y. Qiu, and Y. Wang, *Theoretical modeling of the tensile behavior of low-twist staple yarns: Part I – theoretical model.* Journal of the Textile Institute, 2005. **96**(2): p. 61-68.

583. Shao, X., Y. Qiu, and Y. Wang, *Theoretical modeling of the tensile behavior of low-twist staple yarns: Part II – theoretical and experimental results.* Journal of the Textile Institute, 2005. **96**(2): p. 69-76.

584. Lynch, H.A., et al., *Effect of Fiber Orientation and Strain Rate on the Nonlinear Uniaxial Tensile Material Properties of Tendon.* Journal of Biomechanical Engineering, 2003. **125**: p. 726-731.

585. Mazzoldi, A., D.D. Rossi, and R.H. Baughman, *Electro-mechanical behavior of carbon nanotube sheets in electrochemical actuators.* Proceedings of SPIE, 2000. **3987**: p. 25-32.

586. Hertzberg, R.W., *Deformation and Fracture Mechanics of Engineering Materials*. 4th ed. 1996, New York: John Wiley & Sons, Inc. 786.

587. Nichols, J.A., et al., *Artificial introduction of defects into vertically aligned multiwalled carbon nanotube ensembles: Application to electrochemical sensors.* Journal of Applied Physics, 2007. **102**: p. 064306.

588. McKee, G.S.B., C.P. Deck, and K.S. Vecchio, *Dimensional Control of Multi-Walled Carbon Nanotubes in Floating-Catalyst CVD Synthesis.* Submitted to Carbon, 2008.

589. Powell, R.L. and G.E. Childs, *American Institute of Physics Handbook*. Third ed. 1972: Mcgraw-Hill.

590. Paulson, S., et al., *Tunable Resistance of a Carbon Nanotube-Graphite Interface.* Science, 2000. **290**(5497): p. 1742-1744.

591. Song, B., W. Chen, and W.-Y. Lu, *Compressive mechanical response of a low-density epoxy foam at various strain rates.* Journal of Materials Science, 2007. **42**(17): p. 7502-7507.

592. Beer, F.P., J. E. Russell Johnson, and J.T. DeWolf, *Mechanics of Materials*. 4th ed. 2006, Boston: McGraw Hill.

593. Fox, R.W. and A.T. McDonald, *Introduction to Fluid Mechanics*. 5th ed. 1998, New York: John Wiley & Sons, Inc.

594. Walther, J.H., et al., *Hydrodynamic properties of carbon nanotubes.* Physical Review E, 2004. **69**: p. 062201.

595. Barber, R.W. and D.R. Emerson, *Analytical solution of low Reynolds number slip flow past a sphere*, in *Technical Report*. 2000, Computational Science and Engineering Department: CLRC Daresbury Laboratory.

596. White, F.M., *Fluid Mechanics*. Third ed. 1994, New York: McGraw-Hill.

597. Tang, W. and S.G. Advani, *Drag on a nanotube in uniform liquid argon flow.* The Journal of Chemical Physics, 2006. **236**: p. 174706.

598. Ford, A.N. and D.V. Papavassiliou, *Flow around Surface-Attached Carbon Nanotubes.* Ind. Eng. Chem. Res., 2006. **45**: p. 1797-1804.

599. Ni, C., et al., *Optical determination of the flexural rigidity of carbon nanotube ensembles.* Applied Physics Letters, 2008. **92**: p. 173106.